# The physical oceanography of a broad, mid-latitude fjord : observations, seasonality and wind response of Fortune Bay (Newfoundland, Canada)

Sébastien Donnet

DOCTORAT SCIENCES BRETAGNE DE LA MER LOIRE ET DU LITTORAL

UBO Université de Bretagne Occidentale

# THÈSE DE DOCTORAT DE

L'UNIVERSITE
DE BRETAGNE OCCIDENTALE

ECOLE DOCTORALE N° 598

*Sciences de la Mer et du littoral*

Spécialité : Océanographie physique et Environnement

Par
**Sébastien DONNET**

## The Physical Oceanography of a broad, mid-latitude fjord

Observations, seasonality and wind response of Fortune Bay (Newfoundland, Canada)

**Thèse présentée et soutenue à Plouzané, le 16 décembre 2022**

**Unités de recherche :** **Laboratoire d'Océanographie Physique et Spatiale (LOPS, UMR 6523)**
**Northwest Atlantic Fisheries Centre, Fisheries and Oceans Canada**

**Rapporteurs avant soutenance :**

| | |
|---|---|
| Anna RUBIO | Chercheure, Centre technologique spécialisé dans la Marine et la recherche alimentaire (AZTI), Pasaia (Espagne) |
| Daniel BOURGAULT | Professeur, Université du Québec à Rimouski, Rimouski (Canada) |

**Composition du Jury :**

| | |
|---|---|
| Xavier CARTON | Professeur des universités, Université de Bretagne Occidentale, Plouzané<br>*Président* |
| Anna RUBIO | Chercheure, Centre technologique spécialisé dans la Marine et la recherche alimentaire (AZTI), Pasaia<br>*Rapportrice* |
| Daniel BOURGAULT | Professeur, Université du Québec à Rimouski, Rimouski<br>*Rapporteur* |
| Anne PETRENKO | Professeure des universités, Université Aix-Marseille, Marseille<br>*Examinatrice* |
| Pascal LAZURE | Chercheur, IFREMER Centre Bretagne, Plouzané<br>Directeur de thèse |

# The Physical Oceanography of a broad, mid-latitude fjord

Observations, seasonality and wind response of Fortune Bay (Newfoundland, Canada)

“Le coeur a ses raisons que la raison ne connait point.”

Blaise Pascal, Les Pensées (1670).*

*à mes parents,*

*mes filles,*

*ma femme,*

*et à tout mes amis.*

*** N.B**. my interpretation of it has nothing to do with any religious concept.

# TABLE OF CONTENTS

Foreword and Acknowledgments....9

INTRODUCTION
Fjordic and local environment context....16
State of knowledge....17
References....21

CHAPTER 1: OBSERVATIONS
A comprehensive oceanographic dataset of a subpolar, mid-latitude broad fjord: Fortune Bay, Newfoundland, Canada....27
Abstract....27
Introduction....28
Material and methods....29
Instruments used....31
Instrument limitations and uncertainties....33
ADCP backscatter processing....33
Results....34
Discussion....36
Data limitations and issues....38
QA/QC and data processing methods....38
UTBI depth calculation....40
In situ comparisons (e.g. CTD profile vs. mooring data)....40
ADCP tilt issue....41
Data availability....44
Conclusion....44
Author contributions....45
Competing interests....45
Disclaimer....45
Acknowledgements....45
Financial support....45
Review statement....45
References....46
Appendix A....50
Appendix B....51

CHAPTER 2: SEASONALITY
The Physical Oceanography of Fortune Bay, an overview....61
Abstract....61
Introduction....62
Bathymetric features....63
Temperature and Salinity structure....65
Data reduction....65
Monthly climate....65
Deep water characteristics....67
Stratification vs. rotation....68

Sea Surface Temperature, Freshwater inputs and Sea Ice....69
Wind....74
Tides....76
Currents....77
General characteristics....77
Seasonal statistics....78
Seasonal circulation....78
Spectral analysis....80
Weather band....82
Inner bay (Belle Bay) water exchanges and flushing times....85
Barotropic tide....85
Estuarine circulation....86
Intermediary circulation....87
Deep water renewal....87
Discussion....88
Water structure....88
Mechanical Forcing....90
Ocean Currents....91
Water Exchanges....92
Conclusion....93
Funding....94
References....94
The Physical Oceanography of Fortune Bay, an overview (supplementary)....101
Linear T-S relationships....103
Pulses cross-correlations....115
Pulses frequency of occurrence, duration and excursion....117

CHAPTER 3: WIND RESPONSE
Internal Kelvin waves in a broad, mid-latitude fjord....121
Abstract....121
Introduction....122
Material and Methods....125
Observations....125
Numerical model (FVCOM)....126
Results....129
Observations....129
Numerical Model validation....137
Idealistic model cases....140
Homogeneous wind....141
Local vs Remote wind....142
Spatial aspects....146
Discussion....149
Nature of the process....149
Origin of the process....150
Signal propagation....151
Conclusion....155
Acknowledgments....157

References.....157
Internal Kelvin waves in a broad, mid-latitude fjord (supplementary).....163

CONCLUSION
Concluding remarks and critique.....185
References.....190

Afterword.....195

# Foreword and Acknowledgments

At the end of the defense, I was asked for a few words and offered my thanks to a number of people; but of course, many were left behind. I also had little time to think it through and, hopefully, I can do a better job now.

At the defense, I made the analogy of a marriage when talking about typical relationships with one's PhD supervisor and to acknowledge the importance of mine with Pascal. This analogy was largely inspired by a cartoon I had seen on "PhD comics", a popular website for PhD students; which I would recommend to anyone looking for a good laugh (and whether or not you decide to go through this ordeal). This time, I will take that of parenting, which I think is actually more appropriate, at least in my case. Hence, when I started this research, I had a rather clear idea of what I wanted to accomplish (or I thought I had, anyway). I had written a white paper about it, a sort of letter of intent, quickly followed by the first draft of a proposal to get funds. Pascal, on his end, had started investigating peculiar dynamics around the Saint-Pierre et Miquelon archipelago (SPM), which is located in the zone of interest of this thesis. Our paths naturally crossed, although quite by chance also, and he helped me finalize the proposal. There is little doubt in my mind that I came into his life as a significant, and rather unplanned, disturbance. While he did plan on having PhD students to help him in his investigations of SPM, he certainly did not plan on having one studying internal Kelvin waves propagating into a broad fjord. At the beginning of it all, he might have wondered what he was getting himself into; possibly and equally with the subject matter as with his new student. Having kids of my own made me realize how much of a disturbance it can be. I cannot count the number of times when they would try to do something that, at first sight, does not look all that sensible and seems bound to fail miserably. Yet, each time, I can see clearly that it makes perfect sense to them and that they go at it with all the intensity kids can muster. Most of the time, I am right and failure is the outcome. Sometimes, though, surprising results or successes even, arise. In this, I have to say that Pascal had an incredible open mind and patience with me. I do not recall any moment that I would have felt restricted in my attempts nor, and more importantly, judged badly by what might have seemed rather absurd at times. I was allowed to try, and fail; learning along the way. I sincerely do not think that I could have found a better mentor than Pascal to tackle this endeavour. This is very much subjective, of course, and a lot of it has to do with working compatibility. Yet, I can also say that I have been very fortunate to meet, and learn from, a number of very talented oceanographers during my schooling and professional career. However, Pascal is, objectively, one the few having as much expertise and practical experience in both observing and numerically model the ocean; the two main trades of the field. Merci à toi donc, Pascal. J'espère que nos chemins continuerons à se croiser dans le futur et qu'ils nous amènerons à retravailler ensemble, sur des sujets tout aussi passionnant que celui-ci.

This thesis was accomplished part-time, alongside other duties I undertook while working at the Northwest Atlantic Fisheries Centre of Fisheries and Oceans Canada (St John's) and as such, it is important to acknowledge the support of my management: Dounia Hamoutene, Ben Davis and Barry McCallum. Considering how working conditions changed after their departure from the institute, this importance became especially clear to me over the last 2-3 of years of this long endeavour.

Similarly, I would like to thank close colleagues and mentors who helped and guided me all along this journey: Andry Ratsimandresy, Guoqi Han and Brian Petrie. Whether talking about science formally or about life doing it more informally, they all had a positive impact. In that group should also appear Adam Drozdowski who I have known for many years now and whose numerical skills have always impressed me. Interestingly, whether we work on sediment transport problems or on internal Kelvin waves, our paths seem to interact one way or another.

I also owe a great debt of gratitude to my colleagues and mentors preceding my time at Fisheries and Oceans Canada: Patrick Roussel, Bruce Batstone, Aubrey Beaver, Mark Batt, Steve Hurlburt, Mark MacNeil, Phil Osborne and Gregory Curtiss. It is, for instance, after a few informal discussions I had with Aubrey and Bruce, drawing on napkins (literally), that I finalized the design of our initial moorings which successfully collected the first set of year-round oceanographic observations in Fortune Bay. More generally, all of them taught me something that, in the end, made its way to this work.

The same is true about my former academic teachers and professors who have had a fundamental effect on the way I approach oceanographic problems. Among others, Professor John H. Simpson and Professor Eric D. Barton of the University of Wales-Bangor were certainly two of the most influential and to whom I owe a great deal. Above all, I owe a great debt of gratitude to the staff of Intechmer, the school that first introduced me to the field. In particular to Yann Méar, my first physical oceanography teacher, and to his better-half, Anne Murat; both having such a profound influence on generations of students making their way into this fantastic field of ocean sciences.

The final push on this thesis, i.e. the last year of writing, took place under the sun of Italy, while working at the CNR-ISMAR of Lerici and being exposed to a completely different environment (both geographically and professionally). Despite the sad fact that I was not able to master the language after a full year immersed, it is clear that this experience was beneficial not only on a personal level, but also on a professional one; including for this thesis. Thank you Maristella (Berta) and Annalisa (Griffa) for offering me such an opportunity to work with you. I am looking forward to continuing on our collaborative undertaking with CALYPSO and, possibly, beyond.

I mentioned the members of my thesis committee at the defense: Anne Petrenko, Cedric Chavanne and Yves Morel. This committee, and its members, played an essential part in the good development of this work. There is no doubt in my mind that a different outcome could have arisen should they have not been part of it and been as supportive as they were. I am truly humbled by the breadth of their expertise and by their intellect. In fact, I was very much intimidated when this committee was assembled in the early stages and was very nervous each time we met to present an annual update. Yet, each and every time, they would not only provide me with very insightful suggestions but they would also raise my spirit and motivation in ways I would not have imagined (let alone hoped for). I could not overstate their kindness and positive influence. Merci à vous.

The assistance from the administrative staff of the university should not be forgotten either: Elisabeth Bondu and Aurélie Claude, in particular. I am still having a good laugh at remembering that day I called Elisabeth to present my project and asked how I could apply to the program. I most certainly came out of the blue.

Finally, I would like to thank all the friends who accompanied me along this adventure (as well as on many others): Fred, Max, Nico, Cat, Arnaud, David, Barbara, Flora and Mike on the Canadian side; Romain, Schouk, Cha, Florian, Manue, Aourégan, Gaëlle, Mimie, Pouic, Sylvaine, Anne, Puce, Wolf, Titi, Tételle, Delf, Hélène, Dan and many other Intechmeriens(es) (d'origine ou d'adoption) that I am failing to list here on the French side. Whether it was during peaceful weekends fishing and eating scallops at the cabin, memorable weddings or during my annual visit to Brest, everyone played a role.

In chronological order, I should have mentioned my friend Darrell Mullowney first who, on a rather impromptu invitation to a barbecue one evening, introduced me to Herlé Goraguer from the Ifremer lab of Saint-Pierre et Miquelon. Herlé, a fellow from Intechmer (and in fact, an elder from one of the first generations) in turn introduced me to Pascal and from there the story began. Herlé was also key in coordinating the field efforts between the two countries and more generally to the fruitful collaborations that Fisheries and Ocean Canada and Ifremer now enjoy in this part of the world (this work being only one of a number of others).

Last but not least and in fact, above all, my partner in life and team-mate for so many years now that we don't really count anymore: Daria (Gallardi). Surpassing Pascal for what she had to endure and the patience required to do so, Daria is probably one of the most resilient person I have ever met. She navigated through the roller-coaster a PhD student typically goes through (see PhD comics for great illustrations on that) with both tact and strength; all the while giving birth and raising two beautiful and so incredibly passionate (and intense) little girls.

This is it. Hopefully, I did not forget to mention someone or omit something key here but… I probably did. If your name does not appear here, please don't be mad. If you think it should be here, you probably also know that I can be hopelessly forgetful with things like this. Just let me know, I'll do whatever it takes to make up for it. After all, life is too short and there are so many things we can be happy for, even doing something as frustrating as science can be; just watch children, they will show you how.

# INTRODUCTION

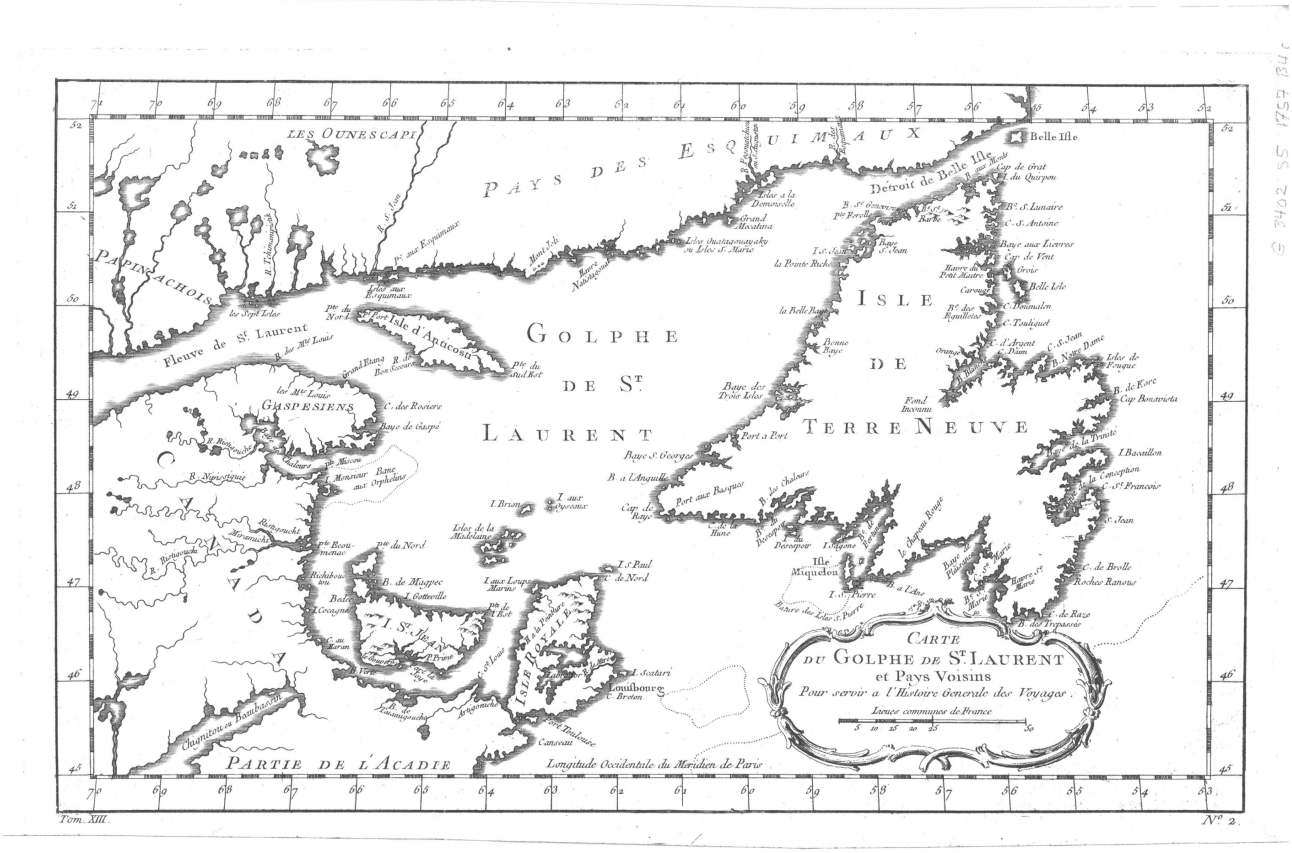


*Early map of the island of Newfoundland and surroundings titled "Carte du Golphe de St. Laurent et pays voisins pour servir à l'Histoire générale des voyages", attributed to Jacques Nicolas Bellin (1703-1772). Fortune Bay ("B^e^. de Fortune") is clearly visible as well as the archipelago of Saint-Pierre and Miquelon although their shapes are very much approximative. Also notable is the labelling "B^e^. du Desespoir" of the last major bay located to the west of Fortune Bay. "B^e^. du Desespoir" is, in fact, a fairly narrow fjord which is known, nowdays, as "Bay d'Espoir"; an interesting turn of traduction ("Desespoir" having the exact opposite meaning of "Espoir", in French). Date of the edition is not well known but might be around 1780.*

*Source: https://collections.banq.qc.ca/ark:/52327/2244594*

This thesis is about observing (chapter 1), describing (chapter 2) and numerically simulating (chapter 3) the physical oceanography of Fortune Bay: a large, mid-latitude, deep and seasonally stratified fjord. The experimental site is located on the south coast of Newfoundland, a large island on the eastern side of Canada (Figure 1). The regional oceanography is dominated by a cold and relatively fresh equatorward current, the Labrador Current, flowing on the shelf (inshore branch) and on the shelf edge (offshore branch).

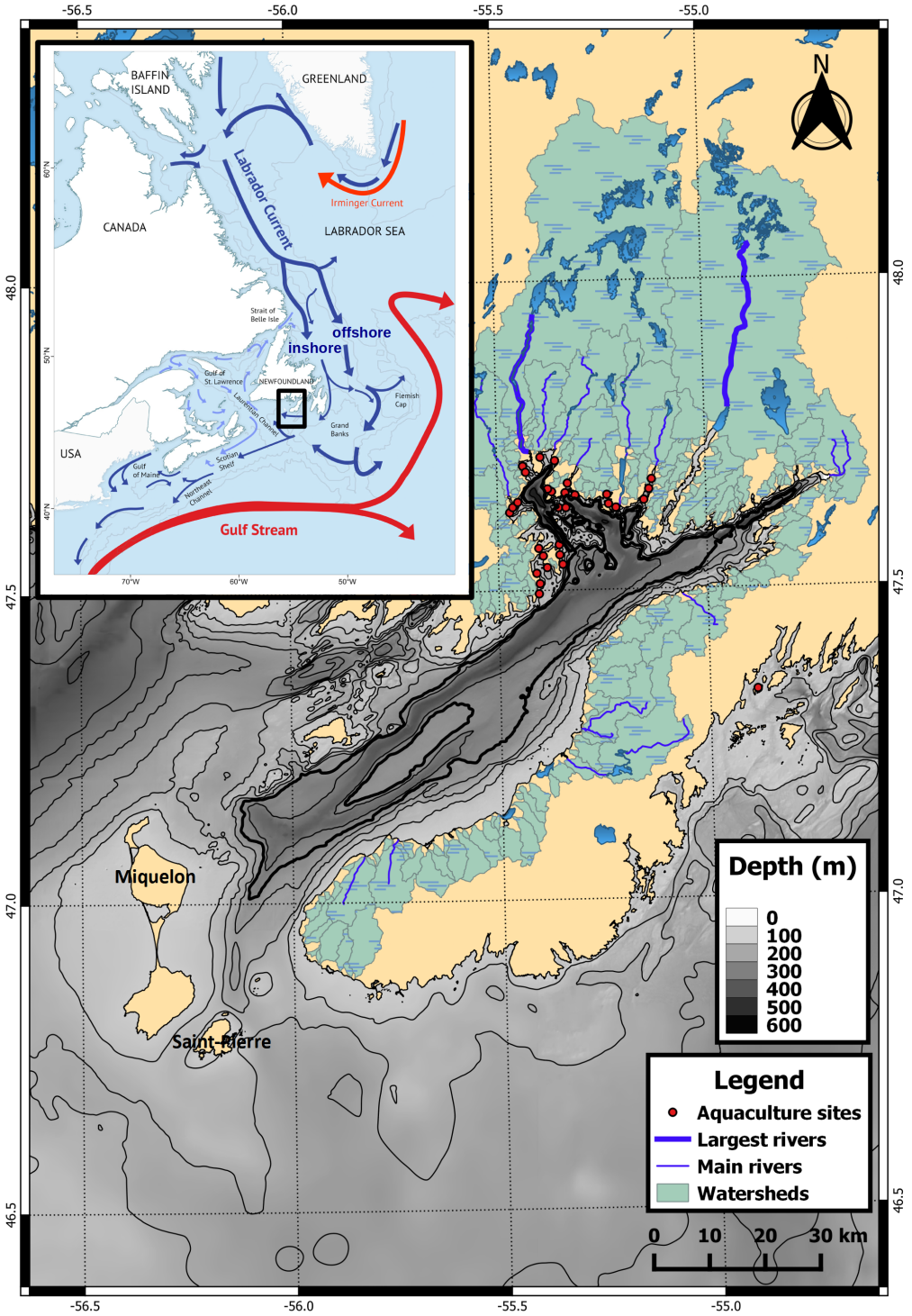


*Figure 1: Study area. Bathymetry, watersheds, main rivers and aquaculture sites are illustrated. Thick black line represent the 200 m depth contour. French archipelago of Saint-Pierre and Miquelon is labelled. Insert illustrates the larger scale, regional oceanographic features; namely the branches of the Labrador Current, Gulf Stream and Irminger Current (source: Bernier et al., 2018).*

# FJORDIC AND LOCAL ENVIRONMENT CONTEXT

Fjords are deep and generally long and narrow estuaries connecting inner lands to the sea. Carved by glaciers' abrasion, these landscapes are thus principally located at high latitudes; most of them formed or appeared during the last de-glaciation period (ca 12,000 years ago). Due to the erosion process, many fjords end with a sill on their offshore boundary (also called "mouth"), separating their deep basin from the ocean; thereby restricting water exchanges with the ocean. As a result, bottom waters can be isolated for long periods of time and become deprived of oxygen. It is also quite common for fjords to have "inner" sills, separating their main basin into several sub-basins; therefore complicating even more the processes of deep water renewal.

As any estuaries, fjords typically receive a sizable amount of freshwater from nearby watersheds but since they are generally located in regions of high relief (mountains), still connected to glaciers for a number of them, their freshwater input (and output) is much more seasonal than mid-latitude estuaries with a large outflow in spring, during the melting season, and low discharge in winter during the freezing season.

As any coastal regions, fjords are subject to forcing from winds, tides, freshwater inputs and forcing from their adjacent ocean. Because of their depths, location in higher latitudes and typically large freshwater input, they are generally very stratified and exhibit a strong seasonal cycle in both temperature and salinity. Their dynamics can therefore be quite complex and have caught the attention of oceanographers since the early days of the discipline(s) in the late 1800s. Hence, they have often be regarded as "natural laboratories" in which a wide range of hydrodynamic processes can be studied with more ease than in the open ocean. Some of the first evidence of internal motions (also called internal waves) for instance, were discovered and studied in fjords.

These coastal features have also been inhabited by humans for a long time in some places such as Norway for being important places for shelter, trades and food supplies. As a result, they have been subject to diverse human-environment interactions which are continuing, and in many cases increasing, to this day. One of the most recent use of fjords is open-net salmonids farming which originated in Norway in the late 60s and rapidly spread worldwide (e.g. Scotland, Canada, Chile and New Zealand). This relatively new usage is adding pressure to an environment and to ecosystems that can be in delicate balance and in places that are still not necessarily well known.

Despite being located in mid-latiudes (47-51 °N), the island of Newfoundland (Canada's east coast), is dented by numerous fjords all along its coasts. Covered under a massive icesheet during the last ice ages (the Laurentide Ice Sheet), this landmass was hence subject to severe glacial scouring. Probably due to its relative remoteness and difficult climate, Newfoundland was inhabited fairly recently (ca 6000 yr) and, while being discovered early (1497) during the European "Age of Discovery" and extensively used economically as fishing grounds thereafter, the island remains scarcely populated.

Fortune Bay is one of Newfoundland's numerous fjords located on its southern shores which has the particularity of being both long (about 130 km) and wide (20 km) and fairly opened to the ocean. Historically, Fortune Bay was one of those numerous embayment where fishing activities (mainly cod) took place from small, scattered communities around its shores. With the abrupt decline of the cod fisheries in the early 1990s, ending with a moratorium, Fortune Bay saw a decline of its population. In the early 2000s, fish farming began and rapidly increased to become one of the largest economic activity of the region.

# STATE OF KNOWLEDGE

We qualify Fortune Bay as “broad” for being wide in comparison to its internal Rossby radius of deformation (few kilometers, typically) an horizontal scale defining, for instance, the offshore extent of coastal upwelling (Charney, 1955 and Yoshida, 1955).

Over the years, the physical oceanography of narrow fjords has been fairly well studied (see Farmer and Freeland, 1983; Inall and Gillibrand, 2010; Stigebrandt, 2012, for reviews). In contrast, broad fjords have received much less attention. This appears to be the case for mid-latitude fjords even more since recent attention turned to high latitude fjords due to their role in our present-day, accelerating anthropogenic climate change (see Cottier et al., 2010 for a review of high latitude fjords). This lack of attention of mid-latitude broad fjords can be understood by the fact that they are not numerous and that they can be expensive to observe, particularly in places where human presence is scarce.

Broad fjords differ from narrow fjords in that, due to their width, the effect of earth rotation becomes significant and one can no longer neglect this (Coriolis) force in studying their oceanic responses to forcing. One of the most evident effect of rotation is that it will tend to deflect surface freshwater plumes, typically originating from the fjord’s head either from rivers or from glaciers calving and melting (e.g. Ingvaldsen et al., 2001, Rabe and Hindson, 2017). Same effect can act on deep water renewal pulses or flow (e.g. de Young and Hay, 1989) or intermediary, neutrally buoyant waters (e.g. Heuze et al. 2017). Similarly, internal tide can take the form of long internal waves which are subject to earth rotation (e.g. Stoylen and Fer, 2014). Finally, another major effect rotation can have is with along-shore wind responses which can be felt independently from a coast to another, thereby generating upwelling on one side and downwelling on the other (e.g. Cushman-Roisin et al., 1994). These disturbances can then propagate around the fjord as a cyclonic propagating trapped motion (e.g. Yao, 1986). They can also be generated outside the fjord, along the surrounding shelf (e.g. Asplin et al., 1999) or nearby large embayment (e.g. de Young et al., 1993). If the bathymetric slopes along the coast are steep, those motions behave as internal Kelvin waves, a simpler (asymptotic) form of the more general motion of “coastal trapped waves” which are shaped by both stratification and topography (see Brink 1991 for a detailed review and Huthnance 2001 for a brief review).

One complication of observing broad fjords’ dynamics, therefore, is that one need to assess both along-shore and across-shore variability, at the same time. Although this does not apply to broad fjords only and that cross-shore motions can be important in narrow fjords as well (e.g. Bourgault et al.?). Another key aspect is to be able to observe both the variability of the pycnocline and water column currents, at the same place and at the same time, over a long-enough period of time and at enough sites around the fjord so that the propagation of such disturbances can be followed in both space and time. In mid-latitude fjords (and higher latitude ones), one would also likely want to resolve the dominant signal which is the seasonal cycle and which defines the stratification; in turn affecting the type of process generated (e.g. baroclinic vs. barotropic) as well as its characteristics (e.g. phase speed, in case of an internal wave).

To achieve the temporal endurance necessary as well as the vertical resolution in water stratification and dynamical characteristics (temperature, salinity and currents) oceanographic moorings are a tool of choice (see Trask and Weller 2001 for a brief review). They are, however, generally quite costly and cannot be deployed in large quantities. Trade-off in the number of mooring lines deployed and their instrumentation load is therefore necessary; affecting both the horizontal and vertical resolution of the parameters needed

to be observed within the domain of interest. To “fill the gaps”, numerical models can thus be extremely useful and have been employed extensively over the last decades to study fjords dynamics (e.g. Klinck 1981, Proehl and Rattray 1984, Asplin et al. 1999, Ingvaldsen et al., 2001, Cottier et al. 2005, Stoylen and Fer, 2014, Jackson et al., 2018, Fraser et al., 2018, Lundesgaard et al. 2019). In this thesis, we will make use of both observations and numerical model simulations to study Fortune Bay’s dynamics at seasonal and daily scales.

The physical oceanography of Fortune Bay and, more generally, of the coastal environment of Newfoundland is not well known. Even though some of the first oceanographic accounts of the region date back from the late 1800s (Gillpatrick and Gibson, 1884), it is not until the 1980s that more thorough investigations took place (de Young 1983 and Richard 1987 theses). These first dedicated studies to Fortune Bay concerned the deep water renewal of the fjord (de Young and Hay 1987, Hay and de Young 1989 and White and Hay 1994) and its lower trophic biology as well as mesopelagic fish communities (Richard and Haedrich 1991). They showed that the bottom layer of the fjord is seasonally vented by two distinct water masses present below sill depth (120 m) in two channels located on the adjacent shelf. In winter and under the influence of northerly winds, the warm (>4 °C) and salty (34.5) water mass present on the western side of the fjord upwells above the sill and flows into the fjord due to Ekman transport. Similarly, in summer and under southerly winds forcing, the cold (<2 °C) and fresh (32-33) water mass present on the eastern side of the fjord upwells into fjord. This type of renewal is rather unusual for a fjord as fjords have access to only one source of deep water, usually. de Young and Hay (1989) further described the influence of rotation on the cold water renewal and White and Hay (1994) documented its variability at tidal and subtidal time scales (2-3 day oscillatory behavior then attributed to potential bottom trapped waves). Little attention was given on the properties and dynamics of the upper layers, at the time. In the early 2000s, renewed interest grew in Fortune Bay’s environment with the rapid development of finfish aquaculture taking place within the head of the fjord and nearby areas. Physical oceanographic observations were performed to provide background information for further studies on aquaculture-environment interactions and were, therefore, more concerned with the upper layers (Donnet et al. 2018a&b, Ratsimandresy et al. 2019 and 2020). Those oceanographic investigations showed the importance of the topography and freshwater runoff in controlling the water column stratification (bottom and surface layers, respectively), the strong seasonality in surface heating and cooling, the weakness of the tides in both currents and water flushing influence, and indicated the importance of the wind as a major forcing mechanism (Salcedo and Ratsimandresy, 2013).

Despite these efforts, important gaps subsisted in the understanding of Fortune Bay’s climate and dynamics. Basic knowledge of the water column seasonal stratification and ocean circulation as well as water exchanges was still limited or lacking. The identification of the dominant process(es) and of their forcing mechanism(s) responsible for the large variability in the ocean currents observed had also not been established. These aspects were strong encouragements for further investigations and led to the work presented in this thesis.

The spatial scales considered here are bay scale, i.e. order of 100s of kilometers long and few kilometers wide. Thus, with respect to the ocean/wave motions, we are in the domain of the long-wave approximation where horizontal scales are much larger than the vertical scale (i.e. depth) and which allows the utilization of the hydrostatic simplification (Gill, 1982 section 5.5). Another characteristic of the long-wave approximation that has been used to resolve the processes analytically is that the along-shore scale is much larger than the cross-shore scale (as noted above). This property, along with subinertial periodicity (see

below) has been used with great success in the past to model the propagation of coastal upwelling and downwelling and of CTW dynamics more generally (e.g. Clarke 1977 and more on that below). Finally, another property of the long-waves is that they are non-dispersive, i.e. their phase speed do not depend on wavenumber (2pi/L where L is the wavelength) and thus, they should not change shape. Non-linearity, however, can complicate this property in changing the shape of the wave as shown and discussed in chapter 3.

Time scales considered are seasonal (chapter 2) to days (chapter 3); that is much larger than the inertial period (~17 hr at Fortune Bay's latitude). This implies the study of currents in geostrophic balance (where rotation applies) and, in a two-layer ocean model forced by wind, the study of the "coastal jet" in particular (Charney, 1955), a major feature of upwelling regions. Since the forcing is not steady, however (and unlike assumed by Charney), the jet varies with/in time and takes the form of an internal Kelvin wave, i.e. a disturbance traveling with the coast on its right (e.g. Gill and Clarke, 1974). Gill and Clarke have shown that at any location along a coast, the depth of the pycnocline (i.e. upwelling and/or downwelling conditions) was a function of both the local response (Ekman transport) and remotely generated disturbance traveling as a Kelvin wave; their forced wave model, using the long-wave approximation, demonstrated good skills in reproducing observations in various places around the world (Great Lakes, Oregon coast, South west Africa and along the Baltic sea; see Clarke 1976 and Clarke 1977). Those were early work in the broader field of coastal-trapped waves which was under significant theoretical development in the late 70s to early 80s, culminating with the solutions provided by Huthnance (1978) and Brink (1982a). Most of those early models were linear, however, and invicid even though some researchers such as Clarke (1976 and 1977) studied the effect of non-linearity and discussed about the potential issues in ignoring mixing effects. According to Clarke (1976, chapter 5) non-linearity would change the phase speed by reducing that of a wave propagating in an upwelled region and increasing that of a wave propagating in a downwelled region. Few years earlier, Bennett (1973) had showed that non-linear effects steepen the downwelling phase of a Kelvin wave while propagating. Another severe limitation of those early models is that they are highly idealized in their geometry and do not consider the complexity of realistic coastline and bathymetry. Coastline is either considered strait or circular (for island cases, see Brink 1999) and the shelf-slope shape is considered homogeneous in the along-shore direction. Clarke (1976 and 1977) also looked at this problem analytically and found that the phase speed of the waves would also be affected by coastline curvature in that it would be slower around capes and faster when propagating around a bay. The effect of bottom friction is only roughly approximated in those models, in the sense of having no bottom boundary layer being strictly defined (Brink 1982b and 2006). As recently pointed out by Brunner et al. (2019), those limitations can prove to be too significant in some (if not many) places; the largest limitations being related to changes in coastline and bathymetry shapes which induce scattering not taken into account by these idealized models. Yet, this theoretical framework and numerical tools (e.g. Brink and Chapman 1987 and Brink 2018a&b) have proven to be rather successful in determining the modal structure of the waves and, to a lesser degree, sea level and along-shore current fluctuations along numerous shelves and continue to be used to this day (e.g. Lazure et al., 2018, Massoud et al., 2019).

With the advent of computing power and great development of hydrodynamic numerical models, which include both non-linearity and internal friction (i.e. turbulences) as well as realistic coastline and bathymetry, more detailed and realistic assessments of coastal-trapped waves can be made (e.g. Illig et al., 2018a&b). However, this also comes at a price of more complexity in the results and, consequently, more

difficulty with the interpretation. Turbulence closure also remains a significant challenge to resolve both theoretically and numerically (Umlauf and Burchard, 2003) and results in the approximation of (or failure to correctly reproduce) dissipation rates, both from internal and bottom friction.

In this study, we use a fully non-linear, 3-dimensional primitive equations model under the hydrostatic and flat bottom assumptions to both test the (simpler) hypothesis of a dominant internal Kelvin wave process and circumvent issues of numerical overmixing due to the complex bathymetry of our study area. It will be shown that the most important factors in reproducing the dynamics observed (i.e. series of upwelling and downwelling events) are the remote effects from the nearby bay (i.e. outside the fjord) and the non-linear interaction between locally generated and remotely generated waves. Nevertheless, it is also evident that the model performed much less adequately at locations where the shelf is the widest (outer part of the fjord) indicating that CTWs-like dynamics are taking place at those locations and that more realistic bathymetry should be included in future simulations.

This thesis is structured in 3 chapters which consist of papers that are either published (chapter 1&2) or proposed for submission (chapter 3). The first chapter describes the 2-year long observations that were undertaken for this study, documenting their reach and limitations. The second chapter provides a descriptive overview of the physical oceanography of the study area at seasonal scale (for the most part). The third chapter is devoted to the investigation of internal Kelvin wave generation and propagation inside the fjord.

# REFERENCES


Asplin, L., Salvanes, A.G.V., Kristoffersen, J.B., 1999. Nonlocal wind-driven fjord-coast advection and its potential effect on plankton and fish recruitment: Nonlocal wind-driven fjord-coast advection. Fisheries Oceanography 8, 255–263. https://doi.org/10.1046/j.1365-2419.1999.00109.x

Bernier, R.Y., Jamieson, R.E., Moore, A.M., 2018. State of the Atlantic Ocean Synthesis Report (Can. Tech. Rep. Fish. Aquat. Sci. No. 3167). Fisheries and Oceans Canada. https://waves-vagues.dfo-mpo.gc.ca/library-bibliotheque/40801755.pdf (accessed 06-Jun-2023)

Brink, K., 1991. Coastal-trapped waves and wind-driven currents over the continental shelf. Annual Review of Fluid Mechanics 23, 389–412.

Brink, K.H., 2018a. Island-trapped waves with stratification, topography, mean flow and bottom friction in Matlab. https://doi.org/10.1575/1912/10526

Brink, K.H., 2018b. Stable coastal-trapped waves with stratification, topography and mean flow. https://doi.org/10.1575/1912/10527

Brink, K.H., 2006. Coastal-trapped waves with finite bottom friction. Dynamics of Atmospheres and Oceans 41, 172–190. https://doi.org/10.1016/j.dynatmoce.2006.05.001

Brink, K.H., 1999. Island-trapped waves, with application to observations off Bermuda. Dynamics of Atmospheres and Oceans 29, 93–118. https://doi.org/10.1016/S0377-0265(99)00003-2

Brink, K.H., 1982a. A Comparison of Long Coastal Trapped Wave Theory with Observations off Peru. Journal of Physical Oceanography 12, 897–913. https://doi.org/10.1175/1520-0485(1982)012<0897:ACOLCT>2.0.CO;2

Brink, K.H., 1982b. The Effect of Bottom Friction on Low-Frequency Coastal Trapped Waves. Journal of Physical Oceanography 12, 127–133. https://doi.org/10.1175/1520-0485(1982)012<0127:TEOBFO>2.0.CO;2

Brink, K.H., Chapman, D.C., 1987. Programs for computing properties of coastal-trapped waves and wind-driven motions over the continental shelf and slope. Woods Hole Oceanographic Institution, Woods Hole, MA. https://doi.org/10.1575/1912/5368

Brunner, K., Rivas, D., Lwiza, K.M.M., 2019. Application of Classical Coastal Trapped Wave Theory to High-Scattering Regions. Journal of Physical Oceanography 49, 2201–2216. https://doi.org/10.1175/JPO-D-18-0112.1

Charney, J., 1955. Generation of oceanic currents by wind. J. Marine Res. 14 (04-20), 477–498.

Clarke, A.J., 1976. Coastal Upwelling and Coastally Trapped Long Waves. (PhD Thesis). University of Cambridge.

Clarke, A.J., 1977. Observational and Numerical Evidence for Wind-Forced Coastal Trapped Long Waves. Journal of Physical Oceanography 7, 231–247. https://doi.org/10.1175/1520-0485(1977)007<0231:OANEFW>2.0.CO;2

Cottier, F., Tverberg, V., Inall, M., Svendsen, H., Nilsen, F., Griffiths, C., 2005. Water mass modification in an

Arctic fjord through cross-shelf exchange: The seasonal hydrography of Kongsfjorden, Svalbard. J. Geophys. Res. 110, C12005. https://doi.org/10.1029/2004JC002757

Cottier, F.R., Nilsen, F., Skogseth, R., Tverberg, V., Skarðhamar, J., Svendsen, H., 2010. Arctic fjords: a review of the oceanographic environment and dominant physical processes. SP 344, 35–50. https://doi.org/10.1144/SP344.4

Cushman-Roisin, B., Asplin, L., Svendsen, H., 1994. Upwelling in broad fjords. Continental Shelf Research 14, 1701–1721. https://doi.org/10.1016/0278-4343(94)90044-2

Donnet, S., Ratsimandresy, A.W., Goulet, P., Doody, C., Burke, S., Cross, S., 2018a. Coast of Bays Metrics: Geography, Hydrology and Physical Oceanography of an Aquaculture Area of the South Coast of Newfoundland (DFO Can. Sci. Advis. Sec. Res. Doc. No. 2017/076). https://waves-vagues.dfo-mpo.gc.ca/library-bibliotheque/40654473.pdf (accessed 26-Sep-2022)

Donnet, S., Cross, S., Goulet, P., Ratsimandresy, A.W., 2018b. Coast of Bays seawater vertical and horizontal structure (2009-13): Hydrographic structure, spatial variability and seasonality based on the Program for Aquaculture Regulatory Research (PARR) 2009-13 oceanographic surveys (DFO Can. Sci. Advis. Sec. Res. Doc. No. 2017/077). https://waves-vagues.dfo-mpo.gc.ca/library-bibliotheque/40655945.pdf (accessed 26-Sep-2022)

Farmer, D.M., Freeland, H.J., 1983. The physical oceanography of Fjords. Progress in Oceanography 12, 147–219. https://doi.org/10.1016/0079-6611(83)90004-6

Fraser, N.J., Inall, M.E., Magaldi, M.G., Haine, T.W.N., Jones, S.C., 2018. Wintertime Fjord-Shelf Interaction and Ice Sheet Melting in Southeast Greenland. J. Geophys. Res. Oceans 123, 9156–9177. https://doi.org/10.1029/2018JC014435

Gill, A.E., 1982. Atmosphere-ocean dynamics. Academic press.

Gill, A.E., Clarke, A.J., 1974. Wind-induced upwelling, coastal currents and sea-level changes. Deep Sea Research and Oceanographic Abstracts 21, 325–345. https://doi.org/10.1016/0011-7471(74)90038-2

Gillpatrick, W.W., Gibson, John, 1884. Newfoundland and Labrador: The Coast and Banks of Newfoundland, and the Coast of Labrador, from Grand Point to the Koksoak River, with the Adjacent Islands and Banks, U.S. Hydrographic Office. Government Printing Office, Washington.

Hay, A.E., de Young, B., 1989. An oceanographic flip-flop: deep water exchange in Fortune Bay, Newfoundland. J. Geophys. Res. 94, 843. https://doi.org/10.1029/JC094iC01p00843

Heuzé, C., Wåhlin, A., Johnson, H.L., Münchow, A., 2017. Pathways of Meltwater Export from Petermann Glacier, Greenland. Journal of Physical Oceanography 47, 405–418. https://doi.org/10.1175/JPO-D-16-0161.1

Huthnance, J.M., 2009. Coastal trapped waves. Elements of Physical Oceanography: A derivative of the Encyclopedia of Ocean Sciences 87–94.

Huthnance, J.M., 1978. On Coastal Trapped Waves: Analysis and Numerical Calculation by Inverse Iteration. Journal of Physical Oceanography 8, 74–92. https://doi.org/10.1175/1520-0485(1978)008<0074:OCTWAA>2.0.CO;2

Illig, S., Bachèlery, M., Cadier, E., 2018a. Subseasonal Coastal-Trapped Wave Propagations in the Southeastern Pacific and Atlantic Oceans: 2. Wave Characteristics and Connection With the Equatorial Variability. J. Geophys. Res. Oceans 123, 3942–3961. https://doi.org/10.1029/2017JC013540

Illig, S., Cadier, E., Bachèlery, M., Kersalé, M., 2018b. Subseasonal Coastal-Trapped Wave Propagations in the Southeastern Pacific and Atlantic Oceans: 1. A New Approach to Estimate Wave Amplitude. J. Geophys. Res. Oceans 123, 3915–3941. https://doi.org/10.1029/2017JC013539

Inall, M.E., Gillibrand, P.A., 2010. The physics of mid-latitude fjords: a review. SP 344, 17–33. https://doi.org/10.1144/SP344.3

Ingvaldsen, R., Reitan, B., Marit, Svendsen, H., Asplin, L., 2001. The upper layer circulation in Kongsfjorden and Krossfjorden-A complex fjord system on the west coast of Spitsbergen (scientific paper). Memoirs of National Institute of Polar Research. Special issue 54, 393–407.

Jackson, R.H., Lentz, S.J., Straneo, F., 2018. The Dynamics of Shelf Forcing in Greenlandic Fjords. Journal of Physical Oceanography 48, 2799–2827. https://doi.org/10.1175/JPO-D-18-0057.1

Klinck, J.M., O'Brien, J.J., Svendsen, H., 1981. A Simple Model of Fjord and Coastal Circulation Interaction. Journal of Physical Oceanography 11, 1612–1626. https://doi.org/10.1175/1520-0485(1981)011<1612:ASMOFA>2.0.CO;2

Lazure, P., Le Cann, B., Bezaud, M., 2018. Large diurnal bottom temperature oscillations around the Saint Pierre and Miquelon archipelago. Sci Rep 8, 13882. https://doi.org/10.1038/s41598-018-31857-w

Lundesgaard, Ø., Powell, B., Merrifield, M., Hahn-Woernle, L., Winsor, P., 2019. Response of an Antarctic Peninsula Fjord to Summer Katabatic Wind Events. Journal of Physical Oceanography 49, 1485–1502. https://doi.org/10.1175/JPO-D-18-0119.1

Masoud, M., Pawlowicz, R., Montazeri Namin, M., 2019. Low frequency variations in currents on the southern continental shelf of the Caspian Sea. Dynamics of Atmospheres and Oceans 87, 101095. https://doi.org/10.1016/j.dynatmoce.2019.05.004

Proehl, J.A., Ratrray, M., 1984. Low-Frequency Response of Wide Deep Estuaries to Non-Loca1 Atmospheric Forcing. Journal of Physical Oceanography 14, 904–921. https://doi.org/10.1175/1520-0485(1984)014<0904:LFROWD>2.0.CO;2

Rabe, B., Hindson, J., 2017. Forcing mechanisms and hydrodynamics in Loch Linnhe, a dynamically wide Scottish estuary. Estuarine, Coastal and Shelf Science 196, 159–172. https://doi.org/10.1016/j.ecss.2017.06.015

Ratsimandresy, A.W., Donnet, S., Goulet, P., 2020. Identification of geographic zones of influence associated with surface circulation for Aquaculture Bay Management Area application. Journal of Marine Systems 204, 103291. https://doi.org/10.1016/j.jmarsys.2019.103291

Ratsimandresy, A.W., Donnet, S., Snook, S., Goulet, P., 2019. Analysis of the variability of the ocean currents in the Coast of Bays area (DFO Can. Sci. Advis. Sec. Res. Doc. No. 2019/008). https://waves-vagues.dfo-mpo.gc.ca/library-bibliotheque/40805116.pdf (accessed 26-Sep-2022)

Richard, J.M., 1987. The mesopelagic fish and invertebrate macrozooplankton faunas of two Newfoundland

fjords with differing physical oceanography (MSc Thesis). Memorial University of Newfoundland. http://research.library.mun.ca/id/eprint/4196 (accessed 26-Sep-2022)

Richard, J.M., Haedrich, R.L., 1991. A comparison of the macrozooplankton faunas in two newfoundland fjords differing in physical oceanography. Sarsia 76, 41–52. https://doi.org/10.1080/00364827.1991.10413465

Salcedo-Castro, J., Ratsimandresey, A.W., 2013. Oceanographic response to the passage of hurricanes in Belle Bay, Newfoundland. Estuarine, Coastal and Shelf Science 133, 224–234. https://doi.org/10.1016/j.ecss.2013.08.031

Stigebrandt, A., 2012. Hydrodynamics and circulation of fjords. Encyclopedia of lakes and reservoirs 327, 344.

Støylen, E., Fer, I., 2014. Tidally induced internal motion in an Arctic fjord. Nonlin. Processes Geophys. 21, 87–100. https://doi.org/10.5194/npg-21-87-2014

Trask, R.P., Weller, R.A., 2001. Moorings, in: Encyclopedia of Ocean Sciences. Elsevier, pp. 1850–1860. https://doi.org/10.1006/rwos.2001.0304

White, M., Hay, A.E., 1994. Dense overflow into a large silled embayment: Tidal modulation, fronts and basin modes. issn: 0022-2402 52, 459–487. https://doi.org/10.1357/0022240943077055

Yao, T., 1986. The response of currents in Trinity Bay, Newfoundland, to local wind forcing. Atmosphere-Ocean 24, 235–252. https://doi.org/10.1080/07055900.1986.9649249

Yoshida, K., 1955. Coastal upwelling off the California coast. Rec. Oceanogr. Works Japan, New Ser. 2, 8–20.

Young, B.D., Hay, A.E., 1987. Density Current Flow into Fortune Bay, Newfoundland. J. Phys. Oceanogr. 17, 1066–1070. https://doi.org/10.1175/1520-0485(1987)017<1066:DCFIFB>2.0.CO;2

Young, B. de, Otterson, T., Greatbatch, R.J., 1993. The Local and Nonlocal Response of Conception Bay to Wind Forcing. Journal of Physical Oceanography 23, 2636–2649. https://doi.org/10.1175/1520-0485(1993)023<2636:TLANRO>2.0.CO;2

# CHAPTER 1: OBSERVATIONS

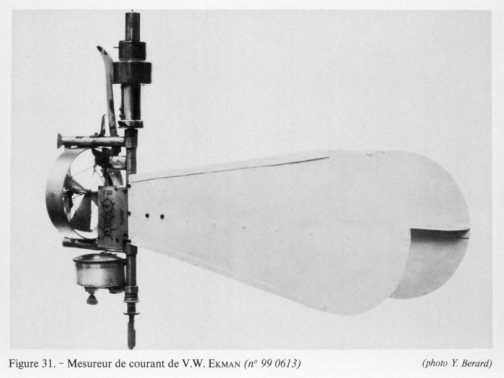

Figure 31. – Mesureur de courant de V.W. Ekman *(n° 99 0613)* *(photo Y. Berard)*

*Some of the first instruments to adequately measure temperature at depth (left) and ocean currents (right). Ocean temperature and currents were key variables of interest to be measured by the program presented in this chapter. The reversing thermometer shown here (left) is from Negretti & Zambra and was made for the for Polar expedition (1875-76). Although not novel in principle (the idea of a reversing thermometer is attributed to George Aimé, who described it in 1845), this thermometer is reported to be the first to have accurately determined the temperature at great depth (see sources below). The Ekman current meter (right) is a mechanical device to measure flow speed and direction. It was invented by the Swedish oceanographer Vagn Walfrid Ekman, in 1903 and has been reported as being both simple and reliable (see sources below for more details).*

*Sources:*

*https://collection.sciencemuseumgroup.org.uk/objects/co2849/deep-sea-reversing-mercury-thermometer-1870-1875-thermometer-mercury (thermometer)*

*https://www.photolib.noaa.gov/Collections/Voyage/History-of-Oceanography-Collection/The-Early-Instruments-Collections/Thermometers-and-Other-Equipment/emodule/1319/eitem/75384 (thermometer)*

*https://commons.wikimedia.org/wiki/File:Ekman_meter.jpg (current meter)*

*Sverdrup H. U., Johnson M. W., Fleming R. H., 1946 (2nd print). The Oceans, Their Physics, Chemistry and General Biology. Prentice-Hall, Inc., New York. See Chapter X (pp 331-388) for a description on observational methods and instrumentation including the Negretti & Zambra reversing thermometer (p 349) and Ekman current meter (pp 368-370).*

# A comprehensive oceanographic dataset of a subpolar, mid-latitude broad fjord: Fortune Bay, Newfoundland, Canada

Sebastien Donnet[1], Pascal Lazure[2], Andry Ratsimandresy[1], and Guoqi Han[1,3]

Published in Earth System Science Data, 12, 1877–1896; https://doi.org/10.5194/essd-12-1877-2020

[1] Fisheries and Oceans Canada, Northwest Atlantic Fisheries Centre, 80 East White Hills Rd, St. John's NL, A1C 5X1, Canada

[2] Ifremer (French Research Institute for Exploitation of the Sea) Laboratoire d'Océanographie Physique et Spatiale, Centre Bretagne, ZI de la Pointe du Diable, CS 10070, 29280 Plouzané, France

[3] Fisheries and Oceans Canada, Institute of Ocean Sciences, P.O. Box 6000, Sidney BC, V8L 4B2, Canada

## ABSTRACT

While the dynamics of narrow fjords, i.e. narrow with respect to their internal Rossby radius, have been widely studied, it is only recently that interest in studying the physics of broad fjords was sparked due to their importance in glacial ice melting (in Greenland, especially). Here, we present a comprehensive set of data collected in Fortune Bay, a broad, mid-latitude fjord located on the northwest Atlantic shores. Aside from being wide (15–25 km width) and deep (600 m at its deepest), Fortune Bay also has the characteristics of having steep slopes, having weak tides and being strongly stratified from spring to fall. Thus, and since strong along-shore winds also characterize the region, this system is prone to interesting dynamics, generally taking the form of transient upwelling and downwelling travelling along its shores, similar to processes encountered in broad fjords of higher latitudes. The dataset collected to study those dynamics consists of water column physical parameters (temperature, salinity, currents and water level) and atmospheric forcing (wind speed and direction, atmospheric pressure, air temperature, and solar radiation) taken at several points around the fjord using oceanographic moorings and land-based stations. The program lasted 2 full years and achieved a good data return of 90 %, providing a comprehensive dataset not only for Fortune Bay studies but also for the field of broad fjord studies. The data are available publically from the SEANOE repository (https://doi.org/10.17882/62314; Donnet and Lazure, 2020).

# INTRODUCTION

Fortune Bay is a broad fjord-like embayment located on the south coast of Newfoundland, a large island in the northwest Atlantic (Figure 1). It is about 130 km long and 15–25 km wide, with a maximum depth of about 600 m. It is semi-enclosed from the shelf by a series of sills of about 100–120 m limiting depth.

While situated in mid-latitudes (about 47 °N) the marine climate of this region can be defined as subpolar due to the cooling effect of the cold, equatorward Labrador Current of Arctic origin (Dunbar, 1951, 1953). As a result, its waters are strongly stratified in summer (de Young, 1983, Donnet et al., 2018a), and its internal Rossby radius Ri is smaller than its width (Ri $\sim$ 5–10 km), making it similar to large polar fjords in that regard (e.g. Cottier et al., 2010). While dynamics of narrow fjords, i.e. narrow with respect to their internal Rossby radius, have been well studied, wide fjord dynamics are much less known (see Farmer and Freeland, 1983; Inall and Gillibrand, 2010; Stigebrandt, 2012, for reviews of narrow fjords). Similarly to narrow fjords, and to any coastal areas, tides, winds, freshwater input and remote forcing (e.g. pycnocline and sea-level differences with shelf water) all play a role in the dynamics of broad fjords (e.g. see Cottier et al., 2010, for a review). However, having a width larger than their internal Rossby radius allows for each side to behave independently or have important “wall-to-wall” effects (e.g. Cushman-Roisin et al., 1994; Jackson et al., 2018). In other words, rotation induces cross-fjord variations, in stratification and/or flow, such as surface freshwater distribution, deep water flow and potential transient wind-induced upwelling/downwelling events (Cottier et al., 2010).

Due to their importance in climate change studies, interest in wide fjords such as those present in Greenland has grown in recent years (e.g. Straneo and Cenedese, 2015; Inall et al., 2015; Jackson et al., 2018). Nevertheless and due to their remoteness, available observational data for those important regions remain very scarce.

The first set of oceanographic studies dedicated to Fortune Bay was conducted by researchers and students of Memorial University of Newfoundland (MUN) from the late 1980s to the mid-1990s and focused on deep-water dynamics (de Young and Hay, 1987; Hay and de Young, 1989; White and Hay, 1994) as well as lower trophic biology (Richard, 1987; Richard and Haedrich, 1991). Later on and with the development of the aquaculture industry in the region, renewed interest led to new studies focusing on general geographic and oceanographic characteristics (Donnet et al., 2018b), hydrography (Ratsimandresy et al., 2014; Donnet et al., 2018a), ocean currents (Ratsimandresy et al., 2019) and more specific dynamics induced by strong wind events (Salcedo-Castro and Ratsimandresy, 2013). Based on these latter studies, which focused on the inner part of the embayment, it became evident that a comprehensive and large-scale (i.e. bay scale) survey would be necessary to understand the dominant dynamics of this region.

To this end, an observation program took place from May 2015 to May 2017. The program was centered on the deployment and recovery of oceanographic moorings, deployment and recovery of weather stations and tide gauges, and the collection of temperature and salinity profiles (Figure 1). The key objective and feature of this program was to measure the water column stratification and currents simultaneously at multiple sites, continuously through the four seasons. Along with the observations, a numerical model is being implemented to help understand the processes involved and to predict the transport of variables of interest (e.g. virus, sea lice or organic material originating from or going into aquaculture farms). The main objective of this paper is to report on the data products, describing the methods, limitations, estimated

uncertainties and main results in the hope of being useful not only to further studies of the region but also more generally to the field of broad fjord dynamics studies.

The dataset and its summary description are available at https://doi.org/10.17882/62314.

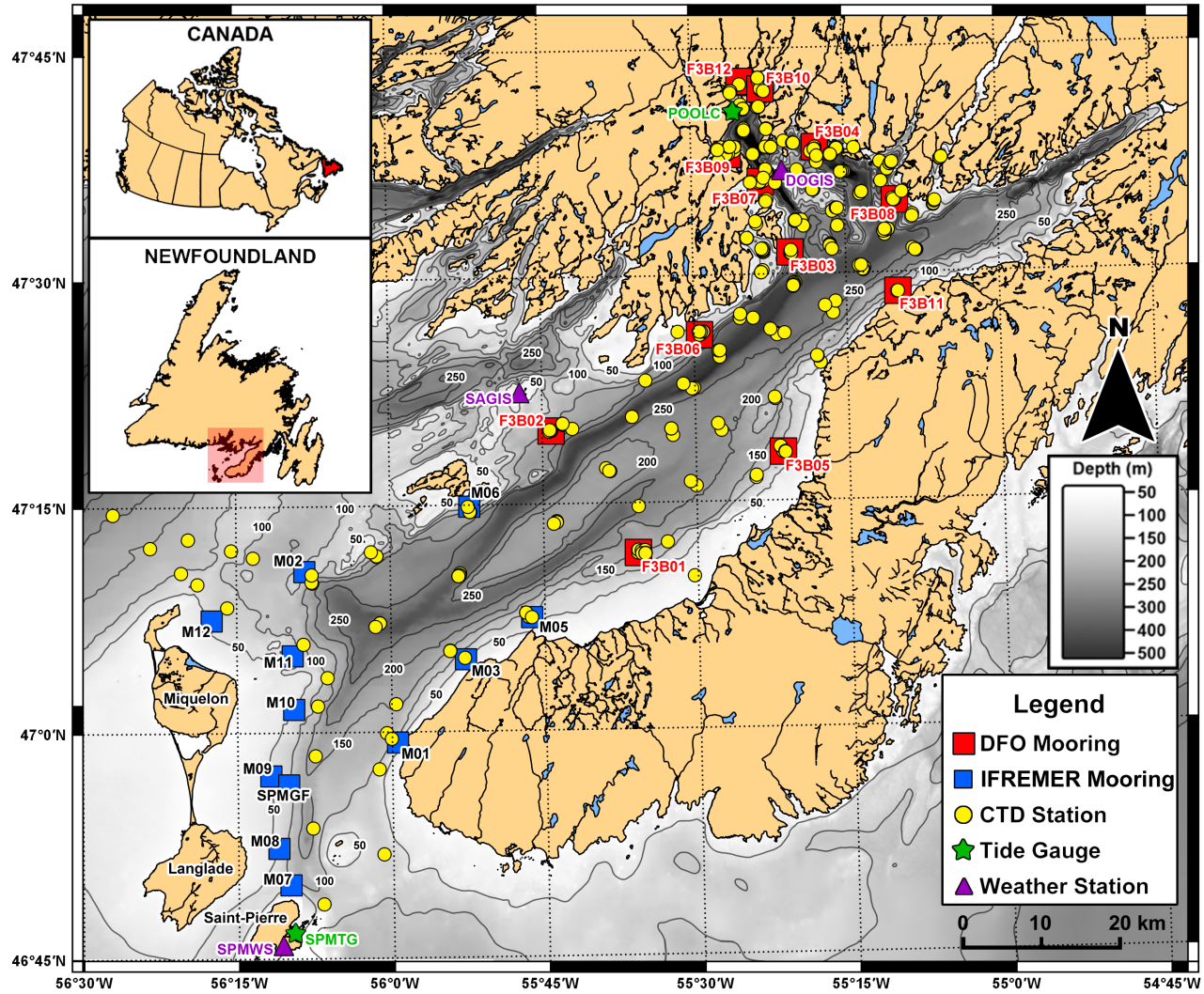


*Figure 1: Study area and summary of the observation program (May 2015–May 2017).*

# MATERIAL AND METHODS

The observation program started in May 2015 with the deployment of eight moorings at four sites (F3B01-04), a weather station (DOGIS) and a tide gauge (POOLC). The program lasted for 2 full years (May 2015–May 2016 defined herein as “year 1” and May 2016–May 2017 defined herein as “year 2”) with maintenance trips occurring every 6 months. Thus, field operations occurred in May and November of each year for about 10–15 d each time, delimiting four observation periods defined herein as “legs”: May–November 2015 (leg 1), November 2015–May 2016 (leg 2), May–November 2016 (leg 3) and November 2016–May 2017 (leg 4). During each trip, additional measurements consisting of CTD (conductivity, temperature and depth) profiles were collected, and a separate trip was organized in August 2016 to get a better seasonal picture of the temperature and salinity field over the whole region. A small opportunistic

survey, restricted to the Belle Bay area, also occurred in June 2016 during the re-deployment of mooring F3B08.

The moorings consisted of a string of thermistors mounted with a couple of CTD sensors (one within each main hydrographic layer) and one (year 2) or two (year 1) Acoustic Doppler Current Profilers (ADCPs) (Figure 2). The setup changed from year 1 to year 2 by merging the originally separated ADCPs and thermistor–CTD sensor lines (by about 100–150 m), thereby doubling the number of main sites being monitored from four (F3B01-04) to eight (F3B01-08). Two other mooring lines were added, F3B09 and 10 and F3B11 and 12 for legs 3 and 4, respectively, to further increase the spatial resolution. With the exception of two moorings during leg 1 (F3B01 and 02), all moorings were of the subsurface, taut-line type. A surface spar buoy was used during leg 1 on F3B01 and 02 in an attempt to measure near-surface conditions and as a deterrent to fishing and shipping activities. The experiment was, however, unsuccessful with the loss of both surface buoys after about 5 months of deployment due to wave action wearing the mooring lines. Of those surface measurements, only one CTD dataset was partially recovered (RBR#60134 from F3B01, found on the shore with its spar buoy). Two main types of mooring were used during year 1 (Figure 2), an “ADCP” type having a set of two upward-looking ADCPs separated by a string of thermistors and a “CTD” type consisting of two CTD sensors separated by a string of thermistors. The CTD type was declined in two versions for leg 1: surface (F3B01 and 02) and subsurface (F3B03 and 04). For leg 2, only the subsurface version was retained, adding a 9 m rope on the top part of F3B01 and 02. In year 2, the “CTD” mooring design of year 1 was used as a base and equipped with an ADCP on the bottom part (around 80 m) to combine water stratification with ocean current measures for most of the sites (F3B01-08). On F3B09 and 10, a simpler design was used due to the shallower depth of the sites and the need for less buoyancy and limitation on available hardware. To minimize drag we used 1/4 in. Dyneema ropes and Open Seas SUBS buoys (Hamilton et al., 1997). CTD sensors were mounted in stainless-steal cages for protection, and thermistors were simply attached to the rope using cable ties and electrical tape. In most cases, acoustic releases were mounted in tandem for redundancy. Cooperation with our partner IFREMER (Institut Français de Recherche pour l’Exploitation de la MER) resulted in other sites being equipped with either bottom-mounted thermistors (M01–10 Mastodon, Lazure et al., 2015) or ADCP moorings (SPMGF) during some of the legs (leg 3 for M01–10 and all along for SPMGF).

The other fixed (and long-term) structures were land-based and consisted of a weather station measuring wind speed and direction (at 2 and 10 m height above ground) as well as barometric pressure, air temperature, solar radiation (Qs) and photosynthetically active radiation (PAR) and of a tide gauge measuring the sea level and sea surface temperature. Two weather station structures were installed on a small, barren island (DOGIS; see Figure 1 for location and Appendix A for an illustration): a 2 m height tripod on which was mounted a wind sensor, a barometer, a temperature sensor, a pyranometer (i.e solar radiation sensor) and a PAR sensor and a 10 m mast on which was mounted another wind sensor. The tide gauge was installed on a wooden wharf at the head of the bay (POOLC; see Figure 1 for location and Appendix A for an illustration) and equipped with a vented pressure sensor mounted below chart datum in a black PVC tube to limit biofouling. These atmospheric and tide observations completed existing sites equipped by other agencies (Figure 1): Sagona Island (SAGIS) weather station (Environment and Climate Change Canada), St Pierre airport weather station (Meteo France) SPMWS and St Pierre harbour tide gauge (Service hydrographique et océanographique de la Marine, France) SPMTG.

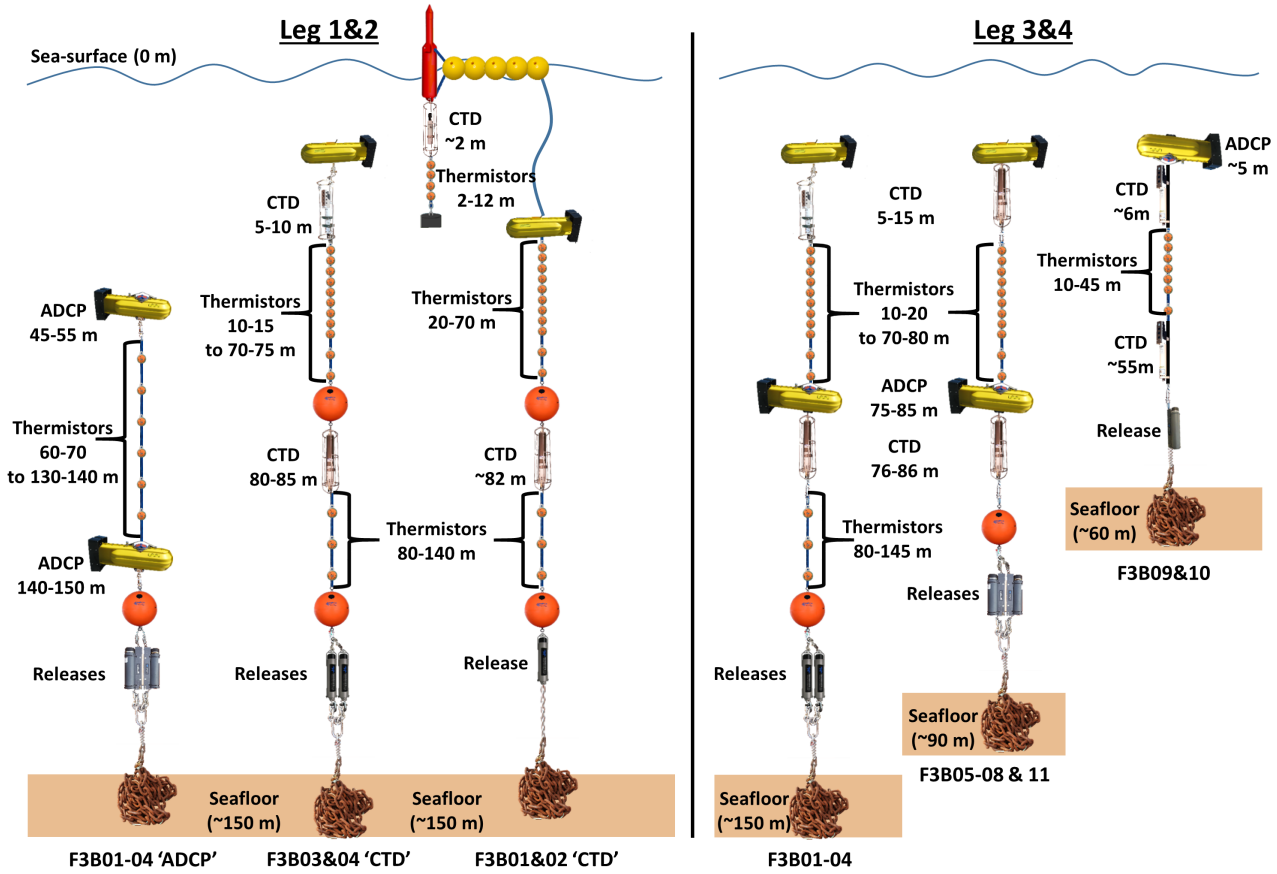


*Figure 2: DFO taut line moorings: legs 1 and 2 (a); legs 3 and 4 (b). In leg 2, F3B01 and F3B02 CTD lines were converted to the F3B03and F3B04 design due to failures of the sea-surface part. A 110 m rope, without thermistors, was added under the bottom CTD of F3B08 to be deployed.*

# INSTRUMENTS USED

A variety of instruments was used during this program, selected for their proven and common use in the field of physical oceanography and atmospheric science. All our ADCPs were WorkHorse models (WH) from Teledyne RDI (T-RDI); most of them were of the 300 kHz type though a few 600 kHz and one 1200 kHz (WH300, WH600 and WH1200) types were also used during the second year. Most of the CTD sensors were Sea-Bird Electronic (SBE) instruments, model 19 ("SeaCAT" manufactured in the 1990s) with a few 37 models ("microCAT" manufactured in the 2000s). A few RBRconcerto CTD sensors as well as XR420 temperature–depth–dissolved oxygen instruments were used on some legs (typically as backup and/or complementary observations). All the thermistors used were disposable Onset HOBO TidbiTs (UTBI), and a few Onset HOBO U20 thermistors equipped with a pressure sensor were also used to complement the UTBI and provide additional depth information of the mooring line. Gill windsonic sensors were used on our weather stations to measure wind speed and direction and were plugged into an Onset HOBO U30 logger on the 2 m tripod and to a Sutron SatLink2 logger with real-time transmitting capability on the 10 m mast. An Onset smart barometric pressure sensor barometer (model S-BPA-CM10), an Onset 12-bit temperature smart sensor air temperature sensor (model S-TMB-M002), an Onset silicon pyranometer smart sensor (S-

LIB-M003) and an Onset PAR smart sensor (S-LIA-M003) were also mounted on the 2 m tripod. A Sutron submersible pressure transducer (model 56-114) was used for the tide gauge, plugged into a Sutron SatLink2 logger with real-time transmitting capability. Characteristics and specifications of all the sensors used are provided in Table 1.

*Table A: Instrumentation used, sampling setup and stated uncertainty (i.e. noise) based on manufacturer specification and sampling setup."Top" and "bottom" refer to ADCP position on the mooring line during legs 1 and 2 (about 50 m vs. 145 m depth, respectively).*

| **Instrument** | **Sampling interval (no. of samples averaged)** | **Uncertainty** |
|---|---|---|
| T-RDI ADCPs | 30 min (120) – legs 1 and 2 top<br>30 min (60) – legs 1 and 2 bottom<br>30 min (200) – leg 3<br>30 min (200) – leg 4 F3B01-02<br>5 min (33) – leg 4 F3B03-12 | 0.7–1.7 cm/s<br>0.03–0.07 °C<br>1.4–3.5 cm |
| SBE19 CTD sensors | 20 min (1) | 0.01 °C<br>0.02 (salinity)<br>10–30 cm (unit dependant) |
| SBE37 CTD sensors | 20 min (1) | 0.002 °C<br>0.006 (salinity)<br>2 % (DO)<br>1 cm |
| RBRconcertos | 20 min (60) | 0.0003 °C<br>0.0008 (salinity)<br>1.3 cm |
| RBR XR420 | 1 min (1) – leg 2<br>20 min (60) – legs 3 and 4 | 0.0004–0.002 °C<br>2 % (DO)<br>4.6–25 cm |
| HOBO UTBI | 10 min (1) | 0.21 °C |
| HOBO U20 | 15 min (1) | 0.44 °C<br>12 cm |
| Mastodon | 1 min (1) | 0.1 °C |
| HOBO U30 | 30 min (1) – legs 1 and 2<br>10 min (30) – legs 3 and 4 | 0.4 %–2 % wind speed<br>0.5–3 ° wind direction<br>0.9–5 mbar (atmospheric pressure)<br>0.04–0.2 °C (air temperature)<br>12–64 W/m$^2$ (solar radiation)<br>40–125 µmol/m$^2$/s (PAR) |
| HOBO U20 (weather station) | 15 min (1) | 0.44 °C (air temperature)<br>12 mbar (atmospheric pressure) |
| SUTRON weather station | 10 min (60) | 0.3 % wind speed<br>0.9° wind direction |
| SUTRON tide gauge | 10 min (1) | 0.3 cm<br>1 °C |

# INSTRUMENT LIMITATIONS AND UNCERTAINTIES

Due to their difference in memory and battery capacity, sampling strategy (i.e. interval) differed from one instrument to another. All the ADCPs were set to sample every 30 min during legs 1–3. For leg 4, a higher sampling rate of 5 min was chosen to increase temporal resolution on moorings F3B03-12. In year 1, ADCPs were set up in "burst mode", that is sampling for a smaller amount of time than their sampling interval (7.5 min vs. 30 min) to avoid possible cross-talk interference since two instruments of the same frequency were used on the same line. In year 2, all the ADCPs were sampling evenly (i.e. continuously) along the sampling average period. Higher vertical resolution (1 m cell) and broadband mode were used during legs 1 and 2 for the near-surface units while lower vertical resolution (3 m cell) and narrowband mode were used for the near-bottom units to maximize range. Overall, a reduction of about 30 % in profile range from the manufacturer specifications was found due to the clarity of the water (i.e. low backscattering volume conditions). Based on first-year results, the sampling strategy was re-thought to increase the horizontal sampling in year 2 (eight or more sites vs. four) while keeping vertical profiling of the stratified part of the water column, i.e. from about 10 to 80 m depth. Cell size was increased from 2 m (leg 3) to 3 m (leg 4) to prevent loss of range during very clear water conditions usually observed in winter. Narrowband mode was used for all our units during year 2 for the same reason.

SBE and RBR CTD sensors were all set to sample at 20 min intervals while the XR420 instruments were set at 1 min intervals during leg 2 and 20 min during legs 3 and 4. The UTBIs were set to 10 min intervals along with the SUTRON weather station and tide gauge (with a 1 min internal average for the SUTRON). The U30 weather station was initially set up with a 30 min interval with no averaging during legs 1 and 2 and then adjusted to a 10 min interval, 30 samples averaged, during legs 3 and 4.

# ADCP BACKSCATTER PROCESSING

To provide some added value, the ADCP backscatter data were processed to convert the raw returned signal strength indicator (RSSI, E in equation below), a measure of acoustic pressure received by the transducers, to a corrected backscatter volume Sv, proportional to the amount (i.e. volume) of particles present in the water column. The method used to do the correction is an updated version of the popular Deines method (Deines, 1999) published by Mullison (2017) and summarized by this equation (Mullison, 2017; Eq. 3):

$$Sv = C + 10log((T_x + 273.16)R^2) - 10log(L_{DBM}) - 10log(P_{DBW}) + 2\alpha R + 10log(10^{Kc(E-Er)/10} - 1)$$

Factory-calibrated values of Kc (count to decibel factor) and Er (noise floor) were used to solve this equation, along with the temperature measured at the transducer head by the instrument ($T_x$). Transducer temperature measured at transducer head and the salinity value selected during instrument setup (ES command; 32 in our deployments) were used to calculate the water absorption (a) along the range (from transducer) R, thereby implying homogeneous water conditions. The transmit pulse length $L_{DBM}$ was calculated using bin size (1–3 m) and beam angle (20°) values. Default values of constant C and transmit power $P_{DBW}$ provided by Mullison (2017, Table 2) were used.

Overall, a combined uncertainty of 5 dB is estimated due to the assumption of water column homogeneity (constant absorption, 0.5 dB maximum error in summer toward the surface); the assumption of constant power source (±3 dB with alkaline batteries, decreasing in transmit power with time) affecting legs 1 and 2 ADCPs more than legs 3 and 4 ADCPs, which were using lithium batteries (featuring a quasi-constant

transmit power all along a deployment), and inherent transducer linearity uncertainties (±1.5 dB according to Deines, 1999). This uncertainty is relatively small in comparison to the 55 dB average range (−90 to −35) observed along the program, i.e. less than 10 %, though not negligible. Note that this uncertainty can be qualified as being “relative” in a sense that it is an uncertainty applicable to any given time series taken separately. In absolute terms, bias can exist due to the assumption made on the constants C and $P_{DBW}$, which may differ from one instrument to another.

# RESULTS

In total, 40 ADCP time series, 60 CTD/TD-DO time series (33 SBE19, 16 SBE37, 6 RBR XR420 and 5 RBRconcerto), 35 UTBI string series, 13 U20 time series, 11 Mastodon thermistor series, 16 weather station series (6 U30, 6 SUTRON and 4 U20) and 4 tide gauge series were collected (Appendix B, Tables B1–B6). Taken together, these time series amount to about 28,715 record days (about 79 years).

Percent coverage presented in Appendix B (Tables B1–B6) is calculated based on the recovered instruments and data only. Lost instruments or instruments from which no data could be recovered are not presented. In total one CTD was lost (RBR#60135 on F3B02, leg 1), one CTD sensor flooded without any possible data recovery (SBE19#1310 on F3B04 leg 2) and 14 UTBIs were lost (5 on F3B01-CTD leg 1, 5 on F3B02-CTD leg 1, 1 on F3B02-ADCP leg 2, 2 on F3B02-CTD legs 2 and 1 on F3B01 leg 3). Outside the failure of F3B01 and 02 top mooring part (10 units lost at once), UTBIs were typically lost during grappling operations when releases could not be triggered. There was also one failed deployment attempt at F3B08 during leg 3 (acoustic release failure in May 2016) which was successfully re-deployed in June 2016 but resulted in about 30 d of observation time lost (from early May to early June).

Percent coverages were calculated based on the good data recovery of current speed, current direction, current vertical speed and water column backscatter volume for the ADCPs; temperature, salinity and depth for the CTD sensors; temperature, dissolved oxygen and depth for the RBR TD-DO sensors; temperature and depth (or atmospheric pressure when used as a weather station sensor) for the U20s; temperature for the UTBIs; depth and temperature for the SUTRON tide gauge; wind speed and direction for the SUTRON weather station; and wind speed, wind direction, atmospheric pressure, air temperature, PAR and solar radiation for the U30 weather station. For each instrument, the percent coverage represents the useable data covering the expected periods of observation; for a multiple-parameter instrument (as listed above) the percent coverage was calculated for each parameter and then averaged per instrument.

Overall, the coverage is about 93 % without considering instrument losses and about 91 % when considering the losses. Illustrations of the data coverage are given in Figures 3 and 4 as Gantt charts.

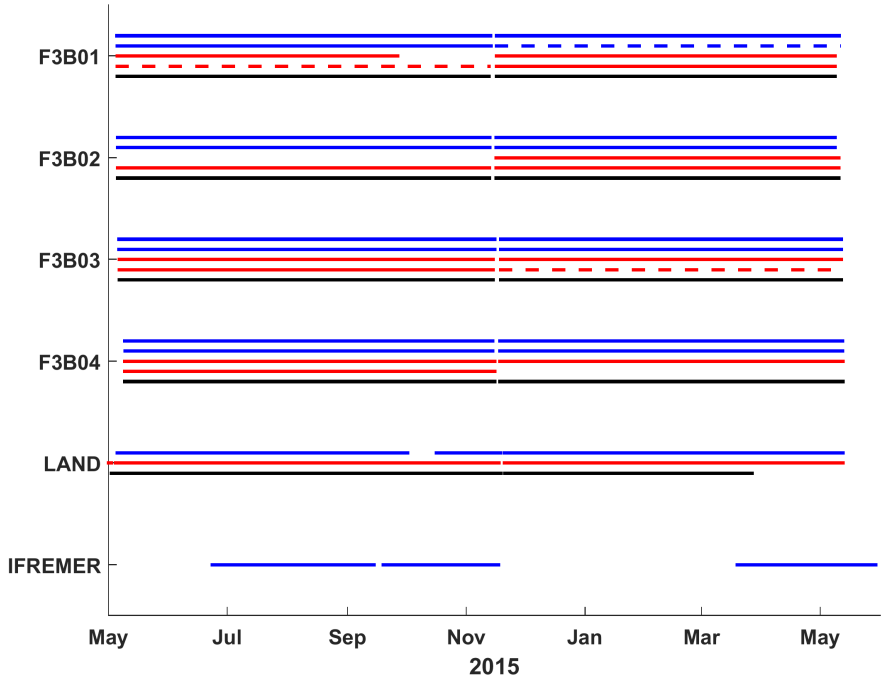


*Figure 3: Data return, legs 1 and 2. For the moorings F3B01-04, ADCPs are in blue, CTD sensors are in red and UBTIs are in black. The top lines correspond to the shallowest unit. For the land-based stations (LAND), DOGIS SUTRON weather station are in blue, DOGIS U30 weather station is in red and POOLC SUTRON tide gauge is in black. IFREMER ADCP data (SPMGF) is in blue. Dashed lines represent partial data recovery (e.g. ADCP tilted, CTD having no or partial salinity return).*

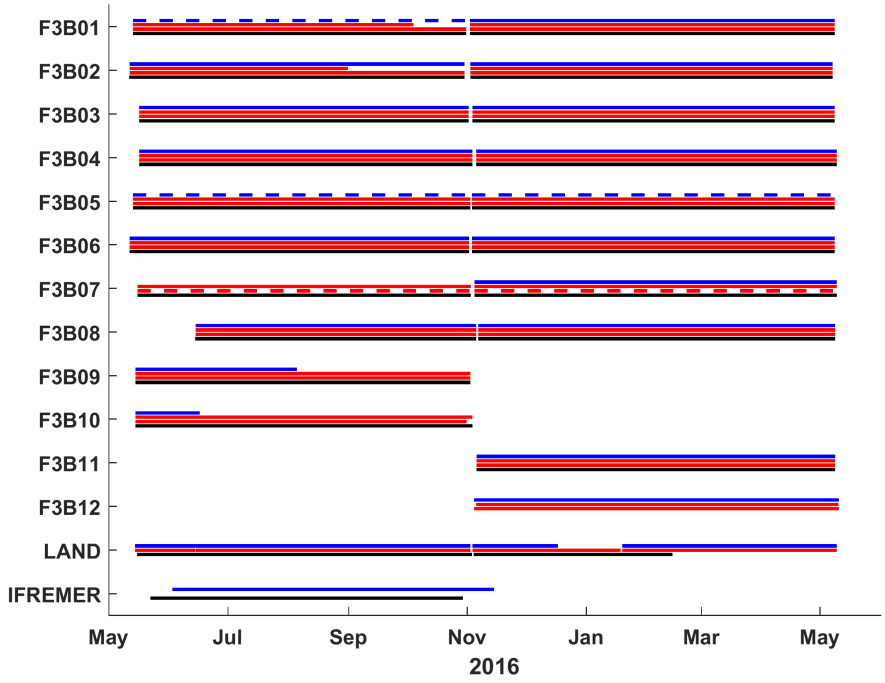


*Figure 4: Data return legs 3 and 4. For the moorings F3B01-12, ADCPs are in blue, CTD sensors are in red and UBTIs are in black. The top lines correspond to the shallowest unit. For the land-based stations (LAND), DOGIS SUTRON weather station is in blue, DOGIS U30 weather station is in red and POOLC SUTRON tide gauge is in black. IFREMER ADCP (SPMGF) and MASTODON (M01-12) data are in blue and black, respectively. Dashed lines represent partial data recovery (e.g. ADCP tilted, CTD having no or partial salinity return).*

# DISCUSSION

The primary objective of this observation program was to collect a robust baseline for studying the main physical processes affecting Fortune Bay. In particular, upwelling and downwelling propagations associated with strong currents along the shoreline were thought to be important features based on previous work done locally (Salcedo-Castro and Ratsimandresy, 2013; Donnet et al., 2018a) and in other embayments of the region (Yao, 1986; de Young et al., 1993; Davidson et al., 2001; Ma et al., 2012). Hence, Fortune Bay's strong seasonal stratification, steep slopes, weak tides, strong along-shore winds and large width all indicated a potential for such "coastally trapped" processes to occur. The observation program was therefore designed to measure water vertical stratification and currents as well as forcing (i.e. wind and sea level) over timescales of tens of minutes to a year and taken at as many locations as possible along the coast, within one internal Rossby radius, to follow potential disturbances travelling around the bay. Such features were indeed observed, and an example of them is presented in Figure 5. The study of those features, including their generation, propagation, scale and importance for particle advection and water renewal, key aspects in studying the effect of aquaculture on the environment, will be the focus of future publications.

The uncertainty estimates presented in Table 1 are based on the instrument specifications and sampling strategy. That is, they represent the expected short-term (i.e. noise) fluctuation around the true measure and assume a perfectly calibrated instrument, i.e. no bias. Laboratory testing and in situ performance checks was performed to further assess these estimates and correct for eventual bias. Laboratory testing were performed in a 3 m depth seawater tank (for the CTD sensors, mainly) to check temperature, salinity and depth measurements, and a stable temperature water bath was used to check temperature measurements (for the UTBI, mainly). In situ checks were obtained using CTD casts taken just after deployment and right before recovery of the moorings and by cross-checking/comparing each instrument from the same mooring line (e.g. pressure measurements). The main biases found were with the pressure sensors of the moored Sea-Bird Electronic model 19 (SBE19) instruments, which could be as large as 6 dbar (~6 m of water depth). A combination of tank test results and in situ checks using the ADCP (and other instruments when available) and mooring line length were used to determine these pressure biases. Both pressure sensor data and corrected backscatter data (i.e. converted to volumetric backscatter values Sv in decibels) were used to determine the in situ depth of the ADCP (i.e. the distance to water surface when using backscatter values), which was then used to crosscheck the depth of the CTD sensors along the line. Biases that could not be determined with reasonable certainty resulted in discarding the data. Except for leg 1, each moored CTD was sent to the manufacturer for calibration prior to deployment. For leg 1, only laboratory tests could be done. All the thermistors used were new, i.e. bought for this program, and the ADCPs were 3–7 years old. The CTD profilers used were sent to the manufacturer for calibration on a yearly basis with a 3-year rotation scheme; i.e. three CTD profilers were available for this program and one profiler was sent per year to be used as a reference for the other two in laboratory and in situ calibration/performance checks. Overall, it is estimated that the absolute depth of each instrument is known to the nearest metre, that the temperature is accurate at ±0.2 °C (UTBIs) or less (CTD sensors), that the salinity is within 0.1 (moored CTD) or less (CTD profiles) from the true value and that the current speed accuracy is ±2 cm/s or better. Note that if further averaging were to be done on those original time series, the uncertainty would go down by the square root of the number of samples taken per sampling average except for the ±1 m uncertainties on depth which can be seen as an unknown bias.

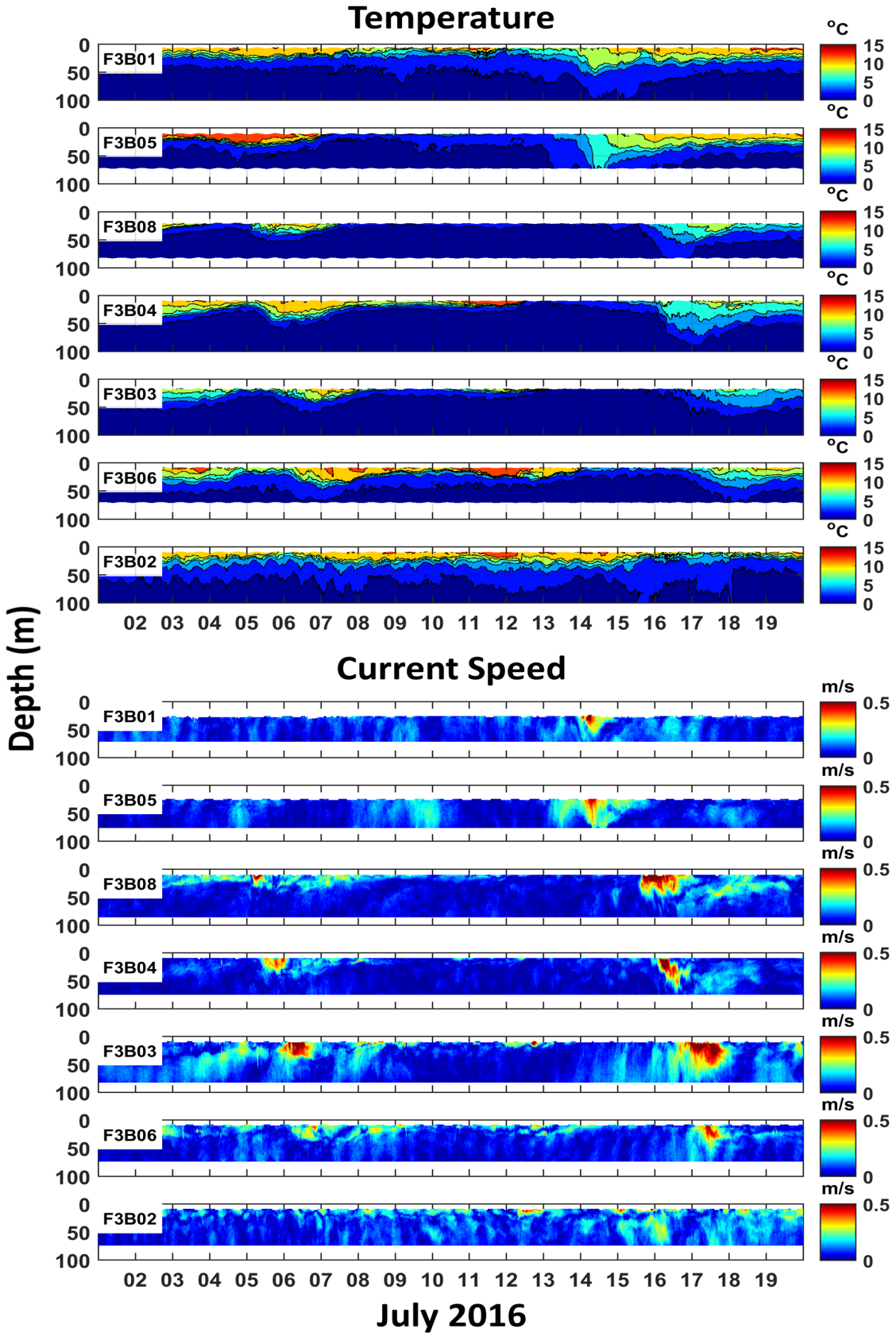


*Figure 5: Fortune Bay water column thermal stratification and cur-rents from 1 to 20 July 2016 showing several upwelling and down-welling events associated with strong current "pulses" travelling around the bay, i.e. from moorings F3B01 to F3B06.*

# DATA LIMITATIONS AND ISSUES

The program suffered from some instrument failures. ADCPs from F3B09 and 10 during leg 3 suffered from a battery failure (F3B09) and from a memory card failure (F3B10), resulting in data coverage of only 48 % (slightly less than 3 months) and 17 % (about 1 month), respectively. Two SBE19 CTDs (no. 1310 and no. 1312) got their electronic casing flooded, resulting in a complete loss of data on F3B04, leg 2 (SBE19#1310) and in partial losses (small leak) on F3B03, leg 2, and on F3B07, legs 3 and 4 (SBE#1312, temperature and salinity data corrupted). The DOGIS SUTRON weather station suffered from a solar panel failure during leg 1, resulting in a reduced coverage of 92 % (a loss of about 12 d) and from a wind sensor failure during leg 3 (56 % coverage, a loss of about 33 d). DOGIS U30 weather station suffered from barometer issues during legs 1, 2 and 3, reducing coverages to 96 %, 83 % and 87 %. The POOLC tide gauge also suffered from sensor failures, during both leg 2 and leg 4 of the program, resulting in reduced coverages of 73 % (47 d lost) and 54 % (86 d lost) and no coverage during the late winter–early spring seasons. The program also suffered from some human errors and practical difficulties. Notably, tangling of mooring ropes has resulted in excessive vertical tilt orientation of the upward-looking ADCP on moorings F3B01, 05 and 07 of leg 3 and on F3B05 of leg 4, corrupting the data (see details below). In the case of leg 3 (F3B01, 05 and 07), problematic deployments in which the mooring line was not properly kept tight prior to releasing the anchor likely played a role. In the case of leg 4 (F3B05) it is less obvious since a stricter mooring deployment procedure was then in place, and those fieldwork records do not indicate any wrongdoing. The use of SUBS buoys, though improving mooring drag and potential “knock-down” from strong currents, increases deployment difficulty when they are placed in the middle of a mooring line (as opposed to the top of a line) since they have a natural tendency of orienting themselves in the flow and thus to have the rope close to their back fin when sinking downward, thereby increasing the chances of being tangled. It should be noted that one case of tangling/excessive ADCP vertical tilt occurred to the bottom ADCP of F3B01 during leg 2, after about 3 weeks of deployment (see below for details and Figure 7), thus not likely due to a deployment issue. Fishing activities may have caused it, though no evidence of it could be found by looking at the data (e.g. rise and fall of the mooring). The data sampling frequency of the ADCP (30 min) prevents a fine examination, though no obvious evidence of mooring movement could be seen with the higher-frequency UBTI records either (10 min), and fishing activities during that time of the year (December) are not very likely. The issue occurred during a strong current event, indicating that strong current shear could potentially be an actor.

# QA/QC AND DATA PROCESSING METHODS

Data were processed and quality checked similarly for all the instruments as follows.

1. Raw data were first converted to the most convenient format known/available to the authors.

2. Time stamp and all variables of interest were extracted from the raw data, and meta-data were associated with the dataset (i.e. station ID, geographical coordinates, deployment and recovery date and time, and instrumentation ID).

3. Using deployment and recovery time, “out-of-water” data were removed.

4. Clock drift and depth offset were assessed and corrected using concurrent data available on the same line. ADCPs were most often used as a reference since their pressure sensors were systematically “zeroed” prior to deployment, and their clock did not drift more than a few minutes per deployment. U20s and RBRs

were usually used as a secondary reference or as a primary one when no ADCPs were available on the same line (e.g. in legs 1 and 2). SBE19 units were the most affected by clock drift and depth offset. A few units (SBE19 as well as UTBI) were also found to have been set up in local time instead of UTC, mistakenly.

5. “Out-of-range” data were removed using automatic filters following the criteria shown in Table 2. ADCP criteria were largely based on the manufacturer recommendations with current speed less than 0 (bad values are actually logged as −32 768; see T-RDI documentation no. P/N 957-6156-00, p. 147), percent good (PG) less than 25 (T-RDI documentation no. P/N 957-6156-00, p.150) and instrument tilt over 15° from the vertical (T-RDI documentation no. P/N 957-6150-00, p. 17) used to remove bad data. Instrument vertical tilt was calculated using the pitch and roll records (see below for details). In addition to those data quality filters, a “surface rejection” filter was applied as a percentage of the range to sea surface (or sea bottom for the downward-looking F3B09 and 10) usually equal to 10 % (i.e. a little higher than the theoretical 6 % stated for 20° beam angle ADCPs, T-RDI documentation no. P/N 951-6069-00 p. 38). Trial and error was performed for this latter filter by examining the velocity, backscatter and correlation profiles of each of the time series. In the case of severely tilted instruments (details below) up to 30 % of the range needed to be removed. Speed, PG and surface rejection filters were applied to all the velocity and backscatter data while tilt filter was only applied to the current velocity direction and “earth”, components of the velocity data (i.e. eastward u, northward v and vertical w; details in technical validation section). For the other instruments, out-of-range filters were based on the expected ranges, i.e. values that would be realistically impossible to attain within the study area, and/or based on default values given automatically to bad data by the logger (e.g. PAR and Qs < 0; see Table 2 for details).

6. A manual “despiking” was finally performed by plotting the data and examining the time series visually. Minimal rejection was done to avoid rejecting potential “outlier events”. As a result, some spurious data points may still be present in some time series.

*Table B: “Out-of-range” filters used to quality control the data.*

| **Instrument** | **Criteria** |
|---|---|
| ADCP | Speed < 0 m/s<br>PG < 25 %<br>Tilt > 15°<br>Surface rejection (8 %–30 % range) |
| CTD | Depth < 0.5 m or > 250 m<br>Temperature < −2 °C or > 25 °C<br>Salinity < 5 or > 37 |
| UTBI | Temperature < −2 °C or > 25 °C |
| U20 | Depth < 0.5 m or > 250 m<br>Temperature < −2 °C or > 25 °C |
| Mastodon | Temperature < −2 °C or > 25 °C |
| Weather stations | Wind speed < 0.05 or > 40 m/s<br>Atmospheric pressure < 850 or<br>> 1069 mbar<br>Temperature < −60 °C or > 60 °C<br>PAR < 0 µmol/$m^2$/s<br>Qs < 0 W m−2 |
| Tide gauge | Depth < 0.5 m or > 5 m<br>Temperature < −2 °C or > 25 °C |

The CTD profiles were processed using SBE data analysis software, and recommended procedure as described in Donnet et al. (2018a). CTD profiles were averaged in 1 m bins and visually checked individually.

## UTBI DEPTH CALCULATION

Since our thermistors (UTBI) did not have embedded pressure sensors, the depth of their temperature records needed to be estimated. This calculation was done in three steps, increasing the accuracy of the estimate at each step.

1. Once a site depth was accurately determined, mean depth of each UTBI was determined using the mooring diagrams providing with the distance from sea bottom of each instrument. Mean depth (with respect to mean sea level, MSL) was then determined as site depth minus height above sea bottom.

2. “Tidal depth”, i.e. depth varying due to the tide alone, was determined using the results of tidal analyses made on the instruments equipped with a pressure sensor (i.e. ADCP, CTD and U20). One reference per mooring line was used, typically the instrument located the closest to the top of the mooring having the highest data coverage so that the overall mooring tilt was best approximated (CTD or U20). Tidal analysis was done using the T_TIDE programs (Pawlowicz et al., 2002), and UTBI “tidal depths” were calculated as MSL depth plus tide.

3. Finally, to take the mooring movement into account, i.e. lateral movements of the mooring line due to current drag, an “absolute depth” was determined using an estimate of the mooring horizontal tilt angle. Tilt angle was determined using the same depth time series from which a tidal analysis was performed for the previous step. A water level residual was then calculated as measured water level (from MSL) minus tide. This residual was then used to calculate a mooring line tilt angle series as tilt = acos(H/L), where H is the instrument height above sea bottom at any given time and L is the instrument height at rest (i.e. its mean height). Using the horizontal tilt angle time series, UTBI series of height above sea bottom were calculated as H = L × cos(tilt), where L is the UTBI height above sea bottom at rest. The “absolute depth” series was then determined as site depth minus H plus tide.

Overall, the mooring lines’ average vertical tilt was below 5° (2–4° with a standard deviation of the order of 1–2°) with maximums on the order of 15–25° during extreme events, corresponding to vertical mooring displacements of about 5–15 m. These vertical “knock-downs” are large compared to the 1–2 m tidal range reported in the region (Donnet et al., 2018b) but relatively small in comparison to the mooring line length (about 5 %–10 %), indicating good mooring performances.

It should be noted that these estimates of tilt and therefore instrument depths assume no other external variation in sea level than the tides. Other factors such as storm surges or shelf waves can affect the sea level on the order of 0.2–1 m in the region (e.g. Tang et al., 1998; Thiebaut and Vennel, 2010; Han et al., 2012; Ma et al., 2015). A preliminary inspection of our tide gauge records (not shown) indicate that residuals, i.e. water level variations not attributed to tides, of the same range were observed during our program.

## IN SITU COMPARISONS (E.G. CTD PROFILE VS. MOORING DATA)

A CTD cast was performed after each mooring deployment and just before mooring recovery (see Figure 6 as an example). Thus, a total of 52 casts were available for in situ checks (F3B03 and F3B04 leg 3 pre-

recovery casts were missed). The primary goal of those checks was to assess the performance of the moored UTBI lines (temperature) and moored CTDs (salinity).

Overall, a mean difference of 0.12 °C and associated mean standard deviation of 0.11 °C were found between the CTD profiles and UBTI observations, and an overall mean salinity difference of 0.07 and mean standard deviation of 0.03 between the CTD profiles and moored CTD sensor were obtained.

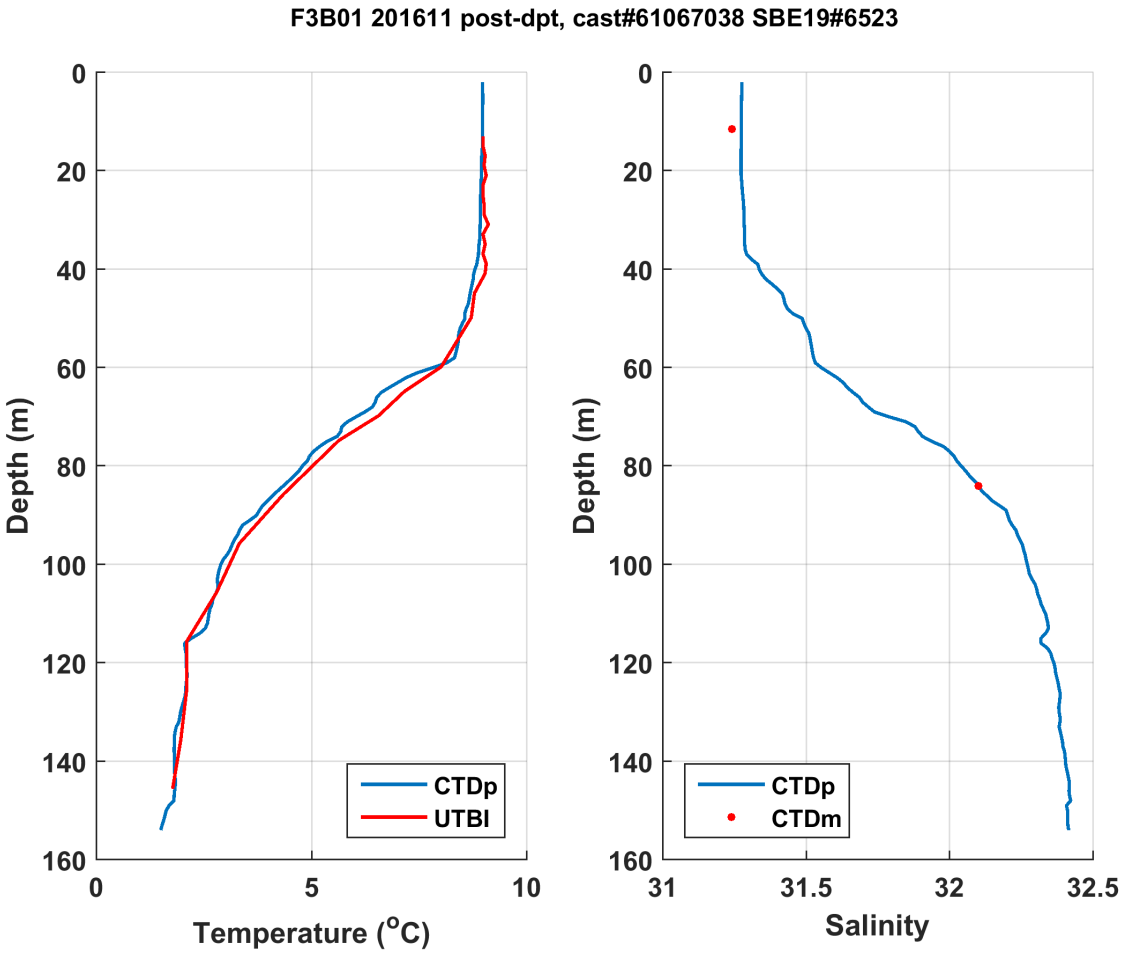


*Figure 6: In situ CTD profile (CTDp) comparison with moored thermistors (UTBI) and moored CTD (CTDm) on 7 November 2016 at F3B01.*

# ADCP TILT ISSUE

Excessive vertical tilt affects ADCPs' gyrocompass by biasing the heading, which corrupts trigonometric rotation from instrument coordinates to earth coordinates (T-RDI, personal communication, 2018, 2020, and details in T-RDI documentation no. P/N 951-6079-00). T-RDI indicates that while their attitude sensor can measure tilts (i.e. pitch and roll) up to about 20°, tilts above 15° will irreversibly corrupt the data (T-RDI documentation no. P/N 957-6150-00 p. 17). If the tilt, however, stays within a measurable range (i.e. 15° to about 20°), bin mapping will still hold (T-RDI, personal communication, 2018; see details in T-RDI documentation no. P/N 951-6079-00), and, thus, horizontal measurements of current speed and backscatter, i.e. variables not affected by erroneous heading, will still be correct and properly "mapped". At

20°, any given beam may end up being oriented horizontally, which prevents the derivation of the horizontal component of the current. A three-beam solution may still work but the flow horizontal homogeneity assumption cannot be assessed (the so-called “error velocity”; see T-RDI documentation no. P/N 951-6069-00 p. 14 and P/N 957-6150-00 p. 14 for details), thereby limiting quality control. Beyond the tilt sensor limits (i.e. in pitch and roll axes) which can be anywhere from 20 to about 25° (see Table 3), current speed calculation and bin mapping will become biased; profile data will then likely be unrecoverable. An illustration of this issue and potential recoverable data is presented in Figure 7. The top 50 m (not affected by over-tilted position) and bottom (over-tilted from 7 December) ADCP profiles are plotted together, showing the effects of the tilt on current direction and current vertical component w but not on current speed and acoustic backscatter.

In our quality control process, a “combined” tilt angle, i.e. combination of pitch and roll angles, was used to filter unreliable current direction and earth coordinate velocities (i.e. u, v and w). This combined tilt was calculated as follows:

$$tilt = acos(cos(pitch) \times cos(roll))$$

This rejection is somehow conservative since this combined angle is always larger than the pitch and roll taken individually.

In addition to this automatic filter, bench tests were performed on each of our ADCPs to determine their maximum pitch and roll angles measurable by placing each unit horizontally on a table on each direction, i.e. beam 1–2 and beam 3–4 axes, which helped us to further assess the quality of our data (Table 3).

Five time series were affected by this issue in total: F3B01 leg 2 (bottom unit), F3B01 leg 3, F3B05 legs 3 and 4, and F3B07 leg 3. Being tilted near both pitch and roll limits, the latter was corrupted beyond repair, and nothing could be saved from it. The other four were generally severely tilted, but below the limits and on one side “only”; current speed and backscatter profiles were saved from those time series.

*Table C: Severely tilted time series screening.*

| **Site and leg** | **Mean pitch (°)** | **Mean roll (°)** | **Max pitch (°) (bench)** | **Max roll (°) (bench)** |
|---|---:|---:|---:|---:|
| F3B01, leg 2 | 18.1 | -0.3 | 24.2 | 23.5 |
| F3B01, leg 3 | -10.1 | 25.9 | 24.8 | 26.4 |
| F3B05, leg 3 | 22.0 | -1.1 | 24.2 | 23.5 |
| F3B07, leg 3 | 24.2 | 23.4 | 24.8 | 24.7 |
| F3B05, leg 4 | 21.5 | -0.3 | 24.2 | 23.5 |

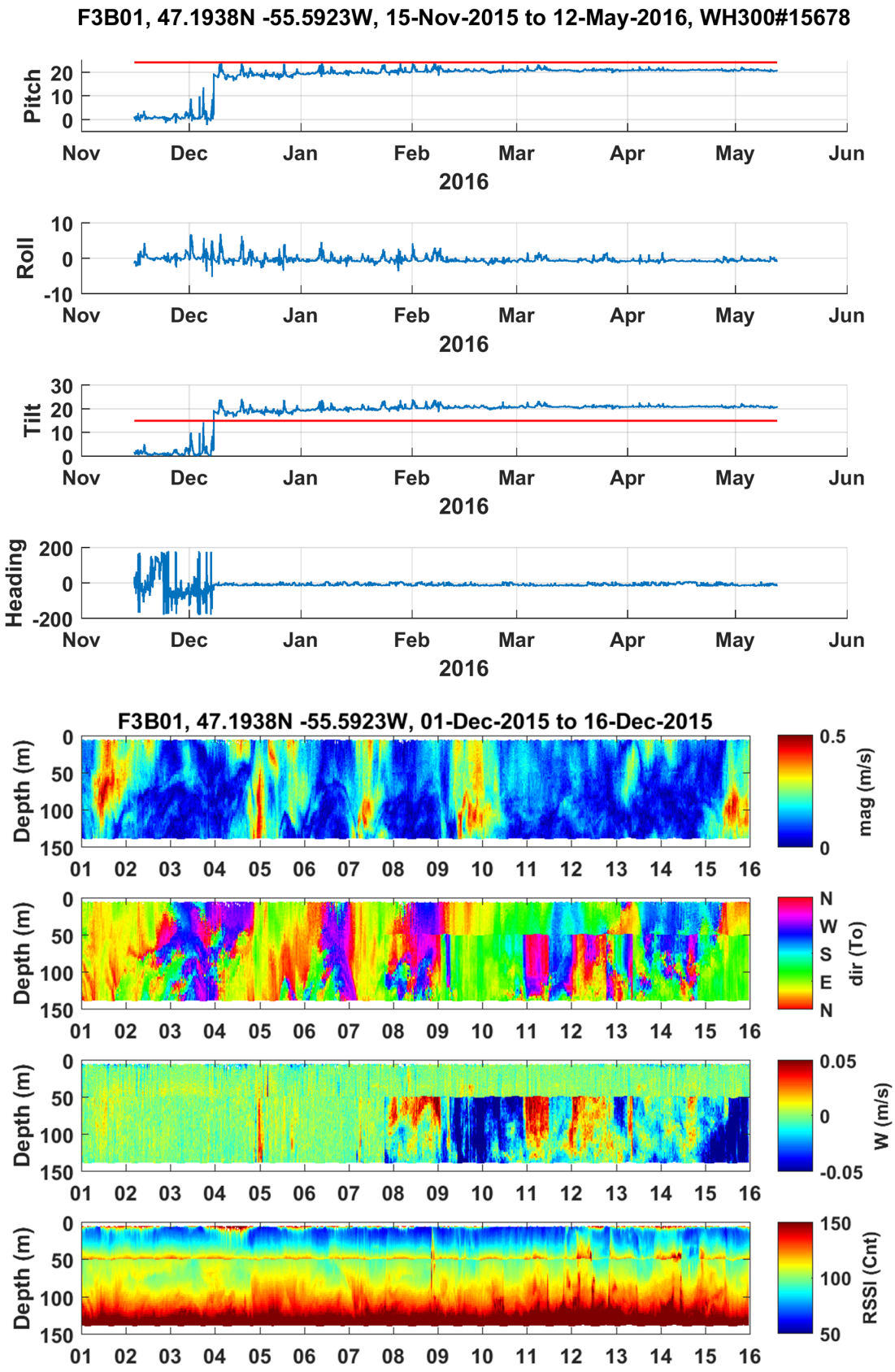


*Figure 7: Example of an ADCP over-tilted issue. The event occurred on 7 December 2015 between 18:30 and 19:30 UTC, tilting the bottom ADCP of the mooring line on the pitch axis. The top four panels show the attitude sensor, pitch (first panel), roll (second panel), calculated "combined" tilt angle (third panel) and heading (fourth panel and as recorded by the instrument). Red lines on the pitch and tilt plots indicate the maximum sensor range as determined by bench test and the maximum accepted tilt angle of our quality control filter. The bottom four panels show current speed(mag), current direction (dir), current vertical component (w) and raw backscatter data (RSSI) zooming on the period 1–16 December2015.*

# DATA AVAILABILITY

Processed data are available from the SEANOE repository (https://doi.org/10.17882/62314, Donnet and Lazure, 2020). One file per time series was created in the NetCDF format containing a header with key metadata (site ID, geographic coordinates, site depth, instrument used, author and date of creation) and the data themselves with consistent variable naming (e.g. time, depth, temperature etc.). UTBI time series were bundled together into one folder per mooring line and, thus, one processed file per time series. CTD profiles were bundled up per survey and formatted as tab-delimited ASCII ODV4 files (Schlitzer, 2019). NetCDF files were created under the MATLAB environment and tested using the NetCDF utilities (ncdump from unidata), Python (with xarray and panda libraries) and the Interactive Data Language (IDL) environments. Care was taken to export as much data from the raw as possible (e.g. ADCP correlation magnitudes), but they are provided as “processed”; that is, bad data flagged by the QA/QC (quality assessment/quality control) process described below were replaced by NaN (not a number) values.

# CONCLUSION

We present an oceanographic dataset collected in a subpolar, mid-latitude, broad fjord. The data collection was centered on the deployment and recovery of oceanographic moorings and a few land-based stations collecting physical parameters such as water temperature and salinity, ocean currents, wind speed and direction, and tide. The main goal of this observation program was to serve as a base to further study the main physical processes affecting this embayment which are likely common to other wide stratified fjords.

To our knowledge, very few embayments alike, i.e. broad fjords, have such comprehensive observations combining numerous and continuous in situ sampling points. Several bays in the region have been well explored in the past but their continuous observation via moorings rarely extended more than a few months during the spring to fall seasons, thus not offering a complete seasonal picture (e.g. Yao, 1986; de Young and Sanderson, 1995; Hart et al., 1999; Schillinger et al., 2000; Tittensor et al., 2002a, b). Abroad, with the increasing interest in polar regions and their importance in climate, many recent studies relied on significant datasets collected in broad fjords (e.g. Straneo et al., 2010; Jackson et al., 2014; Inall et al., 2015; Merrifield et al., 2018). Generally, and most likely due to extremely challenging technical constraints (e.g. massive glacial ice), those datasets remain scarce and limited to a few points and/or few months of observation, however. A notable exception to this scarcity is the important research effort spent in Svalbard since 2002 (see Hop et al., 2019, for a review).

By combining a relatively large number of observation points (up to 21 moorings during leg 3), high vertical resolution in both thermal stratification (2–10 m) and ocean currents (1–3 m), and duration (2 years), we believe that this dataset should be comprehensive enough to study a wide variety of processes, making it of particular interest to be shared.

# AUTHOR CONTRIBUTIONS

SD designed the study with the assistance of PL, AWR and GH. SD designed and directed the fieldwork, including the mooring design and pre-implementation modelling. SD processed all the data except those from the Mastodon, which were processed by PL. SD designed and led the QA/QC procedures and data analyses with contributions from PL, AWR and GH. SD prepared the figures and wrote the manuscript with contributing reviews from PL, AWR and GH.

# COMPETING INTERESTS

The authors declare that they have no conflict of interest.

# DISCLAIMER

The data are published without any warranty, express or implied. The user assumes all risks arising from their use of the data. The data are intended to be research quality. It is the sole responsibility of the user to assess if the data are appropriate for their use and to interpret the data, data quality and data accuracy accordingly. Authors welcome users to ask questions and report problems.

# ACKNOWLEDGEMENTS

A number of people contributed to the field effort and to them we are very grateful; many thanks to Dwight Drover (DFO legs 2–4), Pierre Goulet (DFO legs 1 and 2), Kim Marshall (DFO leg 2), Sharon Kenny (DFO leg 2), Shannon Cross (DFO leg 3), Marion Bezaud (DFO-IFREMER leg 4), Herle Goraguer (IFREMER) and Jean-Pierre Claireaux (DTAM; IFREMER data). We also thank Shannon Cross and Daria Gallardi for their kind assistance in preparing Figure 1 and 2 (respectively). Special thanks are also due to Bruce Batstone and Aubrey Beaver for their very helpful discussions and guidance during the early stages of the mooring design. Finally, we wish to thank the reviewers for their constructive remarks, helping to improve the manuscript.

# FINANCIAL SUPPORT

This program was funded by DFO's ACRDP (Aquaculture Collaborative Research and Development Program) in partnership with Cold Ocean Salmon (COS), Northern Harvest Sea Farms Ltd. and the Newfoundland Aquaculture Industry Association (NAIA). IFREMER's contribution was funded by DTAM (Direction des Territoires de l'Alimentation et de la Mer, Saint-Pierre et Miquelon).

# REVIEW STATEMENT

This paper was edited by Giuseppe M. R. Manzella and reviewed by Vladislav Petrusevich and one anonymous referee.

# REFERENCES


Cottier, F.R., Nilsen, F., Skogseth, R., Tverberg, V., Skarðhamar, J., Svendsen, H., 2010. Arctic fjords: a review of the oceanographic environment and dominant physical processes. SP 344, 35–50. https://doi.org/10.1144/SP344.4

Cushman-Roisin, B., Asplin, L., Svendsen, H., 1994. Upwelling in broad fjords. Continental Shelf Research 14, 1701–1721. https://doi.org/10.1016/0278-4343(94)90044-2

Davidson, F.J.M., Greatbatch, R.J., de Young, B., 2001. Asymmetry in the response of a stratified coastal embayment to wind forcing. J. Geophys. Res. 106, 7001–7015. https://doi.org/10.1029/2000JC900052

de Young, B., 1983. Deep water exchange in Fortune Bay, Newfoundland (MSc Thesis). Memorial University of Newfoundland, St. John's, NL. http://research.library.mun.ca/id/eprint/5754 (accessed 26-Sep-2022)

de Young, B., Hay, A.E., 1987. Density Current Flow into Fortune Bay, Newfoundland. J. Phys. Oceanogr. 17, 1066–1070. https://doi.org/10.1175/1520-0485(1987)017<1066:DCFIFB>2.0.CO;2

de Young, B., Otterson, T., Greatbatch, R.J., 1993. The Local and Nonlocal Response of Conception Bay to Wind Forcing. Journal of Physical Oceanography 23, 2636–2649. https://doi.org/10.1175/1520-0485(1993)023<2636:TLANRO>2.0.CO;2

de Young, B., Sanderson, B., 1995. The circulation and hydrography of conception bay, Newfoundland. Atmosphere-Ocean 33, 135–162. https://doi.org/10.1080/07055900.1995.9649528

Deines, K.L., 1999. Backscatter estimation using broadband acoustic Doppler current profilers, in: Proceedings of the IEEE Sixth Working Conference on Current Measurement (Cat. No. 99CH36331). IEEE, pp. 249–253.

Donnet, S., Cross, S., Goulet, P., Ratsimandresy, A.W., 2018a. Coast of Bays seawater vertical and horizontal structure (2009-13): Hydrographic structure, spatial variability and seasonality based on the Program for Aquaculture Regulatory Research (PARR) 2009-13 oceanographic surveys (DFO Can. Sci. Advis. Sec. Res. Doc. No. 2017/077). https://waves-vagues.dfo-mpo.gc.ca/library-bibliotheque/40655945.pdf (accessed 26-Sep-2022)

Donnet, S., Lazure, P., 2020. Fortune Bay (NL, Canada) oceanographic observations May 2015 - May 2017. https://doi.org/10.17882/62314

Donnet, S., Ratsimandresy, A.W., Goulet, P., Doody, C., Burke, S., Cross, S., 2018b. Coast of Bays Metrics: Geography, Hydrology and Physical Oceanography of an Aquaculture Area of the South Coast of Newfoundland (DFO Can. Sci. Advis. Sec. Res. Doc. No. 2017/076). https://waves-vagues.dfo-mpo.gc.ca/library-bibliotheque/40654473.pdf (accessed 26-Sep-2022)

Dunbar, M., 1953. Arctic and subarctic marine ecology: immediate problems. Arctic 6, 75–90.

Dunbar, M.J., 1951. Eastern arctic waters: a summary of our present knowledge of the physical oceanography of the eastern arctic area, from Hudson Bay to Cape Farewell and from Belle Isle to Smith Sound, Bulletin. Fisheries Research Board of Canada.

Farmer, D.M., Freeland, H.J., 1983. The physical oceanography of Fjords. Progress in Oceanography 12, 147–

219. https://doi.org/10.1016/0079-6611(83)90004-6

Hamilton, J.M., Fowler, G.A., Belliveau, D.J., 1997. Mooring Vibration as a Source of Current Meter Error and Its Correction. Journal of Atmospheric and Oceanic Technology 14, 644–655. https://doi.org/10.1175/1520-0426(1997)014<0644:MVAASO>2.0.CO;2

Han, G., Ma, Z., Chen, D., deYoung, B., Chen, N., 2012. Observing storm surges from space: Hurricane Igor off Newfoundland. Sci Rep 2, 1010. https://doi.org/10.1038/srep01010

Hart, D.J., De Young, B., Foley, J.S., 1999. Observations of Currents, Temperature and Salinity in Placentia Bay, Newfoundland 1998-9 (Data Report No. 99–3). Department of Physics and Physical Oceanography, Memorial University of Newfoundland, St. John's, NL. https://www.physics.mun.ca/~bdeyoung/hart-deyoun_placentia_bay_1999.pdf (accessed 26-Sep-2022)

Hay, A.E., de Young, B., 1989. An oceanographic flip-flop: deep water exchange in Fortune Bay, Newfoundland. J. Geophys. Res. 94, 843. https://doi.org/10.1029/JC094iC01p00843

Hop, H., Cottier, F., Berge, J., 2019. Autonomous Marine Observatories in Kongsfjorden, Svalbard, in: Hop, H., Wiencke, C. (Eds.), The Ecosystem of Kongsfjorden, Svalbard, Advances in Polar Ecology. Springer International Publishing, Cham, pp. 515–533. https://doi.org/10.1007/978-3-319-46425-1_13

Inall, M.E., Gillibrand, P.A., 2010. The physics of mid-latitude fjords: a review. SP 344, 17–33. https://doi.org/10.1144/SP344.3

Inall, M.E., Nilsen, F., Cottier, F.R., Daae, R., 2015. Shelf/fjord exchange driven by coastal-trapped waves in the A rctic. J. Geophys. Res. Oceans 120, 8283–8303. https://doi.org/10.1002/2015JC011277

Jackson, R.H., Lentz, S.J., Straneo, F., 2018. The Dynamics of Shelf Forcing in Greenlandic Fjords. Journal of Physical Oceanography 48, 2799–2827. https://doi.org/10.1175/JPO-D-18-0057.1

Jackson, R.H., Straneo, F., Sutherland, D.A., 2014. Externally forced fluctuations in ocean temperature at Greenland glaciers in non-summer months. Nature Geosci 7, 503–508. https://doi.org/10.1038/ngeo2186

Lazure, P., Le Berre, D., Gautier, L., 2015. Mastodon Mooring System To Measure Seabed Temperature Data Logger With Ballast, Release Device at European Continental Shelf. Sea Technology.

Lazure, P., Le Cann, B., Bezaud, M., 2018. Large diurnal bottom temperature oscillations around the Saint Pierre and Miquelon archipelago. Sci Rep 8, 13882. https://doi.org/10.1038/s41598-018-31857-w

Ma, Z., Han, G., deYoung, B., 2012. Modelling Temperature, Currents and Stratification in Placentia Bay. Atmosphere-Ocean 50, 244–260. https://doi.org/10.1080/07055900.2012.677413

Ma, Z., Han, G., Young, B., 2015. Oceanic responses to H urricane I gor over the G rand B anks: A modeling study. J. Geophys. Res. Oceans 120, 1276–1295. https://doi.org/10.1002/2014JC010322

Merrifield, S., Otero, M., Terrill, E., 2018. Observations of Shelf Exchange and High-Frequency Variability in an Alaskan Fjord. J. Geophys. Res. Oceans 123, 4720–4734. https://doi.org/10.1029/2018JC013931

Mullison, J., 2017. Backscatter estimation using broadband acoustic doppler current profilers-updated, in: Proceedings of the ASCE Hydraulic Measurements & Experimental Methods Conference, Durham, NH, USA. pp. 9–12.

Pawlowicz, R., Beardsley, B., Lentz, S., 2002. Classical tidal harmonic analysis including error estimates in MATLAB using T_TIDE. Computers & Geosciences 28, 929–937. https://doi.org/10.1016/S0098-3004(02)00013-4

Ratsimandresy, A.W., Donnet, S., Goulet, P., Bachmayer, R., Claus, B., 2014. Variation in the structure of the water column as captured by Slocum glider CTD and by CTD from a research vessel and assessment of internal waves, in: 2014 Oceans - St. John's. Presented at the OCEANS 2014, IEEE, St. John's, NL, pp. 1–10. https://doi.org/10.1109/OCEANS.2014.7003283

Ratsimandresy, A.W., Donnet, S., Snook, S., Goulet, P., 2019. Analysis of the variability of the ocean currents in the Coast of Bays area (DFO Can. Sci. Advis. Sec. Res. Doc. No. 2019/008). https://waves-vagues.dfo-mpo.gc.ca/library-bibliotheque/40805116.pdf (accessed 26-Sep-2022)

Richard, J.M., 1987. The mesopelagic fish and invertebrate macrozooplankton faunas of two Newfoundland fjords with differing physical oceanography (MSc Thesis). Memorial University of Newfoundland. http://research.library.mun.ca/id/eprint/4196 (accessed 26-Sep-2022)

Richard, J.M., Haedrich, R.L., 1991. A comparison of the macrozooplankton faunas in two newfoundland fjords differing in physical oceanography. Sarsia 76, 41–52. https://doi.org/10.1080/00364827.1991.10413465

Salcedo-Castro, J., Ratsimandresy, A.W., 2013. Oceanographic response to the passage of hurricanes in Belle Bay, Newfoundland. Estuarine, Coastal and Shelf Science 133, 224–234. https://doi.org/10.1016/j.ecss.2013.08.031

Schillinger, D.J., Simmons, P., De Young, B., 2000. Analysis of the mean circulation in Placentia Bay: spring and summer 1999 (Data Report No. 2000–1). Department of Physics and Physical Oceanography, Memorial University of Newfoundland. https://www.physics.mun.ca/~bdeyoung/schillinger_placentiabay_2000-1.pdf (accessed 26-Sep-2022)

Stigebrandt, A., 2012. Hydrodynamics and circulation of fjords. Encyclopedia of lakes and reservoirs 327, 344.

Straneo, F., Cenedese, C., 2015. The Dynamics of Greenland's Glacial Fjords and Their Role in Climate. Annu. Rev. Mar. Sci. 7, 89–112. https://doi.org/10.1146/annurev-marine-010213-135133

Straneo, F., Hamilton, G.S., Sutherland, D.A., Stearns, L.A., Davidson, F., Hammill, M.O., Stenson, G.B., Rosing-Asvid, A., 2010. Rapid circulation of warm subtropical waters in a major glacial fjord in East Greenland. Nature Geosci 3, 182–186. https://doi.org/10.1038/ngeo764

Tang, C.L., Gui, Q., DeTracey, B.M., 1998. Barotropic Response of the Labrador/Newfoundland Shelf to a Moving Storm. Journal of Physical Oceanography 28, 1152–1172. https://doi.org/10.1175/1520-0485(1998)028<1152:BROTLN>2.0.CO;2

Thiebaut, S., Vennell, R., 2010. Observation of a Fast Continental Shelf Wave Generated by a Storm Impacting Newfoundland Using Wavelet and Cross-Wavelet Analyses. Journal of Physical Oceanography 40, 417–428. https://doi.org/10.1175/2009JPO4204.1

Tittensor, D.P., De Young, B., Foley, J., 2002a. Analysis of physical oceanographic data from Trinity Bay, May-August 2002 (Data Report No. 2002–2). Department of Physics and Physical Oceanography, Memorial

University of Newfoundland. https://www.physics.mun.ca/~bdeyoung/tittensor_trinity_bay_2002-2.pdf (accessed 26-Sep-2022)

Tittensor, D.P., Richard, N., De Young, B., Foley, J., 2002b. Analysis of physical oceanographic data from Trinity Bay, May-August 2001 (Data Report No. 2002–1). Department of Physics and Physical Oceanography, Memorial University of Newfoundland. https://www.physics.mun.ca/~bdeyoung/tittensor_trinitybay_2002-1.pdf (accessed 26-Sep-2022)

White, M., Hay, A.E., 1994. Dense overflow into a large silled embayment: Tidal modulation, fronts and basin modes. issn: 0022-2402 52, 459–487. https://doi.org/10.1357/0022240943077055

Yao, T., 1986. The response of currents in Trinity Bay, Newfoundland, to local wind forcing. Atmosphere-Ocean 24, 235–252. https://doi.org/10.1080/07055900.1986.9649249

# APPENDIX A

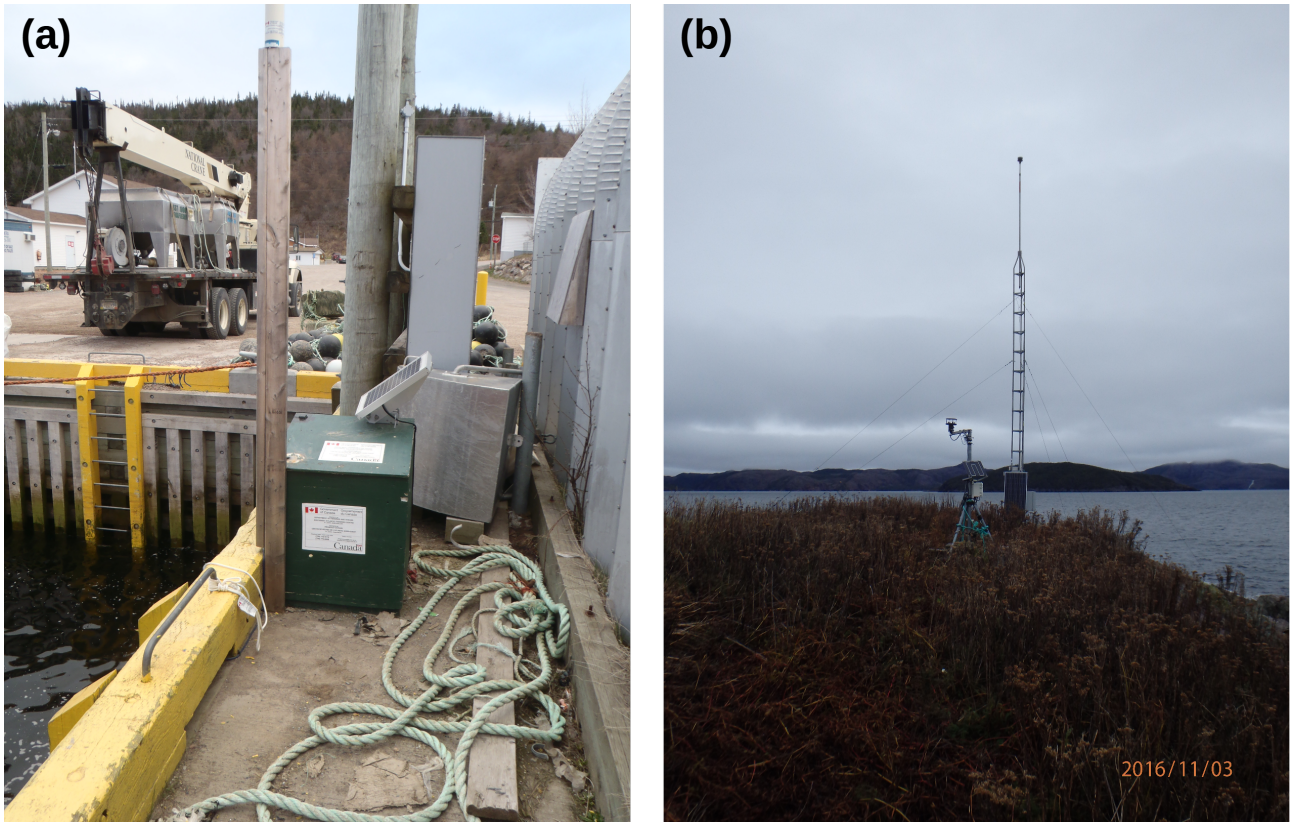


*Figure A1: Pool's Cove (POOLC) tide gauge (a) and Dog Island (DOGIS) weather stations (b).*

*Figure A2: mooring line ready to be deployed.*

# APPENDIX B

*Table B1: Data collection summary, leg 1 (May–November 2015)*

| Site | Instrument | Latitude (°N) | Longitude (°W) | Deployment | Recovery | Site depth | Instrument depth | % coverage |
|---|---|---|---|---|---|---|---|---|
| F3B01 | WH300 #12548 | 47.193717 | -55.590867 | 2015-05-04 12:53:40 | 2015-11-14 15:33:00 | 151 | 51 | 97 |
| F3B01 | WH300 #15678 | 47.193717 | -55.590867 | 2015-05-04 12:53:40 | 2015-11-14 15:33:00 | 151 | 142 | 88 |
| F3B01 | RBR #60134 | 47.194990 | -55.588950 | 2015-05-04 16:24:10 | 2015-11-14 15:47:00 | 151 | 2 | 75 |
| F3B01 | SBE19 #1019 | 47.194990 | -55.588950 | 2015-05-04 16:24:10 | 2015-11-14 15:47:00 | 151 | 81 | 77 |
| F3B01 | U20 #10305634 | 47.194990 | -55.588950 | 2015-05-04 16:24:10 | 2015-11-14 15:47:00 | 151 | 20 | 100 |
| F3B01 | UTBIs | 47.193717 | -55.590867 | 2015-05-04 12:53:40 | 2015-11-14 15:33:00 | 151 | 62-132 | 100 |
| F3B01 | UTBIs | 47.194990 | -55.588950 | 2015-05-04 16:24:10 | 2015-11-14 15:47:00 | 151 | 20-141 | 95 |
| F3B02 | WH300 #15677 | 47.342718 | -55.717833 | 2015-05-04 22:29:35 | 2015-11-14 13:07:00 | 153 | 53 | 98 |
| F3B02 | WH300 #19001 | 47.342718 | -55.717833 | 2015-05-04 22:29:35 | 2015-11-14 13:07:00 | 153 | 142 | 86 |
| F3B02 | SBE19 #1318 | 47.339410 | -55.923850 | 2015-05-04 19:51:20 | 2015-11-14 13:42:00 | 152 | 82 | 100 |
| F3B02 | U20 #10214891 | 47.339410 | -55.923850 | 2015-05-04 19:51:20 | 2015-11-14 13:42:00 | 152 | 21 | 100 |
| F3B02 | UTBIs | 47.342718 | -55.717833 | 2015-05-04 22:29:35 | 2015-11-14 13:07:00 | 153 | 64-134 | 100 |
| F3B02 | UTBIs | 47.33941 | -55.923850 | 2015-05-04 19:51:20 | 2015-11-14 13:42:00 | 152 | 21-142 | 91 |
| F3B03 | WH300 #13951 | 47.557343 | -55.332225 | 2015-05-05 13:22:01 | 2015-11-17 15:17:00 | 157 | 57 | 97 |
| F3B03 | WH300 #13772 | 47.557343 | -55.332225 | 2015-05-05 13:22:01 | 2015-11-17 15:17:00 | 157 | 148 | 86 |
| F3B03 | SBE37 #10571 | 47.557470 | -55.329050 | 2015-05-05 15:09:07 | 2015-11-16 11:57:00 | 154 | 10 | 100 |
| F3B03 | SBE19 #2245 | 47.557470 | -55.329050 | 2015-05-05 15:09:07 | 2015-11-16 11:57:00 | 154 | 81 | 100 |
| F3B03 | UTBIs | 47.557343 | -55.332225 | 2015-05-05 13:22:01 | 2015-11-17 15:17:00 | 157 | 68-138 | 100 |
| F3B03 | UTBIs | 47.557470 | -55.329050 | 2015-05-05 15:09:07 | 2015-11-16 11:57:00 | 154 | 11-142 | 96 |
| F3B04 | WH300 #17956 | 47.635950 | -55.281008 | 2015-05-08 12:56:00 | 2015-11-16 14:39:00 | 146 | 46 | 98 |
| F3B04 | WH300 #11351 | 47.635950 | -55.281008 | 2015-05-08 12:56:00 | 2015-11-16 14:39:00 | 146 | 137 | 91 |
| F3B04 | SBE37 #10572 | 47.632540 | -55.277480 | 2015-05-08 11:46:00 | 2015-11-16 14:54:00 | 260 | 6 | 100 |
| F3B04 | SBE19 #2246 | 47.632540 | -55.277480 | 2015-05-08 11:46:00 | 2015-11-16 14:54:00 | 260 | 78 | 100 |
| F3B04 | UTBIs | 47.635950 | -55.281008 | 2015-05-08 12:56:00 | 2015-11-16 14:39:00 | 146 | 57-127 | 100 |
| F3B04 | UTBIs | 47.632540 | -55.277480 | 2015-05-08 11:46:00 | 2015-11-16 14:54:00 | 260 | 7-139 | 100 |

*Table B2: Data collection summary, leg 2 (November 2015–May 2016).*

| Site | Instrument | Latitude (°N) | Longitude (°W) | Deployment | Recovery | Site depth | Instrument depth | % coverage |
|---|---|---|---|---|---|---|---|---|
| F3B01 | WH300 #12548 | 47.193783 | -55.592287 | 2015-11-15 15:47:00 | 2016-05-12 17:05:00 | 152 | 52 | 98 |
| F3B01 | WH300 #15678 | 47.193783 | -55.592287 | 2015-11-15 15:47:00 | 2016-05-12 17:05:00 | 152 | 143 | 51 |
| F3B01 | RBR #22032 | 47.196250 | -55.587187 | 2015-11-15 16:00:00 | 2016-05-10 16:35:00 | 152 | 11 | 100 |
| F3B01 | SBE19 #1319 | 47.196250 | -55.587187 | 2015-11-15 16:00:00 | 2016-05-10 16:35:00 | 152 | 11 | 100 |
| F3B01 | SBE19 #1309 | 47.196250 | -55.587187 | 2015-11-15 16:00:00 | 2016-05-10 16:35:00 | 152 | 82 | 100 |
| F3B01 | U20 #10305634 | 47.196250 | -55.587187 | 2015-11-15 16:00:00 | 2016-05-10 16:35:00 | 152 | 21 | 100 |
| F3B01 | UTBIs | 47.193783 | -55.592287 | 2015-11-15 15:47:00 | 2016-05-12 17:05:00 | 152 | 63-133 | 100 |
| F3B01 | UTBIs | 47.196250 | -55.587187 | 2015-11-15 16:00:00 | 2016-05-10 16:35:00 | 152 | 11-142 | 96 |
| F3B02 | WH300 #15677 | 47.342547 | -55.717868 | 2015-11-15 13:34:00 | 2016-05-10 12:35:00 | 153 | 53 | 98 |
| F3B02 | WH300 #19001 | 47.342547 | -55.717868 | 2015-11-15 13:34:00 | 2016-05-10 12:35:00 | 153 | 144 | 89 |
| F3B02 | RBR #22031 | 47.339265 | -55.717860 | 2015-11-15 12:52:00 | 2016-05-11 19:00:00 | 152 | 11 | 100 |
| F3B02 | SBE19 #1317 | 47.339265 | -55.717860 | 2015-11-15 12:52:00 | 2016-05-11 19:00:00 | 152 | 11 | 100 |
| F3B02 | SBE19 #1313 | 47.339265 | -55.717860 | 2015-11-15 12:52:00 | 2016-05-11 19:00:00 | 152 | 82 | 100 |
| F3B02 | U20 #10305633 | 47.339265 | -55.717860 | 2015-11-15 12:52:00 | 2016-05-11 19:00:00 | 152 | 19 | 100 |
| F3B02 | U20 #10214891 | 47.339265 | -55.717860 | 2015-11-15 12:52:00 | 2016-05-11 19:00:00 | 152 | 21 | 100 |
| F3B02 | UTBIs | 47.342547 | -55.717868 | 2015-11-15 13:34:00 | 2016-05-10 12:35:00 | 153 | 64-134 | 100 |
| F3B02 | UTBIs | 47.339265 | -55.717860 | 2015-11-15 12:52:00 | 2016-05-11 19:00:00 | 152 | 11-142 | 100 |
| F3B03 | WH300 #13951 | 47.557268 | -55.331988 | 2015-11-17 18:06:00 | 2016-05-13 15:30:00 | 152 | 52 | 98 |
| F3B03 | WH300 #13772 | 47.557268 | -55.331988 | 2015-11-17 18:06:00 | 2016-05-13 15:30:00 | 152 | 143 | 84 |
| F3B03 | SBE37 #10571 | 47.558150 | -55.328900 | 2015-11-17 18:34:00 | 2016-05-13 15:58:00 | 160 | 16 | 100 |
| F3B03 | SBE19 #1312 | 47.558150 | -55.328900 | 2015-11-17 18:34:00 | 2016-05-13 15:58:00 | 160 | 88 | 33 |
| F3B03 | UTBIs | 47.557268 | -55.331988 | 2015-11-17 18:06:00 | 2016-05-13 15:30:00 | 152 | 63-133 | 100 |
| F3B03 | UTBIs | 47.558150 | -55.328900 | 2015-11-17 18:34:00 | 2016-05-13 15:58:00 | 160 | 17-148 | 100 |
| F3B04 | WH300 #11351 | 47.635963 | -55.281208 | 2015-11-17 11:26:00 | 2016-05-13 17:40:00 | 146 | 137 | 82 |
| F3B04 | WH300 #17956 | 47.635963 | -55.281208 | 2015-11-17 11:26:00 | 2016-05-13 17:40:00 | 146 | 46 | 99 |
| F3B04 | SBE37 #10572 | 47.632508 | -55.277488 | 2015-11-17 12:05:00 | 2016-05-13 17:55:00 | 260 | 5 | 100 |
| F3B04 | UTBIs | 47.635963 | -55.281208 | 2015-11-17 11:26:00 | 2016-05-13 17:40:00 | 146 | 57-127 | 100 |
| F3B04 | UTBIs | 47.632508 | -55.277488 | 2015-11-17 12:05:00 | 2016-05-13 17:55:00 | 260 | 7-138 | 100 |

*Table B3: Data collection summary, leg 3 (May 2016–November 2016).*

| Site | Instrument | Latitude (°N) | Longitude (°W) | Deployment | Recovery | Site depth | Instrument depth | % coverage |
|---|---|---|---|---|---|---|---|---|
| F3B01 | WH300 #12548 | 47.193460 | -55.592130 | 2016-05-13 11:11:00 | 2016-10-31 18:30:00 | 150 | 76 | 36 |
| F3B01 | RBR #22031 | 47.193460 | -55.592130 | 2016-05-13 11:11:00 | 2016-10-31 18:30:00 | 150 | 6 | 100 |
| F3B01 | SBE19 #1317 | 47.193460 | -55.592130 | 2016-05-13 11:11:00 | 2016-10-31 18:30:00 | 150 | 6 | 82 |
| F3B01 | SBE19 #1313 | 47.193460 | -55.592130 | 2016-05-13 11:11:00 | 2016-10-31 18:30:00 | 150 | 78 | 100 |
| F3B01 | U20 #10305633 | 47.193460 | -55.592130 | 2016-05-13 11:11:00 | 2016-10-31 18:30:00 | 150 | 14 | 100 |
| F3B01 | U20 #10214891 | 47.193460 | -55.592130 | 2016-05-13 11:11:00 | 2016-10-31 18:30:00 | 150 | 16 | 100 |
| F3B01 | UTBIs | 47.193460 | -55.592130 | 2016-05-13 11:11:00 | 2016-10-31 18:30:00 | 150 | 6-139 | 100 |
| F3B02 | WH300 #15677 | 47.331913 | -55.737182 | 2016-05-11 16:05:00 | 2016-10-31 16:52:00 | 153 | 79 | 98 |
| F3B02 | RBR #22032 | 47.331910 | -55.737180 | 2016-05-11 16:05:00 | 2016-10-31 16:52:00 | 153 | 9 | 100 |
| F3B02 | SBE19 #1319 | 47.331910 | -55.737180 | 2016-05-11 16:05:00 | 2016-10-31 16:52:00 | 153 | 9 | 65 |
| F3B02 | SBE19 #1309 | 47.331910 | -55.737180 | 2016-05-11 16:05:00 | 2016-10-31 16:52:00 | 153 | 81 | 100 |
| F3B02 | U20 #10305636 | 47.331910 | -55.737180 | 2016-05-11 16:05:00 | 2016-10-31 16:52:00 | 153 | 17 | 100 |
| F3B02 | U20 #10305634 | 47.331910 | -55.737180 | 2016-05-11 16:05:00 | 2016-10-31 16:52:00 | 153 | 19 | 100 |
| F3B02 | UTBIs | 47.331910 | -55.737180 | 2016-05-11 16:05:00 | 2016-10-31 16:52:00 | 153 | 9-142 | 97 |
| F3B03 | WH300 #13951 | 47.524650 | -55.340300 | 2016-05-16 17:00:00 | 2016-11-02 18:05:00 | 161 | 87 | 97 |
| F3B03 | SBE37 #10571 | 47.524650 | -55.340330 | 2016-05-16 17:00:00 | 2016-11-02 18:05:00 | 161 | 16 | 100 |
| F3B03 | RBR #60334 | 47.524650 | -55.340330 | 2016-05-16 17:00:00 | 2016-11-02 18:05:00 | 161 | 87 | 100 |
| F3B03 | UTBIs | 47.524650 | -55.340330 | 2016-05-16 17:00:00 | 2016-11-02 18:05:00 | 161 | 17-149 | 100 |
| F3B04 | WH300 #11348 | 47.639650 | -55.297100 | 2016-05-16 15:00:00 | 2016-11-04 16:15:00 | 163 | 79 | 98 |
| F3B04 | SBE37 #10572 | 47.639650 | -55.297130 | 2016-05-16 15:00:00 | 2016-11-04 16:15:00 | 163 | 8 | 100 |
| F3B04 | SBE19 #1315 | 47.639650 | -55.297130 | 2016-05-16 15:00:00 | 2016-11-04 16:15:00 | 163 | 80 | 100 |
| F3B04 | UTBIs | 47.639650 | -55.297130 | 2016-05-16 15:00:00 | 2016-11-04 16:15:00 | 163 | 9-141 | 100 |
| F3B05 | WH300 #15678 | 47.303670 | -55.355600 | 2016-05-13 12:55:00 | 2016-11-02 16:16:00 | 91 | 80 | 38 |
| F3B05 | SBE19 #1316 | 47.303670 | -55.355560 | 2016-05-13 12:55:00 | 2016-11-02 16:16:00 | 91 | 10 | 100 |
| F3B05 | SBE19 #1019 | 47.303670 | -55.355560 | 2016-05-13 12:55:00 | 2016-11-02 16:16:00 | 91 | 82 | 100 |
| F3B05 | UTBIs | 47.303670 | -55.355560 | 2016-05-13 12:55:00 | 2016-11-02 16:16:00 | 91 | 10-72 | 100 |

*Table B3: Data collection summary, leg 3 (May 2016–November 2016). Cont.*

| Site | Instrument | Latitude (°N) | Longitude (°W) | Deployment | Recovery | Site depth | Instrument depth | % coverage |
|---|---|---|---|---|---|---|---|---|
| F3B06 | WH300 #19001 | 47.437130 | -55.490800 | 2016-05-11 21:01:00 | 2016-11-02 14:50:00 | 89 | 78 | 98 |
| F3B06 | SBE19 #1021 | 47.437130 | -55.490810 | 2016-05-11 21:01:00 | 2016-11-02 14:50:00 | 89 | 8 | 100 |
| F3B06 | SBE19 #1237 | 47.437130 | -55.490810 | 2016-05-11 21:01:00 | 2016-11-02 14:50:00 | 89 | 80 | 100 |
| F3B06 | UTBIs | 47.437130 | -55.490810 | 2016-05-11 21:01:00 | 2016-11-02 14:50:00 | 89 | 8-70 | 100 |
| F3B07 | WH300 #13772 | 47.601870 | -55.386500 | 2016-05-15 18:20:00 | 2016-11-03 14:30:00 | 96 | 85 | 0 |
| F3B07 | SBE19 #1483 | 47.601870 | -55.386480 | 2016-05-15 18:20:00 | 2016-11-03 17:00:00 | 96 | 15 | 100 |
| F3B07 | SBE19 #1312 | 47.601870 | -55.386480 | 2016-05-15 18:20:00 | 2016-11-03 14:30:00 | 96 | 87 | 33 |
| F3B07 | UTBIs | 47.601870 | -55.386480 | 2016-05-15 18:20:00 | 2016-11-03 14:30:00 | 96 | 15-77 | 96 |
| F3B08 | WH300 #17956 | 47.580850 | -55.168450 | 2016-06-14 13:09:00 | 2016-11-05 16:24:00 | 209 | 90 | 98 |
| F3B08 | SBE19 #1318 | 47.580833 | -55.168433 | 2016-06-14 13:09:00 | 2016-11-05 16:24:00 | 209 | 19 | 100 |
| F3B08 | RBR #60335 | 47.580833 | -55.168433 | 2016-06-14 13:09:00 | 2016-11-05 16:24:00 | 209 | 91 | 100 |
| F3B08 | UTBIs | 47.580833 | -55.168433 | 2016-06-14 13:09:00 | 2016-11-05 16:24:00 | 209 | 20-82 | 100 |
| F3B09 | WH600 #12391 | 47.633100 | -55.440300 | 2016-05-14 16:56:00 | 2016-11-03 17:47:00 | 58 | 6 | 48 |
| F3B09 | SBE37 #14435 | 47.633100 | -55.440280 | 2016-05-14 16:56:00 | 2016-11-03 17:47:00 | 58 | 7 | 100 |
| F3B09 | SBE37 #14436 | 47.633100 | -55.440280 | 2016-05-14 16:56:00 | 2016-11-03 17:47:00 | 58 | 53 | 100 |
| F3B09 | UTBIs | 47.633100 | -55.440280 | 2016-05-14 16:56:00 | 2016-11-03 17:47:00 | 58 | 8-43 | 100 |
| F3B10 | WH600 #12390 | 47.704750 | -55.384100 | 2016-05-14 17:39:00 | 2016-11-03 19:55:00 | 58 | 6 | 17 |
| F3B10 | SBE37 #14434 | 47.704750 | -55.384060 | 2016-05-14 17:39:00 | 2016-11-03 19:55:00 | 58 | 7 | 100 |
| F3B10 | SBE37 #14433 | 47.704750 | -55.384060 | 2016-05-14 17:39:00 | 2016-11-03 19:55:00 | 58 | 53 | 97 |
| F3B10 | UTBIs | 47.704750 | -55.384060 | 2016-05-14 17:39:00 | 2016-11-03T 19:55:00 | 58 | 8-43 | 100 |

*Table B4: Mooring data collection summary, leg 4 (November 2016–May 2017).*

| Site | Instrument | Latitude (°N) | Longitude (°W) | Deployment | Recovery | Site depth | Instrument depth | % coverage |
|---|---|---|---|---|---|---|---|---|
| F3B01 | WH300 #12548 | 47.194520 | -55.596913 | 2016-11-02 11:24:00 | 2017-05-08 17:40:00 | 156 | 82 | 99 |
| F3B01 | RBR #22031 | 47.194520 | -55.596913 | 2016-11-02 11:24:00 | 2017-05-08 17:40:00 | 156 | 12 | 95 |
| F3B01 | SBE19 #1317 | 47.194520 | -55.596913 | 2016-11-02 11:24:00 | 2017-05-08 17:40:00 | 156 | 12 | 100 |
| F3B01 | SBE19 #1313 | 47.194520 | -55.596913 | 2016-11-02 11:24:00 | 2017-05-08 17:40:00 | 156 | 84 | 100 |
| F3B01 | U20 #10214891 | 47.194520 | -55.596913 | 2016-11-02 11:24:00 | 2017-05-08 17:40:00 | 156 | 22 | 100 |
| F3B01 | U20 #10305633 | 47.194520 | -55.596913 | 2016-11-02 11:24:00 | 2017-05-08 17:40:00 | 156 | 20 | 100 |
| F3B01 | UTBIs | 47.194520 | -55.596913 | 2016-11-02 11:24:00 | 2017-05-08 17:40:00 | 156 | 12-145 | 100 |
| F3B02 | WH300 #15677 | 47.330532 | -55.735460 | 2016-11-02 12:46:00 | 2017-05-08 11:59:00 | 157 | 83 | 100 |
| F3B02 | RBR #22032 | 47.330532 | -55.735460 | 2016-11-02 12:46:00 | 2017-05-08 11:59:00 | 157 | 13 | 95 |
| F3B02 | SBE19 #1319 | 47.330532 | -55.735460 | 2016-11-02 12:46:00 | 2017-05-08 11:59:00 | 157 | 13 | 100 |
| F3B02 | SBE19 #1309 | 47.330532 | -55.735460 | 2016-11-02 12:46:00 | 2017-05-08 11:59:00 | 157 | 85 | 100 |
| F3B02 | U20 #10305634 | 47.330532 | -55.735460 | 2016-11-02 12:46:00 | 2017-05-08 11:59:00 | 157 | 23 | 100 |
| F3B02 | U20 #10305636 | 47.330532 | -55.735460 | 2016-11-02 12:46:00 | 2017-05-08 11:59:00 | 157 | 21 | 100 |
| F3B02 | UTBIs | 47.330532 | -55.735460 | 2016-11-02 12:46:00 | 2017-05-08 11:59:00 | 157 | 13-146 | 97 |
| F3B03 | WH300 #13951 | 47.523800 | -55.340675 | 2016-11-03 13:38:00 | 2017-05-09 13:05:00 | 159 | 85 | 99 |
| F3B03 | SBE37 #10571 | 47.523800 | -55.340675 | 2016-11-03 13:38:00 | 2017-05-09 13:30:00 | 159 | 15 | 100 |
| F3B03 | RBR #60334 | 47.523800 | -55.340675 | 2016-11-03 13:38:00 | 2017-05-09 13:30:00 | 159 | 86 | 100 |
| F3B03 | UTBIs | 47.523800 | -55.340675 | 2016-11-03 13:38:00 | 2017-05-09 13:30:00 | 159 | 15-147 | 100 |
| F3B04 | WH300 #11348 | 47.639702 | -55.297115 | 2016-11-05 14:55:00 | 2017-05-10 11:07:00 | 160 | 76 | 100 |
| F3B04 | SBE37 #10572 | 47.639702 | -55.297115 | 2016-11-05 14:55:00 | 2017-05-10 11:07:00 | 160 | 5 | 100 |
| F3B04 | SBE19 #1315 | 47.639702 | -55.297115 | 2016-11-05 14:55:00 | 2017-05-10 11:07:00 | 160 | 77 | 100 |
| F3B04 | UTBIs | 47.639702 | -55.297115 | 2016-11-05 14:55:00 | 2017-05-10 11:07:00 | 160 | 6-138 | 100 |
| F3B05 | WH300 #15678 | 47.303605 | -55.357987 | 2016-11-03 11:54:00 | 2017-05-08 15:36:00 | 96 | 85 | 39 |
| F3B05 | SBE19 #1316 | 47.303605 | -55.357987 | 2016-11-03 11:54:00 | 2017-05-08 15:36:00 | 96 | 15 | 100 |
| F3B05 | SBE19 #1019 | 47.303605 | -55.357987 | 2016-11-03 11:54:00 | 2017-05-08 15:36:00 | 96 | 87 | 100 |
| F3B05 | UTBIs | 47.303605 | -55.357987 | 2016-11-03 11:54:00 | 2017-05-08 15:36:00 | 96 | 15-77 | 100 |

*Table B4: Mooring data collection summary, leg 4 (November 2016–May 2017). Cont.*

| Site | Instrument | Latitude (°N) | Longitude (°W) | Deployment | Recovery | Site depth | Instrument depth | % coverage |
|---|---|---|---|---|---|---|---|---|
| F3B06 | WH300 #19001 | 47.434265 | -55.490907 | 2016-11-03 11:20:00 | 2017-05-08 13:58:00 | 96 | 85 | 99 |
| F3B06 | SBE19 #1021 | 47.434265 | -55.490907 | 2016-11-03 11:20:00 | 2017-05-08 13:58:00 | 96 | 15 | 100 |
| F3B06 | SBE19 #1237 | 47.434265 | -55.490907 | 2016-11-03 11:20:00 | 2017-05-08 13:58:00 | 96 | 87 | 100 |
| F3B06 | UTBIs | 47.434265 | -55.490907 | 2016-11-03 11:20:00 | 2017-05-08 13:58:00 | 96 | 15-77 | 100 |
| F3B07 | WH300 #13772 | 47.602237 | -55.386593 | 2016-11-04 15:05:00 | 2017-05-10 12:26:00 | 104 | 93 | 95 |
| F3B07 | SBE19 #1483 | 47.602237 | -55.386593 | 2016-11-04 15:05:00 | 2017-05-10 12:26:00 | 104 | 23 | 99 |
| F3B07 | SBE19 #1312 | 47.602237 | -55.386593 | 2016-11-04 15:05:00 | 2017-05-10 12:26:00 | 104 | 95 | 33 |
| F3B07 | UTBIs | 47.602237 | -55.386593 | 2016-11-04 15:05:00 | 2017-05-10 12:26:00 | 104 | 23-85 | 100 |
| F3B08 | WH300 #17956 | 47.579797 | -55.168053 | 2016-11-06 15:00:00 | 2017-05-09 16:30:00 | 206 | 87 | 100 |
| F3B08 | SBE19 #1318 | 47.579797 | -55.168053 | 2016-11-06 15:00:00 | 2017-05-09 16:30:00 | 206 | 16 | 100 |
| F3B08 | RBR #60335 | 47.579797 | -55.168053 | 2016-11-06 15:00:00 | 2017-05-09 16:30:00 | 206 | 88 | 100 |
| F3B08 | UTBIs | 47.579797 | -55.168053 | 2016-11-06 15:00:00 | 2017-05-09 16:30:00 | 206 | 17-79 | 100 |
| F3B11 | WH300 #11351 | 47.478673 | -55.165868 | 2016-11-05 17:25:00 | 2017-05-09 15:13:00 | 98 | 87 | 99 |
| F3B11 | SBE37 #14433 | 47.478673 | -55.165868 | 2016-11-05 17:25:00 | 2017-05-09 15:13:00 | 98 | 16 | 100 |
| F3B11 | SBE37 #14434 | 47.478673 | -55.165868 | 2016-11-05 17:25:00 | 2017-05-09 15:13:00 | 98 | 88 | 100 |
| F3B11 | UTBIs | 47.478673 | -55.165868 | 2016-11-05T 17:25:00 | 2017-05-09 15:13:00 | 98 | 17-79 | 100 |
| F3B12 | WH1200 #13990 | 47.712317 | -55.416800 | 2016-11-04 13:22:00 | 2017-05-11 10:43:00 | 10 | 8 | 112 |
| F3B12 | SBE37 #14436 | 47.713567 | -55.418317 | 2016-11-05 12:00:00 | 2017-05-11 11:05:00 | 8 | 3 | 100 |
| F3B12 | SBE37 #14435 | 47.712317 | -55.416800 | 2016-11-04 13:22:00 | 2017-05-11 10:43:00 | 10 | 8 | 100 |

*Table B5: Land-based data collection summary for the whole program (May 2015–May 2017).*

| Site | Instrument | Latitude (°N) | Longitude (°W) | Deployment | Recovery | Sitepth | Instrument depth | % coverage |
|---|---|---|---|---|---|---|---|---|
| DOGIS | SUTRON #1204160 | 47.61463 | -55.35221 | 2015-05-04 16:50:00 | 2015-10-15 16:25:00 | -10 | -20 | 92 |
| DOGIS | SUTRON #1204160 | 47.61463 | -55.35221 | 2015-10-15 16:30:00 | 2015-11-19 17:00:00 | -10 | -20 | 100 |
| DOGIS | SUTRON #1204160 | 47.61463 | -55.35221 | 2015-11-19 17:30:00 | 2016-05-14 13:30:00 | -10 | -20 | 98 |
| DOGIS | SUTRON #1204160 | 47.61463 | -55.35221 | 2016-05-14 13:50:00 | 2016-11-03 12:30:00 | -10 | -20 | 99 |
| DOGIS | SUTRON #1204160 | 47.61463 | -55.35221 | 2016-11-03 15:20:00 | 2017-01-19 12:30:00 | -10 | -20 | 56 |
| DOGIS | SUTRON #1204160 | 47.61463 | -55.35221 | 2017-01-19 13:40:00 | 2017-05-09 18:00:00 | -10 | -20 | 98 |
| DOGIS | U30 #10072354 | 47.61463 | -55.35221 | 2015-05-03 19:00:00 | 2015-11-19 18:05:00 | -10 | -12 | 96 |
| DOGIS | U30 #10072354 | 47.61463 | -55.35221 | 2015-11-19 18:30:00 | 2016-05-14 12:00:00 | -10 | -12 | 83 |
| DOGIS | U30 #10072354 | 47.61463 | -55.35221 | 2016-05-14 12:30:00 | 2016-06-14 15:40:00 | -10 | -12 | 100 |
| DOGIS | U30 #10072354 | 47.61463 | -55.35221 | 2016-06-14 16:00:00 | 2016-11-03 12:30:00 | -10 | -12 | 87 |
| DOGIS | U30 #10072354 | 47.61463 | -55.35221 | 2016-11-03 15:50:00 | 2017-01-19 14:30:00 | -10 | -12 | 99 |
| DOGIS | U30 #10072354 | 47.61463 | -55.35221 | 2017-01-19 14:40:00 | 2017-05-09 18:00:00 | -10 | -12 | 99 |
| DOGIS | U20 #10305631 | 47.61463 | -55.35221 | 2015-05-03 19:00:00 | 2015-11-19 18:05:00 | -10 | -12 | 100 |
| DOGIS | U20 #10305631 | 47.61463 | -55.35221 | 2015-11-19 18:19:00 | 2016-05-14 14:00:00 | -10 | -12 | 100 |
| DOGIS | U20 #10305631 | 47.61463 | -55.35221 | 2016-05-14 15:00:00 | 2016-11-03 12:30:00 | -10 | -12 | 100 |
| DOGIS | U20 #10305631 | 47.61463 | -55.35221 | 2016-11-03 16:15:00 | 2017-05-09 18:30:00 | -10 | -12 | 100 |
| POOLC | SUTRON #1112700 | 47.67993 | -55.43002 | 2015-05-01 18:40:00 | 2015-11-19 22:00:00 | 3 | 2 | 100 |
| POOLC | SUTRON #1112700 | 47.67993 | -55.43002 | 2015-11-19 22:10:00 | 2016-05-15 12:00:00 | 3 | 2 | 73 |
| POOLC | SUTRON #1112700 | 47.67993 | -55.43002 | 2016-05-15 13:10:00 | 2016-11-04 10:48:24 | 3 | 2 | 99 |
| POOLC | SUTRON #1112700 | 47.67993 | -55.43002 | 2016-11-04 11:00:00 | 2017-05-11 14:00:00 | 3 | 2 | 54 |

*Table B6: IFREMER data collection summary.*

| Site | Instrument | Latitude (°N) | Longitude (°W) | Deployment | Recovery | Site depth | Instrument depth | % coverage |
|---|---|---|---|---|---|---|---|---|
| SPMGF | WH300 | 46.9581 | -56.2293 | 2015-06-22 13:11 | 2015-09-15 16:51 | 78 | 77.5 | 98 |
| SPMGF | WH300 | 46.9581 | -56.2293 | 2015-09-18 13:08 | 2015-11-18 18:58 | 81 | 80.5 | 86 |
| SPMGF | WH300 | 46.9581 | -56.2293 | 2016-03-18 13:04 | 2016-05-30 17:54 | 81 | 80.5 | 87 |
| SPMGF | WH300 | 46.9581 | -56.2293 | 2016-06-02 17:04 | 2016-11-15 16:24 | 79 | 78.5 | 98 |
| M01 | MASTODON #03070 | 46.9880 | -55.9900 | 2016-05-22 12:00 | 2016-10-30 00:00 | 60 | 60 | 100 |
| M02 | MASTODON #03081 | 47.1780 | -56.1390 | 2016-05-22 12:00 | 2016-10-30 00:00 | 60 | 60 | 100 |
| M03 | MASTODON #03089 | 47.0700 | -55.8800 | 2016-05-22 12:00 | 2016-10-30 00:00 | 60 | 60 | 100 |
| M05 | MASTODON #03066 | 47.1250 | -55.770 | 2016-05-22 12:00 | 2016-10-30 00:00 | 60 | 60 | 100 |
| M06 | MASTODON #03062 | 47.2400 | -55.870 | 2016-05-22 12:00 | 2016-10-30 00:00 | 60 | 60 | 100 |
| M07 | MASTODON #03077 | 46.8250 | -56.1667 | 2016-07-13 20:00 | 2016-10-30 00:00 | 60 | 60 | 100 |
| M08 | MASTODON #03041 | 46.8667 | -56.1833 | 2016-07-13 20:00 | 2016-10-30 00:00 | 60 | 60 | 100 |
| M09 | MASTODON #03051 | 46.9500 | -56.1833 | 2016-07-13 20:00 | 2016-10-30 00:00 | 60 | 60 | 100 |
| M10 | MASTODON #03046 | 47.0250 | -56.1533 | 2016-07-13 20:00 | 2016-10-30 00:00 | 60 | 60 | 6 |
| M11 | MASTODON #03060 | 47.0917 | -56.1667 | 2016-07-13 20:00 | 2016-10-30 00:00 | 60 | 60 | 100 |
| M12 | MASTODON #03067 | 47.1250 | -56.2833 | 2016-07-13 20:00 | 2016-10-30 00:00 | 60 | 60 | 100 |

# CHAPTER 2: SEASONALITY

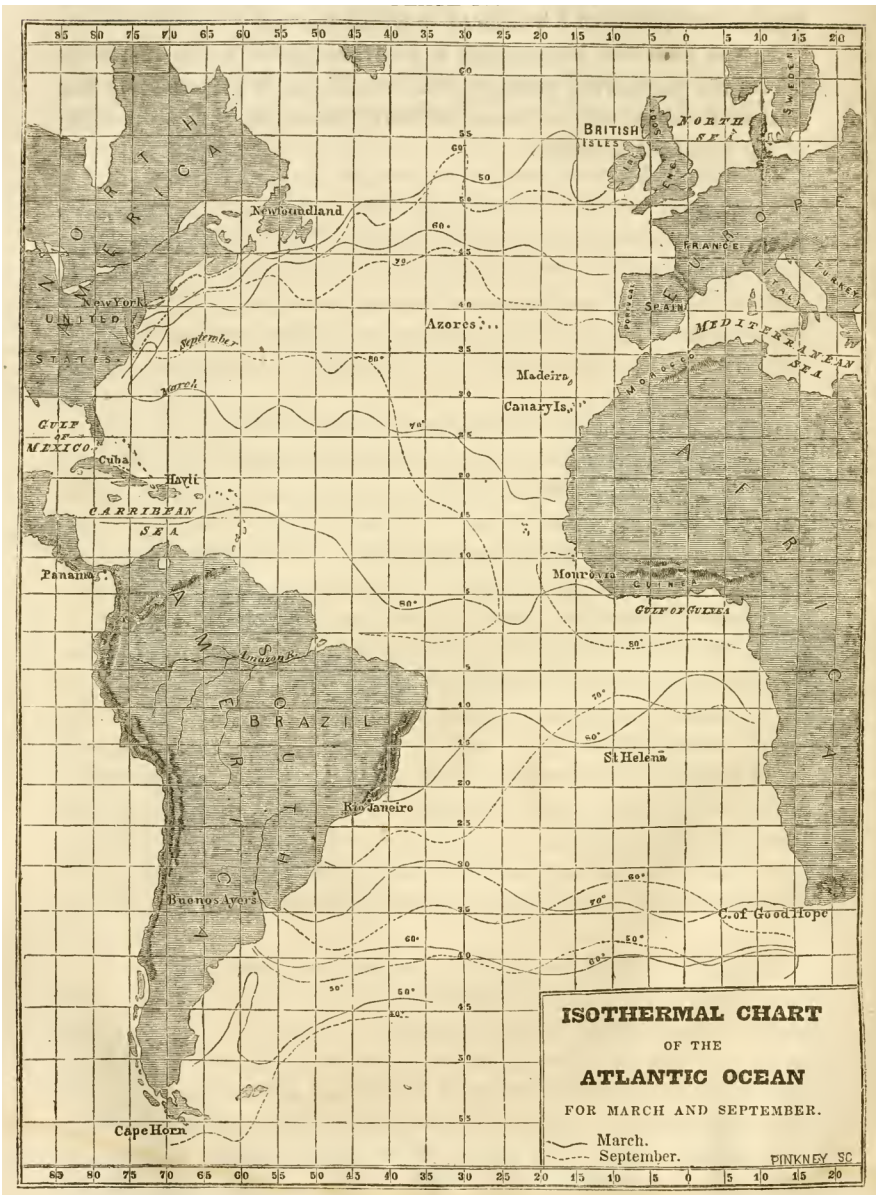


*One of the earliest map of sea surface temperature made from observations over the Atlantic ocean stored at the US National Observatory. The latitudinal migration of the isotherms with seasons is clearly shown as well as some delineations of the Gulf Stream. Note: the units are in °F.*

*Source: Maury, 1855. The Physical Geography of the Sea (1st edition). Plate IV. Harper & Brothers publishers, London. Full text available at: https://archive.org/details/physicalgeograph01maur/page/92/mode/2up*

# The Physical Oceanography of Fortune Bay, an overview

Sebastien Donnet[1,4], Pascal Lazure[2], Andry Ratsimandresey[3] and Guoqi Han[1]

Published in Regional Studies in Marine Science 56 (2022), https://doi.org/10.1016/j.rsma.2022.102698

[1] Fisheries and Oceans Canada, Institute of Ocean Sciences, 9860 West Saanich Road, Sidney, BC, V8L 4B2, Canada.

[2] Ifremer (French Research Institute for Exploitation of the Sea) Laboratoire d'Océanographie Physique et Spatiale, Centre Bretagne, ZI de la Pointe du Diable, CS 10070, 29280 Plouzané, France.

[3] Fisheries and Oceans Canada, Northwest Atlantic Fisheries Centre, 80 East White Hills Rd, St. John's NL, A1C 5X1, Canada.

[4] Université de Bretagne Occidentale, Ecole Doctorale N°598 Science de la Mer et du littoral, Brest, France.

## ABSTRACT

This paper describes the physical oceanography of Fortune Bay, a broad, mid-latitude fjord located in Newfoundland (Canada). Fortune Bay is subject to a strong seasonal stratification (0-16 °C sea-surface temperature range with up to 1 °C/m vertical gradient) influenced by local freshwater runoff, wind forcing and shelf inputs. Sea-ice is seldom present in the bay and unlikely to be of importance on the seasonal stratification and mixing processes. Fortune Bay is warmer than its adjacent shelf both at the surface (by about 2 °C) and at intermediate depths (by about 1 °C from 50-150 m). While the former is likely due to local freshwater runoff stratification influence, the latter is probably related to the warm, deep water input occurring in winter below sill depth and subsequently mixed with the intermediate layer via the input of a colder water mass flowing in summer and which eventually reaches the bottom as well. Currents are dominated by the 'weather band' (2-20 d) and characterized by energetic pulses associated with downwelling and upwelling events. Mean circulation is rather weak and the seasonal pattern obtained here did not reveal either the presence of a distinct estuarine circulation nor a strong influence of the main coastal current. Tidal currents are weak also and no inertial signal was observed. Estimates of water exchange between the inner and outer part of the bay were calculated using several methods and led to residence times of the order of a few to several months for the upper layers and of the order of a year for the bottom layer with a probable strong seasonal variability (larger residence time in summer for the upper layers). The "baroclinic pumping" processes, which include the downwelling/upwelling events, appear to be important players but more work is needed to better understand their nature and actual contribution.

**Key words:** broad fjord, hydrographic climate, wind, tides, circulation, along-shore current pulses, water exchanges.

# INTRODUCTION

Fortune Bay is a large fjord-like embayment about 130 km long and 15 to 25 km wide located on the south coast of Newfoundland, a large island of eastern Canada (Figure 1).

The physical oceanography of Fortune Bay is not well known. Some of the first accounts of its characteristics can be found in the detailed aid to navigation compiled by Gillpatrick (1884) which states that the “currents are irregular in this bay”; a description that went virtually unchanged until now in subsequent aid to navigation publications (see Canadian Hydrographic Survey, 2022 for the most recent available). To our knowledge, it was not until the 1980-90’s and the efforts of researchers and students from the Memorial University of Newfoundland (MUN) that the first oceanographic investigations were performed in Fortune Bay as part of two Master theses (de Young 1983 and Richard 1987) and subsequent papers (de Young and Hay 1987, Hay and de Young 1989, White and Hay 1994 and Richard and Haedrich, 1991). de Young’s thesis focussed on deep water exchange between Fortune Bay and the adjacent shelf channels of Saint-Pierre and Hermitage (Figure 1) while Richard’s thesis described and discussed Fortune Bay’s lower trophic biology as well as mesopelagic fish communities in relation to its physical oceanography. The deep water exchange studies (de Young and Hay 1987, Hay and de Young 1989 and White and Hay 1994) showed that Fortune Bay is seasonally vented by two very different water masses below sill depth (i.e. below about 120 m): cold and relatively fresh water (<2 °C and 32-33 in salinity) from Labrador Current origin water in summer (Labrador Current Water - LCW); warm and salty water from Atlantic origin (>4 °C and about 34.5 in salinity) in winter (Modified Slope Water – MSW, McLellan, 1957; Lauzier and Trites 1958). This seasonal venting is due to the regional seasonality in wind, forcing these deep and dense waters over the sills: southwesterly wind in summer upwelling LCW over the sill of Saint-Pierre; northerly winds in winter upwelling MSW over the sill of Miquelon. de Young and Hay (1987) showed that the cold deep water renewal was 3 dimensional in nature, the width of the fjord being large enough for the dense, bottom flow to be affected by earth rotation. Hay and de Young (1989) described the seasonal processes of renewal and explained their forcing mechanisms while White and Hay (1994) showed that the cold water renewal flow is strongly modulated by the tide as well as by the interaction of the cold density current with bottom-trapped wave or interior basin modes at periods of 2-3 days.

With a rapid development of finfish aquaculture in Belle Bay and surrounding areas in the early 2000s, an ambitious oceanographic program was started in 2009 by the Department of Fisheries and Oceans (DFO) to provide with the necessary background to study aquaculture-environment interactions. Of particular interest were the water column stratification and currents, key aspects to consider in aquaculture related studies such as dissolved oxygen depletion and particles dispersion (e.g. viruses, parasites and organic waste). The program focussed primarily on the collection of CTD+DO (Conductivity, Temperature and Depth + Dissolved Oxygen) profiles, moored ADCP (Acoustic Doppler Current Profiler) timeseries and drifter experiments (see DFO, 2016 for a summary of the program and its key results and Donnet et al., 2018a&b, Ratsimandresy et al., 2019 and Ratsimandresy et al., 2020 for more details). The Coast of Bays was found to consist of three main regions with distinct geographic characteristics: Bay d’Espoir, Connaigre Penninsula and Fortune Bay (Figure 1). Topography and freshwater runoff were found to be key aspects of differentiation (e.g. narrow fjord vs. broad bay and large vs. small runoff) influencing water column stratification and hydrodynamics (i.e. currents). A strong regional atmospheric heating and cooling seasonal cycle stratifies the near-surface water, i.e. top 20 meters, a process amplified by the regionally variable

freshwater runoff. The annual amplitude in sea-surface temperature is about 7 °C, i.e. 14 °C range, with stronger stratification in Bay d'Espoir and lesser stratification in Connaigre Penninsula (Donnet et al., 2018a). Tidal ranges in the region are small, about 2 m large tides and 1.4 m mean tides. Combined with the great depth of the bays considered, they result in small tidal currents except in areas of significant constrictions (e.g. sills of Bay d'Espoir) and in large flushing times from this forcing alone (order of months, or more). Wind, on the other hand, was found to be a major contributor to the generation of the very variable ocean currents observed (Salcedo and Ratsimandresy, 2013).

Despite those significant efforts, knowledge remains limited and the understanding of Fortune Bay ocean physics and dynamics is very much incomplete. The water column stratification annual cycle, coastal circulation and surface water exchange (or flushing) in particular, are unknown. The dominant processes affecting the ocean currents, their periodicity (if any exist) and effect on water exchanges, within the bay itself and/or with the shelf, for instance, have not been determined despite their importance to the studies of aquaculture-environment interactions.

The main objective of this paper is to provide a comprehensive and descriptive overview of the physical oceanography of Fortune Bay with a particular focus on upper water stratification and ocean currents including an assessment of their main physical drivers. Estimates of dominant energy bands of ocean currents, in the frequency domain, and of water exchanges will also be given to complement present knowledge.

Some figures and tables, herein labelled with an "S" prefix, are provided as supplementary material and are available along with the data used for and obtained from this study at: https://doi.org/10.6084/m9.figshare.13526366.

# BATHYMETRIC FEATURES

Fortune Bay is deep, reaching about 430 m within its main SW-NE oriented basin and about 600 m within its SE-NW oriented head (Belle Bay); on average, the bay is about 160 m deep. Fortune Bay has the particularity, compared to the other major bays surrounding Newfoundland, of being quasi-enclosed due to the presence of the Saint-Pierre and Miquelon (SPM) archipelago at its west and southwest boundary and to a series of islands, shallows and sills along most of its west to northwest boundary (Figure 1). The limiting depth of the sills are about 110 m (Saint-Pierre) and 125 m (Miquelon and Sagona) restricting deep water exchange with the shelf. Two main channels, more than 200 m deep, and a shallower bank form the topography of Fortune Bay's southern part while its northern part is made of one main channel leading to Belle Bay, its most prominent head, and to a narrow inlet forming its much smaller NE head (about 15 km long, 2.5 km wide and more than 400 m in its deepest). The main channel connecting Fortune Bay to Belle Bay runs along the northern side, it is about 500 m maximum depth and ends by a sill of 100 m limiting depth connecting it to a widening head. On the southern side, a very narrow and steep canyon (about 500 m wide and about 600 m maximum depth) is separated from Fortune Bay by a sill about 210 m depth. Belle Bay's own head is made of a wide and deep basin (about 5x5 km for 600 m maximum depth) connected to the canyon via a partial and deep sill. Belle Bay's center consists of a shallow bank (<100 m) on which rise several shoals and a few islands. Numerous side bays are present in Belle Bay, typically formed by one or more basins and one or more shallower sills (see Donnet et al., 2018a for details).

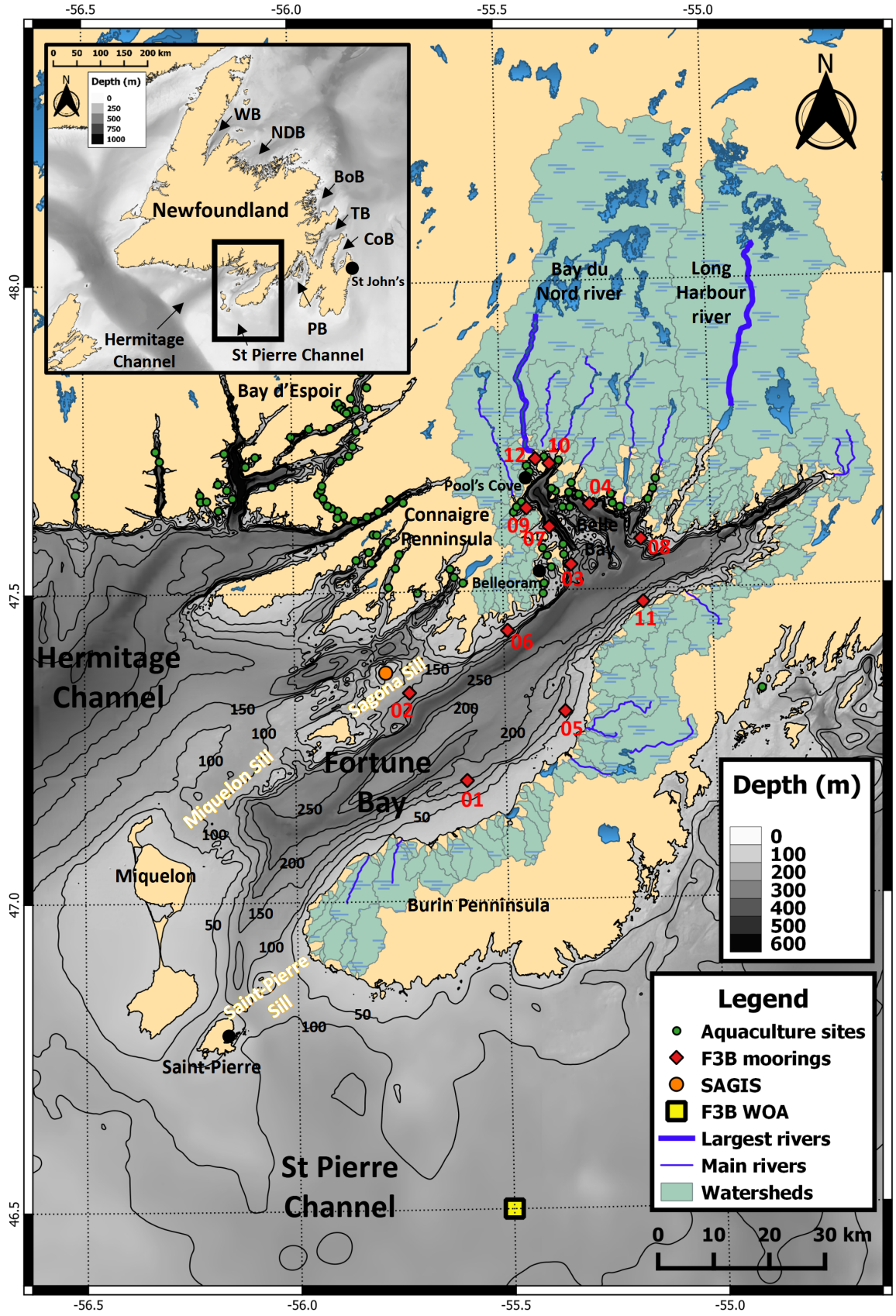


*Figure 1: study area. Mooring sites from which ocean currents and water column temperature profiles were collected from 2015-17 are represented by red diamonds; the WOA temperature and salinity climatology data point is shown as a yellow square and the local, long-term, weather station is shown as an orange dot. Aquaculture sites (licences) are also represented, as green dots. Main bays surrounding the island of Newfoundland are indicated in the top-right corner insert (clockwise from the North: White Bay (WB), Notre Dame Bay (NDB), Bonavista Bay (BoB), Trinity Bay (TB), Conception Bay (CoB) and Placentia Bay (PB)).*

# TEMPERATURE AND SALINITY STRUCTURE

## DATA REDUCTION

Temperature and salinity data were mined from the Department of Fisheries and Oceans (DFO) Bedford Institute of Oceanography (BIO, http://www.bio.gc.ca/science/data-donnees/base/data-donnees/climate-climat-en.php, see also Gregory, 2004) and Northwest Atlantic Fisheries Center (NAFC) archives to make a monthly climatology. The data consists primarily of XBT (eXpendable BathyThermograph), CTD and bottle profiles collected over the years on the Newfoundland shelves from a variety of platforms and institutions. The dataset was completed using recent CTD profiles collected by NAFC's aquaculture section (Ratsimandresey et al., 2014 and Donnet et al., 2018b).

All data available within a square defined from 46.2 to 48 °N and 57.5 to 54.5 °W were first extracted from the databases within the largest possible time-period (01-Jan-1900 to 31-Dec-2018). The dataset was subsequently reduced to the Fortune Bay area using a polygon (Figure S1). In total, 810 profiles from BIO, 1130 profiles from NAFC and 806 profiles from NAFC's aquaculture section databases were extracted. The data was combined daily and spatially using a radius of 500 m; resulting in a dataset of 1750 averaged casts sampled over 911 stations. The earliest cast occurred the 15th of October 1925 and latest cast the 2nd of June 2018. Most of the sampling occurred after 1950 with a first broad peak from the late 50s to early 80s and a second from the mid-90s onward (Figure S2), however, most of the data prior to the mid-90s consisted of temperature profiles only. An important sampling effort occurred in 1981 and the recent sampling effort led by NAFC's aquaculture section from 2009 to 2017 is noticeable also. The dataset was split into two sub-polygons (areas): Fortune Bay (FB) and Belle Bay (BB), illustrated in Figure S1. The separation was based on the Region of Freshwater Influence (ROFI) estimated in Donnet et al., 2018a; that is, a region where the surface density field is likely dominated by freshwater inputs and thus where the surface water structure is likely to differ from the rest of the bay. The profiles were checked visually to remove dubious casts or spikes. Temperature and Salinity values at depth shallower than 1 m and salinity values below 20 were removed due to uncertainty in the data. Practical Salinity values (as provided in the databases) were converted to Absolute Salinity values using TEOS-10 relationships (IOC et al., 2010; McDougall and Barker, 2011) and assuming a δSA equal to 0 (as advised in Pawlowicz, 2013 when working with coastal waters).

Monthly averages were calculated by first spatially averaging every daily cast of each month on a year by year basis and then averaging this monthly series to obtain a monthly climate for each area. Standard deviations were calculated from this latter average, thus representing a measure of interannual variability. Monthly climate profiles were finally smoothed using a 'bin-median' filter, i.e. the median over a bin of a set depth range. A bin size of 5-50 m was used, varying amongst months and with depth, to take seasonal and vertical as well as sampling variability into account. Sampling coverage, both temporal and spatial, varies widely amongst this monthly climatology as illustrated in Figure S2; best coverage was obtained during the spring (April to June) while July and the winter season (January to March) are much less sampled, particularly in salinity.

## MONTHLY CLIMATE

Temperature and salinity climate of FB and BB are illustrated in Figure 2. To compare the conditions of the

bay with the shelf, monthly climatology data from the National Oceanic and Atmospheric Administration (NOAA) 1 degree gridded World Ocean Atlas (WOA18) were retrieved (https://www.nodc.noaa.gov/OC5/woa18/) and are also illustrated in Figure 2. The closest 'upstream' data point with respect to the main coastal current of the region, i.e. the inner Labrador Current (see Loder et al., 1998 for a review) was used (see location in Figure 1). To highlight the surface seasonal cycle, only the top 200 m are presented in Figure 2.

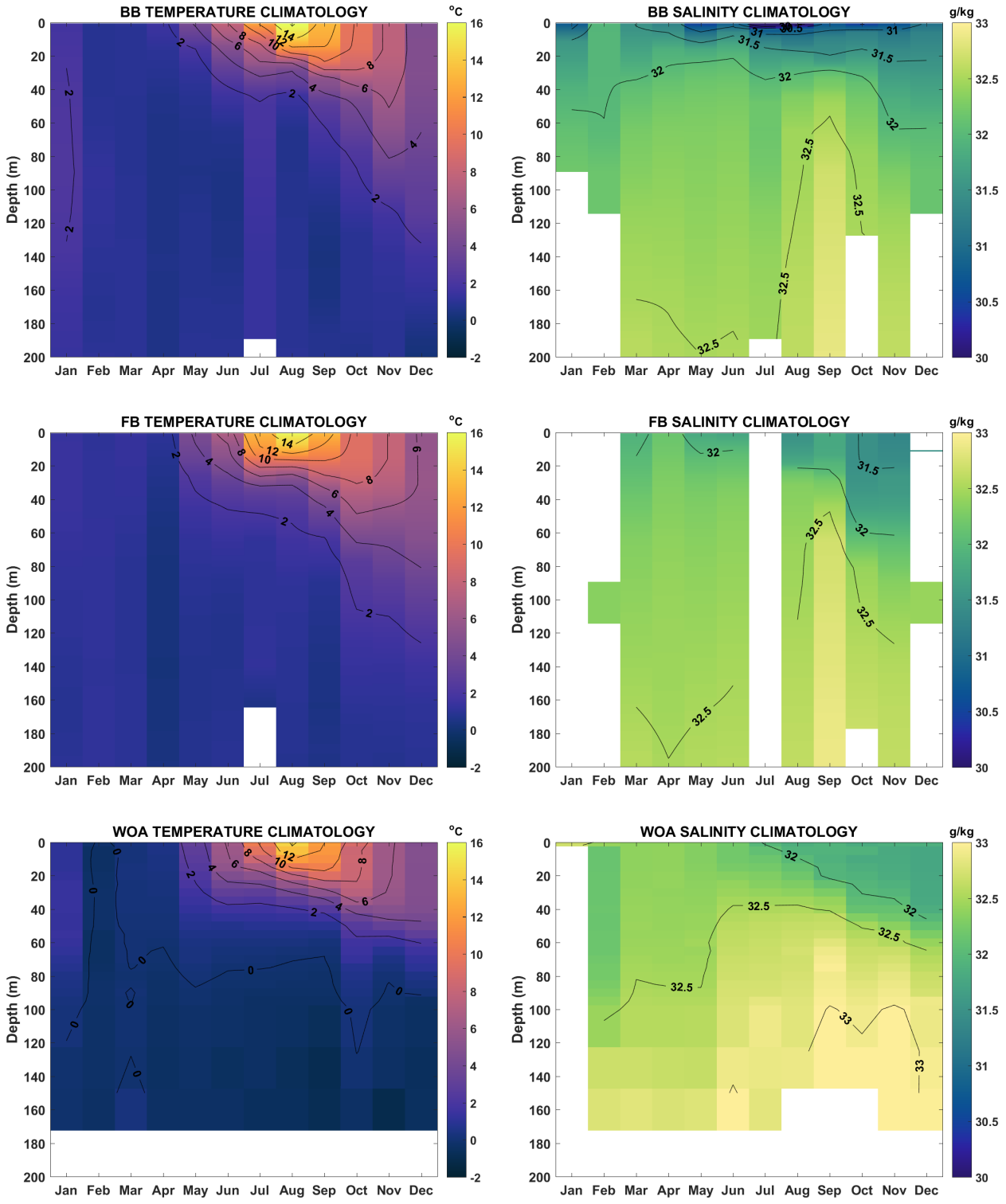


*Figure 2: Temperature and Salinity monthly climate of Belle Bay (BB), top, Fortune Bay (FB), middle, and shelf (WOA), bottom.*

The temperature climate results are consistent with the regional knowledge of the Newfoundland shelf (see Cyr et al., 2022 for the most recent update): a cold (<2 °C) near-homogenous winter water column starts to stratify in early spring (April) and reaches a peak in August (about 15-16 °C near-surface, on average) before having its stratification breaking down in the fall and being completely mixed again by January. The temperature structure is similar in both BB and FB, though FB summer thermocline appears broader and BB near-surface temperature is slightly higher during the summer peak (August; by about 0.5 °C). Both areas are, more noticeably, warmer than the shelf in both the near surface (by about 2 °C in July) and at depth (by 1-2 °C below 50 m). Interannual variability, expressed as standard deviations, is on the order of 1 °C or less (below 100-150 m, in particular) but can be as high as about 3.5 °C in late summer to early fall (August-September) in sub-surface (10-40 m).

The spatial contrast is more pronounced in salinity with the presence of a stronger surface halocline in BB from spring to fall (10-20 m depth). Near surface salinity in BB is less than 31 g/kg during these seasons (May-November); reaching a low of about 29.5 g/kg in July. In contrast, FB's near-surface salinity does not go below 31 g/kg and appears to be the lowest in October-November though we cannot tell what the situation is like during winter due to the lack of data for this season. Both regions, however, show a strong decrease in salinity at depth during the fall, illustrated by the deepening of the 32 g/kg isohaline (from about 40 m to more than 100 m). Interannual variability is smaller than 0.5 g/kg for the most part but can reach values up to 1 g/kg during summer months in BB (July-September). Overall, the variability is higher in BB than in FB within the upper 20 m (0.3 g/kg vs. 0.2 g/kg, annual average) while below that seasonal layer the variability is generally about 0.1 g/kg in both regions (annual average). Due to the scarcity of data, particularly for the months of January, February, July, October and December in FB, those estimates on interannual variability should be regarded as an order of magnitude. On the shelf outside the bay, the salinity structure is characterized by a seasonal freshening at the surface starting in summer, deepening in fall and most likely peaking in December (no data in January) with salinity within 31.5-32 g/kg range. Deeper, salinity appears to rise sharply in late spring (June) before stabilizing in summer and gradually decreasing in fall. These contrasting cycles (surface freshening vs. increasing salinity at depth) result in the making of the sharpest gradient in fall (Oct-Dec) around 50-60 m.

# DEEP WATER CHARACTERISTICS

Monthly Temperature-Salinity (T-S) regressions were made to better examine the seasonality of the water masses (details in supplementary material). This analysis shows the presence of a well-defined intermediate layer between the seasonally variable surface and bottom regions from June to September (characterized by a T-S slope of about -0.1 g/kg/°C). Warmer and saltier conditions are found from March to June and colder conditions were found from September to October below 120 m in both FB and BB (i.e. below outer sill depth). While reversals from warm to cold and from cold to warm occur in August and November in FB (respectively) it is not before September that the effects of cold water renewal are seen in BB's climatology and no clear reversal happen in November in this inner area of the fjord; indicating a time-lag of about a month in the change of deep water properties from FB to BB. Albeit limited by data coverage, these results are consistent with those presented by Hay and de Young (1989) who described influx of warm MSW from December to June and influx of cold LCW from May to December into Fortune Bay's main basin.

Using the most recent data collected (i.e. post 2010) and best covered months (i.e. May and November) it is possible to extend earlier investigations further and shed more light on spatial as well as interannual

variability. It is also possible to illustrate potential changes in DO, this latter parameter being measured more systematically in recent years (see also Donnet et al., 2018b). Casts made in the deepest parts of Fortune Bay's outer basin (FB south) and Belle Bay's inner basin (BB north) were selected and are presented as T-S diagrams in Figure 3 (A-D). The seasonal cycle is clear for both surface-intermediary waters (left from the black dots) as well as deep waters (to the right from the black dots). The straightening of the T-S curves (A vs. B and C vs. D) indicates that mixing took place between the surface and sub-surface from May to November; probably both due to surface forcing from the wind and sub-surface mixing due to LCW influx which initially occurs at intermediate depth before gradually eroding the bottom layer (Hay and de Young, 1989). This process(es) also tend to 'erase' the interannual variability (clearly visible in A&C but less so in B&D), particularly in the outer basin. At depth, the presence of MSW mixture, illustrated by a rising 'tail' below sill depth (black dots) is evident in May in the outer basin (A). In the inner basin (C), the tail is much less pronounced and even show an opposite trend in some years, i.e. cooling with depth (years 2015&16). In November, this rising tail is still present (or newly re-formed) in the outer basin while being largely absent in the inner basin (B vs D). Overall, the outer basin waters are warmer than the inner basin waters below sill depth in May (by about 1 °C; see A vs. C) but can be slightly cooler in November by the presence of a more distinctive cold water 'knee' (B vs. D). The deepest part, however, show the presence of colder waters in the inner basin (indicated by a sharp dipping tail in D).

Both basins are fairly well oxygenated, with values of DO never below 8.5 mg/L and generally being well above 10 mg/L above sill depth in May (A&C). A seasonal cycle is also evident for this parameter, waters being more oxygenated in spring than in fall except, however and noticeably, in the deep part of the inner basin for some years (2015&16). Interestingly, these are associated with cooler water, even though the cold LCW, the likely origin of the cool temperatures, is much more oxygenated than the MSW (>10 mg/L vs. <6 mg/L, respectively; Donnet et al., 2018b). This may be an indication of longer stagnation/residence time in the inner basin. In general, and for both month presented, DO levels are higher in the outer basin than in the inner basin below sill depth (by about 1 mg/L; see A vs. C and B vs. D).

## STRATIFICATION VS. ROTATION

By considering a surface layer thickness of 20 m (spring), 30 m (summer) and 80 m (fall) for the bay as a whole, density differences with the intermediate layer of 1 kg/m$^3$ (spring and fall in FB, and fall in BB), 2 kg/m$^3$ (spring in BB, summer in FB) and 4 kg/m$^3$ (summer in BB) and an average bay depth of 160 m, an internal Rossby radius range of 4-9 km is found. This range is smaller than the width of the bay (15 – 25 km) and implies an important effect of earth's rotation on Fortune Bay's water dynamics. Note that for the purpose of calculating this simple scaling parameter, we took a surface layer thickness corresponding to the bottom of the continuously stratified surface layer which occurs from spring to late fall. Those values are either smaller than (spring and fall) or larger than (summer) the limits found with the regression analysis using the 'inflection points' shown in Table S1 and Table S2.

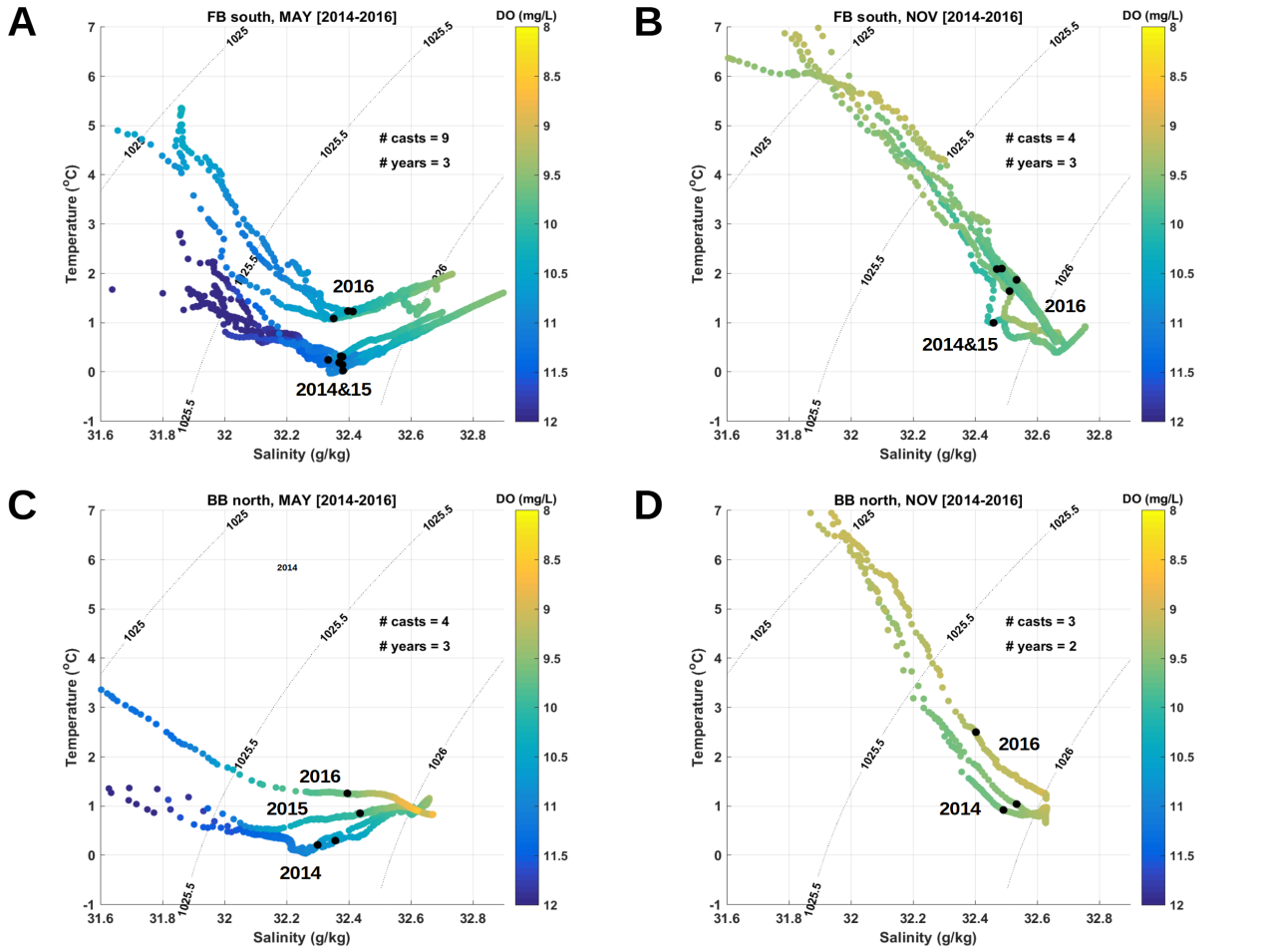


*Figure 3: T-S diagrams of Fortune Bay inner bassin (FB south; C&D) and Belle Bay inner bassin (BB north; E&F). TEOS-10 conservative temperature and absolute salinity are used. Water density is indicated by dotted lines (0 m reference level). Dissolved Oxygen (DO) values are represented in color and the black dots indicate outer sill depth (120 m). Depth decrease (increase) to the left (right) of those dots. Number of casts used and years of observation are indicated on the figures as well as the years of the profiles. Note that most of the surface waters of BB (S<31.6) are not represented.*

# SEA SURFACE TEMPERATURE, FRESHWATER INPUTS AND SEA ICE

Sea Surface Temperature (SST) is a useful observation to identify frontal areas (e.g. Cyr and Larouche 2015), areas of significant mixing (e.g. Bisagni et al., 2001) and potential advection processes (e.g. Verbrugge and Reverdin, 2003). As it has been routinely and globally measured since the early 1980s from satellites, it is also a useful parameter to assess seasonal variations and long-term trends.

SST of the region were extracted from the National Oceanic and Atmospheric Administration (NOAA) Advanced Very High Resolution Radiometer (AVHRR) Pathfinder 5.3 reanalysis (Saha et al., 2018). Pathfinder 5.3 horizontal resolution is 4 km and its temporal resolution is daily from 25 August 1981 to present (see Casey et al., 2010 for a more complete description). Previous Pathfinder data compared favourably with in-situ data in the region (Galbraith and Larouche 2013 and references therein) and a more recent comparison using this version also showed good agreement with the most extensive in-situ data available of the region (Poitevin et al., 2022); providing some comfort to its use here. Data were first extracted for the time period

covering 25 August 1981 to 31 December 2018 and for a region defined by an area 46.5 to 48 °N and 57.5 to 54.5 °W. To reduce potential land contamination, a buffer of 2 km, i.e. half a pixel size, was used along the NRCan high resolution coastline (see Donnet et al., 2018a for details of this later dataset).

Monthly average series were made from spatially averaging the daily series within a polygon of Fortune Bay, i.e. covering the whole bay. A total of 138 pixels were selected within the polygon (Figure S8). The monthly series obtained were then averaged per calendar month to get a monthly climate (Figure S9). Standard deviation was calculated from this latter average, representing a measure of interannual variability. Minimum and maximum of each averaged month of the monthly series were retained; representing coldest and warmest months observed within the period analysed (1985-2018). Data coverage is uneven both spatially and temporally, being substantially lower in Fortune Bay than in the domain covered in Figure 4 (by about a factor 2, on average; Figure S10). On average, the coverage does not exceed 10% at any given point in Fortune Bay and is lower from November to February (<5% on average) and the highest in August (~8%). Maximums, representing the value at one single pixel, range between 4% (in December) to 16% (in September). Interestingly, a 'dip' appears in June-July (~5% coverage, on average), most likely reflecting the heavy fog conditions often experienced in this region during this period of the year (Canadian Hydrographic Survey, 2021).

To compare the SST annual cycle with Air Temperature (AT), local observations measured at Environment and Climate Change Canada (ECCC) Sagona Island (SAGIS) weather station (see Figure 1 for location) were extracted to make a monthly climatology. The climatology (Figure S9) was created similarly to that of the SST for a slightly smaller period of available data (1994-2018). SST and AT are closely linked seasonally, peaking and lowering at the same time (August and February, respectively) although the coldest period lasts longer for the SST (Feb-Mar). August air and sea mean values are very close in August, 15.9 °C vs. 15.3 °C, respectively, but the sea is substantially warmer in February by more than 3 °C (-3.3 °C vs. 0 °C). Mean AT range is thus much larger at about 19.2 °C vs. 15.5 °C for the SST. Standard deviations were similar for both series and of the order of 1 °C although for the SST, it varies seasonally from a low of 0.7 °C in March to a high of 1.4 °C in July.

To get an idea of potential spatial variability in SST over the area of interest, seasonal maps were also created using data from the original extraction area. Straight monthly means were then calculated from the daily series at each available data point. Maps representative of the 4 seasons are presented in Figure 4; to highlight spatial differences, the color ranges of each map were adjusted to a mean ±1 std (standard deviation) range. Spatially, the most striking feature is the apparent propagation of a 'pulse' of cooler water propagating westward from winter to fall and a persistent cold water area along the eastern and southern shore of the Burin Peninsula during all seasons but fall. The colder water appears to generate from Placentia Bay at its southern offshore boundary, to travel through the Saint-Pierre-Burin channel in spring, extending northward in summer before spreading and veering westward, following the Newfoundland coast in fall. While the propagation pattern probably results from advection of cold water by the Labrador Current (Loder et al., 1998), the persistent area of cold water on the eastern side of the peninsula could, in part, be attributed to upwelling-favorable winds as shown by Ma et al. (2012; see also next section on wind showing prevailing southwesterlies from spring to fall). A cool area along the Burin Peninsula, in Fortune Bay, also appears in fall (November) but is difficult to interpret since it also corresponds to poor data coverage.

In the current context of rapid climate change, it is useful to get a sense of long-term SST trend. We

calculated this trend for Fortune Bay by calculating annual means from the monthly averaged series used to create the monthly climatology described above. By using a linear fit on those annual means, a linear trend of 0.04 °C/yr was found, corresponding to an increase of 1.5 °C over the 37 full years of the observations (1982-2018; Figure S11). The same analysis was run on the monthly averaged series to evaluate the potential seasonality of this trend. Monthly trends are larger than the annual trend from July to November and lower in the other months (Figure S12). It peaks in August with a value close to 0.07 °C/yr and is the lowest in June at about 0.03 °C/yr. These results suggest an increase in the potential for summer heatwaves and a comparatively weaker decrease in the potential for winter superchill (i.e. sub-zero temperatures).

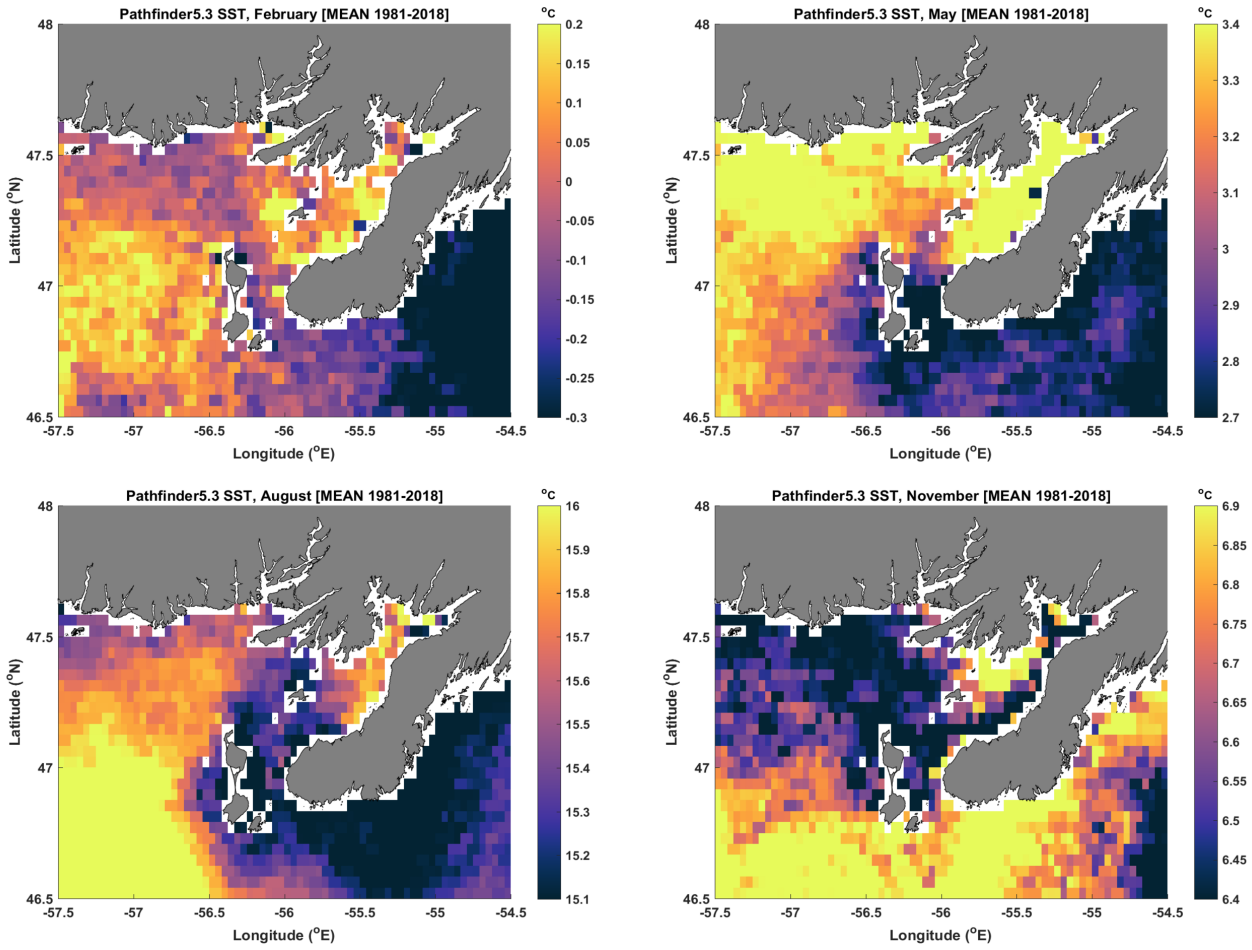


*Figure 4: SST climatology of months representing seasonal peaks. Colorbar ranges were set to be from mean-1 std to mean+1 std where std is the standard deviation associated to the mean fields presented.*

Watershed areas and runoff into Fortune Bay were estimated in Donnet et al. (2018a). As only one river, Bay du Nord river (BDNRI, Figure 1) has been monitored (and continues to be) by ECCC (https://wateroffice.ec.gc.ca/search/statistics_e.html, station 02ZF001), the inputs from all the other rivers to the region were estimated from it, i.e. using area ratios (see Donnet et al. 2018a for details). BDNRI's discharge presents two peaks: a main one in April corresponding to the 'spring freshet' (~70 $m^3/s$ average) and a smaller one in Nov-Dec (~50 $m^3/s$ average); its lowest rate occurs in summer (~20 $m^3/s$ in Jul-Aug) and its annual average is about 40 $m^3/s$ (Figure 5). Using those data, the total annual mean runoff to Fortune Bay was estimated at 163 $m^3/s$ with a peak at 280 $m^3/s$ in April, a low at 80 $m^3/s$ in Jul-Aug and a second peak at 214 $m^3/s$ in December; about 4 times BDNRI's output.

The effect of freshwater inputs on the bay's stratification, i.e. its change in salinity, can be looked at by comparing these inputs with the salinity climatology presented earlier and with near-surface salinity timeseries data recently collected (Donnet et al. 2020). We used BDNRI's monthly climate discharge described above and monthly climate of salinity at 5 m depth presented in Figure 2 to make a 'climatology comparison' (Figure 5) while BDNRI's monthly average timeseries were used for comparison with the recent timeseries collected from oceanographic moorings (Figure 6). Four moorings were deployed during two full years (May 2015 to May 2017) with a CTD moored within the first 2-16 m. The timeseries were filtered using a moving average with a window of 30 days to remove the high frequency signals and get a better picture of the seasonal cycle.

The spatial transition from oceanic waters of the shelf (WOA series) to the coastal ROFI of Belle Bay (BB series) is once again evident with salinities decreasing by about 0.2 g/kg in winter (Feb) to more than 1 g/kg in summer (Aug) from WOA to BB (Figure 5). FB values lie roughly in the middle as a transitory region. Considering standard deviations of the order of 0.2 g/kg, 0.3 g/kg and 0.2 g/kg for FB, BB and WOA, respectively, there are some overlap amongst the series, however. BB's near-surface salinity cycle appears to be almost in phase with the freshwater discharge, that is: high values in winter and low values in summer. April and November-December peaks of discharge do appear to have a small effect, lowering the salinity in May (thus, one month after) and November, but the lowest values seen in July-August seem at odds with a locally forced system.

The timeseries comparison, Figure 6, confirms the low frequency salinity cycle with a low in summer and a high in winter (more visible in 2015-16) although the cycle appears to be modulated by higher frequency 'freshening events' in BB (F3B03&04 series of November, March and May, in particular). Those events appear to be in phase or occurring just about a month after a peak of river discharge. It should be noted that the interpretation of these data is complicated by the uneven vertical distribution of the observations. The freshening lag seen between F3B03 and F3B04 in Feb-Mar and Nov 2016, for instance, might be due to the deeper measurement made at F3B03 during these time periods (16 m vs. 5-8 m at F3B04). Important interannual variability was observed also, with a difference of about 0.5 g/kg observed between the summers of 2015 and 2016.

We consulted the latest Sea Ice Climatic Atlas to assess Fortune Bay's ice climate (CIS, 2011). The maximum frequency of occurrence of new ice in Fortune Bay from this atlas is 1-15% during the weeks of February 26, March 12 and March 19 (to a much lesser extent for the latter); thus a total of 3 weeks over the November 12 – August 27 period reported by the atlas. This frequency of occurrence is calculated over a period of 30 years (1981-2010); so that sea ice would be observed in Fortune Bay about once every 7-100 years. Local knowledge reported in de Young (1983) indicated that ice presence in Fortune Bay is very seldom other than in small harbours and coves and that advected ice from the Gulf to this region can occur in late winter to early spring of heavy ice years. Our discussions with finfish farmers and local fishermen during our own monitoring program (2015-17) led to the same observations.

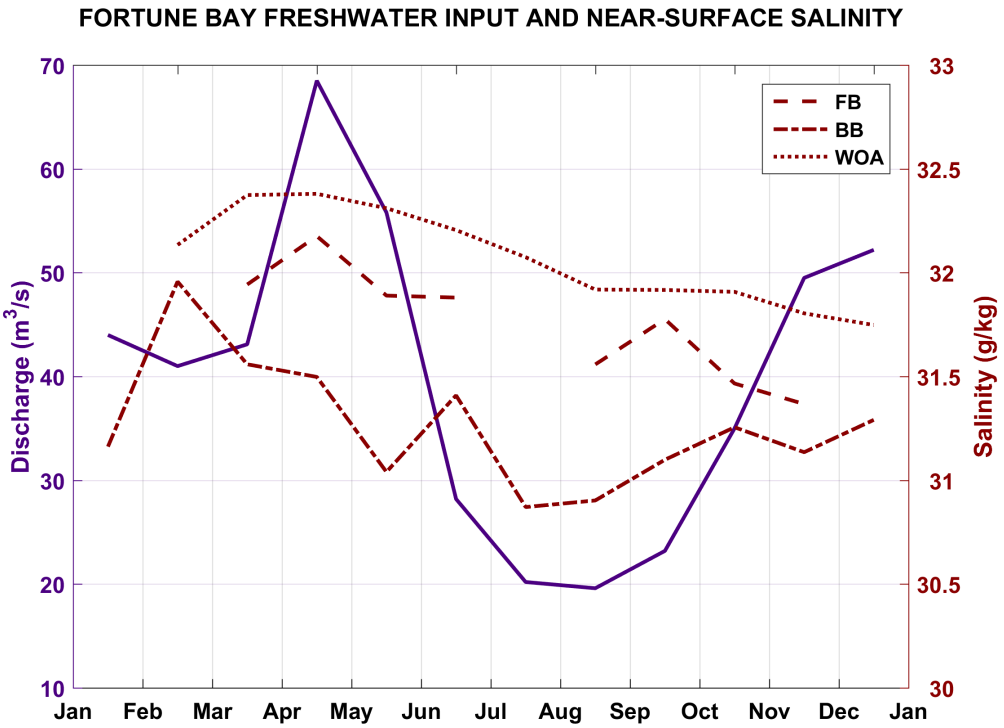


*Figure 5: Bay du Nord River discharge and Fortune Bay near-surface salinity climate (FB and BB polygon areas).*

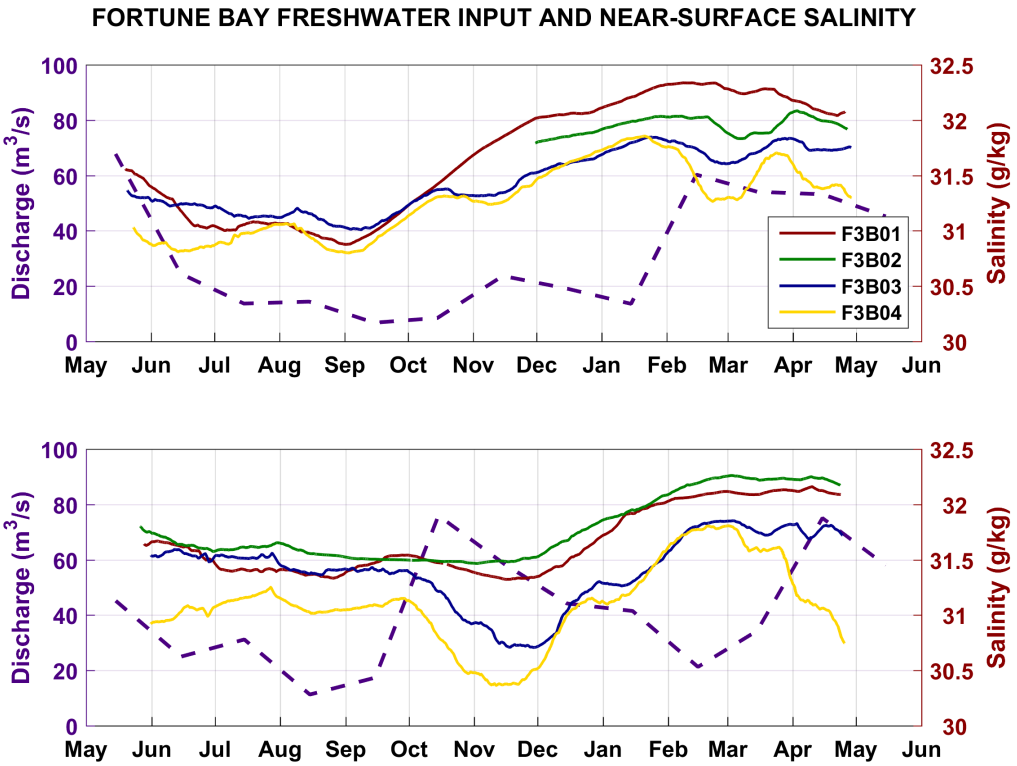


*Figure 6: Bay du Nord river input (dashed) vs. near surface salinity measured at F3B01 (red), F3B02 (Green) in FB and F3B03 (Blue) and F3B04 (Gold) in BB. Top panel is the 2015-2016 period while bottom panel is the 2016-2017 period.*

# WIND

Monthly wind roses as well as general characteristics of the wind climate of the Fortune Bay region was recently presented by Donnet et al. (2018a). For the purpose of this paper, the analysis was extended using a slightly longer timeseries available (25 years vs. 20 years) and a focus was given on forcing aspects that are thought to be important to the ocean dynamics (and response) of the embayment, i.e. directionality and frequency of occurrence of strong events.

ECCC weather station hourly data from Sagona Island (SAGIS, Figure 1) were downloaded from February 1994 to January 2019, covering 25 years but with significant gaps. In total, about 3 full years (2008, 2014 and 2018) and about 19 other full months (Jun-Jul 1994, Jun-Jul 2001, Feb-Mar 2002, Apr-Jul 2002, Jul-Aug 2005, Mar-Sep 2011 and Feb-Aug 2015) are missing from the timeseries. The data was further reduced for more statistical robustness to include solely days with 16 or more hours of data and months with 20 days or more of data leading to a timeseries consisting of 7250 days and 238 months, corresponding to about 20 years of useable wind data. Wind speed values were also adjusted to 10 m above mean sea level before the analyses using the Large and Pond (1981) formula (from a measurement height of 70 m above mean sea level).

Seasonal wind roses are illustrated in Figure S13; showing the annual cycle in both speed and dominant direction. Overall, prevailing winds are from the west, as expected for the region, but strong winds can come from any direction and spring and fall winds are more variable. Computing a monthly wind speed climate from the hourly timeseries (same method than with the AT), it was found that there is a factor of almost two in wind speed between the windy month of January (10±1 m/s average) and the more gentle month of July (5.5±0.5 m/s average).

Given the orientation of the Fortune Bay – Belle Bay system, wind blowing along the main axis of the bays, i.e. from the SW and NE (along FB), SE and NW (along Belle Bay) are expected to produce the largest oceanic response (e.g. in the form of upwelling or downwelling and/or sea level setup and setdown). To illustrate the seasonal change in direction, a monthly percent of occurrence wind direction plot was made using the four main axes directions mentioned above and using full quadrants (e.g. 0-90 $^{o}$N range for NE winds) (Figure 7A). The strong seasonal variation in wind direction is evident from this latter plot with a clear shift from prevailing NW winds in winter to prevailing SW winds in summer.

To get a sense of the frequency and importance of wind forcing on the embayment, a persistence analysis was carried out. The same four main directions described above were chosen for the analysis along with a wind speed value of 10 m/s. The number of events with wind blowing for a duration equal or superior to 6 hr, 12 hr, 18 hr and 24 hr were computed for each direction and each of the months of the timeseries and then averaged monthly to produce a monthly climate. The 6 hr scenario is illustrated in Figure 7B. Strong seasonality is again evident from this latter plot, showing frequent stormy conditions (>=8 wind events lasting 6 hr or more from any direction per month) from September to May, i.e. 2/3 of the year. From May to September, a much calmer period occurs (2-6 events from any direction, per month). Same directional shift pattern (from prevailing NW to prevailing SW winds) is observed from this analysis. 12 hr events are about twice less frequent than 6 hr ones with northerly winds (NE and NW) and 3 to 5 times less frequent with southerly winds (SW to SE, respectively). Wind events equal to or larger than 18 hr in duration occur 5 to 10 times per year, on average (NE and SW winds and NW winds, respectively). Events equal to or larger

than 24 hr in duration are rare (1 occurrence of NE and SW winds; 5 occurrences of NW winds, on average per year).

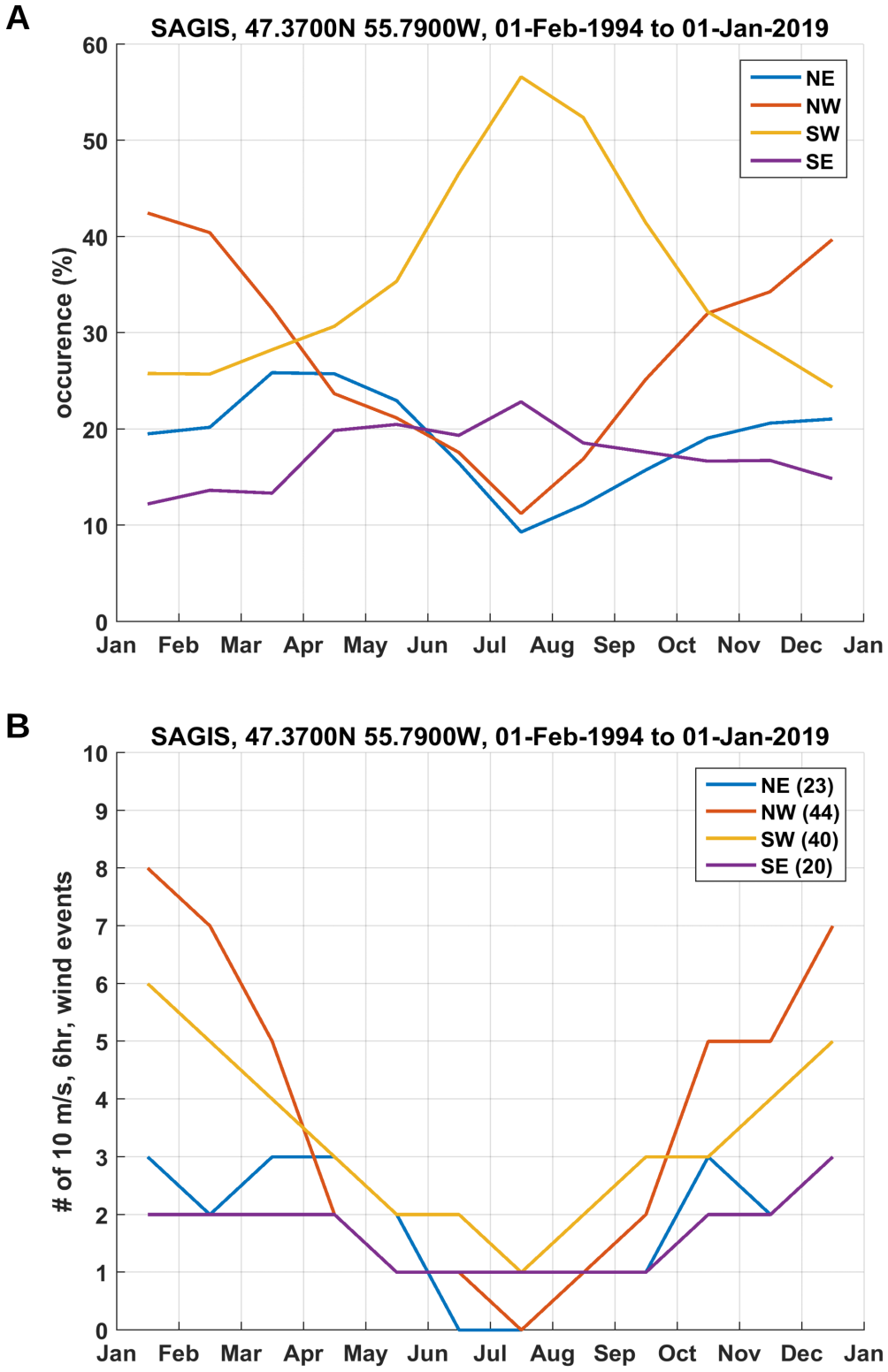


*Figure 7: wind direction (From) monthly climate from SAGIS along the four main axes of the Fortune Bay - Belle Bay system (A). Persistence of 10 m/s wind blowing 6 or more hours along the four main axes of the Fortune Bay - Belle Bay system; total (annual) number of events for each direction is given in bracket in the legend (B).*

# TIDES

Analyses of tides of the area were presented in Donnet et al. (2018a) and Ratsimandresey et al. (2019) who reported sea-level and currents characteristics, respectively. Both studies focussed on the inner part of the bay (Belle Bay) and used relatively short timeseries (usually a few months long), however.

The objective of this section is therefore to complete the previous studies using newly collected and longer timeseries (see Donnet et al., 2020 for details) and by examining the importance of the non-tidal component of the sea-level. Information on the tidal currents vertical structure and seasonal variation will be offered in the next section along with the non-tidal components of the circulation.

A tide gauge is installed at the head of the Belle Bay, on the wharf of Pool's Cove since May 2015, recording sea-level and water temperature at 10 min interval (see Figure 1 for location). The gauge has been continuously maintained since its deployment but has suffered from a number of sensor failures, resulting in gaps in the timeseries. The longest continuous record available, from May 2015 to March 2016 (331 days), was used for analyses.

Tidal constituents were first extracted from the series using the T_Tide harmonic analysis programs (Pawlowicz et al., 2002). Residual (non-tidal) water level variations were subsequently calculated by subtracting the determined tidal signal from the original series. A wavelet analysis was finally performed to determine the periods of potential transient signals in the residual series using Grinsted's wavelet coherence programs (Grinsted et al., 2004). The original record along with the results of those analyses are presented in Figure 8. The major constituents are M2 (0.65 m), S2 (0.18 m), N2 (0.14 m), O1 (0.07 m) and K1 (0.07 m); leading to a form factor F (K1+O1 / M2+S2) equal to 0.17. Tides in Fortune Bay can therefore be defined as semi-diurnal (Courtier, 1938). As seen in Figure 8, the tidal range is about 2 m at spring tides and 1 m at neap tides.

Residuals account for only about 4% of the raw signal variance but can have substantial magnitude (order of 0.5 m). Those notable events are transient in nature but more frequent and stronger in fall-spring (October to April). Wavelet analysis indicates that those events have periods of 1-2 days (d) generally and sometime longer (4-5 d). A Butterworth band-pass filter analysis performed on this 1-5 d band indicates that those events can have an amplitude of the order of 10-30 cm. At higher frequencies, frequent signals occur in the 0.125 day (3 hr) and 0.02 day (0.5 hr) bands which are close to Fortune Bay and Belle Bay's natural mode 1, respectively (about 2 hr using a 130 km long Fortune Bay and about 0.5 hr using 30 km long Belle Bay; both 160 m depth). This latter observation indicates frequent occurrence of seiche activity particularly during the late fall to early spring when numerous strong wind events occur in the region. A 0.014-0.25 d (20 min to 6 hr) band-pass filter revealed amplitudes of those seiche to be of the same order of magnitude as the low frequency signals (1-5 d band). Given a 10 min sampling of the timeseries, however, aliasing effects can also be expected. Some signals also occur within the 0.5 d band which may be due to the imperfection of the tidal analysis.

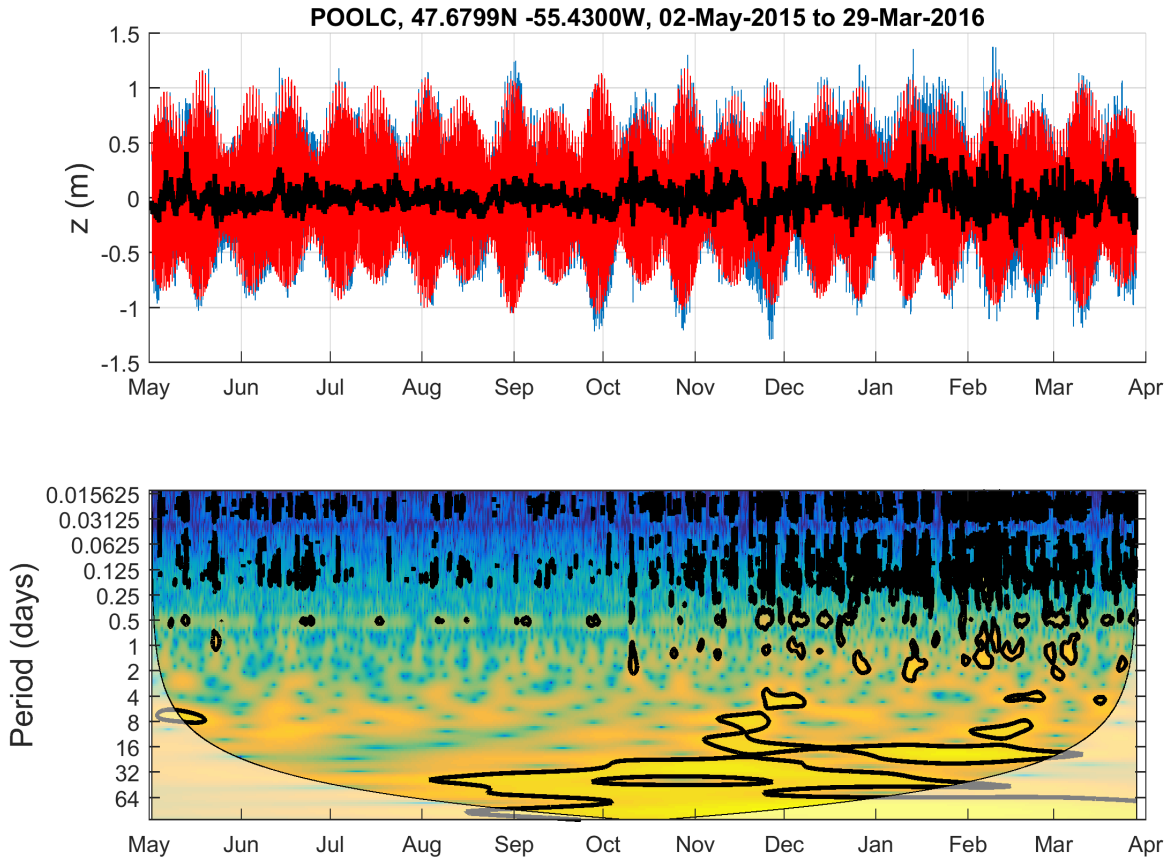


*Figure 8: sea level record (blue), tide (red) and residual (black) at POOLC (Belle Bay), top; residual wavelet analysis, bottom. On the wavelet plot, the thick black contour designates the 95% significance level against red noise and the cone of influence (COI) where edge effects might distort the picture is shown as a lighter shade.*

# CURRENTS

Currents in the inner part of bay (Belle Bay) were assessed statistically for 2 layers (0-20 m and 20 m to sea-bottom) in Ratsimandresey et al. (2019) using a number of ADCP records collected at various locations, principally near aquaculture sites.

The objective of this section is to expand the previous work by providing more information on the vertical structure and temporal variation at seasonal scale for the bay as a whole as well as providing quantitative estimates of the dominant energy bands using recently collected and longer ADCP timeseries (see Donnet et al., 2020 for details).

## GENERAL CHARACTERISTICS

An example of current speed and direction series, taken from May 2015 to May 2016 is presented in Figure 9. These observations were obtained from two upward looking ADCPs (300 kHz) mounted on the same line at about 55 and 150 m; low scattering conditions resulted in small data gaps between 50 and 70 m. The main features of this series are representative of the region, that is: stochastic ‘events’ appearing more frequently from October to March and a directionality dominated by low-frequency oscillations (N-S in

Figure 9). Effects of stratification is more evident during the summer season (Jul-Sep) with localised 'pulses' toward the surface though signs of layering processes, i.e. changes of direction with depth and maximum speed dipoles on the vertical, appear throughout the year. Strong, near-bottom to mid-depth (50-100m from bottom) events also occur frequently during the fall to spring season (late Oct – early May).

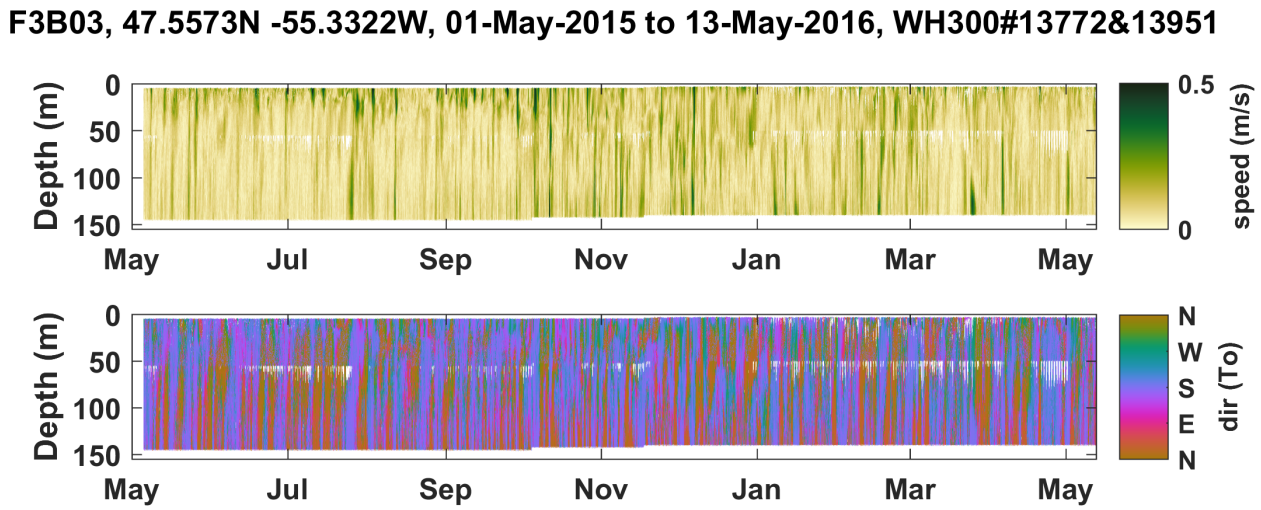


*Figure 9: ocean current speed and direction observed at the mouth of Belle Bay (west side; see Figure 1 for F3B03 location, site depth = 155 m).*

## SEASONAL STATISTICS

To get a sense of the seasonal variability, some basic statistics were calculated by time-averaging the ADCP profiles seasonally (see Figure S11 for a representative example). The analysis was performed using the observations made from May 2015 to May 2017 at 12 locations around the bay (F3B01-12, see Figure 1 for location and Donnet et al., 2020 for details). Overall, mean current speeds are about 8±5 cm/s, maximums are on the order of 40 cm/s and both vary, on average, by a factor of about 2-2.5 with depth and a factor of about 1.5 seasonally at any given site (2-20 cm/s range, altogether for the means, 10-90 cm/s range for the maximums). The strongest currents are usually found near-surface (upper 20 m) and the weakest toward the middle of the water column (F3B02&03) or near-bottom (F3B01&04 and all sites <100 m depth). Maximums were also found in subsurface (20-60 m) at some sites (F3B01, 03, 04 and 05) in fall. Seasonally, the fall period is the most dynamic while the spring is the least dynamic (closely followed by the summer). Spatially, currents are stronger in the outer part than in the inner part of the fjord by about 50%, on average, in mean speed. Large spatial variability is, however, to be expected given the region's complex bathymetry.

## SEASONAL CIRCULATION

Vector averaging the currents at 10 (1.5 at F3B12), 70 and 135 m depth, a seasonal picture of the mean circulation was obtained (Figure 10). We define those depths as representative of 'surface', 'middle' and 'bottom' layers, respectively, taking the hydrographic structure presented above into account. Note that 135 m, the deepest level we could use from our data, is probably a little too shallow to be fully representative of the bottom layer. Indeed, a depth of 200-300 m would be more appropriate to represent

the bottom layer and its processes as shown in de Young (1987) and Hay and de Young (1989). Similarly, 70 m is a little too shallow to be representative of the intermediate layer in fall but was the deepest available data from the moorings F3B05-11. The maps presented in Figure 10 are a composite using the 2016-17 surface and mid-depth observations and 2015-16 bottom currents at all sites but F3B01. Due to data gaps in current direction, we used data from the 2015-16 observations at all depths for the spring, summer and fall periods and used data from the 2016-17 observations to represent the winter period surface and mid-depth layers for this latter site. Except for F3B02 in spring, the results were coherent over the 2 years of observations. At F3B02, surface currents flowed toward the SW in spring 2015 (as opposed to the NW in 2016) and mid-depth currents toward the W (N in 2016); currents were about the same strength at the near-surface level in both years but much weaker at mid-depth in 2015 (about 3 times less). Mean circulation is rather weak, on the order of 1-5 cm/s except in the Bay du Nord river estuary (F3B12) where mean surface outflow is about 15 cm/s in winter (factor 3 scaling applied in Figure 10's arrow). The near-surface flow is oriented outward the bay at all sites and seasons except at F3B04 where it is inward in spring and summer. Flow is roughly oriented the same way at mid-depth except at F3B01&11 in winter where it is in opposition (inward). Bottom currents are not shown at F3B01 for the winter, spring and fall seasons due to a lack of current direction observations, reducing the coverage below the 80% seasonal representativeness threshold chosen. For the same reason, currents are not represented at F3B05 (all seasons) and F3B07 in spring and fall. F3B11 was deployed only from November 2016 to May 2017 and from June 2016 to May 2017 at F3B08, reducing the coverage to the winter at F3B11 and to the winter, summer and fall seasons at F3B08, using a 80% threshold. Using all the data available, a moderate near-surface inward flow appears in spring and a strong near-surface outward flow appear in fall at both F3B08 and F3B11. At mid-depth, flow is outward at F3B08 and inward at F3B11 in both spring and fall, however, while being rather strong in fall (~5 cm/s) it is very weak in spring (<1 cm/s) at F3B11. At F3B01, bottom currents are inward in both spring and fall (see Figure S12 for an illustration).

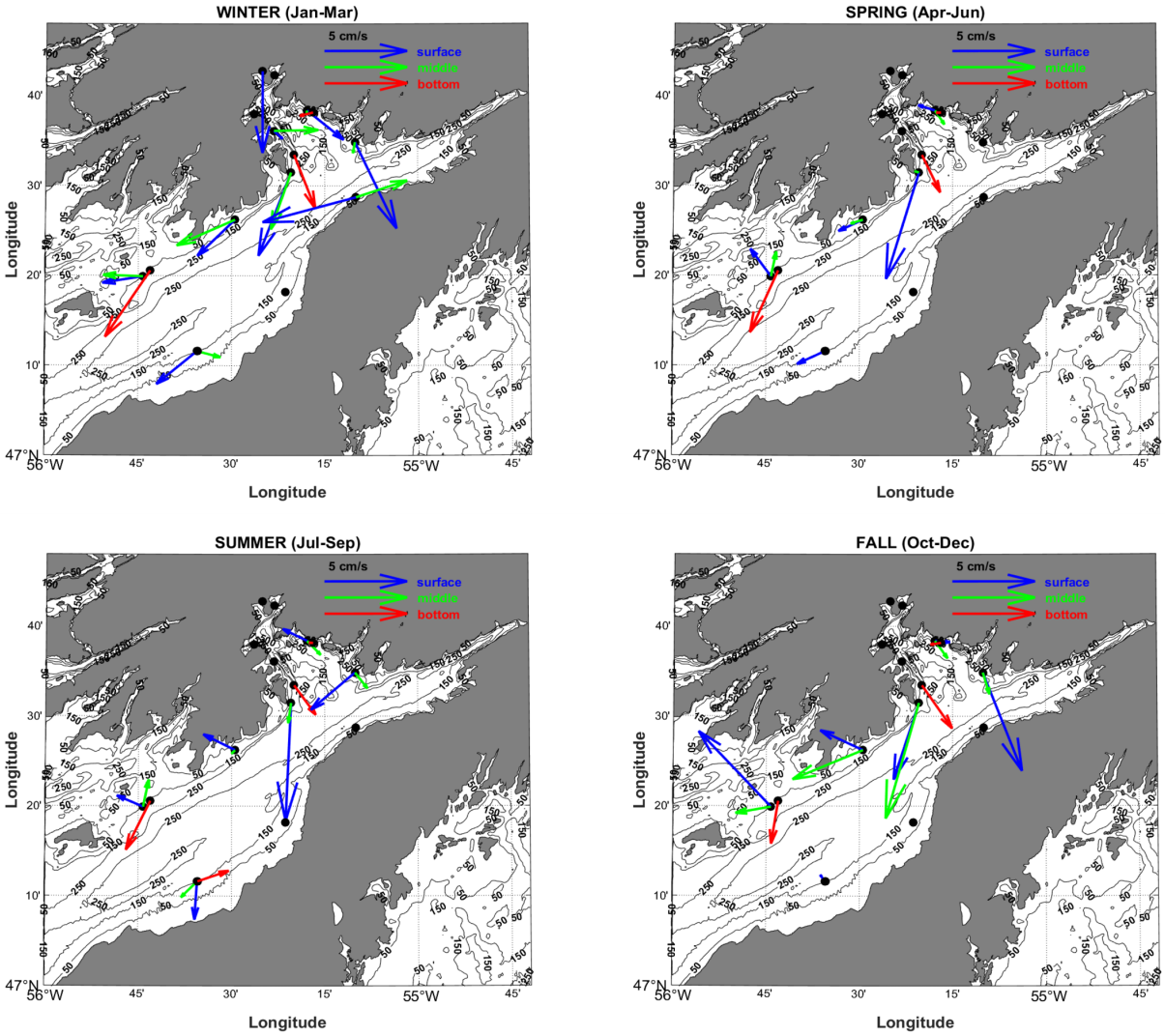


*Figure 10: mean, seasonal, circulation near-surface (10 m), middle (70 m) and near-bottom (135 m) layer. Scaling by a factor of 3 was applied to near-surface currents at F3B12 (winter) due to their much larger magnitude.*

# SPECTRAL ANALYSIS

To investigate the higher frequencies, a spectral analysis was carried out. The analysis was done on the dominant along-shore component (about 2-2.5 times larger, on average, than the cross-shore component) at each mooring site described above and for the same depths as those of the mean circulation maps analysis presented above (i.e. 10, 70 and 135 m). We used a classic Fast Fourier Transform (FFT) algorithm following the Welch's method with a 85-day half-length overlapping Hanning window (4 degree of freedom over a one year timeseries) to perform the analysis. Selected illustrations are presented in Figure 11; only results from moorings F3B01-04, year 1, are presented as they were found to be representative of the region and observed period (2015-17) as a whole. In general, the spectrums are red with a large plateau at low-frequency ending around 0.5 cycle per day (cpd, i.e. 2 d period) followed by a sharp decrease and a prominent peak corresponding to the semi-diurnal tides (with a notable exception at F3B04). No significant peak at the inertial frequency (1.47 cpd) was observed at any of our monitored sites. At high frequencies, from about 10 cpd (2.4 hr period), the surface layer spectrum (10 m) falls off rapidly while deeper levels spectrums (70 and 135 m) tend to flatten at all sites. From the inertial frequency to the 10 cpd inflection

point the slope was found to be -2 on average (-2.7 to -1.7 range). While this slope is consistent with the Garrett-Munk spectrum model of internal waves (Garrett and Munk 1972 and 1975), the latter was developed using open-ocean data. This suggests that energy dissipation due to internal waves may exist in Fortune Bay in a similar way than in the open ocean. We can also note the departure from this slope at higher frequencies (10 cpd) where the spectral energy falls off near the surface while it flattens at depth. This is at odds with the findings of Levine et al. (1983) which showed flattening of high frequency energy to happen in the upper part of the ocean and suggest intensification of internal processes near the bottom rather than towards the surface in Fortune Bay. F3B06 spectrums are similar to those of F3B03 and F3B08 are similar to those of F3B04. F3B11 resembles that of F3B04&08 with a more discernible peak at semi-diurnal frequencies. Integrating under the spectrum, we estimated the energy of three main bands, 2-20 d (low frequency, or 'weather band'), 6-30 hr ('tidal band') and 2-6 hr ('high frequency' band) expressed as a variance, and compared it with the total signal (by computing a % ratio). We also used a 5th order Butterworth band-pass filter to check and complete the analysis at all depths and found the same results. The distinction between those bands were based on visually inspecting variance preserving spectrums (not shown) for the weather band and by assuming that most of the tidal energy would be restricted to the diurnal to quarter-diurnal band. The high frequency band was defined as simply being anything of higher frequency than the other 2 bands. Overall, the weather band contributes to half or more of the total signal variability (47% on average, 20-63% range across all depths and sites) while the tidal band contributes to about 20% (9-34% range) and the high frequency band accounts for less than 5% (1-14% range) only. Expressed as RMS (Root Mean Squares), the weather band currents are found to be about 6 cm/s, on average (1-12 cm/s range), the tidal band current about 3 cm/s average (1-6 cm/s range) while the high frequency currents are only about 1 cm/s on average (1-3 cm/s range) for a total signal of about 8 cm/s (2-16 cm/s range). It should be noted that the tidal band used here is rather large and probably includes energy from other processes than the tide. Similarly, the low frequency and high frequency bands may include tidal harmonics of lower or higher periods than the, assumed, dominant diurnal to quarter-diurnal band.

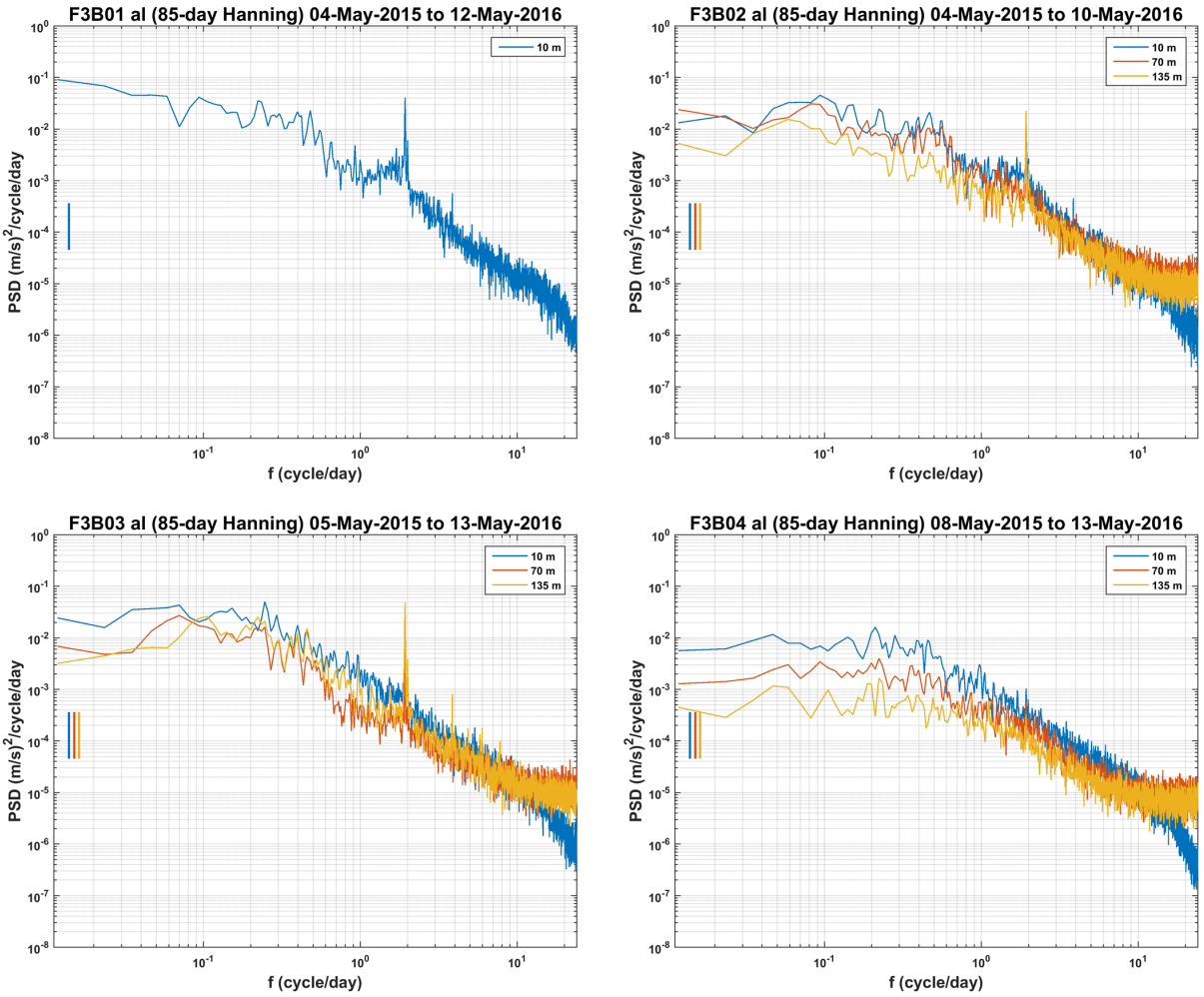


*Figure 11: annual spectrums of the along-shore current component at F3B01-04 sites (F3B01&02 in FB, F3B03&04 in BB). 95% confidence interval of each spectrum is represented by a vertical bar on the left hand side of each plot. Note that because of mooring deployment issues, F3B01 along-shore currents at 70 and 135 m depth are not available.*

# WEATHER BAND

Pulses of current characterize the weather band and appear more transitionary in nature than periodic (explaining the rather flat PSD distribution in the spectrum). A couple of examples of these pulses using the along-shore component are presented in Figure 12. Along-shore currents are defined as being positive for a flow going into the bay (red color), i.e. northeast-ward in the outer part and northwest-ward in Belle Bay, and negative (blue color) for an outgoing flow. Top panel of Figure 12 illustrates the frequent occurrence of those events affecting most of the water column during the fall season while the bottom panel shows an example of the more sporadic occurrence of those events taking place over a more restricted portion of the water column (upper 50 m) in summer. In both cases, the response appears coherent, progressing around the bay in a cyclonic motion (F3B01 to F3B03 in the fall illustration, F3B08 to F3B06 in the summer one). In the fall example, 4 large pulses occurring 2-3 days apart (23, 25, 28 and 30th of October) are clearly visible at F3B01 (FB, southernshore). Currents of about 0.5 m/s associated with isotherms vertical migration of the order of 25 m to 100 m (6 °C and 2 °C isotherms, respectively) characterize those pulses. Interestingly, while the inflow appears principally barotropic in nature (i.e. currents going in the same direction with depth), the outflow are clearly baroclinic with a current inversion occurring around 50 m depth. Though much less

energetic and more baroclinic in nature, those four pulses occur at F3B04 and F3B03 with about half the flow speed, less vertical migration of isotherms (10-50 m) and 1 and 1.5 d delay from F3B01, respectively (as an upper layer outflow at F3B03, in October 25, 26.5, 29.5 and 31.5). F3B02 stands out from the other sites with relatively strong currents but varying less distinguishably as pulses and showing a more stable 6 °C isotherm. The latter is subject to semi-diurnal signals, however, of about 5 m amplitude, which are probably of tidal origin. The cyclonic propagation is more visible in the summer example with a large downwelling (50-100 m range) associated with strong currents (~0.5 m/s) occurring at all sites around Belle Bay (F3B08, 04 and 03) and on the northern shore of FB (F3B06). Not shown (no along-shore current data), F3B01 and F3B05 also experienced a strong downwelling event (almost 100 m for the 2 °C isotherm), occurring about 2 days earlier than at F3B08 (July 13). Similar to the fall, F3B02 (not shown) appears uncorrelated with the other sites with the exception of a rising and falling 2 °C isotherm during the downwelling and upwelling phase observed at F3B01 from the 13 to the 16 of July.

Results of cross-correlation analyses (see details in the supplementary materials) show that those pulses are well correlated amongst most sites both in terms of isotherms (Jun-Dec) and along-shore currents (throughout the year). The correlations are stronger amongst mooring pairs from F3B08 to F3B06 and the lowest with F3B02 and their lags consistently indicate a cyclonic propagation (as seen in Figure 12). Using the correlation' lags and distance between mooring sites, we obtained phase speed estimates of 0.5-2 m/s, increasing from spring to fall.

Further statistics were calculated to get a sense of the frequency of occurrence, duration and excursion associated with those pulses (see the supplementary materials for details). Those latter analyses reveal the occurrence of 28±3 pulses per year of 23±12 h (ingoing or outgoing flow) and associated excursion of 10±7 km, on average and across all sites. Seasonally, a peak of activity is found from September to December when 3-6 pulses of 24 h duration or more (in either direction) can occur at any given site (and depth) per month (i.e. about 1 event of 48 h duration every 5-10 d). These pulses are not necessarily balanced in term of flow strength and duration and may therefore lead to a net transport (at any given depth, or even vertically integrated). Net transports of up to almost 20 km, at any given depth, were found using timeseries presented in Figure 12.

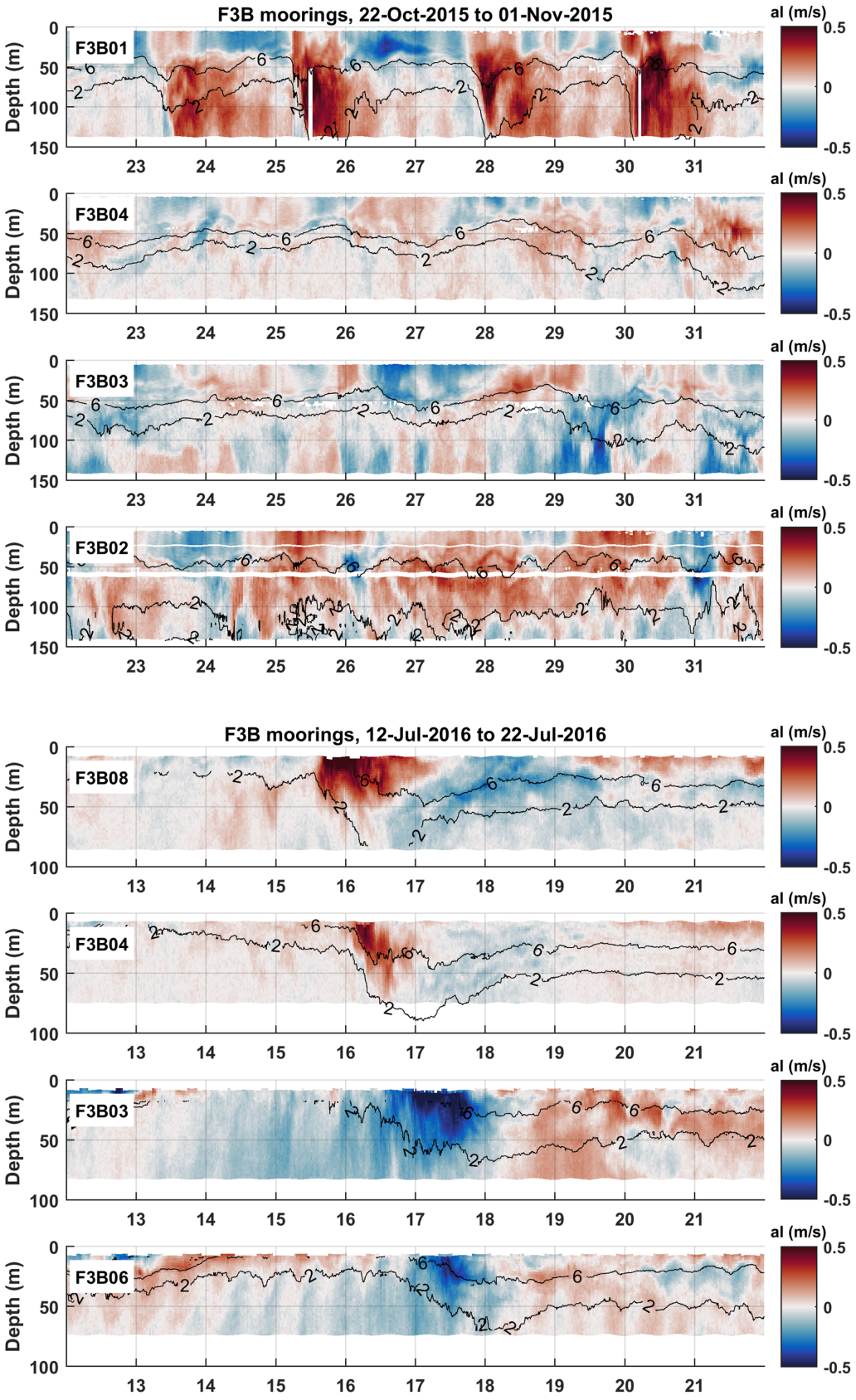


*Figure 12: fall (top) and summer (bottom) along-shore current events observed around Fortune Bay (see mooring location in Figure 1). Isotherms 2 °C and 6 °C are represented by black lines.*

# INNER BAY (BELLE BAY) WATER EXCHANGES AND FLUSHING TIMES

In the context of fisheries and aquaculture activities occurring in Fortune Bay, knowledge of water exchanges (and hence of flushing or residence times) is of primary importance. It has direct applications for a better understanding of issues such as larval retention (and dispersion), dissolved oxygen depletion (e.g. within finfish farms), finfish parasites dispersion (e.g. sea-lice) and virus outbreaks. Here, we will attempt to quantify the main exchange processes between the inner (Belle Bay), where the aquaculture sites are located, and outer part of the bay using the data presented herein and simple formulas that have commonly been used for estuaries and fjord environments (e.g., those used in Inall et al., 2015, in particular, which were applied to a broad fjord). Three main processes will be assessed: barotropic tide, estuarine circulation and the so-called 'intermediary circulation' (see Stigebrandt, 2012 for a review of those processes in fjords). The water exchange rate estimates provided, Q (given in $m^3/s$), correspond to the rate of water exchanged by a given process and the flushing time estimates, T (given in days), are based on the total amount of time necessary to renew the entire volume of interest (either whole basin or layer) from that process alone. Note that except for the barotropic tide, which takes place over the whole water column, T is evaluated for the replacement of the upper layers (surface and intermediate). Deep water renewal will be assessed separately based on previous studies findings.

## BAROTROPIC TIDE

A first estimate of Belle Bay's flushing time by the barotropic tide ($T_{tide}$) was given in Donnet et al. (2018a) using a simple version of the tidal prism method and led to a 70 d value. We will refine this first estimate using a slightly modified version of the tidal prism method proposed by Gillibrand (2001):

$$T_{tide} = (V + V_{tide}) / (V_{tide}(1-\lambda)) * Tp_{tide}$$

which includes a parameterization (1-λ) to account for the mixing efficiency of the return flow. V is the basin volume (54,100 $x10^6$ $m^3$, for Belle Bay at low water level), $V_{tide}$ is the volume of water brought in and out of the basin by the tide (450 $x10^6$ $m^3$, using a mean tidal range of 1.4 m and Belle Bay area of 310 $km^2$ at mean sea level), $Tp_{tide}$ is the dominant tidal period (12.42 hr, M2) and λ is the efficiency parameter.

The original tidal prism method assumes complete mixing of the tidal volume during each flood and complete removal from the system during each ebb. This is highly unlikely in Belle Bay given the vertical stratification observed. λ account for the proportion of the flow that is being returned to the system during each flood tide (as volume of original water). Hence, 1-λ account for the proportion of water that is being effectively recycled during each tidal cycle. A λ value of 0 would correspond to complete mixing and flushing, an unrealistic situation in Belle Bay, while a value of 1 would correspond to no mixing and flushing, also an unrealistic situation. Determining a suitable value of λ is difficult since it implies knowing precisely how much water gets mixed and gets flushed away, without coming back, during each tidal cycle.

Using a conservative approach and assuming that the fraction of water being effectively removed from the system during each tidal cycle would solely be due to the mean current determined earlier at F3B03 (Figure 10), i.e. order of 5 cm/s year round for all layers, a λ value of 0.95 is obtained (i.e. 1-(0.05 x $Tp_{tide}$ / 2 / 24,500) where 24,500 is the width of Belle Bay mouth, in meters). This would then lead to a flushing time of the order of 1,255 d. While this latest estimate is likely overestimated, it might be closer to the reality of

(barotropic) tidal flushing given the weakness of the tides acting in Belle Bay. Water exchange (or flushing rate, $Q_{tide}$) can be estimated using the tidal volume and period as:

$$Q_{tide} = V_{tide}(1-\lambda)/Tp_{tide}$$

Which gives a range of 1.25 x$10^3$ to 10 x$10^3$ $m^3$/s (λ = 0.95 to 0, respectively).

# ESTUARINE CIRCULATION

Net volume flux of the (fresh/brackish) surface layer, balanced by the (salty) lower layer of an estuarine circulation can be found using the Knudsen relations based on salt and volume conservation (see Burchard et al., 2018 for a recent review) which gives:

$$Q_{est} = (Q_f * S2)/(S2-S1)$$

$$T_{est} = V_{up}/Q_{est}$$

Where $Q_f$ is the freshwater discharge (71+39 = 110 $m^3$/s annual mean, 35+19 = 54 $m^3$/s to 121+67 = 188 $m^3$/s range; August to April rivers discharge into Belle Bay + that of Long Harbour river, respectively; see Donnet et al., 2018a for details), S1 is the averaged surface layer salinity and S2 is the averaged lower (intermediate, in this case) layer salinity. $V_{up}$ is the volume of the surface and intermediate layers (combined) estimated at 41,500 x$10^6$ $m^3$ using a limiting sill depth of 210 m (separating Belle Bay from Fortune Bay). Simply interpreted, this relation means that, in a 2-layer ocean, the (surface) outgoing flow ($Q_{est}$) is balanced by the (subsurface) ingoing flow which is equal to the product of freshwater runoff ($Q_f$) with a salinity fraction representing entrainment of the incoming, salty ocean water by the fresh, surface flow (then becoming brackish as time and distance from the source increases). It assumes steady states and is applicable when S1 and S2 are not equal. S1 and S2 must therefore represent time-averaged conditions, i.e. representative of a mean flow. Due to entrainment, the outgoing flow is generally much larger than the freshwater runoff. Using a minimum of 29.5 g/kg (July) and maximum of 32 g/kg (February) for S1 and a constant value of 32.4 g/kg for S2, representative of our climatological conditions, we get a flushing rate range of 0.6 x$10^3$ to 15 x$10^3$ $m^3$/s and corresponding flushing time range of 31 to 796 d. This range is large and reflects uncertainties as well as the strong seasonality observed in both freshwater discharge and surface salinities; with weakest flushing conditions in summer and strongest from fall to spring (i.e. when surface salinities are within 31-32 g/kg and Qf >100 $m^3$/s).

It should be noted that the Knudsen relations reflect averaged conditions, i.e. the net effects of all forcing, including those of wind and tides. As MacCready et al. (2018) recently showed, flushing processes are very closely linked and overall mixing inside the bay can be approximated via a modified Knudsen relation. Thus, equating $Q_{est}$ with $Q_{tide}$, we could estimate values of λ which would be representative of the (averaged) inner bay mixing efficiency. Using the numbers used above lead to a λ ranging from <0 to 0.95. Negative values are unrealistic/unphysical and implies uncertainties in our data (either in our salinities such as S1 being too large or in our estimate of $Q_f$ and/or tidal volume being too large or too low, respectively; the former being more likely than the latter two). Using yearly averaged values (S1 = 30.7-31.7, S2 = 32.4 where the range in S1 reflects near-surface and depth-averaged values of the surface layer, and $Q_f$ = 110 $m^3$/s) gives a λ of 0.5-0.8 and a flushing time of 94-229 d (3-8 months).

# INTERMEDIARY CIRCULATION

The intermediary circulation was defined as being the circulation (i.e. currents) generated by density variations outside the fjord above sill depth (also called 'baroclinic pumping'; see Stigebrandt 2012 for a review). An empirical formula quantifying this water exchange is given as (Aure et al. 1996):

$$Q_{int} = \beta * \sqrt{(g * Bm * Ht * Af * \delta M / \rho_0)}$$

where β is an empirical coefficient (17 x$10^{-4}$), g is the gravity constant (9.81 m/$s^2$), Bm is the width of the mouth (24.5 km), Ht is the sill depth (210 m), Af is the horizontal area of the fjord (310 $km^2$), δM is the vertical integral of water density standard deviation profiles taken outside the fjord from sea-surface to sill depth (25 kg/$m^2$ in spring, 28 kg/$m^2$ in summer and 37 kg/$m^2$ in fall; using FB's temperature and salinity data presented above) and $\rho_0$ is a reference density (1,026 kg/$m^3$). Using those values for FB (as 'outside fjord' forcing conditions) and Belle Bay (as the 'receiving fjord') we get a flushing rates of 33 x$10^3$ $m^3$/s (spring), 35 x$10^3$ $m^3$/s (summer), 40 x$10^3$ $m^3$/s (fall) and corresponding flushing times of 12-14 d.

It can be noted that this baroclinic pumping relation does not make any consideration to mixing nor to potential reflux of water at the mouth, which is unrealistic and certainly leads to an overestimation (underestimation) of flushing rates (times). Yet, it can also be noted that those rates are 3-4 times larger than the rates estimated from the tidal forcing alone, even when considering the same assumptions of complete mixing and flushing for the latter (i.e. λ = 0; $Q_{tide}$ = 10 x$10^3$ $m^3$/s).

# DEEP WATER RENEWAL

A timescale of 300 d was estimated by Hay and de Young (1989) for the cold LCW to replace all the bottom water (i.e. below sill depth or 120 m) of the bay as a whole. Since the renewal by this water mass only occurs for about half of the year (from May to December) it is unlikely that the LCW can renew the basin fully within a year. However, during the remaining half of the year (December to June), the basin is subject to renewal by the warm MSW which appears to renew it at about the same rate (as illustrated by their Fig. 11). As a result, it seems reasonable to expect a total replacement of Fortune Bay bottom water on a yearly timescale. This renewal has, however, distinct consequences on the properties of Fortune Bay's bottom water; on a semi-annual timescale. Other than the difference in physical characteristics of the two sources, one being cold (<2 °C) and the other being comparatively warm (>4 °C), these two water masses (LCW and MSW, respectively) are also very distinct in their chemistry. Hence, while the LCW is oxygen rich (>10 mg/L), the MSW is comparatively poor (<6 mg/L). As a result, the bottom water of Fortune Bay should experience a semi-annual cycle of not only temperature (warm in winter to spring, cold in late summer to fall) but also of dissolved oxygen (higher in fall, lower in spring). Latest available data, taken in months of May and November, thus representing spring and fall conditions, indicate that while the inner basin (located in Belle Bay) does exhibit lower DO concentration in spring than in fall, the outer basin does not. Considering the T-S characteristics, showing a rising in bottom temperature in November in the outer basin, and therefore indicating the onset of the warm, DO poor, MSW renewal season earlier than found in earlier studies, we interpret this result as due to a slightly longer residence time of the bottom waters in the inner basin (Belle Bay) than in the outer basin. Nevertheless, all considered, a yearly timescale for deep water renewal of both the outer and inner basin is probably the right order.

# DISCUSSION

## WATER STRUCTURE

Fortune Bay's seasonally stratified, three layered, water structure is typical of a deep fjord separated from the shelf by a sill (see Farmer & Freeland 1983, Inall and Gillibrand, 2010 and Cottier et al., 2010 for reviews). The temperature and salinity climate of the fjord and adjacent shelf presented in this study (Figure 2) highlights the result of 4 processes creating and destructing this seasonal stratification: atmospheric forcing, winter overturning convection, freshwater runoff and water exchange with the shelf.

The atmospheric forcing acts both as a stratification agent via solar radiation and as a mixing agent via wind stress. Thermal stratification starts in April and steadily increases until August after which the effect of atmospheric cooling and wind stress are indicated by a decrease in surface temperature and deepening of the isotherms. Surface temperature ranges from 0±1 °C (Feb-Mar) to 16±1 °C (Aug) while sub-surface (below 50 m depth) temperature stays below 2 °C for the most part of the year before increasing in late summer (September) by a few degrees due to important surface mixing and decreasing back to an homogeneous 2 °C or less in January. Vertical gradient of temperature in the surface layer (0-20 m) is thus maximum in August with a rate of decrease of 0.5-1 °C per meter (larger in BB and smaller in FB). Untangling the effect of wind forcing vs. surface cooling in mixing the water column is difficult since strong cooling (Air-Sea temperature difference >= 2 °C) occurs at the same time as strong wind forcing (mean wind speed of 9 m/s or more); that is: from November to March. Nevertheless, given the large loss of heat observed (order of 15 °C at the surface) and the extent of the vertical mixing (order of 200 m or more) we suspect this (convective overturning) process to play a substantial role. We note that, unlike high-latitude fjords, this convective process would be due to cooling effect solely as sea-ice, when present, is limited to small side bays and coves subject to freshwater runoff (thus, not associated with a brine rejection process).

Freshwater runoff effect is most visible in BB; as expected for it receives more than 2/3 of all the freshwater discharge flowing into Fortune Bay (110 $m^3$/s vs 160 $m^3$/s annual mean, respectively). Freshwater runoff peaks in April (280 $m^3$/s) and December (210 $m^3$/s) and is the lowest in Jul-Aug (80 $m^3$/s) (Figure 5); this is manifested by BB's near-surface salinity (upper 10 m) albeit with some phase delay. The lowest near-surface salinity of our climatology occurs in July, which suggests a slow propagation of the freshwater input from rivers mouths to the inner bay as a whole and/or reflects the combined effect of wind forcing (stronger from fall to spring) with summer heating on near-surface mixing (weaker in summer). We also observed an important interannual variability in river discharge (discharge peaked in May and February in 2015-16 vs. October and April in 2016-17; Figure 6) as well as in near-surface salinity (Jun-Sep values about 0.5 g/kg higher in 2016 than in 2015, Figure 6). Given the spatial reach of this latter variability (all sites affected about same way), it may have had more to do with shelf conditions (e.g. fresher in winter-spring 2015 or fall 2014) than from local river discharge, however. Important spatial variations between BB and FB and between FB and the shelf are also worth noting. While BB is characterised by a distinct and shallow (about 5-10 m depth) halocline present almost all-year round except from mid-winter to early spring (Feb-Apr), shelf waters show a clear seasonal cycle of higher salinity values (about 0.7 g/kg higher than BB within the upper 20 m, on average) with a much broader surface freshening occurring, gradually, over the upper 50 m from July to December (Figure 2). This 'freshwater pulse' is a well-known feature on the Newfoundland Shelf which takes its origin much further North from a combination of sea-ice melting, outflow from the

Baffin Bay and Hudson Strait and significant runoff from the Labrador coast (e.g. Loder et al., 1998). The pulse thus travels southwards with the Labrador Current and typically peaks in September at the long-term monitoring Station 27 located just offshore St John's (Myers et al. 1990). Assuming an advection rate of 0.1-0.2 m/s, a typical range given to the inner branch of the Labrador Current (e.g. Petrie and Anderson, 1983), this freshwater pulse should be seen about a month or two later in the vicinity of Fortune Bay (~450 km downstream of Station 27 when going into Placentia Bay and out; see Ma et al. 2012 for details on this bifurcation). The WOA climatological data presented here (south-eastern mouth of Fortune Bay) indicate a low in December (albeit without data in January, Figure 2 and Figure 5), suggesting a smaller advection rate; but our climatology of FB (Figure 2) does show a significant drop in surface and subsurface salinity values in October (thus, more consistent with this advection rate) as evidenced by the large deepening of the 32 isohaline (from about 30 m to 60 m). In BB, about the same magnitude drop of the 32 isohaline is seen about a month later, in November. The seasonal cycle of salinity differs also at depth (i.e. below 50 m) where a broad but distinct peak of salinity (S>32.5 g/kg) occurs from Jun-Dec on the shelf and is only apparent in September-October in both FB and BB; a much narrower period. This latter feature suggests an either limited advection of sub-surface water from the shelf to the fjord and/or important sub-surface mixing processes occurring within the fjord as previously reported by Hay and de Young (1989). The advective influence of the inner Labrador Current surface water on the other hand, seems to be limited to the outer part of the bay, for the most part, as illustrated by our SST climatology which shows a westward propagation of colder waters from May to November (Figure 4). Nevertheless, our recent observations of near-surface salinity within the bay do show an annual signal (of about 1-1.5 g/kg range) that is most likely related to the shelf variability (Figure 6). Taken all together, these different observations indicate that while the inner Labrador Current transport is the highest in winter and lowest in summer (Han, 2005, Han et al., 2008, Han et al. 2011, Wang et al. 2015 and Ma et al. 2016) and is of a sizeable amount of water (0.5-1 Sv upstream, offshore St John's, according to Ma et al. 2016), its influence on the water properties of Fortune Bay would be the highest during the summer-fall seasons and more important on the intermediate layer (50-150 m) than on the surface layer.

Overall, BB surface water appears to be directly affected by land-runoff and to slowly export its freshwater content during the summer before being subject to a significant vertical mixing in fall (Figure 2). In contrast, FB appears to be a transitional region affected both by input of freshwater from BB (in summer in particular) and by input from the shelf (in late summer-fall in particular). The background shelf water (S>31.5 g/kg) would thus be modified by the local forcing and mixing in FB, lowering its salinity (by increasing its freshwater content) within its surface layer and at intermediary depth. Interestingly, Fortune Bay (as a whole) is also noticeably warmer than the shelf at both surface and sub-surface levels (by about 2 °C and 1 °C, respectively) as evidenced by both our temperature and SST climatology (Figure 4) and this would suggest an either limited advection of the cold Labrador Current waters into the fjord again and/or the advection of warmer water going into (and mixing within) the fjord. While the difference of surface temperature may be due to the strongest haline stratification occurring in Fortune Bay (limiting vertical mixing at the surface and thus 'trapping' heat in the near-surface), the seasonal advection of deep MSW (below sill depth, in winter) described by Hay and de Young (1989) could be the source of warm water responsible for the difference observed at depth. Hay and de Young (1989) reported an increase of up to 2.7 °C at 420 m in winter (Dec-Jun) with peaks of 0.5-1 °C over 4 years of observations (Fig. 5 of their paper). A close look at our climatology points to a warming of the order of 1.4 °C below 300 m in FB, from a low of 0.1 °C in September to a high of 1.5 °C in April. As indicated by Hay and de Young (1989) the mixing of this

warm water within the basin (during cold LCW summer renewal, in particular) must be important given the weak stratification that is found in our monthly averaged profiles (a rise of temperature only discernible below 300 m) and it would explain the warmer, sub-surface, temperatures observed in our climatology of Fortune Bay vs. that of the shelf (Figure 2). Given the recent warming and deoxygenating trend of the MSW (Galbraith et al., 2021 and Blais et al., 2021) it is conceivable that the deep and intermediate waters of Fortune Bay would follow a similar slope; although certainly much less important than in the Gulf of St Lawrence given the input and opposite effect of the LCW. On the long-term, i.e. last 37 years (1982-2018), the near-surface temperature of Fortune Bay has risen at a rate of 0.04 °C/yr. This is large in comparison to the global rate of 0.01 °C/yr found for a similar period (1971-2010; IPCC 2014) but is comparable to recent estimates of the region (e.g. 0.04 °C/yr given by Belkin, 2009 for the Newfoundland-Labrador shelf from 1982 to 2006 and 0.06 °C/yr given by Galbraith and Larouche, 2013 for the NAFO region 3L -offshore St John's- from 1985 to 2012) and comparable to other areas such as the Mediterranean Sea (0.041 °C/yr) considered as a world 'hotspot' (Pisano et al., 2020). It should be noted that those estimates are sensitive to the period of observation as well as the dataset used/chosen; using the same period as that of Galbraith and Larouche (2013) the same trend (0.06 °C/yr) was found using our dataset. Nevertheless, and even at 0.04 °C/yr, the trend is substantial and can be expected to have important effects on the ecosystem. With this in mind, a monthly trend analysis was performed and indicated this recent warming to be driven up by summer months (July to November) which have warmed at a rate of up to 0.07 °C/yr (August) rather than by the winter months which show positive trends, nevertheless (0.03-0.04 °C/yr). This suggest that the probability for marine heatwaves may have increased but also that the probably for superchill events (i.e. subzero temperatures) may have decreased from 1982 to 2018; both conditions having negative effects on marine finfish aquaculture, for instance (Hargrave et al., 2005).

# MECHANICAL FORCING

Wind and tide (water level), the two main mechanical forces of coastal areas, were assessed statistically in this study to extract their main characteristics. Our results are consistent with previous studies (de Young, 1983 and Donnet et al., 2018a) describing a strong seasonality of the wind regime (strong, 10 m/s average, northwesterly dominant winds in winter and mild, 5 m/s average, southwesterly dominant winds in summer) and small tidal ranges for a coastal region (2 m spring tides; 1 m neap tides).

The strong wind seasonality in direction reminds that of the Western European shelf as a mirror image (so called 'SOMA' cycle; Pingree et al., 1999) and, as for the European shelf, has a strong influence on the shelf and slope currents; notably by modulating the inner Labrador Current flow (stronger in winter, milder in summer; Han, 2005). The region is dominated by succession of extra-tropical storms (cyclones) which are particularly strong in winter (Plante et al., 2015). Plante et al. (2015) showed that most cyclones endured in Newfoundland travel from the southwest and rapidly intensify as they travel along the eastern North American coast (due to their interaction with the ocean, warmer in winter). Interestingly, they also found that cyclones are as frequent in summer as in winter, though much less intense during the former (see their Fig. 1, in particular). Overall, they counted an average of 7 cyclones per winter and summer season (3 months) and 6 cyclones per spring and fall season; that is about 2 cyclones or more per month all year round (26 in total per year). Our persistence analysis, which considered a wind speed threshold of 10 m/s, indicates that a duration between 12 hr (49 events per year) to 18 hr (20 events per year) would be necessary to correspond to this cyclones frequency. Considering a cyclone growth and decay over a period

of about 4 days (Plante et al., 2015, Fig. 2) it appears that our 10 m/s threshold would correspond to the fully developed stage period of the typical storms occurring in the region.

Fortune Bay's water level variability is dominated by tidal fluctuation (96%) but residuals are large compared to the tidal range (±0.5 m setup/setdown; vs. 1-2 m tides). Our wavelet and band-pass filtering analyses of the water level indicate that those noticeable events are larger and occur more frequently from fall to spring and have associated periods of the order of 1-5 d. We attribute those events as the response to the frequent atmospheric disturbances occurring in the region which produce both local (inverse barometric) and remote effects (usually in the form of Continental Shelf Waves -CSW- as described in Tang et al., 1998, Thiebaut and Vennell, 2010, Han et al., 2012, Ma et al., 2015 and Bezaud et al., 2020). The influence of those sea-level variations on the circulation could be important and will require further investigations.

# OCEAN CURRENTS

Currents are characterized by along-shore pulses traveling cyclonically around the bay and associated with important downwelling and upwelling (order of tens of meters scale) as illustrated in Figure 12. An average of 28±3 pulses of 23±12 hr duration (ingoingor outgoing flow) and having excursion length of 10±7 km (ingoing or outgoing) occur in Fortune Bay per year. These pulses occur more frequently from September to December at most sites and affect most of the water column from 0 to 150 m (surface and intermediate layers). They appear also more frequently within the surface layer (0-20 m) along the northern and western shores from May to September (Figure S17). Given their frequency of occurrence, their scale (horizontal and vertical) and potential non-linearity (Figure S18), they may be an important source of transport within the bay.

Those pulses are well correlated within the bay, particularly from the northern to the western shore; suggesting efficient propagation of signals from the former to the latter (Figure S16). Lower correlation with the southern shore indicates that this part of the bay would be subject to other (or additional) processes, maybe influenced or induced by the shelf, or that signals either imported to or generated within the main basin would change characteristics (amplitude and phase) within the inner basin before traveling out. We found that the phase propagation speeds are on the order of 0.5-2 m/s, increasing from spring to early fall. These observations correspond relatively well with the 2-layer ocean theory of long internal wave propagation (e.g. Gill 1982, section 6.2) which gives a range of 0.4 m/s in spring to 1 m/s in summer with a 0.7 m/s value in fall using the hydrographic characteristics presented herein. These results resemble previous observations and modelling findings from two other large embayment of Newfoundland (Yao 1986, de Young et al. 1993 and Davidson et al., 2001; in Trinity Bay and Conception Bay – TB and CB, respectively, in Figure 1) which show the propagation of internal Kelvin waves along the coast of those bays during the stratified seasons. One can also note that the average number of pulses occurring in the bay corresponds to the average number of cyclones crossing the region (28 vs. 26, respectively), indicating a potential link between this regional atmospheric forcing and locally observed oceanic response which also be consistent with previous findings. This suggests regional similarities and importance of such processes on the coastal environment of Newfoundland (i.e. upwelling and downwelling propagation as long, coastally trapped, internal waves).

Compared to this 'regime of pulses' which is a part of the 2-20 d weather band, the tidal regime (0.5-1 d)

and mean circulation (>20 d) are rather weak. Mean tidal currents are about 3 cm/s and mean circulation is on the order of 1-5 cm/s. Statistically, mean pulses current speeds are about 12 cm/s (10 km excursion in 23 hr). In general, pulses are seen as currents of about 20 cm/s or more in any given timeseries that we have worked with in this study.

Consequently, tidal excursion is very small compared to, albeit more stochastic in nature, pulses excursion: 1.4 km using a maximum tidal current of 10 cm/s, an upper bound value, vs. 10±7 km for the pulses, on average. Evidences of internal tides were observed, on the other hand (Figure 12), which have been commonly reported as being an important process in fjords' interior waters mixing and preconditioning (e.g. for deep water renewal to take place; see Stigebrandt, 2012 for a review). Given the low level of energy at tidal and higher frequency bands observed in general, this process is unlikely to play a major role in Fortune Bay, however. Preconditioning is also not necessary for deep water renewal to occur in Fortune Bay due to its topographic and shelf's hydrographic particularities (three-basins system, see Hay and de Young, 1989 for details). Nevertheless, an understanding of the effect of this latter process on Fortune Bay's distinct interior water structure (compared to that of the shelf) would benefit from further investigations.

The results of the mean circulation presented in Figure 10 are puzzling. They show a near-surface outgoing flow across the whole bay and along nearly all the seasons. An homogenous outflow of brackish waters is expected from narrow fjords where the flow is constrained by lateral boundaries. Fortune Bay, however, is wide (15-25 km for the most part) and one would expect to see the effect of the rotation on the flow of that brackish surface layer, i.e. a deflection to the right on side of river(s) mouth(s). Since most of the freshwater input to Fortune Bay occurs in BB, along the northernshore (about 2/3 Fortune Bay's total) and along the southernshore (from the Burin Pennisula; the remaining 1/3) one would then expect a cyclonic circulation to take place on the near-surface. This near-surface cyclonic circulation might occur from spring to summer as indicated by inflows at F3B11, F3B08 and F3B04 when using all available data (Figure S15) but it remains uncertain due to insufficient data coverage. Perhaps even more surprisingly, the outflow across all sites monitored and seasons (fall to winter, in particular) is also apparent further at depth (70 m) suggesting a return flow present either deeper or in the middle of the bay (as volume conservation prescribes). Using all data available again, a sub-surface (70 m) return flow appears from fall to winter on the southern shore (F3B01&11), however. Likewise, the effect of the Labrador Current, which should appear as an inflow along the southershore is not visible, suggesting little influence of this otherwise major regional feature from the adjacent shelf on Fortune Bay's upper circulation. Deeper, at 135 m, the circulation appears cyclonic and more in line with previous knowledge and expectations, i.e. deep water inflow from the Saint-Pierre sill and from the Miquelon sill flowing northward and subject to earth rotation and topographic steering (de Young and Hay, 1987 and Hay and de Young, 1989). This deep influx could also account for the upper outflow.

# WATER EXCHANGES

Three main mechanisms of water exchange (flushing) between the inner and outer part of the bay were assessed, that is: barotropic tides, estuarine circulation and baroclinic pumping. Large ranges of flushing rate were found, reflecting both large uncertainties with the approaches as well as a strong seasonal variability (as reflected by the salinity climate). The effect of baroclinic pumping process appears to dominate the exchanges but this result should be tempered by the important limitations and assumptions involving the estimates. Hence, the method used to quantify the effect of baroclinic pumping process on water renewal is based on empirical data collected on the Norwegian shelf which may not be representative

of our region. As stated by Aure et al. (1996), the empirical coefficient β depends on the distribution of the (baroclinic) forcing frequency which is probably area-specific. For fjords wider than their internal Rossby radius, which is our case, they also state that the transport would be reduced. Perhaps more importantly, the method assumes complete advection and does not consider the effect of mixing efficiency (or lack of) nor that of a return flow which are both likely and which can be significant; particularly for short-term events such as illustrated in Figure 12. Finally, all the processes are very likely closely linked in the real world, as was demonstrated by MacCready et al. (2018) with the tidal and estuarine circulations. All together and since the Knudsen formulas provide with a net result from all the processes, they probably offer the most reliable estimates. Using those formulas and annual mean values of salinity and runoff, a complete flushing of the upper layers of Belle Bay is expected to take on the order of a few to several months (about 3-8 months).

# CONCLUSION

We provided a physical oceanography overview of Fortune Bay, a broad fjord located in mid-latitude (47.5 °N) on the southern shore of Newfoundland, a large island of eastern Canada's shores (Figure 1). Fortune Bay can be defined as a fjord for being a deep embayment, carved by glaciers and surrounded by a series of shallower sills (Fader et al., 1982). It can be qualified as 'broad' in the sense that it is wide (15-25 km) with respect to its internal Rossby radius (5-10 km), an horizontal scale of motion determining, for example, the extent of cross-shore coastal upwelling excursion.

In many regards, Fortune Bay is similar to higher latitude Arctic fjords: it is deep, broad, strongly stratified seasonally, probably subject to important winter convection overturning (although not saline) and to important exchanges with the shelf (particularly with respect to deep water renewal) and is dominated by wind forcing for processes such as surface and subsurface circulation and vertical mixing. However, Fortune Bay is notably different from Arctic fjords by its large absence of sea-ice processes, absence of katabatic winds (although similarly subject to strong along-shore winds from regional cyclonic activity) and by an influx of a cold intermediate water masse instead of a relatively warm one for many known Arctic fjords. In this sense, Fortune Bay could perhaps be defined as a 'broad, sub-Arctic fjord'. Two other important topographic characteristics distinguish Fortune Bay from other fjordic systems: it is 'semi-opened' to the coastal ocean, being surrounded by long sills (<100 m mean depth) and subject to renewal from two basins (reservoir) of very distinct water masses which greatly affect its renewal dynamics (e.g. limited to no need for 'preconditioning').

We investigated the seasonal cycle of its physical water structure (temperature and salinity) and of the forces acting upon it (freshwater input, tide and wind). These forces, in turn drive the motion of its waters. Special attention is given to the upper layers (above sill levels) circulation, by extracting and quantifying the main components (mean seasonal circulation, weather band, tidal band and high-frequency band) and describing what appear to be the dominant dynamics (qualified herein as 'pulses'). Previous studies on bottom water renewal are summarized and slightly extended using water profiles collected more recently. Estimates of water exchanges from the main processes identified and corresponding flushing times of the inner part of the bay, where the aquaculture activities occur, are also provided to get a quantitative sense of their importance. Limited attention was given to the long-term and interannual variability, largely due to lack of data to do it but also because the focus of this study was on what is likely to be the dominant cycle

(seasonal) and modes of variability (weather band). Yet, an estimate of recent sea-surface warming is provided which is both important in comparison with the global rate (factor 4) and characterized by a strong seasonality (factor 2 between the largest rate in summer and the lowest rate in winter).

From this study, it appears that wind forcing and baroclinic pumping, to which the wind certainly plays a role, are the dominant sources of currents variability and thus, possibly of water exchange within the fjord itself but also between the fjord and the shelf. Very similar processes have been reported in other large embayments of Newfoundland which suggest their potentially ubiquitous nature in the region. While we hope to fill an important knowledge gap of this interesting and economically important area, much remains to be elucidated. Most importantly, perhaps, will be to clearly identify the nature and origin of the current 'pulses', described herein, i.e. the physical process and the forcing responsible for their generation. The role of the wind as the main forcing mechanism and the ocean response time to this forcing need to be assessed more definitely, for instance, and this will be the focus of further studies. Given their importance to the ecosystem and aquaculture as well as fisheries activities occurring in this region, dedicated studies based on more elaborate methods such as box modelling or fully three dimensional modelling will also be needed to refine the first estimates of flushing provided herein.

# FUNDING

This research was supported by the Aquaculture Collaborative Research and Development Program (project #15-1-N-02).

# REFERENCES

Aure, J., Molvær, J., Stigebrandt, A., 1996. Observations of inshore water exchange forced by a fluctuating offshore density field. Marine Pollution Bulletin 33, 112–119. https://doi.org/10.1016/S0025-326X(97)00005-2

Belkin, I.M., 2009. Rapid warming of Large Marine Ecosystems. Progress in Oceanography 81, 207–213. https://doi.org/10.1016/j.pocean.2009.04.011

Bezaud, M., Lazure, P., Le Cann, B., 2020. Wind-induced barotropic oscillations around the Saint Pierre and Miquelon archipelago (North-West Atlantic). Continental Shelf Research 195, 104062. https://doi.org/10.1016/j.csr.2020.104062

Bisagni, J.J., Seemann, K.W., Mavor, T.P., 2001. High-resolution satellite-derived sea-surface temperature variability over the Gulf of Maine and Georges Bank region, 1993–1996. Deep Sea Research Part II: Topical Studies in Oceanography 48, 71–94. https://doi.org/10.1016/S0967-0645(00)00115-6

Blais, M., Galbraith, P.S., Plourde, S., Devred, E., Clay, S., Lehoux, C., Devine, L., 2021. Chemical and Biological Oceanographic Conditions in the Estuary and Gulf of St. Lawrence during 2020 (DFO Can. Sci. Advis. Sec. Res. Doc. No. 2021/060). https://waves-vagues.dfo-mpo.gc.ca/library-bibliotheque/41012008.pdf (accessed 26-Sep-2022)

Burchard, H., Bolding, K., Feistel, R., Gräwe, U., Klingbeil, K., MacCready, P., Mohrholz, V., Umlauf, L., van der Lee, E.M., 2018. The Knudsen theorem and the Total Exchange Flow analysis framework applied to the

Baltic Sea. Progress in Oceanography 165, 268–286. https://doi.org/10.1016/j.pocean.2018.04.004

Canadian Hydrographic Survey, 2022. Canadian Sailing Directions, Newfoundland, Southwest Coast (No. 2022/05). Fisheries and Oceans Canada. https://waves-vagues.dfo-mpo.gc.ca/Library/chs-shc-ATL103-eng-202205-41058070.pdf (accessed 26-Sep-2022)

Canadian Hydrographic Survey (CHS), 2021. Canadian Sailing Directions, General Information, Atlantic Coast (No. 12/2021). Fisheries and Oceans Canada. https://waves-vagues.dfo-mpo.gc.ca/Library/chs-shc-ATL100-eng-202112-4105457x.pdf (accessed 26-Sep-2022)

Canadian Ice Services (CIC), 2011. Sea Ice Climatic Atlas. East Coast 1981-2010. Environment Canada. https://publications.gc.ca/collections/collection_2013/ec/En57-38-2010-eng.pdf (accessed 26-Sep-2022)

Casey, K.S., Brandon, T.B., Cornillon, P., Evans, R., 2010. The Past, Present, and Future of the AVHRR Pathfinder SST Program, in: Barale, V., Gower, J.F.R., Alberotanza, L. (Eds.), Oceanography from Space. Springer Netherlands, Dordrecht, pp. 273–287. https://doi.org/10.1007/978-90-481-8681-5_16

Cottier, F.R., Nilsen, F., Skogseth, R., Tverberg, V., Skarðhamar, J., Svendsen, H., 2010. Arctic fjords: a review of the oceanographic environment and dominant physical processes. SP 344, 35–50. https://doi.org/10.1144/SP344.4

Courtier, A., 1939. Classification of tides in four types. The International Hydrographic Review.

Cyr, F., Larouche, P., 2015. Thermal Fronts Atlas of Canadian Coastal Waters. Atmosphere-Ocean 53, 212–236. https://doi.org/10.1080/07055900.2014.986710

Cyr, F., Snook, S., Bishop, C., Galbraith, P.S., Chen, N., Han, G., 2022. Physical oceanographic conditions on the Newfoundland and Labrador shelf during 2021 (DFO Can. Sci. Advis. Sec. Res. Doc. No. 2022/040). https://waves-vagues.dfo-mpo.gc.ca/library-bibliotheque/40960754.pdf (accessed 26-Sep-2022)

Davidson, F.J.M., Greatbatch, R.J., de Young, B., 2001. Asymmetry in the response of a stratified coastal embayment to wind forcing. J. Geophys. Res. 106, 7001–7015. https://doi.org/10.1029/2000JC900052

de Young, B., 1983. Deep water exchange in Fortune Bay, Newfoundland (MSc Thesis). Memorial University of Newfoundland, St. John's, NL. http://research.library.mun.ca/id/eprint/5754 (accessed 26-Sep-2022)

de Young, B., Hay, A.E., 1987. Density Current Flow into Fortune Bay, Newfoundland. J. Phys. Oceanogr. 17, 1066–1070. https://doi.org/10.1175/1520-0485(1987)017<1066:DCFIFB>2.0.CO;2

de Young, B., Otterson, T., Greatbatch, R.J., 1993. The Local and Nonlocal Response of Conception Bay to Wind Forcing. Journal of Physical Oceanography 23, 2636–2649. https://doi.org/10.1175/1520-0485(1993)023<2636:TLANRO>2.0.CO;2

DFO, 2016. State of Knowledge of the Oceanography and Water Exchange on the South Coast of Newfoundland to Support the Development of Bay Management Areas for Finfish Aquaculture (DFO Can. Sci. Advis. Sec. Sci. Advis. Rep. No. 2016/039). Fisheries and Oceans Canada. https://waves-vagues.dfo-mpo.gc.ca/library-bibliotheque/40595134.pdf (accessed 26-Sep-2022)

Donnet, S., Ratsimandresy, A.W., Goulet, P., Doody, C., Burke, S., Cross, S., 2018a. Coast of Bays Metrics: Geography, Hydrology and Physical Oceanography of an Aquaculture Area of the South Coast of Newfoundland (DFO Can. Sci. Advis. Sec. Res. Doc. No. 2017/076).

https://waves-vagues.dfo-mpo.gc.ca/library-bibliotheque/40654473.pdf (accessed 26-Sep-2022)

Donnet, S., Cross, S., Goulet, P., Ratsimandresy, A.W., 2018b. Coast of Bays seawater vertical and horizontal structure (2009-13): Hydrographic structure, spatial variability and seasonality based on the Program for Aquaculture Regulatory Research (PARR) 2009-13 oceanographic surveys (DFO Can. Sci. Advis. Sec. Res. Doc. No. 2017/077). https://waves-vagues.dfo-mpo.gc.ca/library-bibliotheque/40655945.pdf (accessed 26-Sep-2022)

Donnet, S., Lazure, P., Ratsimandresy, A., Han, G., 2020. A comprehensive oceanographic dataset of a subpolar, mid-latitude broad fjord: Fortune Bay, Newfoundland, Canada. Earth Syst. Sci. Data 12, 1877–1896. https://doi.org/10.5194/essd-12-1877-2020

Fader, G.B., King, L.H., Josenhans, H.W., 1982. Surficial geology of the Laurentian Channel and the western Grand Banks of Newfoundland. Ottawa, Canada: Fisheries and Oceans, Scientific Information and Publication.

Farmer, D.M., Freeland, H.J., 1983. The physical oceanography of Fjords. Progress in Oceanography 12, 147–219. https://doi.org/10.1016/0079-6611(83)90004-6

Galbraith, P.S., Chassé, J., Shaw, J.L., Dumas, J., Caverhill, C., Lefaivre, D., Lafleur, C., 2021. Physical Oceanographic Conditions in the Gulf of St. Lawrence during 2020 (DFO Can. Sci. Advis. Sec. Res. Doc. No. 2021/045). https://waves-vagues.dfo-mpo.gc.ca/library-bibliotheque/40980856.pdf (accessed 26-Sep-2022)

Galbraith, P.S., Larouche, P., 2013. Trends and variability in eastern Canada sea-surface temperatures., in: Aspects of Climate Change in the Northwest Atlantic off Canada, Can. Tech. Rep. Fish. Aquat. Sci. pp. 1–18. https://waves-vagues.dfo-mpo.gc.ca/Library/350208.pdf (accessed 26-Sep-2022)

Garrett, C., Munk, W., 1975. Space-time scales of internal waves: A progress report. J. Geophys. Res. 80, 291–297. https://doi.org/10.1029/JC080i003p00291

Garrett, C., Munk, W., 1972. Space-Time scales of internal waves. Geophysical Fluid Dynamics 3, 225–264. https://doi.org/10.1080/03091927208236082

Gillibrand, P.A., 2001. Calculating Exchange Times in a Scottish Fjord Using a Two-dimensional, Laterally-integrated Numerical Model. Estuarine, Coastal and Shelf Science 53, 437–449. https://doi.org/10.1006/ecss.1999.0624

Gillpatrick, W.W., Gibson, John, 1884. Newfoundland and Labrador: The Coast and Banks of Newfoundland, and the Coast of Labrador, from Grand Point to the Koksoak River, with the Adjacent Islands and Banks, U.S. Hydrographic Office. Government Printing Office, Washington.

Gregory, D.N., 2004. Climate : Une base de données d'observations de la température et de la salinité pour le nord-ouest de l'Atlantique (DFO Can. Sci. Advis. Sec. Res. Doc. No. 2004/075). Fisheries and Oceans Canada. https://waves-vagues.dfo-mpo.gc.ca/library-bibliotheque/284130.pdf (accessed 26-Sep-2022)

Grinsted, A., Moore, J.C., Jevrejeva, S., 2004. Application of the cross wavelet transform and wavelet coherence to geophysical time series. Nonlin. Processes Geophys. 11, 561–566. https://doi.org/10.5194/npg-11-561-2004

Han, G., 2005. Wind-driven barotropic circulation off Newfoundland and Labrador. Continental Shelf

Research 25, 2084–2106. https://doi.org/10.1016/j.csr.2005.04.015

Han, G., Lu, Z., Wang, Z., Helbig, J., Chen, N., de Young, B., 2008. Seasonal variability of the Labrador Current and shelf circulation off Newfoundland. J. Geophys. Res. 113, C10013. https://doi.org/10.1029/2007JC004376

Han, G., Ma, Z., Chen, D., deYoung, B., Chen, N., 2012. Observing storm surges from space: Hurricane Igor off Newfoundland. Sci Rep 2, 1010. https://doi.org/10.1038/srep01010

Han, G., Ma, Z., deYoung, B., Foreman, M., Chen, N., 2011. Simulation of three-dimensional circulation and hydrography over the Grand Banks of Newfoundland. Ocean Modelling 40, 199–210. https://doi.org/10.1016/j.ocemod.2011.08.009

Hargrave, B.T., Silvert, W., Keizer, P.D., 2005. Assessing and Managing Environmental Risks Associated with Marine Finfish Aquaculture, in: Hargrave, B.T. (Ed.), Environmental Effects of Marine Finfish Aquaculture, Handbook of Environmental Chemistry. Springer-Verlag, Berlin/Heidelberg, pp. 433–461. https://doi.org/10.1007/b136021

Hay, A.E., de Young, B., 1989. An oceanographic flip-flop: deep water exchange in Fortune Bay, Newfoundland. J. Geophys. Res. 94, 843. https://doi.org/10.1029/JC094iC01p00843

Inall, M.E., Gillibrand, P.A., 2010. The physics of mid-latitude fjords: a review. SP 344, 17–33. https://doi.org/10.1144/SP344.3

Inall, M.E., Nilsen, F., Cottier, F.R., Daae, R., 2015. Shelf/fjord exchange driven by coastal-trapped waves in the A rctic. J. Geophys. Res. Oceans 120, 8283–8303. https://doi.org/10.1002/2015JC011277

IOC, SCOR, IAPSO, 2010. The international thermodynamic equation of seawater – 2010: Calculation and use of thermodynamic properties (Manuals and Guides No. 56). UNESCO.

IPCC, 2014. Climate Change 2014: Synthesis Report. Contribution of Working Groups I, II and III to the Fifth Assessment Report of the Intergovernmental Panel on Climate Change. IPCC, Geneva, Switzerland. https://www.ipcc.ch/site/assets/uploads/2018/02/SYR_AR5_FINAL_full.pdf (accessed 26-Sep-2022)

Large, W.G., Pond, S., 1981. Open Ocean Momentum Flux Measurements in Moderate to Strong Winds. Journal of Physical Oceanography 11, 324–336. https://doi.org/10.1175/1520-0485(1981)011<0324:OOMFMI>2.0.CO;2

Lauzier, L.M., Trites, R.W., 1958. The Deep Waters in the Laurentian Channel. J. Fish. Res. Bd. Can. 15, 1247–1257. https://doi.org/10.1139/f58-068

Levine, M.D., Paulson, C.A., Briscoe, M.G., Weller, R.A., Peters, H., 1983. Internal waves in JASIN. Phil. Trans. R. Soc. Lond. A 308, 389–405. https://doi.org/10.1098/rsta.1983.0011

Loder, J.W., Petrie, B., Gawarkiewicz, G., 1998. The coastal ocean off northeastern North America: A large-scale view. The sea 11, 105–138.

Ma, Z., Han, G., Chassé, J., 2016. Simulation of Circulation and Ice over the Newfoundland and Labrador Shelves: The Mean and Seasonal Cycle. Atmosphere-Ocean 54, 248–263. https://doi.org/10.1080/07055900.2015.1077325

Ma, Z., Han, G., deYoung, B., 2012. Modelling Temperature, Currents and Stratification in Placentia Bay.

Atmosphere-Ocean 50, 244–260. https://doi.org/10.1080/07055900.2012.677413

Ma, Z., Han, G., Young, B., 2015. Oceanic responses to H urricane I gor over the G rand B anks: A modeling study. J. Geophys. Res. Oceans 120, 1276–1295. https://doi.org/10.1002/2014JC010322

MacCready, P., Geyer, W.R., Burchard, H., 2018. Estuarine Exchange Flow Is Related to Mixing through the Salinity Variance Budget. Journal of Physical Oceanography 48, 1375–1384. https://doi.org/10.1175/JPO-D-17-0266.1

McDougall, T.J., Barker, M., 2011. Getting started with TEOS-10 and the Gibbs Seawater (GSW) Oceanographic Toolbox (No. ISBN 978-0-646-55621-5). SCOR/IAPSO WG127.

McLellan, H.J., 1957. On the Distinctness and Origin of the Slope Water off the Scotian Shelf and its Easterly Flow South of the Grand Banks. J. Fish. Res. Bd. Can. 14, 213–239. https://doi.org/10.1139/f57-011

Myers, R.A., Akenhead, S.A., Drinkwater, K., 1990. The influence of Hudson Bay runoff and ice-melt on the salinity of the inner Newfoundland Shelf. Atmosphere-Ocean 28, 241–256. https://doi.org/10.1080/07055900.1990.9649377

Pawlowicz, R., 2010. What every oceanographer needs to know about TEOS-10 (The TEOS-10 Primer). Unpublished manuscript. Available at www. TEOS-10. org.

Pawlowicz, R., Beardsley, B., Lentz, S., 2002. Classical tidal harmonic analysis including error estimates in MATLAB using T_TIDE. Computers & Geosciences 28, 929–937. https://doi.org/10.1016/S0098-3004(02)00013-4

Petrie, B., Anderson, C., 1983. Circulation on the newfoundland continental shelf. Atmosphere-Ocean 21, 207–226. https://doi.org/10.1080/07055900.1983.9649165

Pingree, R.D., Sinha, B., Griffiths, C.R., 1999. Seasonality of the European slope current (Goban Spur) and ocean margin exchange. Continental Shelf Research 19, 929–975. https://doi.org/10.1016/S0278-4343(98)00116-2

Pisano, A., Marullo, S., Artale, V., Falcini, F., Yang, C., Leonelli, F.E., Santoleri, R., Buongiorno Nardelli, B., 2020. New Evidence of Mediterranean Climate Change and Variability from Sea Surface Temperature Observations. Remote Sensing 12, 132. https://doi.org/10.3390/rs12010132

Plante, M., Son, S.-W., Atallah, E., Gyakum, J., Grise, K., 2015. Extratropical cyclone climatology across eastern Canada. Int. J. Climatol. 35, 2759–2776. https://doi.org/10.1002/joc.4170

Poitevin, P., Lazure, P., Roy, V., Donnet, S., Chauvaud, L., 2022. The 18.6-year lunar nodal cycle may affect ecosystems on the Northwest Atlantic continental shelves. Journal of Marine Systems 235, 103783. https://doi.org/10.1016/j.jmarsys.2022.103783

Ratsimandresy, A.W., Donnet, S., Goulet, P., 2020. Identification of geographic zones of influence associated with surface circulation for Aquaculture Bay Management Area application. Journal of Marine Systems 204, 103291. https://doi.org/10.1016/j.jmarsys.2019.103291

Ratsimandresy, A.W., Donnet, S., Goulet, P., Bachmayer, R., Claus, B., 2014. Variation in the structure of the water column as captured by Slocum glider CTD and by CTD from a research vessel and assessment of internal waves, in: 2014 Oceans - St. John's. Presented at the OCEANS 2014, IEEE, St. John's, NL, pp. 1–10.

https://doi.org/10.1109/OCEANS.2014.7003283

Ratsimandresy, A.W., Donnet, S., Snook, S., Goulet, P., 2019. Analysis of the variability of the ocean currents in the Coast of Bays area (DFO Can. Sci. Advis. Sec. Res. Doc. No. 2019/008). https://waves-vagues.dfo-mpo.gc.ca/library-bibliotheque/40805116.pdf (accessed 26-Sep-2022)

Richard, J.M., 1987. The mesopelagic fish and invertebrate macrozooplankton faunas of two Newfoundland fjords with differing physical oceanography (MSc Thesis). Memorial University of Newfoundland. http://research.library.mun.ca/id/eprint/4196 (accessed 26-Sep-2022)

Richard, J.M., Haedrich, R.L., 1991. A comparison of the macrozooplankton faunas in two newfoundland fjords differing in physical oceanography. Sarsia 76, 41–52. https://doi.org/10.1080/00364827.1991.10413465

Saha, K., Zhao, X., Zhang, H.-M., Casey, K.S., Zhang, D., Baker-Yeboah, S., Kilpatrick, K.A., Evans, R.H., Ryan, T., Relph, J.M., 2018. AVHRR Pathfinder version 5.3 level 3 collated (L3C) global 4km sea surface temperature for 1981-Present. https://doi.org/10.7289/V52J68XX

Salcedo-Castro, J., Ratsimandresy, A.W., 2013. Oceanographic response to the passage of hurricanes in Belle Bay, Newfoundland. Estuarine, Coastal and Shelf Science 133, 224–234. https://doi.org/10.1016/j.ecss.2013.08.031

Stigebrandt, A., 2012. Hydrodynamics and circulation of fjords. Encyclopedia of lakes and reservoirs 327, 344.

Tang, C.L., Gui, Q., DeTracey, B.M., 1998. Barotropic Response of the Labrador/Newfoundland Shelf to a Moving Storm. Journal of Physical Oceanography 28, 1152–1172. https://doi.org/10.1175/1520-0485(1998)028<1152:BROTLN>2.0.CO;2

Thiebaut, S., Vennell, R., 2010. Observation of a Fast Continental Shelf Wave Generated by a Storm Impacting Newfoundland Using Wavelet and Cross-Wavelet Analyses. Journal of Physical Oceanography 40, 417–428. https://doi.org/10.1175/2009JPO4204.1

Verbrugge, N., Reverdin, G., 2003. Contribution of Horizontal Advection to the Interannual Variability of Sea Surface Temperature in the North Atlantic. J. Phys. Oceanogr. 33, 964–978. https://doi.org/10.1175/1520-0485(2003)033<0964:COHATT>2.0.CO;2

Wang, Z., Yashayaev, I., Greenan, B., 2015. Seasonality of the inshore Labrador current over the Newfoundland shelf. Continental Shelf Research 100, 1–10. https://doi.org/10.1016/j.csr.2015.03.010

White, M., Hay, A.E., 1994. Dense overflow into a large silled embayment: Tidal modulation, fronts and basin modes. issn: 0022-2402 52, 459–487. https://doi.org/10.1357/0022240943077055

Yao, T., 1986. The response of currents in Trinity Bay, Newfoundland, to local wind forcing. Atmosphere-Ocean 24, 235–252. https://doi.org/10.1080/07055900.1986.9649249

# The Physical Oceanography of Fortune Bay, an overview

**Supplementary Material**

Sebastien Donnet[1,4], Pascal Lazure[2], Andry Ratsimandresey[3] and Guoqi Han[1]

Published in Regional Studies in Marine Science 56 (2022), https://doi.org/10.1016/j.rsma.2022.102698

[1] Fisheries and Oceans Canada, Institute of Ocean Sciences, P.O. Box 6000, Sidney BC, V8L 4B2, Canada.

[2] Ifremer (French Research Institute for Exploitation of the Sea) Laboratoire d'Océanographie Physique et Spatiale, Centre Bretagne, ZI de la Pointe du Diable, CS 10070, 29280 Plouzané, France.

[3] Fisheries and Oceans Canada, Northwest Atlantic Fisheries Centre, 80 East White Hills Rd, St. John's NL, A1C 5X1, Canada.

[4] Université de Bretagne Occidentale, Ecole Doctorale N°598 Science de la Mer et du littoral, Brest, France.

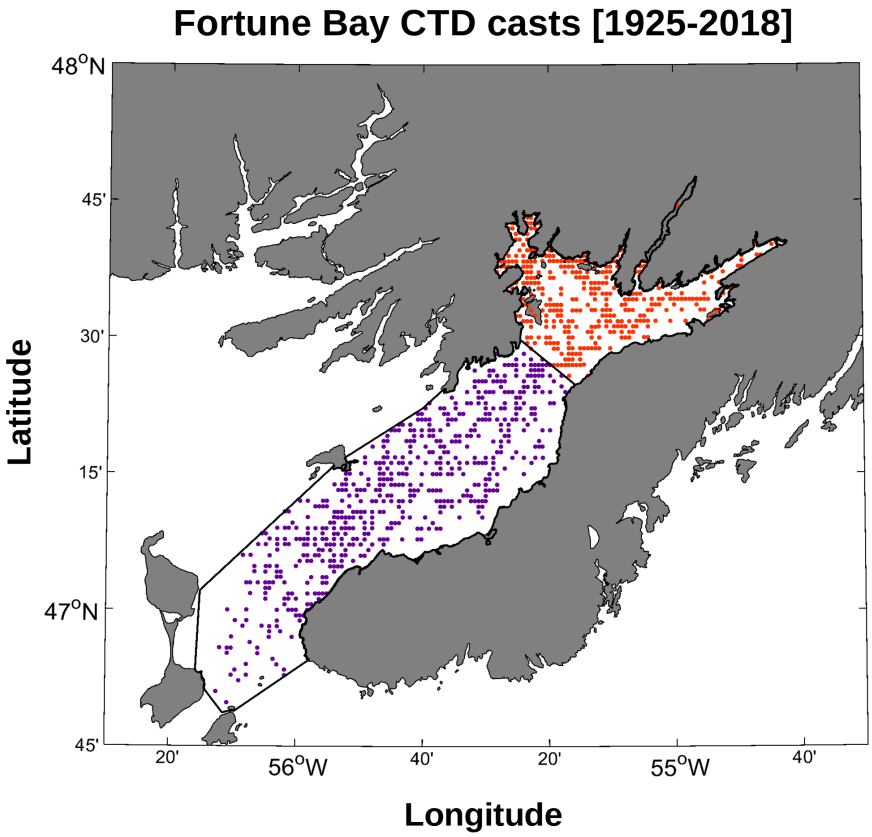


*Figure S1: available hydrographic profiles in Fortune Bay. The region is separated in two areas, BB (red dots) and FB (purple dots).*

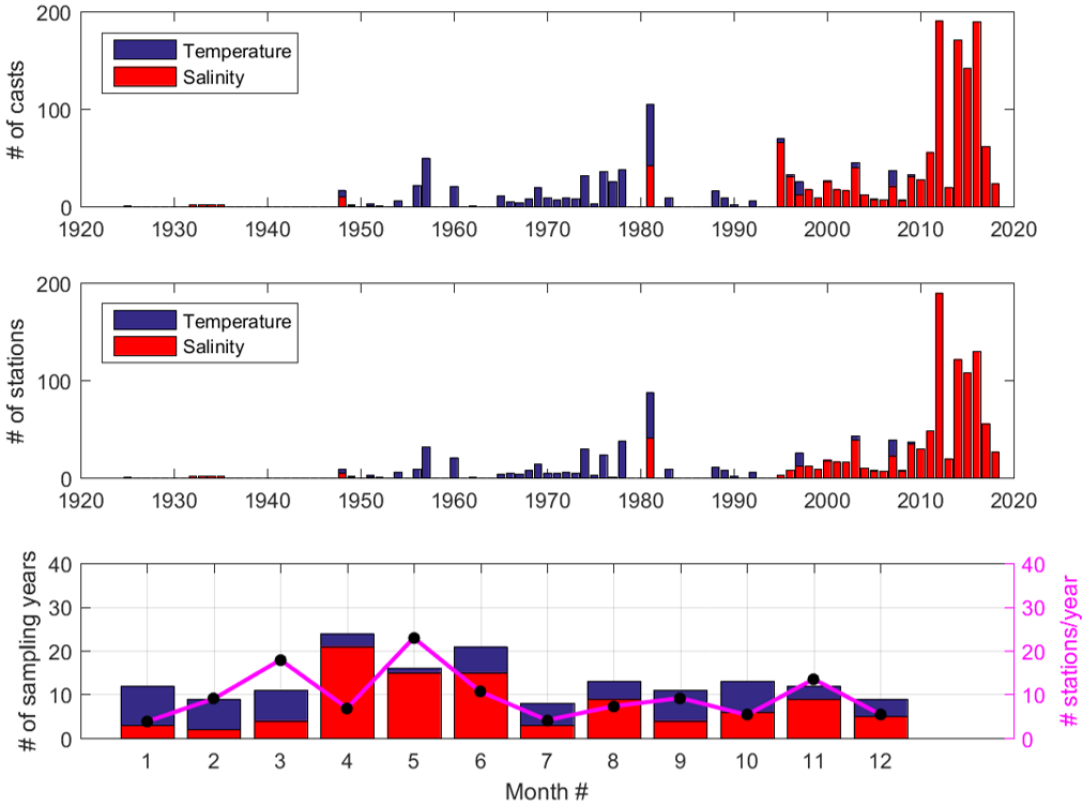


*Figure S2: available hydrographic profiles in Fortune Bay (as a whole). # of sampling years correspond to the number of years with at least 1 cast within the area of interest while (i.e. a measure of temporal coverage) # stations/year is average number of stations used per year for any given calendar month (i.e. a measure of spatial coverage).*

# LINEAR T-S RELATIONSHIPS

A linear regression analysis was performed on monthly Temperature-Salinity (T-S) diagrams to both derive T-S relationships allowing the determination of salinity from temperature data and study water masses. Illustrations of T-S relationship are given in Figure S3-S6 and a summary of the regression analysis is provided in Table S1 and Table S2. Up to 3 regressions were needed to fit the T-S scatters, varying from month to month and corresponding to the water masses observed for each month. The number of regressions, and depth ranges chosen to make them, were determined by visual inspection of inflection points; corresponding to changes in the seasonal stratification and deep water characteristics.

Overall, good fits ($R^2 > 0.7$) are found with the largest part of the water column for most months with enough data. Near-surface and near-bottom regions, however, have much more scattered values resulting in much lower correlations (e.g. Mar, Sep and Oct in both FB and BB). Poorly sampled months of Dec-Feb are either unknown (in FB) or not well resolved (in BB). July is also a month that has not been well sampled both with respect to time (Figure S2) and to space (no data in FB and limited range in BB).

The robustness of the regression analysis results was tested using data collected recently in the area during which CTD profiles were taken nearby oceanographic moorings equipped with thermistor lines (Donnet et al., 2020). Generally, while we found that the salinity profiles derived from thermistor lines compared reasonably well with the profiles taken by the CTD, the 'model' appears sensitive to the depth chosen for the 'inflection' points, i.e. the depths ranges, or layers, used to make the linear fits. This results in steps in the profiles derived from the regression (Figure S7). Overall, a mean difference of 0.15 g/kg with a mean standard deviation of 0.08 g/kg and RMS value of 0.17 g/kg was found between the 62 CTD and thermistors derived salinity profiles taken between May 2015 and May 2017.

The regression analysis also allows the examination of the seasonality of the surface layer and deep water mass and to infer on the latter's renewal processes described earlier. The presence of a well-defined intermediate layer between these two seasonally variable regions appears from June to September and is characterized by a T-S slope of about -0.1 g/kg/°C (note that a surface layer is not defined for the month of August in FB). Warmer and saltier conditions are found from March to June below 120 m in both FB and BB as illustrated in Figures S3&S5 and indicated by the positive T-S relationship slope in Tables S1&S2. Omitting the poorly sampled month of July (short profiles and discontinuity in the data at depth) these warm conditions seem to last until August in BB while a reversing (i.e. cooling) trend occur in FB that month (negative slope; Figures S4&S6). Colder (but still salty) conditions are thus found from August to October in FB before reversing back to a positive (warmer) trend again by November. In BB, no reversal is found before the end of the year though data are too poorly sampled in December to determine whether or not it would occur that month. This seasonal bottom water cycle is consistent with the previous studies (see Hay and de Young, 1989 in particular) that described inflow (bottom water renewal) of warm MSW during the winter (December to June) and inflow of cold LCW during the summer (May to December). The time-lag seen between FB and BB areas, BB lagging by about a month in T-S characteristics, may reflect the effect of the inner sills present between FB and BB (see Figure 1 and introduction of the main text); limiting the exchange of deep water below 210 m (depth of the deepest inner sill between the main deep basin of each area).

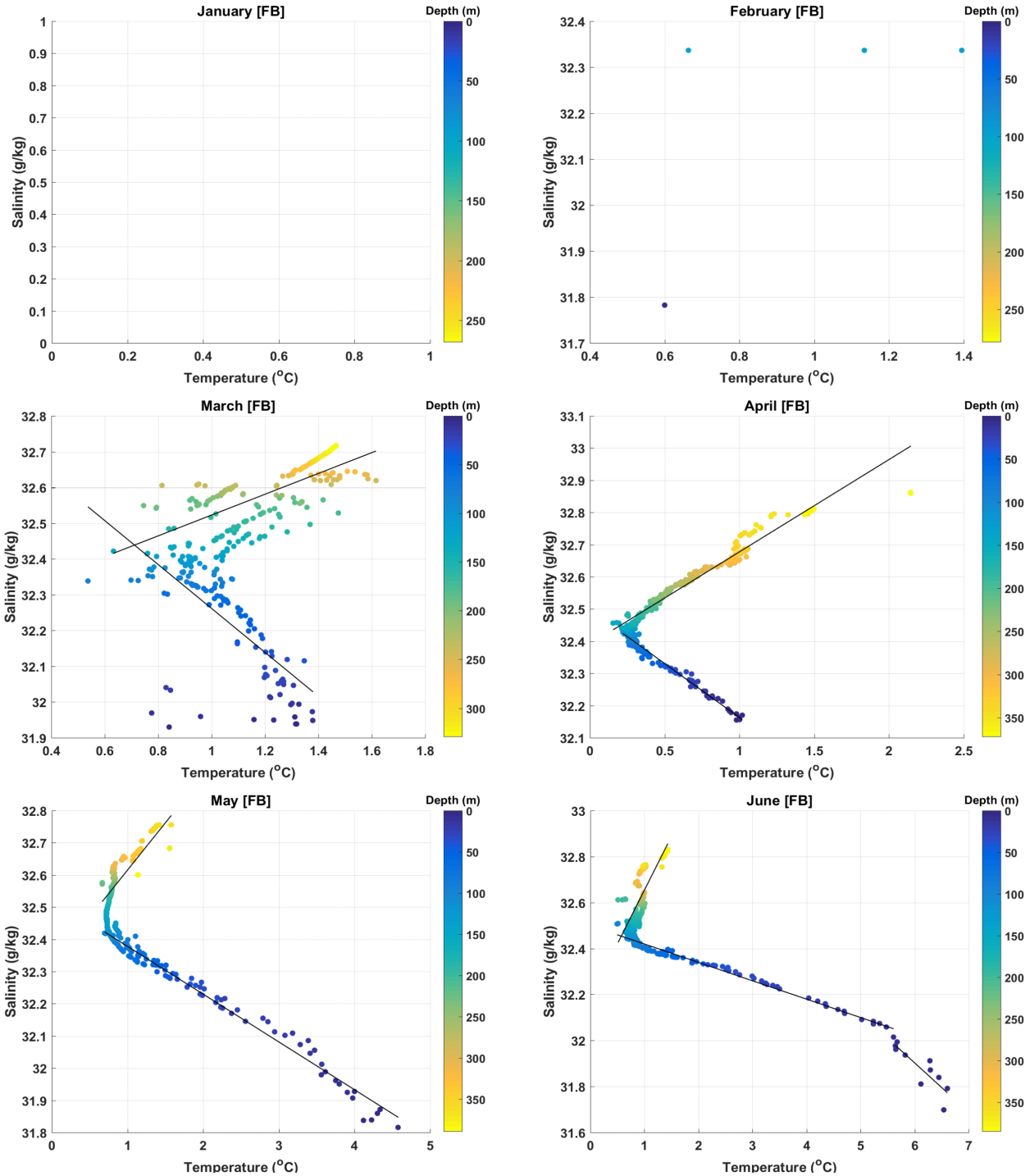


*Figure S3: Fortune Bay area (FB) T-S regressions (January to June). Linear regression lines are illustrated in black.*

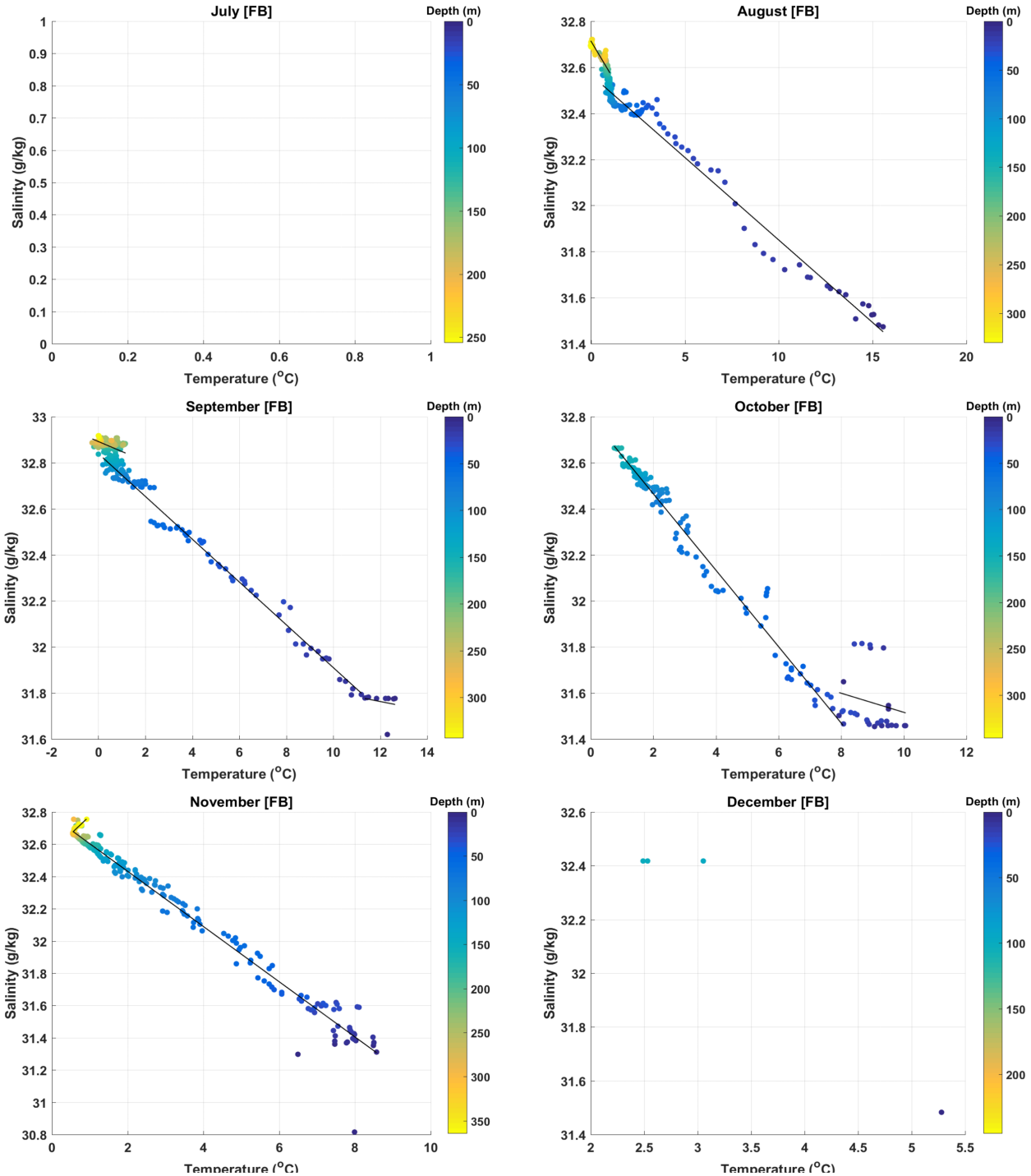


*Figure S4: Fortune Bay area (FB) T-S regressions (July to December). Linear regression lines are illustrated in black.*

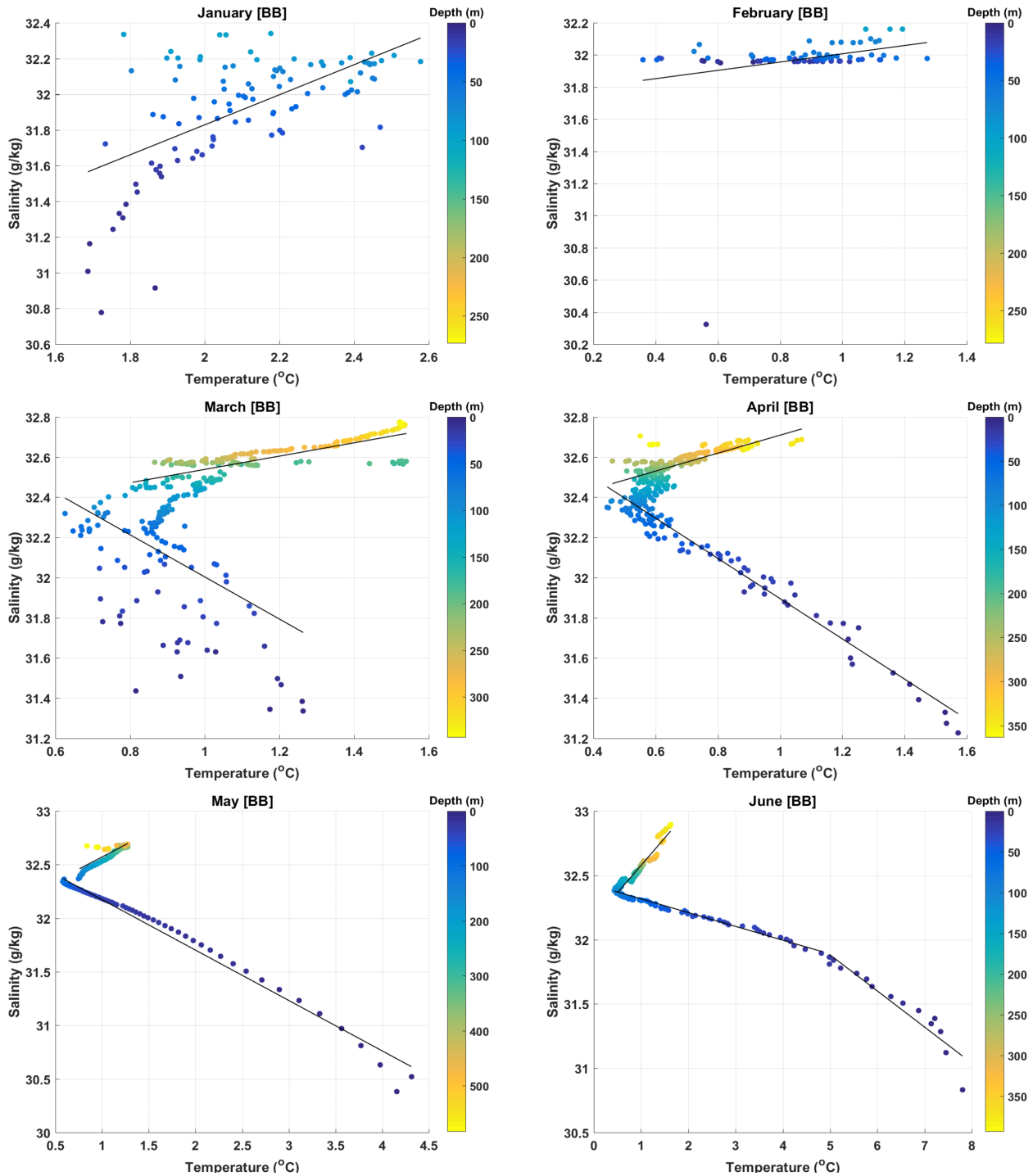


*Figure S5: Belle Bay area (BB) T-S regressions (January to Jun). Linear regression lines are illustrated in black.*

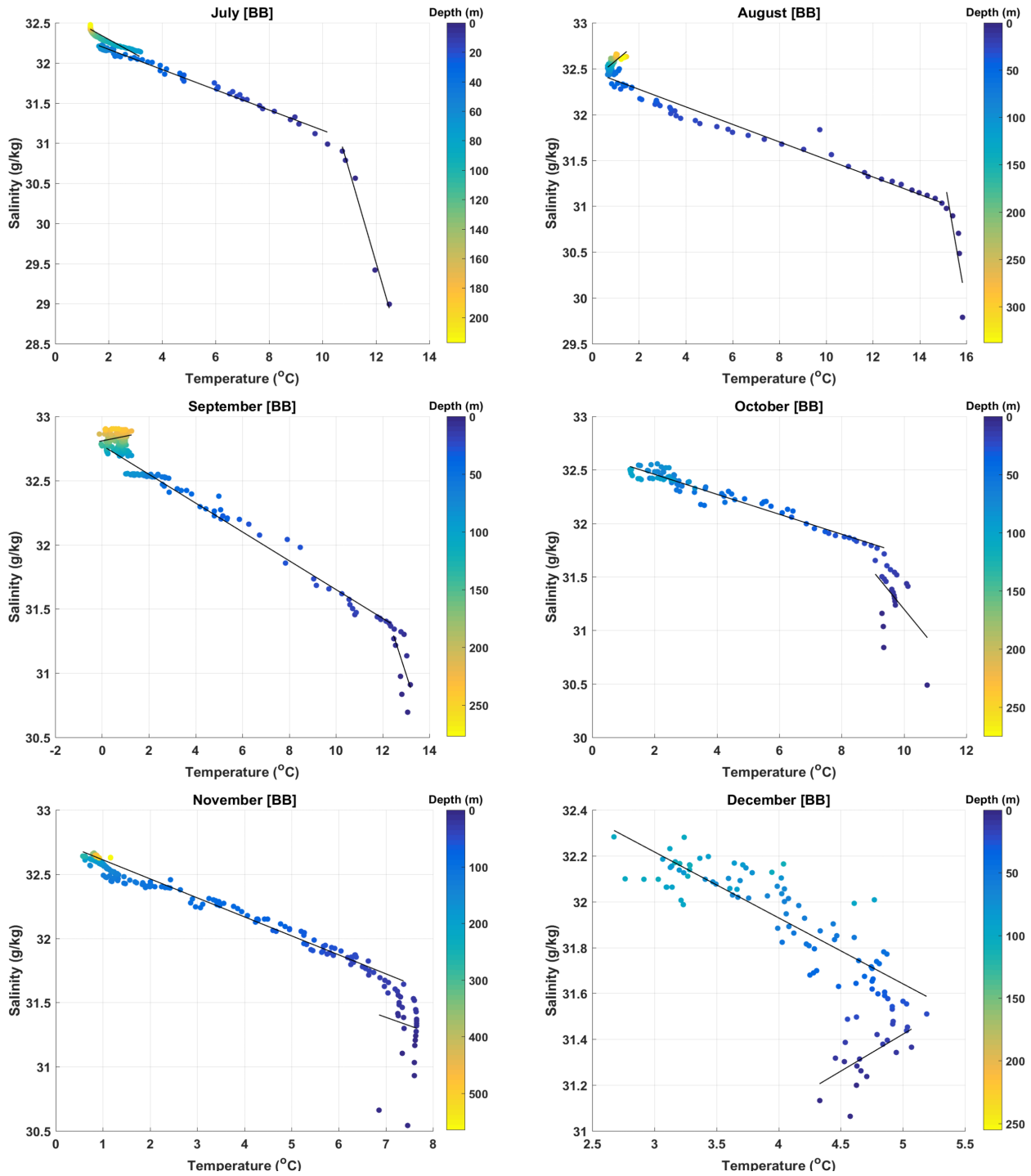


*Figure S6: Belle Bay area (BB) T-S regressions (July to December). Linear regression lines are illustrated in black.*

*Table S1: FB monthly climate T-S regressions summary. Highlighted in yellow are the regressions that should be used with caution and in red the ones that should not be used (no correlation). Salinity S = Slope x T + Intersect.*

| FB | Jan | Feb | Mar | Apr | May | Jun | Jul | Aug | Sep | Oct | Nov | Dec |
|---|---|---|---|---|---|---|---|---|---|---|---|---|
| **Surface Layer depth (m)** | N/A | N/A | 0-120 | 0-120 | 0-120 | 0-10 | N/A | 0-120 | 0-10 | 0-30 | 0-300 | N/A |
| **Slope** | N/A | N/A | -0.61 | -0.34 | -0.15 | -0.21 | N/A | -0.07 | -0.02 | -0.04 | -0.17 | N/A |
| **Intersect** | N/A | N/A | 32.88 | 32.5 | 32.53 | 33.19 | N/A | 32.57 | 32.1 | 31.93 | 32.77 | N/A |
| **$R^2$** | N/A | N/A | 0.50 | 0.97 | 0.98 | 0.75 | N/A | 0.98 | 0.04 | 0.03 | 0.98 | N/A |
| **Mid-Layer depth (m)** | N/A | N/A | N/A | N/A | N/A | 10-120 | N/A | N/A | 10-120 | N/A | N/A | N/A |
| **Slope** | N/A | N/A | N/A | N/A | N/A | -0.08 | N/A | N/A | -0.09 | N/A | N/A | N/A |
| **Intersect** | N/A | N/A | N/A | N/A | N/A | 32.5 | N/A | N/A | 32.84 | N/A | N/A | N/A |
| **$R^2$** | N/A | N/A | N/A | N/A | N/A | 0.98 | N/A | N/A | 0.99 | N/A | N/A | N/A |
| **Deep Layer depth (m)** | N/A | N/A | 120-max | 120-max | 120-max | 120-max | N/A | 120-max | 120-max | 30-max (160) | 300-max | N/A |
| **Slope** | N/A | N/A | 0.29 | 0.29 | 0.29 | 0.47 | N/A | -0.14 | -0.04 | -0.17 | 0.22 | N/A |
| **Intersect** | N/A | N/A | 32.23 | 32.39 | 32.32 | 32.19 | N/A | 32.71 | 32.89 | 32.8 | 32.55 | N/A |
| **$R^2$** | N/A | N/A | 0.50 | 0.96 | 0.62 | 0.55 | N/A | 0.69 | 0.21 | 0.98 | 0.81 | N/A |

*Table S2: BB monthly climate T-S regressions summary. Highlighted in yellow are the regressions that should be used with caution and in red the ones that should not be used (no correlation). Salinity S = Slope x T + Intersect.*

| BB | Jan | Feb | Mar | Apr | May | Jun | Jul | Aug | Sep | Oct | Nov | Dec |
|---|---|---|---|---|---|---|---|---|---|---|---|---|
| **Surface Layer depth (m)** | 0-max (100) | 0-max (100) | 0-120 | 0-120 | 0-120 | 0-15 | 0-5 | 0-5 | 0-10 | 0-20 | 0-30 | 0-20 |
| **Slope** | 0.84 | 0.26 | -1.05 | -1.00 | -0.47 | -0.28 | -1.14 | -1.46 | -0.56 | -0.36 | -0.13 | 0.32 |
| **Intersect** | 30.15 | 31.75 | 33.05 | 32.9 | 32.64 | 33.29 | 43.25 | 53.32 | 38.31 | 34.75 | 32.30 | 29.81 |
| **$R^2$** | 0.36 | 0.07 | 0.23 | 0.96 | 0.98 | 0.90 | 0.98 | 0.68 | 0.37 | 0.22 | 0.01 | 0.35 |
| **Mid-Layer depth (m)** | N/A | N/A | N/A | N/A | N/A | 15-120 | 5-70 | 5-70 | 10-130 | N/A | N/A | N/A |
| **Slope** | N/A | N/A | N/A | N/A | N/A | -0.11 | -0.13 | -0.10 | -0.11 | N/A | N/A | N/A |
| **Intersect** | N/A | N/A | N/A | N/A | N/A | 32.42 | 32.42 | 32.47 | 32.77 | N/A | N/A | N/A |
| **$R^2$** | N/A | N/A | N/A | N/A | N/A | 0.97 | 0.99 | 0.97 | 0.98 | N/A | N/A | N/A |
| **Deep Layer depth (m)** | N/A | N/A | 120-max | 120-max | 120-max | 120-max | 70-max (210) | 70-max | 130-max (240) | 20-max (100) | 30-max | 20-max (110) |
| **Slope** | N/A | N/A | 0.33 | 0.45 | 0.46 | 0.43 | -0.18 | 0.21 | 0.04 | -0.09 | -0.15 | -0.29 |
| **Intersect** | N/A | N/A | 32.21 | 32.26 | 32.12 | 32.15 | 32.66 | 32.37 | 32.81 | 32.64 | 32.76 | 33.08 |
| **$R^2$** | N/A | N/A | 0.66 | 0.56 | 0.66 | 0.92 | 0.87 | 0.51 | 0.08 | 0.95 | 0.97 | 0.76 |

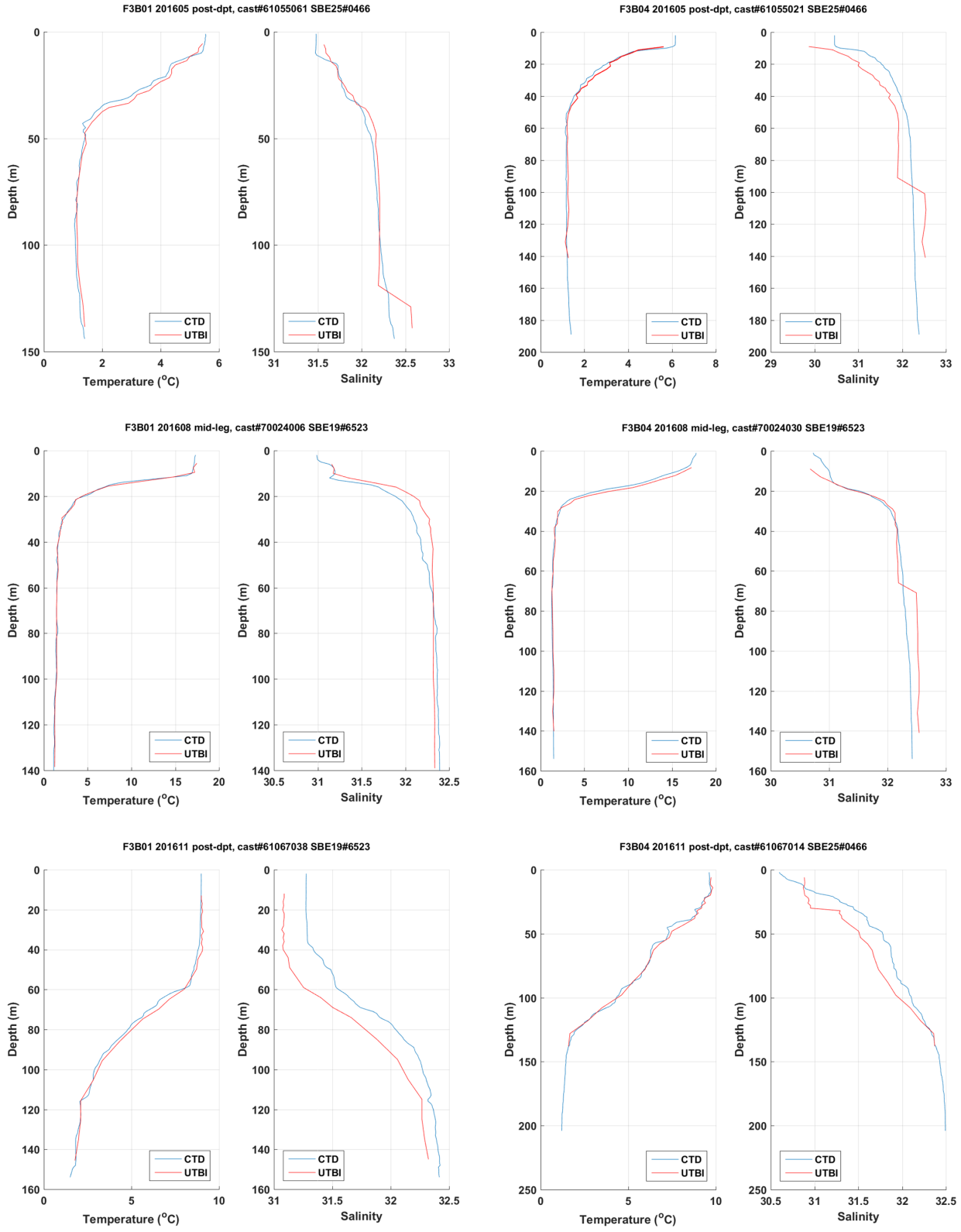


*Figure S7: CTD profiles (CTD) vs. moored thermistors (UTBI); UTBI salinity were calculated using the regression analysis results presented in Table S1&S2.*

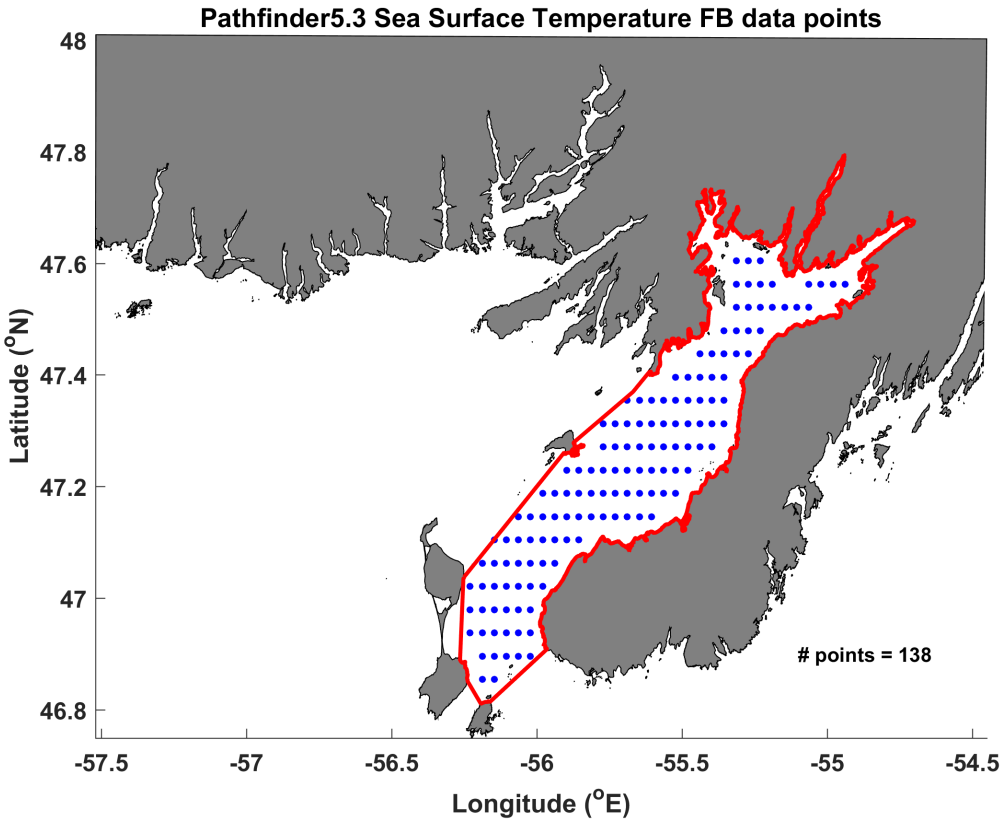


*Figure S8: Pathfinder v5.3 Sea Surface Temperature spatial coverage in Fortune Bay (FB).*

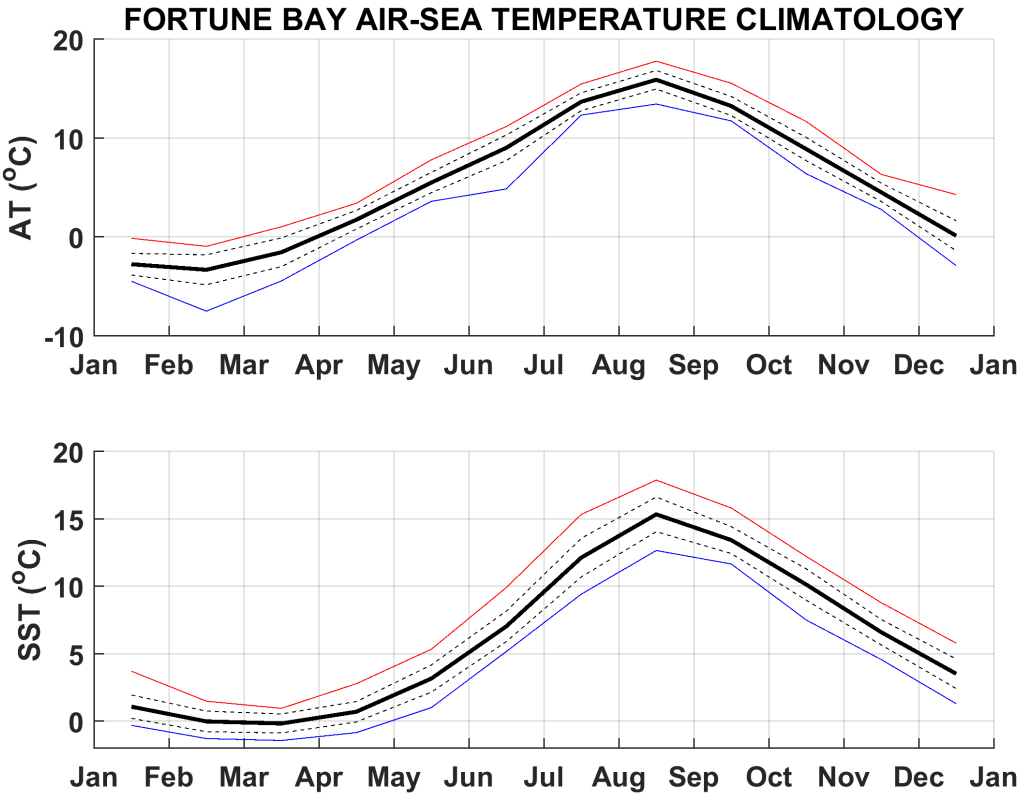


*Figure S9: air-sea temperature climate (AT and SST, respectively)*

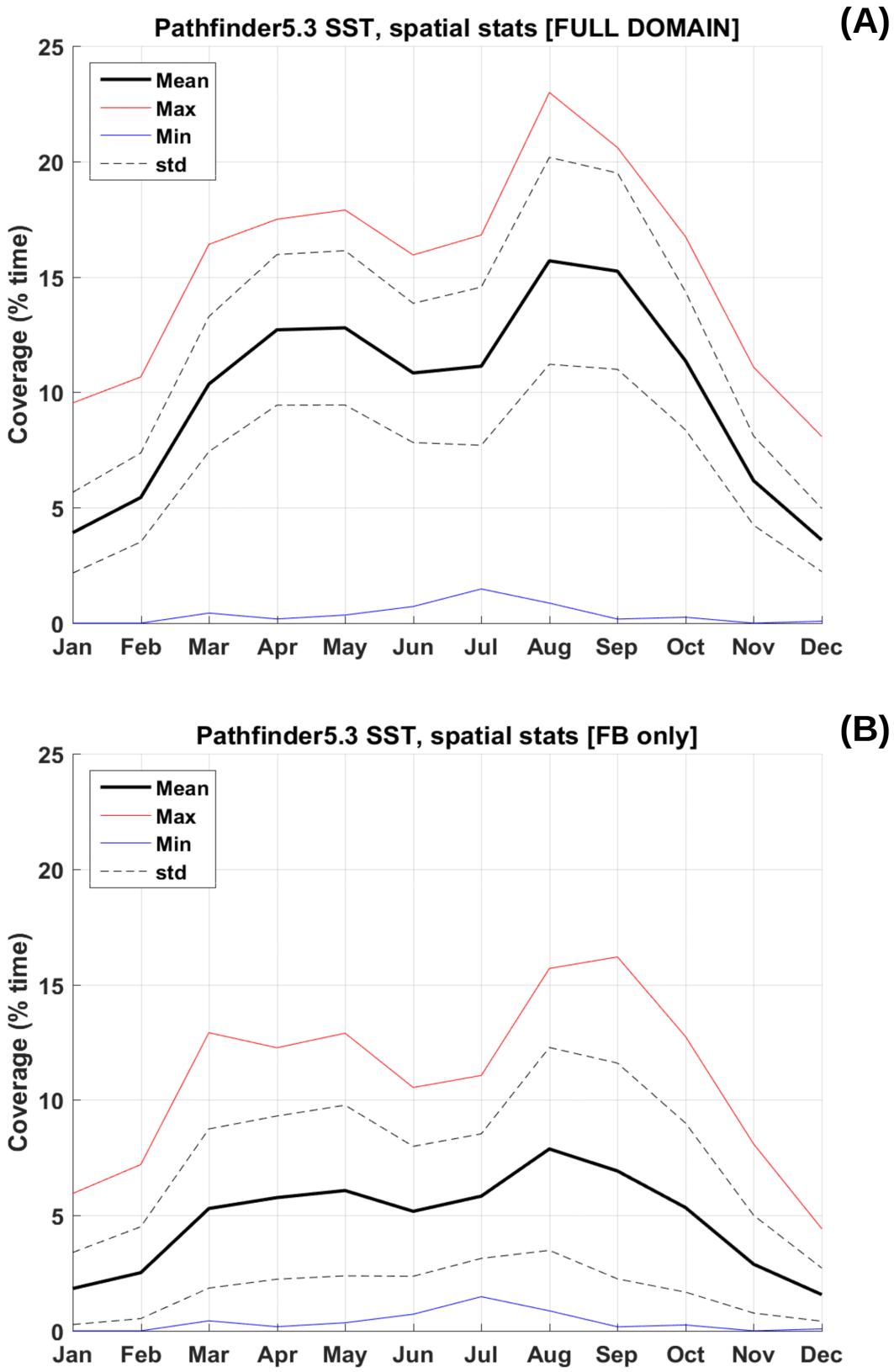


*Figure S10: Pathfinder v5.3 Sea Surface Temperature (SST) temporal coverage over the full domain considered in Figure 3 (main text) (A), i.e. 46.5 to 48 °N and 57.5 to 54.5 °W, and over Fortune Bay (FB) only (B). Statistics are calculated for the whole area considered, e.g. the mean is an average of the coverage over the area while the maximum is the maximum coverage found at one given point. The percentages are calculated as 100 x number of good SST values / number of samples (including bad or missing) for each point (or pixel).*

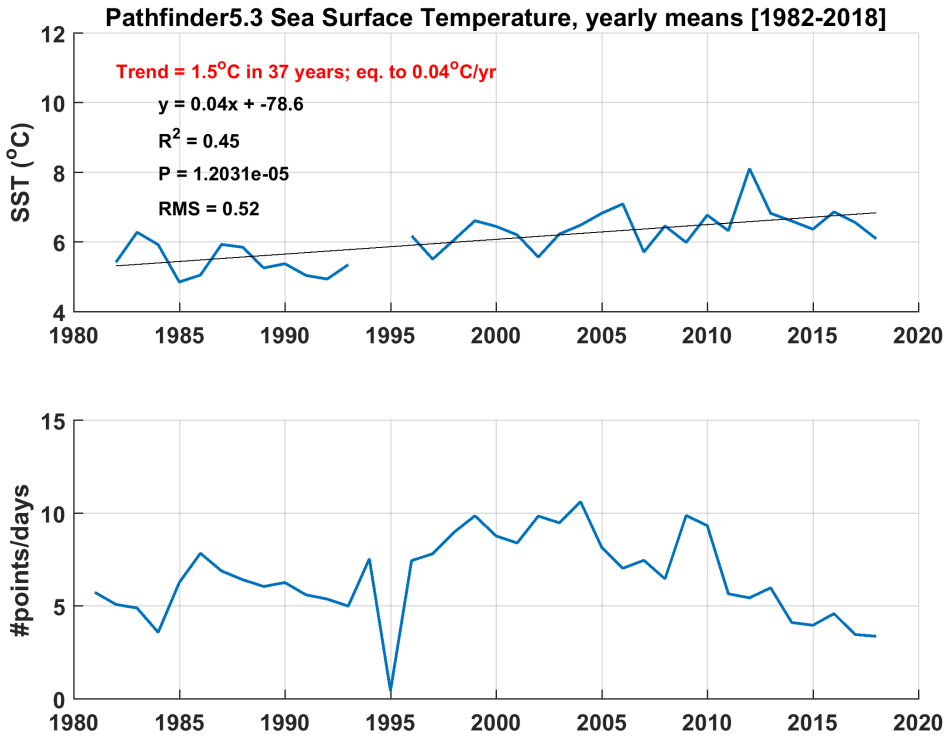


*Figure S11: Pathfinder 5.3 Sea Surface Temperature (SST) long term (1982-2018) trend and data coverage in Fortune Bay.*

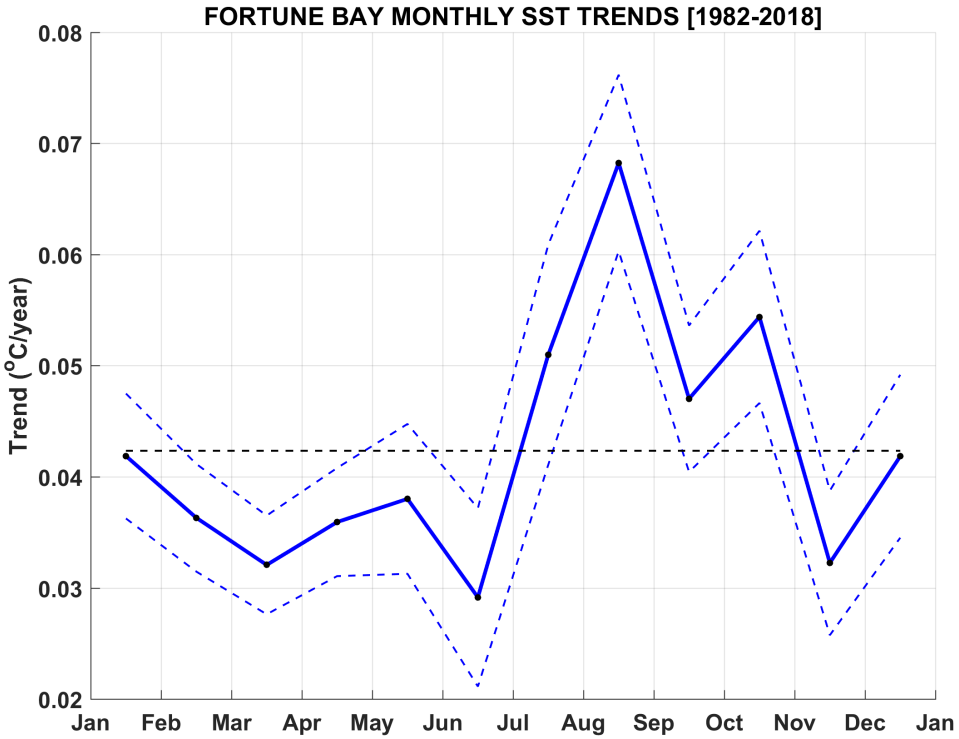


*Figure S12: Fortune Bay long-term Sea Surface Temperature monthly trends calculated over the period 1982-2018 from Pathfinder 5.3 data. The black horizontal dash line represent the annual mean trend as represented in Figure S11. The blue dashed lines represent the 68% confidence interval (about ±1 standard deviation).*

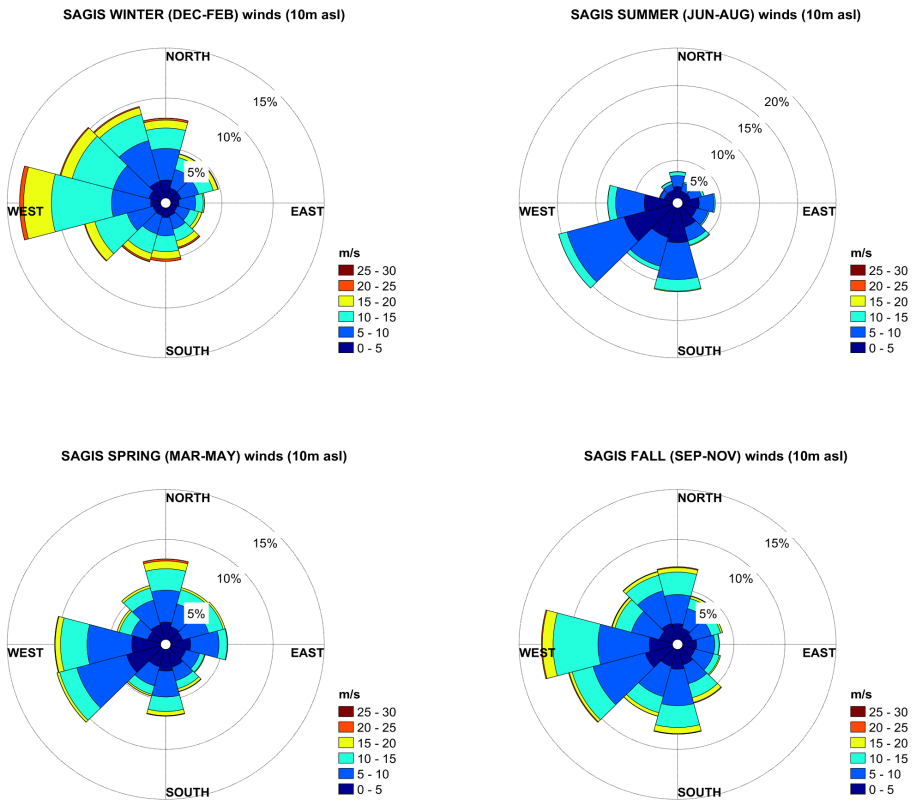


*Figure S13: seasonal wind climate from Sagona Island (SAGIS) at 10 m above sea level (asl).*

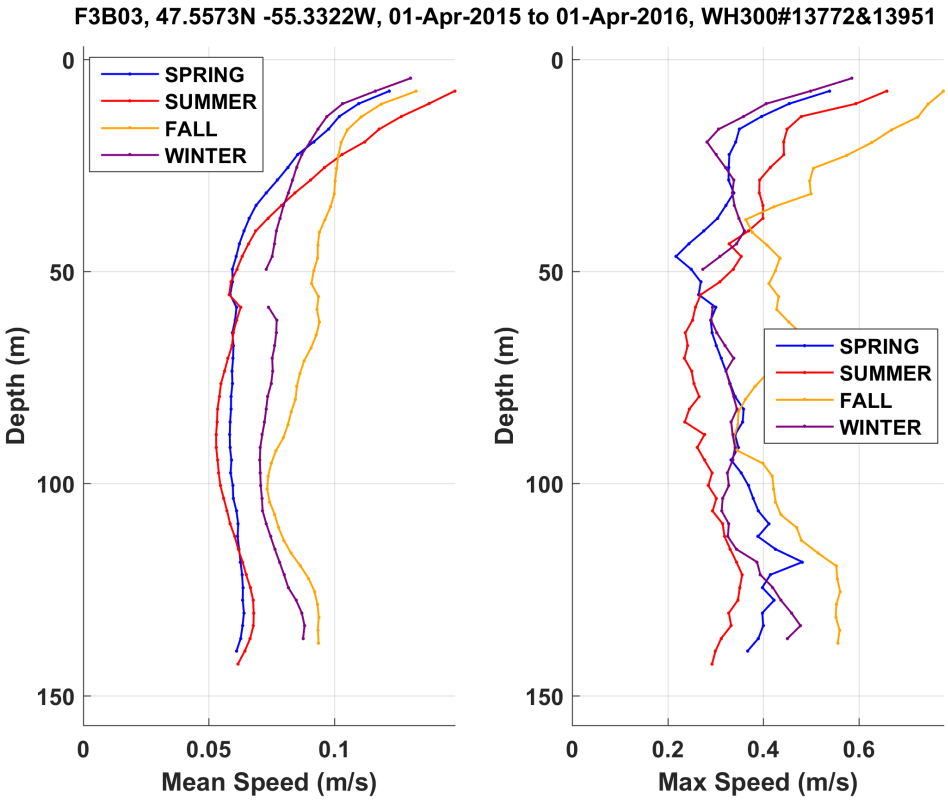


*Figure S14: time-averaged and maximum current speed profile as observed at F3B03 (west of Belle Bay mouth).*

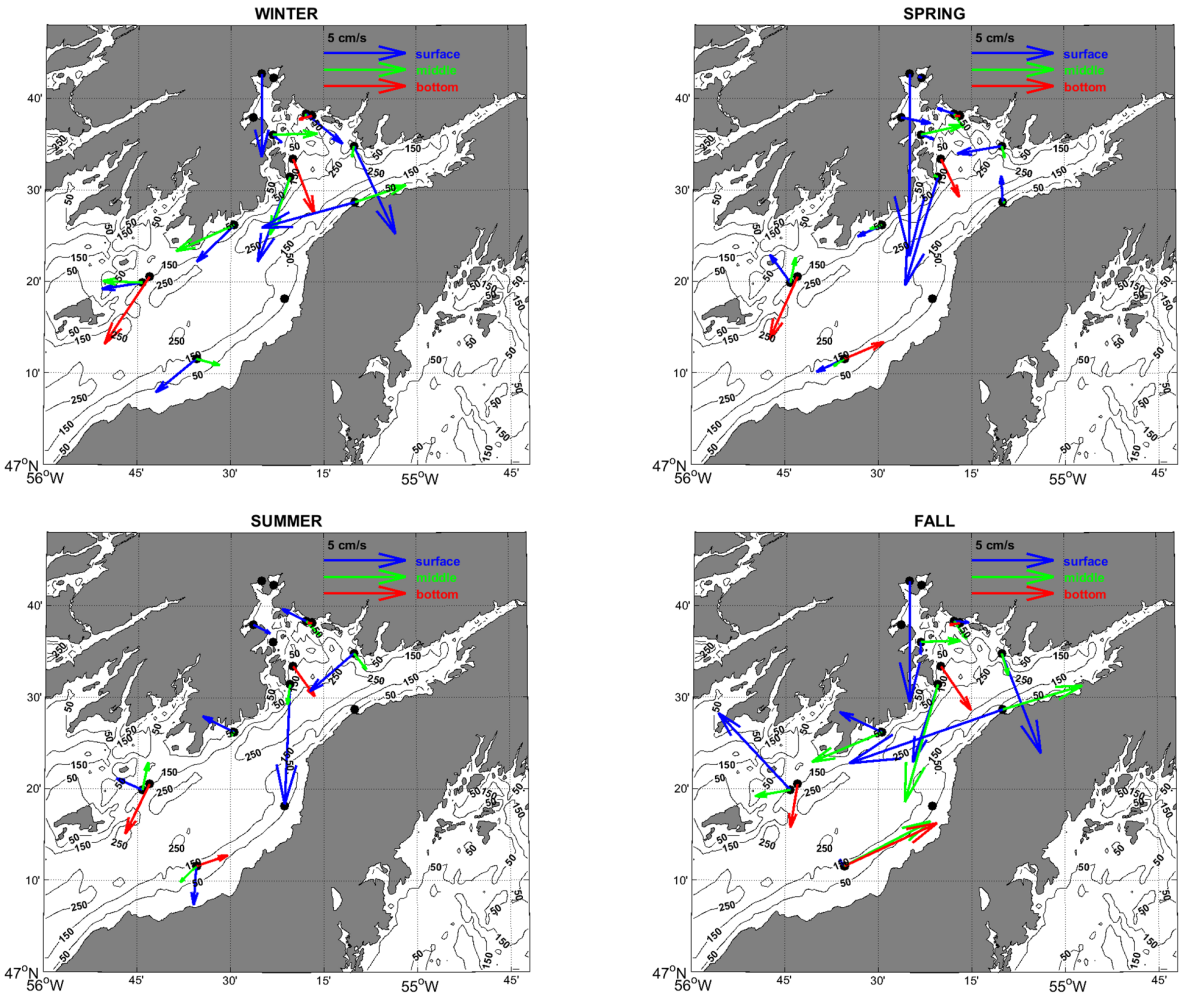


*Figure S15: mean, seasonal, circulation near-surface (10 m), middle (70 m) and near-bottom (135 m) layer. Scaling by a factor of 3 was applied to near-surface currents at F3B12 (winter) due to their much larger magnitude. All data available were used; resulting in shorter coverage at F3B08, 11 and 12 (see main text for details).*

# PULSES CROSS-CORRELATIONS

To quantify the relationship of the signals, lagged cross-correlation was performed amongst all sites. The 5 °C isotherm depth was selected to make the analyses as well as the currents' along-shore component at 3 depths (10, 70 and 135 m with year 1 data, 10, 40 and 70 m with year 2 data). Along-shore currents were band-pass filtered prior to analysis to use the dominant low-frequency 2-20 d band. 10, 20 and 30 d non-overlapping windows were used for all the runs set to look at maximum lags of 5-10 d (5 d with 10 d windows, 10 d with 20 d and 30 d windows). 816 runs were performed in total (including runs done on isotherms 2 °C, 4 °C, 6 °C and 8 °C before a final selection of the 5 °C isotherm) from which an example using year 1 data with 10 d windows and 5 d lags is presented in Figure S16. Isotherms correlations equal to or greater than 0.7, i.e. almost 50% variance explained, are found during the stratified period amongst most sites (Jun-Dec) while equivalent along-shore currents correlation levels are found amongst most sites and depths throughout the year. Correlations are markedly stronger and more consistent, however, amongst mooring pairs from F3B08 to F3B06 and are usually the lowest with F3B02; particularly with the isotherms. Near surface currents (10 m) tend to be more correlated during the stratified period while sub-surface currents (40, 70 and 135 m) can be correlated throughout the year. Window's size has a significant effect, generally decreasing the correlation levels when widening (except for the most strongly and frequently correlated sites such as F3B04-03). Strongest correlations generally occur at 0-4 d lags, giving phase speeds of the order of 0.5-2 m/s (when using along-slope distance between mooring pairs). Phase speeds tend to increase from spring to fall before tapering off in winter.

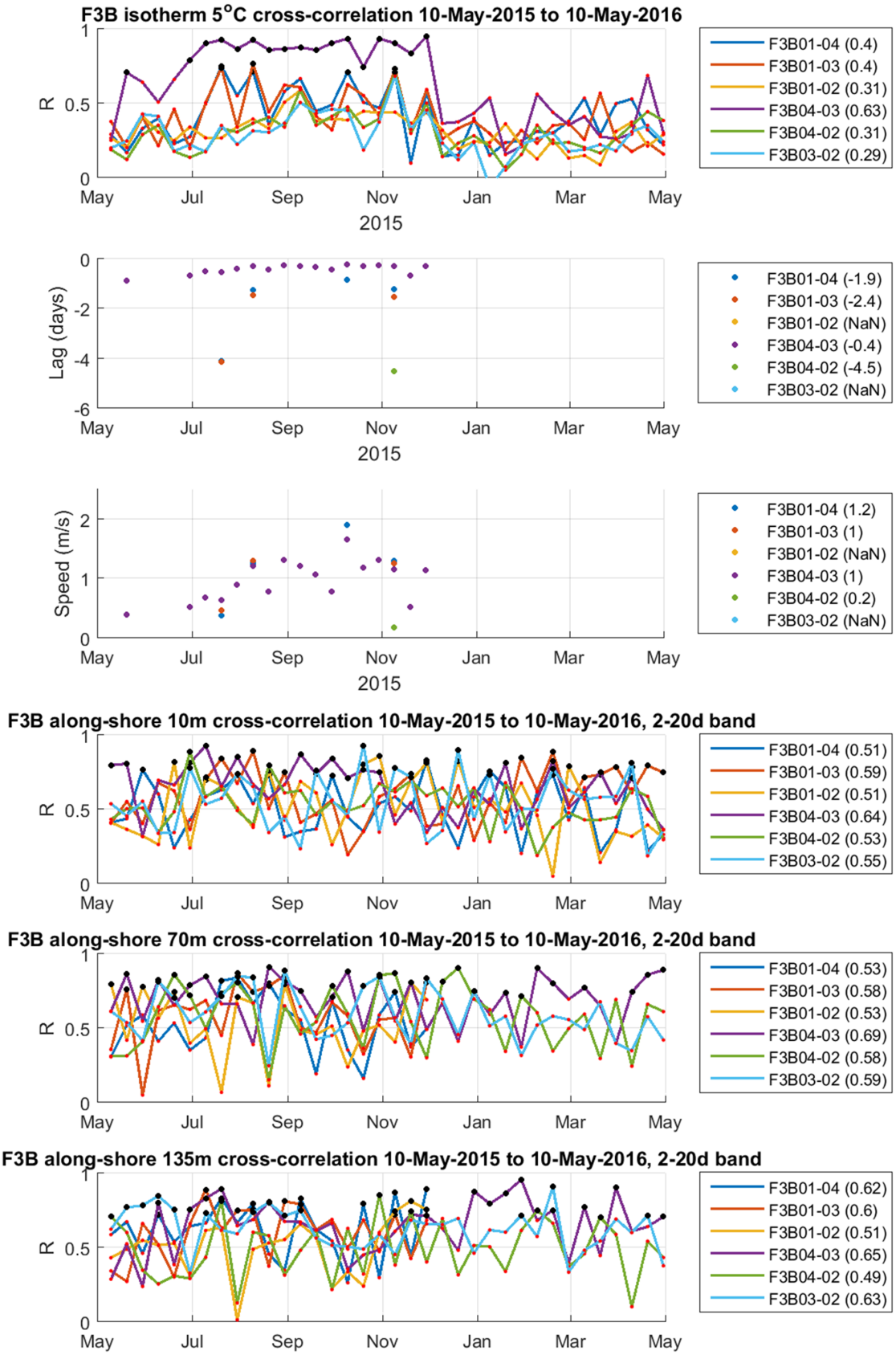


*Figure S16: lagged cross-correlation results. Correlations (R) correspond to the maximum positive correlation found within a given window (10 d length) and (associated) negative lags are shown; only lags and phase speed for correlation (R) >= 0.7 are shown in the isotherm plot. Black dots are values corresponding to correlations (R)>=0.7 and phase speeds >2 m/s are not shown. Mean values are indicated in bracket in the legends.*

# PULSES FREQUENCY OF OCCURRENCE, DURATION AND EXCURSION

To get a sense of the frequency of occurrence, duration and excursion associated with those pulses, extraction and persistence analyses were carried out on the along-shore currents, bandpass filtered for a 2-20 d period range as for previous analyses. Pulses were defined as periods of current speed larger than its mean + 1 std (calculated on the whole series length). Standard deviations were found to be about twice as large or more near-surface than near bottom for mean speeds of about the same magnitude (i.e. 1-8 cm/s). Extraction was done on both positive and negative components, representing ingoing flow at F3B01, 05, 11, 08 and 04 and outgoing flow at F3B07, 03, 06 and 02, respectively. For each pulse identified, its duration and associated excursion were extracted and persistence was calculated for durations of 6, 12, 24, 36 and 48 hr. Excursion (given in km) was calculated by integrating the speed over the duration of a pulse, in each direction (separately). Persistence analysis was run monthly and a maximum pulse duration was also calculated for each month. The analyses were conducted on all available series and depths observed. Overall, an average of 28±3 pulses per year were extracted at each monitored site and depth. Each pulse flows during 23±12 hr on average in either direction (ingoing or outgoing) and has an associated excursion of 10±7 km. A maximum pulse duration of 111 hr and a maximum excursion of 63 km were observed although maximums, at any given site, are on the order of 79±14 hr and 40±15 km on average. Seasonally, a peak of activity from September to December is revealed by the persistence analysis at most sites (see a representative example using a threshold of 24 hr on year 1 dataset in Figure S10). During the peak activity period, 3-6 pulses of 24 hr duration or more (in either direction) can occur at any given site (and depth) per month (i.e. about 1 event of 48 hr duration every 5-10 d). It should be noted that while pulses occurrence, duration and excursion are statistically equivalent in either direction, i.e. in terms of annual means, standard deviations and maximums, they are not necessarily symmetrical on a case by case basis. Taking the examples shown in Figure 12 for instance, representative of strong events, a net transport of more than 15 km can occur at any given depth after a few pulses (Figure S18). This asymmetry can be ‘balanced’ when integrating over depth (e.g. F3B03 & 04 in October 2015) but can also result in a net transport in either direction when integrating all (e.g. F3B01 in October 2015) or a portion of the water column only (e.g. F3B03 in July 2016; which is a site of 160 m depth).

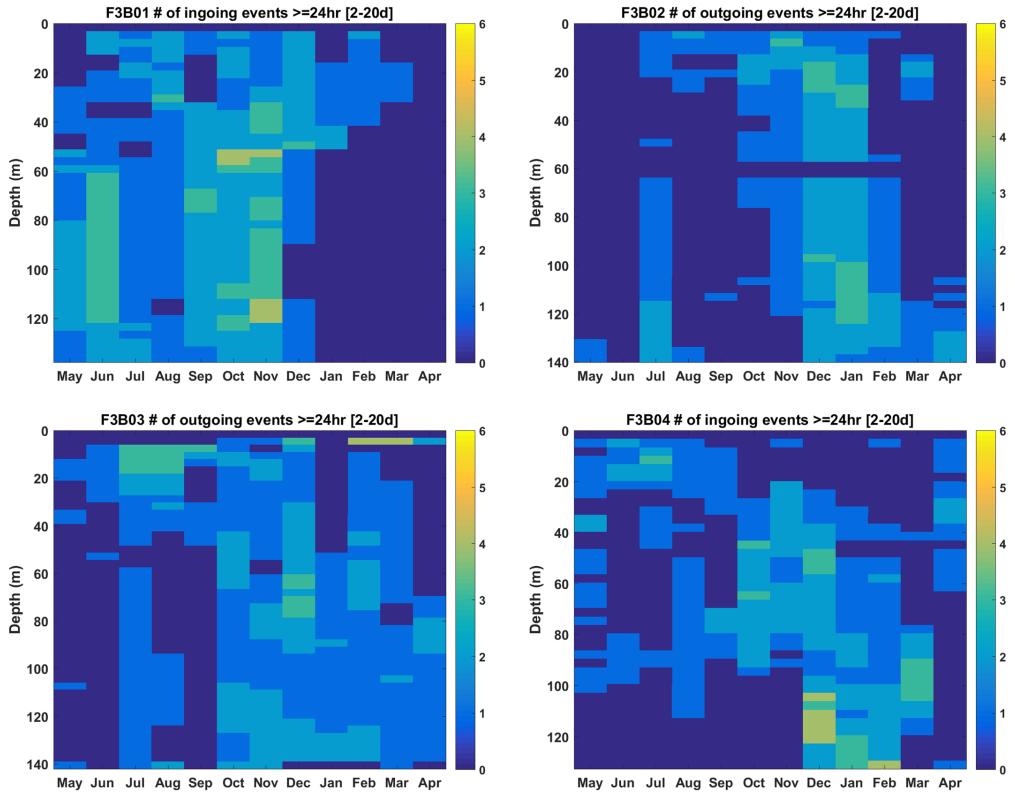


*Figure S17: frequency of occurrence of along-shore current pulses of 24 hr duration or more (in one direction) within the bay in 2015-16.*

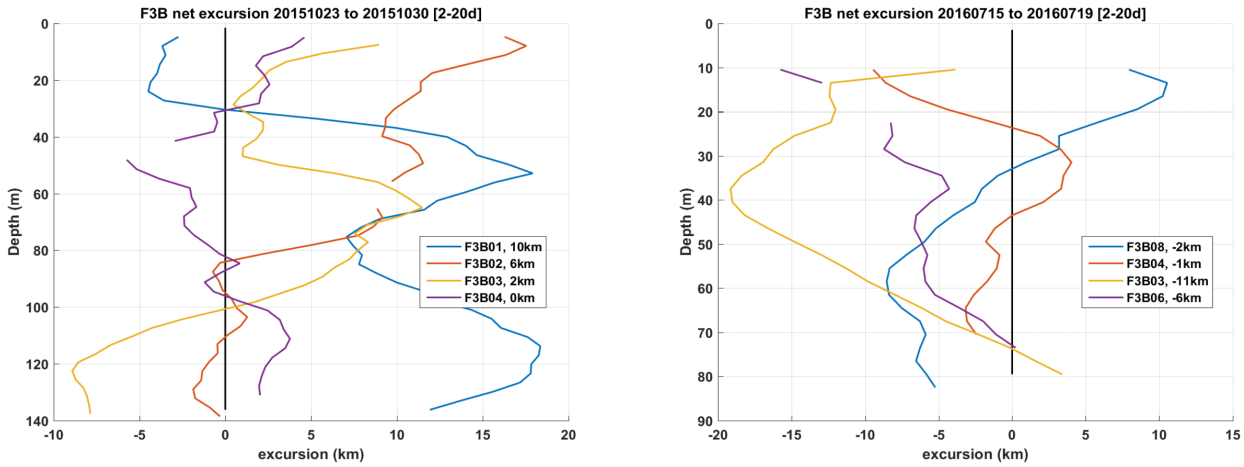


*Figure S18: net excursion of water induced by the events represented in Figure 12 (main text). The distances are calculated over a period of 7 days (3 pulses) in October 2015 (left) and 4 days (1 pulse) in July 2016 (right), shifting the start of the integration for each site to account for the phase delay (e.g. 1 d between F3B01 and F3B04 in October 2015; see main text for more details). The depth-averaged value of each profile is indicated in the legend.*

# CHAPTER 3: WIND RESPONSE

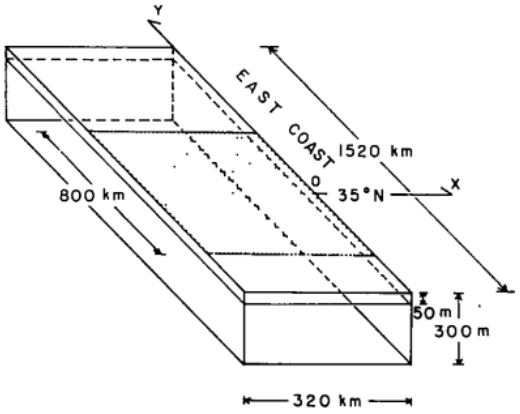


Fig. 2. Schematic view of the model ocean basin for case A. Shadow zone indicates the forced region by $\tau_y$.

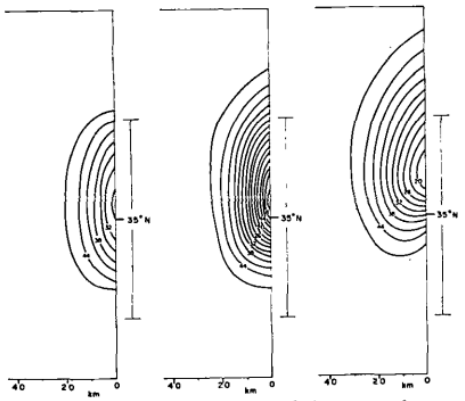

Fig. 7. Sequential patterns of the upper layer thickness in m, from left to right after 3, 6, and 9 days. Contour line of 50 m is not drawn, because the pattern is chaotic due to the presence of the inertio-gravity waves.

*Results from one of the earliest attempts to numerically model the onset, and propagation, of an upwelling; i.e. a wind response of a coastal ocean. Note the northward propagation of the upwelling region during and after applying a longitudinally variable wind (region illustrated in Fig 2), blowing southward for a duration of 6 days.*

*Source: Suginohara, N., 1974. Onset of coastal upwelling in a two-layer ocean by wind stress with longshore variation. Journal of the Oceanographical Society of Japan 30, 23–33. https://doi.org/10.1007/BF02112888*

# Internal Kelvin waves in a broad, mid-latitude fjord

Sebastien Donnet[1,4], Pascal Lazure[2], Andry Ratsimandresey[3] and Guoqi Han[1]

To be submitted to Journal of Geophysical Research: Oceans

[1] Fisheries and Oceans Canada, Institute of Ocean Sciences, P.O. Box 6000, Sidney BC, V8L 4B2, Canada

[2] Ifremer (French Research Institute for Exploitation of the Sea) Laboratoire d'Océanographie Physique et Spatiale, Centre Bretagne, ZI de la Pointe du Diable, CS 10070, 29280 Plouzané, France

[3] Fisheries and Oceans Canada, Northwest Atlantic Fisheries Centre, 80 East White Hills Rd, St. John's NL, A1C 5X1, Canada

[4] Université de Bretagne Occidentale, Ecole Doctorale N°598 Science de la Mer et du littoral, Brest, France.

## ABSTRACT

Broad embayment, such as some Fjords, can host the generation and propagation of internal Kelvin waves should the ratio of their stratification level to shelf-slope width, commonly called "Stratification parameter" or "Burger number", be important (i.e. >>1). A number of high latitude fjords fall under that category and were recently investigated in relation to heat exchange with neighbouring shelf waters (and consequent rapid melting of glacial ice). Here, we report on such a process in a broad, mid-latitude, fjord where the upper-layer dynamics are dominated by sub-inertial baroclinic motions. This fjord is of particular interest due to recent development of the aquaculture industry and to being historical fishing grounds. Using a fully non-linear, three-dimensional primitive equation numerical model we show that the large majority of the thermocline vertical fluctuations (80%) and much of the along-shore currents (50%) can be reproduced with a flat-bottom assumption, i.e. the Kelvin wave assumption. We use the model to determine the origin of the process, which is expressed by upwelling and downwelling disturbances (from a state of rest) travelling cyclonically around the bay. We find that the wind generates local and remote (from a large and deep neighboring bay) responses which travel as forced (during wind forcing) and freely propagating long, coastally trapped, internal waves into and around the fjord. The resulting dynamics within the fjord can therefore be complex, particularly in the fall season during which nearly continuous and directionally variable winds occur. Under such forcing conditions and given the irregularity of the regional coastline, signals combine to form temporarily and spatially varying responses, enhancing or diminishing transient upwelling or downwelling and their associated along-shore current pulses.

# INTRODUCTION

In a stratified and broad embayment, broad defined here as by being wide with respect to its internal Rossby radius, interesting dynamics can take place. Each side of the bay can behave independently, e.g. a side can be subject to an upwelling while the other is subject to a downwelling, and a wave motion generated (by upwelling or downwelling forcing and/or relaxation) can propagate around as a 'trapped' motion with the coast to its right (Northern hemisphere). Should the bathymetric slopes along the coast be steep enough, those motions behave as internal Kelvin waves (iKWs), an asymptotic and simpler form of the more general motion of "coastal trapped waves" (CTWs, Gill and Clarke 1974) which are modified by both stratification and topography. In essence, CTWs are an hybrid of Kelvin and Continental Shelf Waves, CSWs which are long waves propagating on shelf-slope region in a homogeneous fluid. A useful parameter that can be used to predict which type of motion is likely to take place is the Stratification parameter S, or Burger number (Burger, 1958):

$$S = N^2H^2/(f^2L^2)$$

Where N is the buoyancy frequency representative of the stratification (rad/s), H is the embayment/ocean depth (m), f is the Coriolis parameter (rad/s) and L is the cross-shore length of the shelf-slope region (m). This number is, hence, dimensionless and a representation of the importance of the internal Rossby radius (NH/f) over the shelf-slope length scale L (i.e. a ratio). If S << 1, the motion is mostly barotropic and takes the form of a CSW and if S >> 1 the motion is mostly baroclinic, taking the form of an iKW (Huthnance, 1978).

A Kelvin wave (KW) has the following characteristics (see Thomson, 1880 for the original publication and Wang 2002 for a short review): it can be coastally or equatorially trapped (i.e. 2 main types), it is unidirectional (i.e. it will always travel with the coast to the right in the northern hemisphere and to the left in the southern hemisphere, and travel eastward along the equator), its amplitude is the largest at the boundary (i.e. coast or equator) and decays exponentially from it (its e-folding scale being the Rossby radius), it induces no cross-shore motion and it is non-dispersive (i.e. no change of shape, or wavelength, while travelling) when linear. In a vertically homogeneous ocean, there can only be one mode: the external, or barotropic, mode. In a continuously stratified ocean, an infinite number of modes can exist: the internal, or baroclinic, modes. Each mode travels with its own phase speed; the barotropic one being the fastest, travelling at the speed of a shallow water gravity wave (C = sqrt(gH)), while the internal modes propagate much more slowly (two orders of magnitude less, typically) and decrease as the mode number increases.

Evidence of coastally trapped iKWs have been reported in many parts of the world: in large lakes (e.g. Mortimer 1968, Csanady and Scott 1974, Saggio and Imberger 1998, Lemmin et al. 2005), in wide straits (e.g. Proehl and Rattray, 1984), in the Gulf of Mexico (e.g. Hallock et al., 2009), Peruvian Coast (e.g. Romea and Smith 1983), Japan (e.g. Kitade et al., 1998, Masunaga et al., 2017), India (Shah et al. 2019), Caspian Sea (e.g. Weber and Ghaffari, 2014) in the Mediterranean sea (e.g. Vilibic and Orlic, 1999; de Ruggiero et al., 2018), on the western European shelf (e.g. Batifoulier et al., 2012), in the Baltic Sea (e.g. Walin 1972, Fennel et al., 2010), Svalbard (e.g. Svendsen et al., 2002, Stoylen and Fer 2014), along the Arctic ocean/Beaufort Sea (e.g. Carmack and Kulikov 1998) and in Antarctica (e.g. Albrecht et al., 2006). Their widespread geographical representation owing to the basic set of physical characteristics necessary to their existence: stratification, coastal boundary and steep slope (also commonly called coastal wave guide). In

many cases, however, the effect of bathymetry is not negligible and the response take the more complex form of CTWs (e.g. along the US west coast, Southwest Australia coast, Southeastern Africa coast and Southeastern America coast, western European shelf, Caspian Sea and Black Sea).

Since iKWs can transmit upwelling and downwelling conditions away from their generation area, they are a very important process to consider when studying coastal ecosystems and human interactions with them. While confined to a narrow band near the coast (internal Rossby radius scale; few kilometers to few tens of kilometers, typically) and representing less than 1% of the global ocean surface, upwelling regions sustain about a quarter of the world fisheries (FAO, 2020). Marine aquaculture, a fast growing resource of seafood, is also largely located within few kilometers from the coast and thus potentially subject to upwelling-downwelling conditions. iKWs are also a key player with respect to earth climate. iKW is an important process regulating the ENSO (e.g. Wang, 2002, Wang and Picaut, 2004) and have, more recently, been shown to be an important mechanism of heat transport in Arctic fjords which can lead to accelerated rate of glacial melting (e.g. Jackson et al., 2018 and Fraser et al. 2018).

The Newfoundland shelf is characterized by a strong seasonal stratification (see Cyr et al., 2022 for the most recent update) and its rugged coastline presents large and deep bays (Figure 1). The shelf is also dominated by a cold and relatively fresh, equatorward current from Arctic origin; wrapping the island with its inner branch (see Smith et al., 1937, Loder et al., 1998, Ma et al., 2016 and references therein). Occurrences of iKWs have been documented on the north coast of Newfoundland by Yao (1986), de Young et al. (1993) and Davidson (2001) but have not been investigated on the south coast where the main ocean dynamics are still poorly known. Fortune Bay is one of those large bays located on the south coast of the island. It is about 130 km long, 20 km wide and has the particularity of having its mouth quasi closed due to the presence of the Saint-Pierre and Miquelon (SPM) archipelago at its SW boundary but to be semi-opened on its western boundary which consist of a series of islands and shallow sills (76 m mean and 125 m max depth from Miquelon to Brunette island and 53 m mean and 108 m max from Brunette to the main land, see Donnet et al., 2018a for details and Figure 1). Fortune Bay is deep, reaching more than 400 m in its main basin, oriented SW-NE, and about 600 m in its prominent head, Belle Bay, oriented SE-NW. Hence, its sides are steep and while the maximum cross-shore length of the shelf-slope region reaches about 15 km in the outer part, it is generally well below 5 km (see Figure 1, using the 200 m contour as representative of the bottom of the slope). In Belle Bay, L is very small and can be close to 0 km (i.e. a vertical wall). In a recent oceanographic review of the area, the internal Rossby radius was estimated to range between 5 to 10 km from spring to fall using a monthly hydrographic climatology and a 2 layers approximation (chapter 2). Same order is found in this study using a normal modes approach (details below). Thus, the stratification parameter of Fortune Bay is generally larger to much larger than 1 and iKW dynamics can be expected.

A first set of oceanographic investigations took place from the 1980s to early 1990s in Fortune Bay, with a focus on deep water renewals (de Young and Hay 1987, Hay and de Young 1989 and White and Hay 1994). In the early 2000s, further studies were undertaken following a rapid development of the aquaculture industry (Newfoundland south coast in general and Belle Bay in particular) which led to a geographic and hydrographic description of the area (Donnet et al. 2018a&b) as well as ocean currents and water exchange studies (Ratsimandresy et al. 2019 & 2020). Following those latter works, an oceanographic study, focused on Fortune Bay, was launched in 2015 to investigate the main physical processes affecting the upper layers of the fjord and their forcing mechanisms. An important motivation to this work, aside from the aquaculture development, was the results of a first effort looking at the ocean response of Belle Bay to

strong wind (Salcedo-Castro and Ratsimandresy, 2013) as well as of the results of earlier studies done in other large bays mentioned above. The works of Yao (1986) and de Young et al. (1993), in particular, largely influenced the sampling design and main hypothesis of this new study. On the other hand, while Salcedo-Castro and Ratsimandresy (2013) described important bay scale responses to strong winds (barotropic and baroclinic) they could not determine their nature nor geographical origin(s) from the data available at the time, which was an added motivation to investigate these aspects.

A first paper presents the result of these recent observations and illustrates the presence of upwelling and downwelling disturbances travelling within the bay (Donnet et al., 2020). A second paper describes this process and associated currents in more details; showing a cyclonic propagation and bay-scale correlation of the isotherms and along-shore variations (Donnet et al., 2022). The objectives of this third paper are to:

- determine the nature of the dominant physical process responsible for the strong current pulses described earlier, with respect to an iKW hypothesis, in particular.
- determine the origin of this process (forcing and spatial location) including local vs. remote effects.
- describe the characteristics of the signal propagation within the fjord.

An emphasis on numerical modelling will be given in this study to provide with a more detail view of the process in time and space, including its physical dimension (along and across shore), its propagation and fate within the bay (potential modification and exit) while observations will be used to both validate the numerical model simulations and better assess the nature and characteristics of the main process studied. In turn, the results of these numerical simulations could be used in future studies to predict the transport of variables of interest such as virus, sea-lice or organic material originating from aquaculture farms or larvae from species of economical interest (e.g. local fisheries).

This paper is organized as follow: a first section describes the observations and numerical model used (Material and Methods), a second section presents the results starting with a description of the observations, followed by a validation of the model and finishing with idealized runs allowing us to identify and describe the main process involved (Results), a third section discusses the results in light of the objective stated above (Discussion) and a fourth section concludes our findings and provides some perspectives (Conclusion).

Data used and generated through this study as well as illustrations (model output, mainly) are available at https://doi.org/10.20383/103.0636 and a supplementary material is also available to provide additional illustrations of our results (figures labelled with an “S” prefix herein).

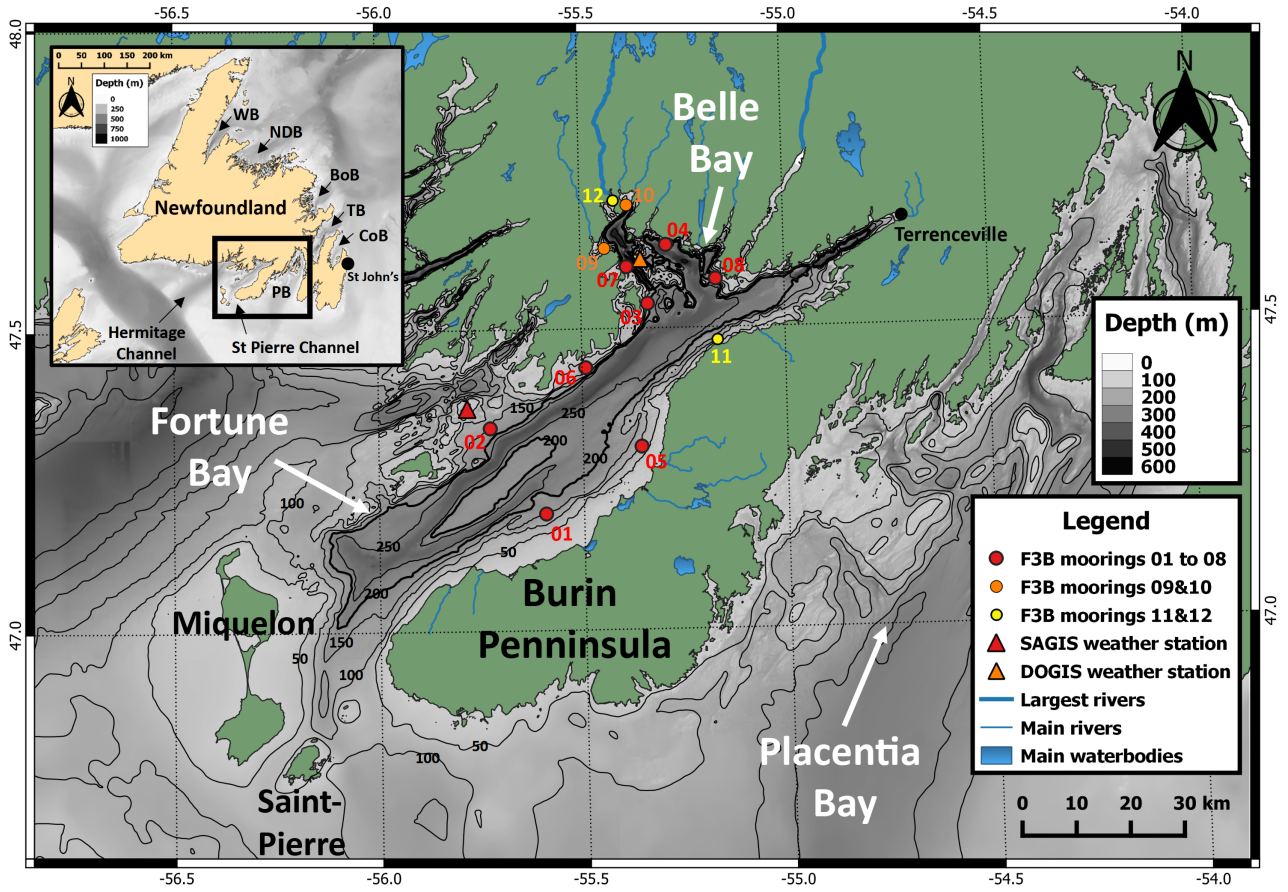


*Figure 1: study area. Dots represent oceanographic mooring observation sites (water column temperature and ocean currents data) and triangles represent weather stations (wind data). In red are the primary sites used in this study (F3B01-08 moorings and SAGIS weather station), in orange are the secondary sites used for complementary information (F3B09-10 moorings and DOGIS weather station) and in yellow are cited sites not used herein due to period coverage differing from that studied (F3B11&12). Bathymetric contour represented in bold is that of the 200 m isobath, corresponding to the bottom of the continental slope of Fortune Bay. Other isobaths represented by thin black lines are from 50 to 250 m; spaced every 50 m.*

# MATERIAL AND METHODS

## OBSERVATIONS

The majority of the data used for this study were collected during an observation program that spanned May 2015-17 and that focused on the collection of continuous temperature and ocean currents profiles. 12 sites were monitored in total, during 6 (F3B09-12), 12 (F3B05-08) and 24 (F3B01-04) months (see sites location in Figure 1). Temperature profiles were collected for nearly all the water column (5-10 m depth to 5-10 m above sea bottom) while current profiles spanned either about the same or just over half the water column for the most part (i.e. from 80 m up). All the moorings but two (F3B08 & F3B12) were deployed on the slope: F3B01-04 in 150-160 m depth and F3B05-07&11 in 90 m. F3B08 was deployed at the bottom of a nearly vertical slope in 210 m depth and F3B12 was deployed in a river mouth in 10 m depth. Details of this monitoring program, limitations and data return are presented in Donnet et al. (2020) with data available at

https://doi.org/10.17882/62314. For this study, F3B01-08 data collected during the stratified period of year 2 (May-November 2016) are used to validate the numerical model simulations and to help determining the nature and propagation characteristics of the processes investigated. Note that, on a cyclonic sense (which will be shown to be the propagating sense of the main signals) the moorings sequence is: F3B01, 05, 08, 04, 07, 03, 06 and 02. Wind data collected during this program (DOGIS, Figure 1) are also used to illustrate the spatial variability of this parameter.

These data are complemented by wind speed and direction timeseries from Environment and Climate Change Canada (ECCC) Sagona Island weather station (SAGIS in Figure 1) which are used as our primary wind data for our analyses and numerical simulations and by a temperature and salinity monthly climate presented in Donnet et al., 2022 (with data available at https://doi.org/10.6084/m9.figshare.13526366) which are used to initialise the model.

In addition, spatial wind and Sea Surface Temperature (SST) fields are used to illustrate the atmospheric forcing and ocean surface response during selected events (for model setup and validation). Wind data came from the European Centre for Medium-Range Weather Forecasts (ECMWF) ERA5 reanalysis (~25 km horizontal resolution, hourly fields, Hersbach et al., 2018) and ECCC high resolution model High Resolution Deterministic Prediction System (HRDPS, ~2.5 km horizontal resolution, hourly fields, ECCC, 2022). SST came from 3 different dataset: (the 4 km resolution, daily, AVHRR Pathfinder v5.3 re-analysis (PFv5.3, Saha et al., 2018), the 1 km resolution, daily, Global Foundation SST analysis (G1SST, JPL 2010 and Chao et al., 2009) and the 1 km resolution, daily, MUR Global Foundation SST analysis v4.1 (MURSST, JPL 2015 and Chin et al., 2017).

## NUMERICAL MODEL (FVCOM)

We used the Finite Volume Community Ocean Model (formerly known as Finite Volume Coastal Ocean Model, FVCOM, Chen et al., 2003 and 2013). FVCOM is a fully non-linear, free-surface, three-dimensional hydrodynamic model solving the primitive equations (Navier-Stokes) on an unstructured computational grid (mesh) in the horizontal and on terrain-following coordinates in the vertical. FVCOM uses the finite volume method to solve the governing equations in an integrated form and invokes the time-spliting method separating the barotropic and baroclinic modes to increase computation efficiency. We used FVCOM v4.1 in prognostic mode (i.e. time-varying density fields) and under the hydrostatic approximation. The latter being justified by an expected horizontal scale of the process studied large compared to its vertical scale (kilometers vs tens of meters). Given the latitudinal scale of the study area (order of 100 km) we also choose to use the f-plane approximation (i.e. constant Coriolis parameter) and Cartesian horizontal coordinates (Universal Transverse Mercator, UTM). Although we investigated the potential effect of the bathymetry (details in the discussion) we use a flat-bottom approximation for all the simulations presented herein to test the hypothesis of iKWs as a main physical process.

The mesh was created using the Aquaveo Surface-water Modeling System software (SMS v13, Community Version) and following the constraints recommended by FVCOM users' manual (Chen et al., 2013, Chapter 20). The coastline data came from the Global Self-consistent, Hierarchical, High-resolution Geography Database (GSHHS v2.3.5, Wessel and Smith, 2018 and Wessel and Smith, 1996) providing an original resolution of about 100 m. Using SMS resampling tool, and considering an internal Rossby radius on the order of 5-10 km, a minimum horizontal resolution of 1 km was selected within the area of interest (i.e.

Fortune Bay) to ensure proper representation of the expected cross-shore dynamics (upwelling & downwelling, in particular). The SPM archipelago was resampled at 1.5 km (Saint-Pierre) to 2.5 km (Miquelon) while the rest of the coastline was resampled at 5 km and was very much simplified (removal of many islands and small inlets). The open-boundary (shelf area) was resampled at 10 km. Early simulations with a minimum of 5 km resolution in Fortune Bay were attempted and succeeded in reproducing the main dynamics observed, i.e. upwelling and downwelling events, but the cross-shore scale of the processes did not appear optimum. Much higher resolutions were tested when using a realistic bathymetry, down to a 100 m value, which will be discussed later. Given the relatively small domain, relative low resolution, use of an unstructured grid and computing power available, a conservative external time step of 1 s (with a mode ratio of 10) was used all along and for all the mesh resolutions without falling under the Courant-Friedrichs-Levy (CFL) criterion/condition (about 80 m minimum cell size for a maximum depth of 600 m). Two flat bottom mesh were created at 1 km resolution: a 'local' mesh, centered on Fortune Bay and an 'extended' mesh including the neighboring Placentia Bay to test the hypothesis of potential remote effects from this other large bay on Fortune Bay. These effects were further assessed using idealized wind scenarios in which wind was applied on restricted areas of the extended mesh (Figure 2).

Three vertical coordinates systems are available with FVCOM: uniform, geometric and generalized. The uniform system distributes the levels evenly with depth, the geometric system increases resolution near the surface and near the bottom to improve calculation of the Ekman layers dynamic and the generalized system leaves the user to define spacing in the upper and lower layers down to a, also user defined, depth . Upon a number of trials, we found that a generalized coordinates system was the most appropriate with flat bottom simulations and that 20 (using a 150 m bottom) to 40 (using a 300 m bottom) layers were sufficient to reproduce the vertical density profile and its evolution when comparing with the observations. We used a vertical resolution of 5 m for the first 50 m (10 layers) and 10 m for the last 50 m (5 layers) leading to a resolution of 8-10 m for the rest of the water column. Sensitivity of the model with depth was gauged by running all the simulations used for validation with 150 m and 300 m depth, roughly corresponding to mid and bottom slope at most observation sites, respectively. While 150 m and 300 m simulations led to nearly equivalent results, the 300 m ones were slightly better correlated with the observations (with currents, in particular) and were so retained for all the results presented herein.

The initial conditions of temperature and salinity were taken from the spatially homogeneous monthly climatology presented in Donnet et al. (2022). Even though a good set of observations were available, we did not use them for initial conditions because: 1) only temperature was collected nearly all along the water column (10-140 m) while salinity was collected at 2 depths only (about 10 and 90 m); 2) observations are affected by important variability (some of which we intend to study) and 3) this is a process study in which we will try to determine if the main dynamics can be reproduced with limited input (such as with a flat bottom, an hydrographic climatology and single point wind observation). Data covering Fortune Bay as a whole were used to create a "summer" profile (i.e. an average of July, August and September profiles) for the July 2016 events simulations and to create an August profile for the September 2016 events simulations (the 2 main scenarios selected for this study). Those profiles were found to correspond best with the observations available for these periods (see Figure S1).

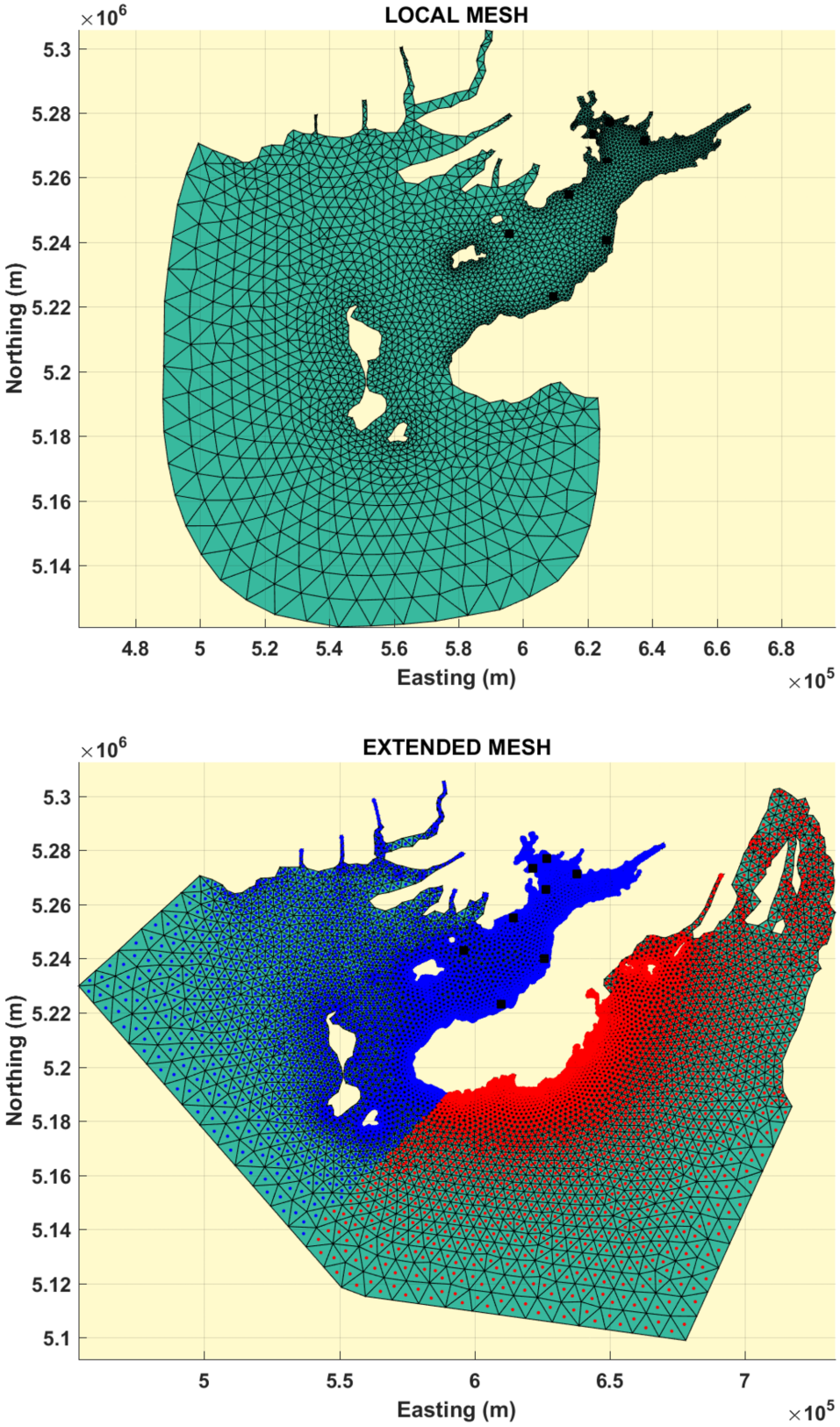


*Figure 2: meshes used for the numerical simulations. 'Local' and 'Extended' meshes represented here use a flat bottom approximation. Observation points (mooring sites) used for validation are represented by black squares and are located 2 elements or nodes away from the coast (i.e. about 2 km away). Elements used for ideal wind forcing local ('FB only') vs. remote ('PB only') scenarios are represented in blue and red, respectively.*

Winds from ECCC SAGIS weather station were used as surface boundary conditions and assumed horizontally homogeneous. Since SAGIS is located on a small barren island roughly in the middle of the domain, it was considered to be representative of the wind field of the area. This assumption is justified here also by the limited study area which is much smaller than the synoptic scale (i.e. weather systems). The validity of this assumption was tested by plotting spatial wind fields from the ECMWF ERA5 re-analysis and ECCC's HRDPS model data(see Figure S2 and hourly snapshots provided in https://doi.org/10.20383/103.0636). Both sources show a largely homogenous spatial field over our area of interest, especially during strong wind events (e.g. July 4-5) and they both compare very well with SAGIS observations (Figure S3). SAGIS winds are available hourly and were gap-interpolated when and where necessary (3 hours maximum gap found for the periods simulated). Input wind speed is converted by FVCOM to wind stress using the Large and Pond (1981) relationship. On the offshore boundary, and while data from the Saint-Pierre tide gauge (SHOM, 2022) were used for model testing and validation purposes (e.g. barotropic tides simulations) the water level was 'clamped' to zero for all the simulations presented herein (i.e. no sea-level variation allowed along the offshore open boundary). Tides have very little influence on the currents in the region (Ratsimandresey et al., 2019; Donnet et al., 2022) and we wanted to focus the analysis on the response to wind forcing. Clamping the offshore boundary can have undesirable effects, however, such as limiting the generation of a signal near the southeastern boundary, i.e. bottom on the Burin Peninsula, for instance in the case of the generation of an upwelling or downwelling. A sponge layer of 15 km (1-2 elements) was prescribed along the offshore boundary and the 'no gradient' condition was used for all simulations. No surface heat or precipitation fluxes, no groundwater fluxes, no atmospheric pressure, no river input, and no open ocean conditions were stipulated; reducing the forcing to a wind-only one applied to the computational domain.

We used the Mellor-Yamada level 2.5 (MY-2.5) vertical turbulent closure sub-model with a background vertical mixing coefficient of 1 x$10^{-5}$ $m^2$/s for all simulations presented herein. Sensitivity tests, varying this coefficient by a factor of 10, did not show any significant effect on the results. For horizontal mixing, we used a constant coefficient of 0.3 $m^2$/s. We found that while using a constant coefficient within a range of 0-0.3 $m^2$/s had very little effect on the flat bottom simulations, using the available Smagorinsky parametrization (Smagorinsky, 1963) would increase horizontal spreading and lower currents strength well below that observed. Both horizontal and vertical Prandtl number were set to 0.1. A logarithmic bottom layer is used in FVCOM and a roughness height of 0.001 m and maximum drag coefficient of 0.0025 were chosen.

# RESULTS

## OBSERVATIONS

Figure 3 illustrates the strong seasonality in stratification experienced in the region, peaking in august with sea surface temperature about 16 °C and salinity mostly below 31 g/kg lying above waters less than 2 °C and more than 32 g/kg in salinity. Although individual profile taken at any given time can show a surface mixed layer these monthly climate results are smooth, and density profiles show a continuous stratification from spring (May) to fall (November). In summer, this continuous stratification occurs in the first 30-40 m while it is somewhat shallower in spring (about 20 m) and much deeper in fall (about 80 m). Differences of density

of 1 kg/$m^3$ (spring) to 3 kg/$m^3$ (summer) are found between the surface and sub-surface layer (which is an intermediate layer, in the case of Fortune Bay; see Donnet et al., 2022 for details) and the buoyancy frequency peaks around 0.03 rad/s in summer corresponding to a natural oscillation period of about 3 min. In spring and fall, peak values of N are on the order of 0.01 rad/s (about 10 min natural periods).

Using these seasonal profiles and performing a normal mode analysis (Klinck, 1999; see Figure 3 and Figure S5 for illustrations) yields to mode 1 internal wave phase velocities of 0.4 m/s in spring (May) to 0.7 m/s in fall (November) in water depth H=300 m. Summer conditions used for the modeling simulations (details below) lead to a mode 1 phase speed of 0.6 m/s with an inversion around 50 m (August profile; September events scenario) to 65 m (Jul-Sep averaged profile used to reproduce the July events and for the idealized scenarios; Figure 3) in H=300m. Mode 2 and 3 velocities are about half and third of mode 1 values, respectively. At the latitude of Fortune Bay (47.5 °N), this leads to a, mode 1, internal Rossby radius of about 4 to 7 km from spring to fall (using $f=1x10^{-4}$ rad/s) with a value of 6 km for the modelling scenarios considered herein.

Timeseries of wind and thermocline depth during the most stratified period of the year (from May to November 2016) are illustrated in Figure 4. Two weather stations series are represented, that of DOGIS, located in the middle of Belle Bay, and that of SAGIS, located more offshore (Figure 1); overall, the two series are consistent with each-other although winds from the North are generally stronger at DOGIS while winds from the west and southwest are generally stronger at SAGIS. Thermocline depth is presented using the 2 °C isotherm which roughly corresponds to the bottom of the surface stratification (Figure 3). Wind forcing is characterized by intense but relatively short-lived peaks of 5-10 m/s speed (or more) and, typically, 2-4 d in duration ('through to through'). Those strong events can occur from just about any direction but with a predominance of winds from the Northwest (NW) and from the Southwest (SW). Few strong events from the Northeast (NE) and Southeast (SE) are notable though, such as the one of mid-July (NE-NW event). The frequency and intensity of the events visibly increase during the fall.

In this paper, oceanic motions will be described as 'events' and 'pulses' which are defined as follows: an event is a perturbation consisting of a descending (downwelling) and an ascending (upwelling) phase of the isotherms. A pulse is defined as unidirectional currents (inflow or outflow) generally associated to a phase (either downwelling or upwelling). Thus, a downwelling event is a period generally starting with a downwelling pulse and, generally, finishing with an upwelling pulse; conversely, an upwelling event starts with an upwelling pulse and finish with a downwelling pulse. Atmospheric forcing events usage differs a little in a sense that an event is defined as a sustained period of wind going in the same direction using the four main quadrants listed above. Along-shore and accross-shore components will also be used, for both wind forcing and oceanic responses, using Fortune Bay's main axis orientation as a reference, i.e. 40 °N, for the wind and using site specific isobaths orientation for the ocean currents.

Thermocline depth measured around the bay shows important upwelling and, even larger, downwelling (Figure 4). Those events appear transient until late summer (September) when they start to be more frequent to the point of appearing periodic (around 2-5 d). Typical downwelling range is on the order of tens of meters, reaching around 60 m during the largest event in July. Statistical analyses presented in Donnet et al. (2022) showed strong isotherms correlation amongst mooring pairs from F3B08 to F3B06 (anti-clockwise) and the lowest correlation of F3B02 with any other. The latter being visibly distinctive from the other in Figure 4. Donnet et al. (2022) also showed that these upwelling and downwelling events were

associated with strong pulses of along-shore current, travelling cyclonically around the bay.

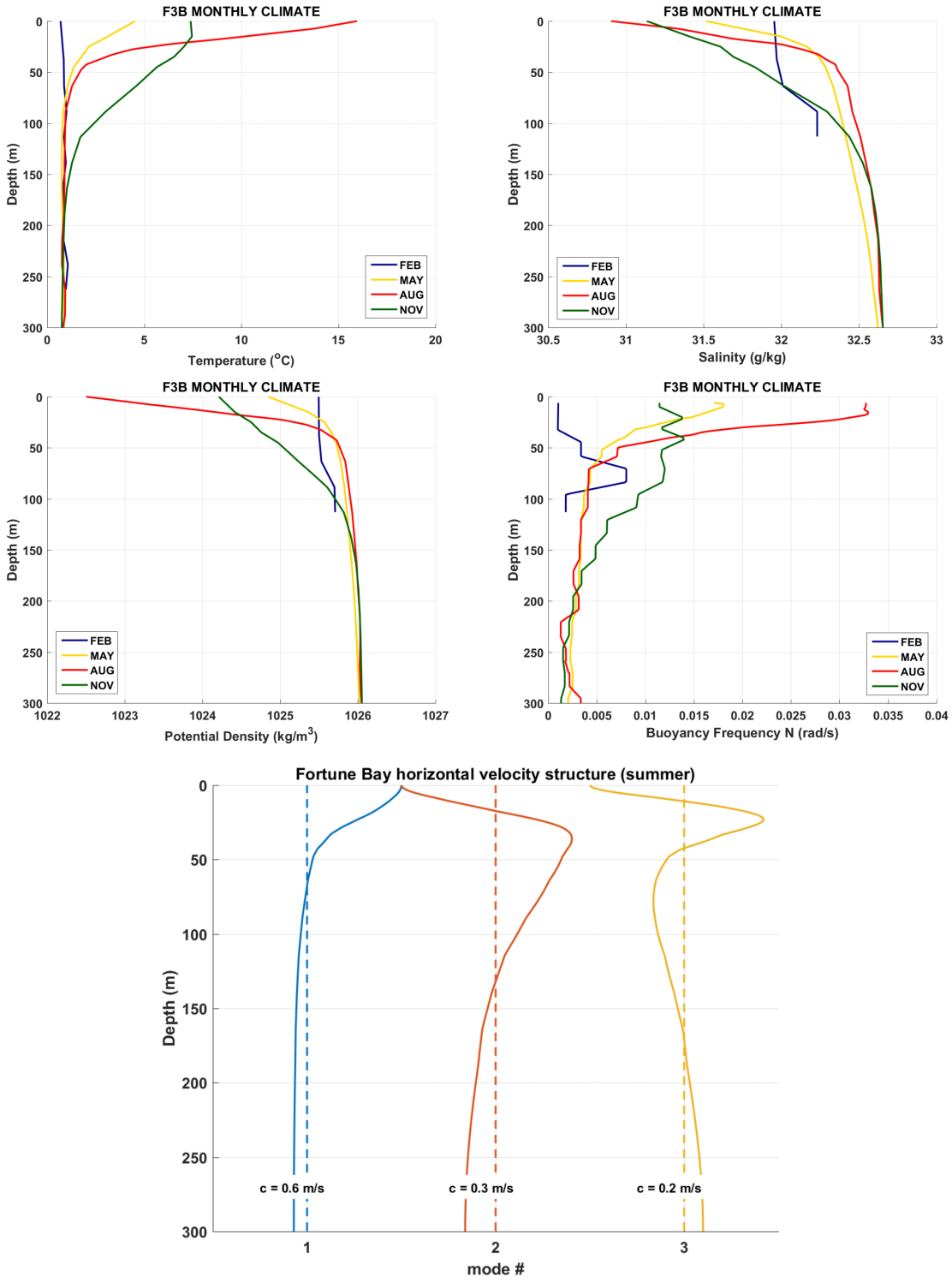


*Figure 3: water stratification profiles (top 4 panels). Seasons are represented by their 'peak' month (FEBruary for winter, MAY for spring, AUGust for summer and NOVember for fall). Bottom panel illustrates the vertical structure of freely propagating waves horizontal currents (first 3 vertical modes) calculated from on an averaged Jul-Sep hydrographic profile (using Klinck, 1999).*

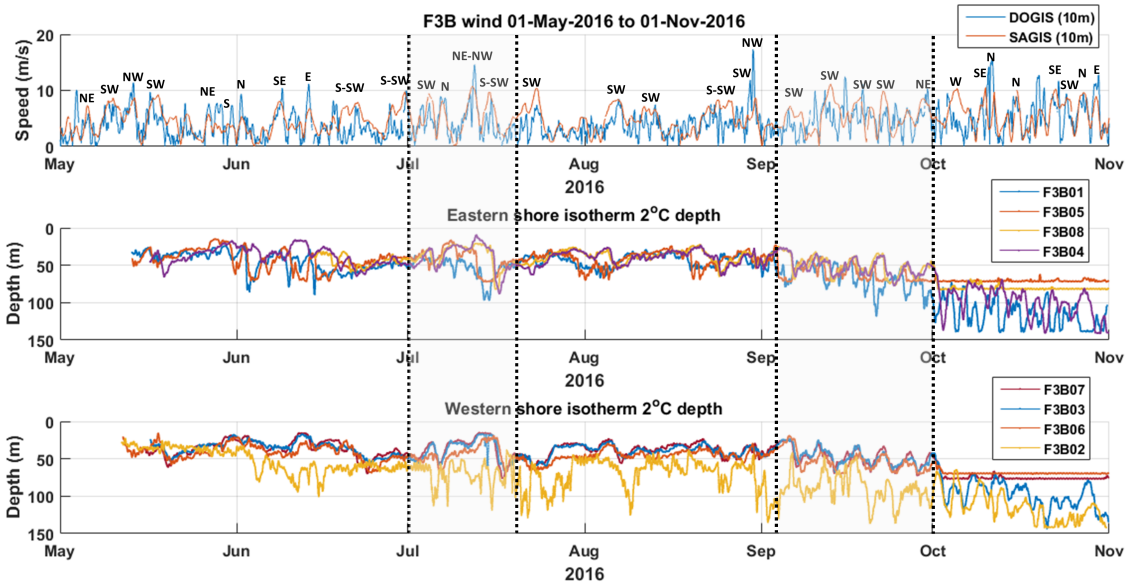


*Figure 4: wind speed and thermocline depth timeseries (6hr moving-averaged). Wind direction (from) is indicated on top of main events (N for North, NW for NorthWest, etc.). Thermocline depth is illustrated via the depth of the 2 °C isotherm, the flat lines towards the end of the series indicate a depth of the isotherm larger than the deepest sensor located on the mooring, affecting F3B05, 06, 07 & 08 (about 80 m limiting depth). Timeseries are grouped in two shores corresponding to main cardinal directions. In shaded grey are the periods selected for analyses and numerical modeling.*

Results of a wavelet analysis (using Grinsted et al., 2004 programs; see Figure S6 for illustrations) performed on along and across wind speed components of Fortune Bay (40 °N orientation for the along component) indicate that strong episodic wind events are generally located within the 1-4 d band (numerous higher frequency events are also apparent but are much less energetic; about 1/4-1/8 in power). 1-2 d events are more frequent in the along-shore component than on the across-shore component. Long, 4-8 d events are only showing up on the along-shore component during the first half of July and second half of September, in particular. Analysis of near-surface (10 m) and sub-surface (70 m) along-shore currents from F3B08 to F3B02 (i.e. excluding F3B01&05, the southeast shore of the bay, due to data limitations) show longer lasting low-frequency pulses (> 1 d period) than the wind. In the near-surface, the period of early-July to mid-August and mid-September to mid-October are particularly active with signals located in the 4-8 d band. Within that same band, near-surface events appear to also become more continuous from F3B08 to F3B06. Sub-surface currents are dominated by lower-frequency signals (>4 d periods), particularly at F3B04. A large band, centered on the 16-36 d periods is also visible at all sites. Although not continuous, the semi-diurnal tide band, centered around 0.5 d, is clearly visible at F3B02 (near-surface and sub-surface) and at F3B06 (sub-surface).

Two periods were selected to investigate the process responsible for those upwelling&downwelling events propagating cyclonically: July 01-20 and September 04-30 (Figure 4). The former is an example of transient events (including the largest downwelling event of the timeseries) while the latter is an example of quasi-periodic events. Figure 5 illustrates wind forcing, isotherms variations and associated currents of those events. Wind forcing is represented by the along-shore stress which was calculated using the relationship of Large and Pond (1981) and is positive when going into the bay. Due to data limitation (see Donnet et al., 2020) current speed (scalar) only are represented for F3B01&05 while along-shore currents are shown for

the other sites. Along-shore currents are defined as being positive for a flow going into the bay (red color), i.e. northeast-ward in the outer part and northwest-ward in Belle Bay, and negative (blue color) for an outgoing flow. They were calculated by rotating the eastward (u) and northward (v) components to follow the isobaths (along and across) at each site.

In July, four main wind events occurred: a first couple starting on July 3 with a positive along-shore stress event and followed by a negative stress event ending on July 8 and a second couple starting on July 10 with a negative along-shore stress event and followed by a positive stress event ending on July 17. The signal of each couple of events is fairly symmetrical, each event of wind stress (either positive or negative) being of about the same duration, i.e. just over 2 days for the first couple and just over 3 days for the second one. Each event peak around 0.1-0.15 $N/m^2$. Meanwhile, 2 main downwelling events can be accounted for (dash lines and double-headed arrows): from the 3$^{rd}$ to the 10$^{th}$ and the 12$^{th}$ to the 20$^{th}$ and beyond (across sites). The downwelling phase takes about 2 days to propagate, cyclonically, around the bay the first time and about 4 days the second time (from F3B01 to F3B06). Both downwelling and upwelling phases are associated with an increase in along-shore currents speed but the downwelling phase appear clearly more energetic and logically occupies a much larger proportion of the water column. Downwelling ranges are up to about 20 m and 40 m (first and second event, respectively; using the 4 °C isotherm as indicator) and each event last about 4 d (first event) to 6 d (second event). Note that prior to the downwelling phase of the second event an upwelling phase also occurred, from the 11$^{th}$ (F3B01, weak) to 16$^{th}$ (F3B06, stronger), i.e. during negative wind stress forcing (11-13). The duration and timing of the oceanic events appear compatible with the wind forcing, indicating a system locally forced, i.e. downwelling during positive stress and upwelling during negative stress along the east side of the bay (F3B01&05) with a cyclonic propagation around the bay (from F3B01 to F3B06). However, one can note that the second (and also largest) downwelling event starts 1 to 2 days prior to the wind stress becoming positive (on July 13th at F3B05 and on July 12th at F3B01) and thus, during a phase of locally upwelling favorable wind (11-13). A downwelling event is also clearly visible between the 8$^{th}$ and 9$^{th}$ at F3B01 and 05 while there were no along-shore wind (i.e. zero stress) and appears to propagate cyclonically (as seen on F3B04-06). The dynamic appears therefore more complex than solely responding to local wind forcing.

In September, three main positive peaks (11-16, 16-19 and 21-24) and 2 negative peaks (19-21, smallest, and 28-30, largest) of along-shore wind stress occurred. Cyclonic propagation of events is again evident but the isotherms and currents picture is more complex. Performing a zero-crossing analysis on the clearest period of the low-pass filtered 4 °C isotherm series (September 09-29, 24 hr window running average) yields to the identification of 6 (F3B01) to 3 (F3B08 to 06) main downwelling events of 3 (F3B01) to 6 (F3B08 to 06) days duration (or period) with vertical ranges of 13 m (F3B01) to 24 m (F3B04), on average (Figure 5, dash lines and numbers). Hence, the signal seems to change frequency (from high to low) and to be enhanced (in amplitude) as it travels from Fortune Bay's main basin to Belle Bay and out. A 'transition zone' can also be noted between F3B08 and F3B04 where, for instance, the near-surface current oscillates between the events 1 & 2. Downwelling associated currents appear, here also, clearly more energetic (order of 0.5 m/s in downwelling vs 0.25-0.5 m/s in upwelling).

Cross-correlations between mooring pairs F3B01-06, F3B01-08 and F3B08-06 were performed to quantify the relationships and to get an idea of the signals phase propagation speed (Table 1 and Figures S6-S7 for illustrations). For the September events, the analysis was done on the same time window as the zero-crossing, i.e. September 09-29, and using the same isotherm. While correlations with no lag are generally

low (<10% of variance), high correlations are found with lags on order 1-4 d (as expected from Figure 5). Higher correlations are found with the July events than with the September events for the pairs F3B01-06 & F3B01-08 while the F3B08-06 pair stayed highly correlated for both periods. As noticed above while describing Figure 5, a remarkable difference in propagation time is found between the first and second event of July increasing from about 2 d in July 01-10 to 4 d in July 10-20 between F3B01 and 06; i.e. a factor 2 increase. The largest change occurs between the mooring pair F3B01-08 which show a factor 3 increase in lag time from the first to second event (from 0.8 d to 2.4 d). In comparison, mooring pair F3B08-06 show an increase of about 30% only (from 1.1 d to 1.4 d). Thus, the second downwelling event of July clearly propagated much more slowly than the first one, particularly between F3B01 and F3B08. Using mooring distance between pairs leads to estimates of phase speed of the order of 0.5 m/s (second event for all pairs and first event between F3B08-06) to 1 m/s (first event between F3B01-08) in July and about 1 m/s in September (all mooring pairs). There are uncertainties with these latter estimates, however, due to the complex coastline which made the computation of distances difficult. We assumed, notably, that the signal would travel back and forward within both Terrenceville inlet (about 15 km long) and in the head of Belle Bay (F3B12; about 10 km long) even though their cross-sections are about 3 km; that is, smaller than the internal Rossby radius (estimated at 6 km earlier). Model results presented below show, however, that the signals do propagate within these narrow features (in and out). Another remarkable result is on the change of signal amplitude which significantly increased along the bay during the first event of July (by 185% from F3B01 to F3B06) while decreasing slightly during the second event (by about 20% from F3B01 to F3B06, Table 1). Most of the amplitude enhancement of the first event occurred between moorings 01 and 08, in contrast to the modest reduction observed between moorings 08 and 06 during the second event. On the other hand, the events of September show little changes in both signal phase speed and amplitude from F3B01 to F3B08. It should be noted, however, that other than for the F3B08-06 pair, the correlations are not high for this period (0.4-0.5); reflecting the important change in signal frequency (from F3B01 to F3B06) noted above.

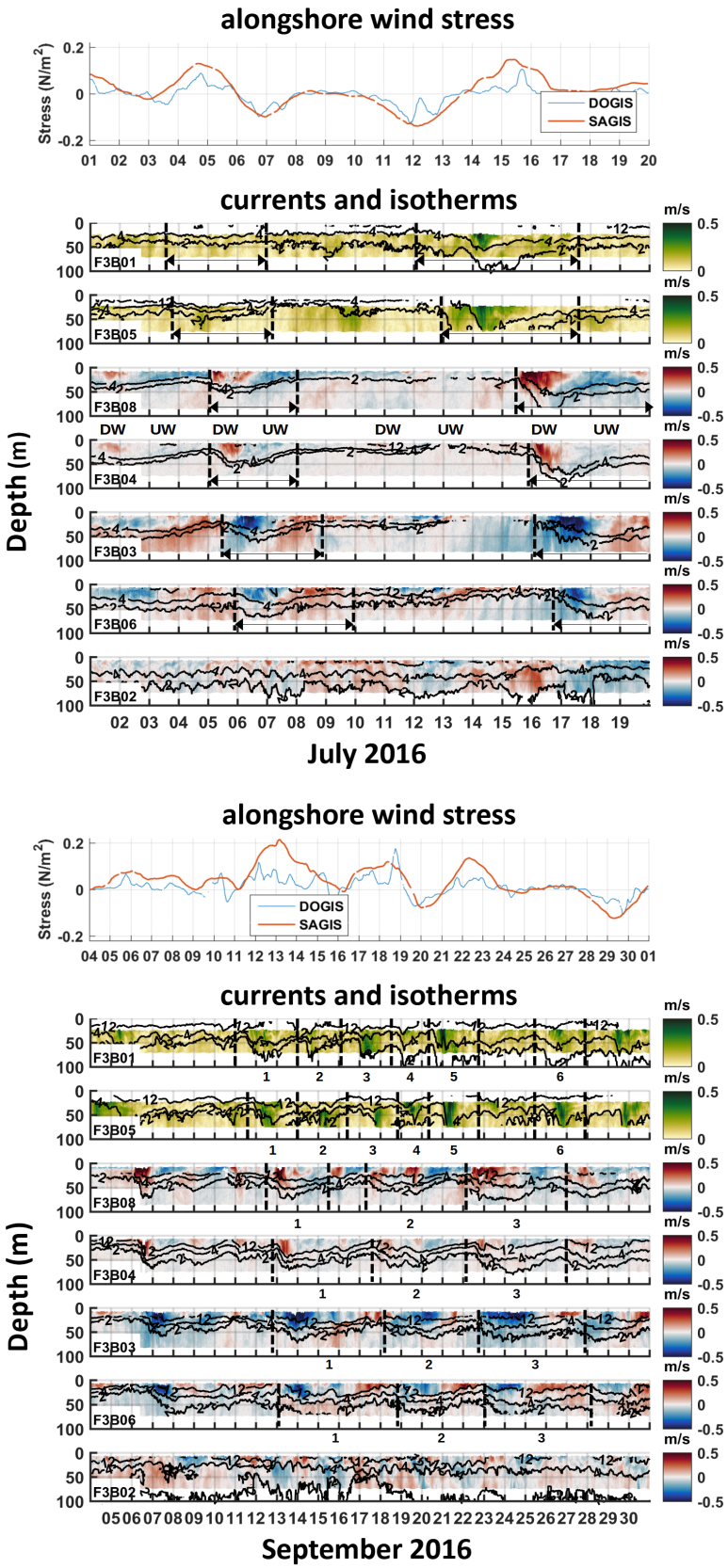


*Figure 5: Temperature and current speed profiles at mooring sites around Fortune Bay. Along-shore currents (positive into the bay) are represented for F3B08, 04, 03, 06 and 02 while scalar only (modulus) is presented for F3B01 and F3B05 due to data limitations (see Donnet et al., 2020 for details). Downwelling (DW) and upwelling (UW) events are also indicated (using numbers on the September plots). Selected events for the analysis are further indicated by the dash lines (and horizontal double-headed arrows on the July plots).*

Considering the events duration and phase speed determined above, wavelengths can be estimated using the relationship L = CxT where L is the wavelength, C the phase speed and T the wave period (or event duration). Thus, for a phase speed ranging from 0.5-1 m/s (second and first event, respectively) and event duration ranging from 4 to 6 d (first and second event, respectively) we obtain wavelengths of the order of 260 km (second event) to 350 km (first event). In September, this range increases from 260 km (3 d event duration) to 520 km (6 d event duration) using a constant phase speed of 1 m/s. Given the uncertainties associated to the determination of the phase speed and events duration noted above, there are inherent uncertainties with those estimates. Nevertheless, they provide with a first order of magnitude (2-3 times the bay's length) which will be refined using the results of the numerical model.

Downwelling and upwelling is expected on the eastern shore (F3B01&05) during positive and negative along-shore wind stress, respectively. These disturbances are also expected to propagate cyclonically around the bay as iKWs should the cross-shore scale, i.e. bay width, allows them to do so; a valid expectation in Fortune Bay which is 20 km wide for an internal Rossby radius less than 10 km. Though positive along-shore wind stress and downwelling events appear correlated, particularly during the July events, it is, however, more difficult to discern the effect of negative along-shore stress (both in July and in September) and to untangle the apparent change of frequency between the main basin (F3B01&05) and the head of the fjord (F3B08, 04 & 03) during the September events. Assessing the nature of the process responsible for the propagation of those events as well as its forcing mechanisms more definitively (i.e. positive vs. negative stress) will be the focus of the following section using the numerical model. Suspected remote effect(s) and a further assessment of signal propagation will also be given using the results of this tool.

*Table 1: lagged cross-correlation observations results. Lag (L) is negative when first mooring of the pair is leading the second (e.g. F3B01 leading F3B06). C = phase speed calculated as distance between mooring pair (indicated in bracket) divided by L. DWdiff = Downwelling amplitude difference between the mooring pair; a positive sign indicates second mooring observed a larger downwelling than the first (e.g. F3B06 downwelling of 01-10 July was larger than F3B01 one by 9 m).*

| Mooring pair | Event | R (lag=0) | Rmax (%var) | L (Rmax) | C | DWdiff (% change) |
|---|---|---|---|---|---|---|
| **F3B01-06 (180 km)** | 01-10 July | -0.17 (3%) | 0.82 (67%) | -1.9 d | 1.1 m/s | 9 m (185%) |
| **F3B01-08 (120 km)** | 01-10 July | 0.65 (42%) | 0.87 (76%) | -0.8 d | 1.7 m/s | 8 m (156%) |
| **F3B08-06 (60 km)** | 01-10 July | 0.08 (1%) | 0.96 (92%) | -1.1 d | 0.6 m/s | 1 m (11%) |
| | | | | | | |
| **F3B01-06 (180 km)** | 10-20 July | -0.50 (26%) | 0.96 (91%) | -3.8 d | 0.5 m/s | -4 m (20%) |
| **F3B01-08 (120 km)** | 10-20 July | 0.17 (3%) | 0.92 (85%) | -2.4 d | 0.6 m/s | -1 m (5%) |
| **F3B08-06 (60 km)** | 10-20 July | 0.21 (5%) | 0.81 (66%) | -1.4 d | 0.5 m/s | -3 m (17%) |
| | | | | | | |
| **F3B01-06 (180 km)** | 09-29 Sep | -0.31 (9%) | 0.49 (24%) | -2.2 d | 0.9 m/s | 0 m (1%) |
| **F3B01-08 (120 km)** | 09-29 Sep | -0.19 (4%) | 0.43 (19%) | -1.3 d | 1.0 m/s | 5 m (45%) |
| **F3B08-06 (60 km)** | 09-29 Sep | 0.38 (15%) | 0.89 (80%) | -0.9 d | 0.8 m/s | -5 m (38%) |

# NUMERICAL MODEL VALIDATION

Figure 6 shows the thermal and currents structure evolution in time of July (A) and September (B) events as observed and as modelled (flat bottom local and extended mesh runs). Only F3B01 and F3B06 are shown for conciseness and for being representative of 'upstream' and 'downstream' conditions (i.e. of signals propagating cyclonically as seen in Figure 5). More complete comparisons using the 4 °C isotherm depth and along-shore currents between the observation and model results, which were used for quantification, are shown in the supplementary material (Figures S8-11). We selected the 4 °C isotherm as representative of the thermocline depth and as a good marker between the surface and lower layers (as shown in Figure 6). Along-shore currents were calculated as a depth average from the surface to the 4 °C isotherm depth, therefore representing a depth varying surface layer. Nodes and elements used for the comparisons were taken about 2 km from the coast to be as representative as possible considering a flat bottom approximation and average across-shore distance from moorings of about 2 km (0.5 to 7.5 km range).

In July (Figure 6A), the largest differences between the model runs and observations occur at F3B01. The local model overshoots the first downwelling event (July 4) but underestimates the second one (July 14-16) significantly. The local model is also late by about 1 day for this second event and misses the downwelling event of July 9$^{th}$ (observed by the 2 °C isotherm). While the extended model also overshoots the first event, it does a much better job at reproducing the second event being both in phase with the observation (July 14-16) and about the right magnitude with the 4 °C isotherm. The 2 °C isotherm downward migration is, however, lesser with the extended model than observed and rebound of both the 2 °C and 4 °C are slower (taking about 3 days to go back to pre-event depths instead of about 2 in the observations). A downwelling event is also represented on July 9th by the extended model (unlike the local model) but last longer than the observations and affect a larger part of the water column as indicated by the 4 °C isotherm. At F3B06, both models reproduce the observations reasonably well (in amplitude and phase). Interestingly, the extended model does not reproduce the second, and largest, downwelling occurring on the 17$^{th}$ (i.e. 3 days after F3B01) any better than the local model this time. This is in fact the case from the site F3B08 and all-around Belle Bay (F3B04, 07 and 03; see Figures S8&9). The observed downwelling of July 12$^{th}$ is also represented by both models. High frequency variability (<1 d) are present in both models for which spectral analyses (not shown) indicate as being from near-inertial (~17 hr) band origins. Spectral analyses made on the observations indicate semi-diurnal signals of likely tidal origin (at F3B02, in particular) but do not reveal any near-inertial peaks (see Donnet et al., 2022 for more details). Since the models were run without tidal forcing; we suspect the model signals to be the result of Poincaré waves propagating freely in the domain. Modeled near-inertial and observed semi-diurnal signals are on the order of few meters (5 m at most) in isotherm amplitudes and of the order of few cm/s (0.05 m/s at most) in currents speed. Interestingly, they are most prominent at F3B02, about half the amplitude at F3B01, 05 and 06 and hardly visible anywhere in Belle Bay in both model and observations results. These are small signals, however, compared with the downwelling and upwelling events and will therefore not be considered any further in this study.

In September (Figure 6B), both models reproduce the observations better at F3B06 than at F3B01. At F3B01, the first modelled downwelling event (Sep. 5-7) is too small and the large downwelling events observed by the 2 °C isotherm from the 11$^{th}$ to the period's end are not as distinct in the models. The quasi-absence of the first event might be explained by model spin-up time, however, and by the fact that this event may have originated from a previous wind event, not included in the forcing timeseries. The difference in variability of the 2 °C isotherm, on the other hand, may be, in part, explained by the difference

of that isotherm depth between the initial conditions and the observations (about 40 m vs. 60 m, respectively) and/or the results of other processes not taken into consideration by the models. Although less large, some of the variability is captured nonetheless and some difference between the local and extended models can be noted. The extended model does not overshoot the event of the 10$^{th}$ to 11$^{th}$ as does the local model and captures the large event of the 20-23 better than the local model (although late by about 1 day). Both models miss the notable downwelling event centered on the 26$^{th}$, however. At F3B06, the first event (7-11) is also largely underestimated by both models, as we could expect, but the next three (14-16, 19-21 and 23-25) are reasonably reproduced. The last downwelling event (28-29) is largely missed by both models. The upper layer currents are reasonably well reproduced by the models at F3B06 and in fact from F3B08 to F3B06 (Figures S10&11) but the modeled lower layer currents appear weaker. The choice of the bottom depth influences this, and the 150 m simulations provided slightly better results for that layer at that site. It should be noted that current inversion, occurring around 40-50 m during some events (14-16 and 19-21, in particular) do not systematically occur as the model would suggest.

SST data were analysed as a mean of validation during upwelling events, which are expected to be manifested by bands of colder water near the coast. To make the results comparable, hourly model output was daily averaged. Unfortunately, examination of daily snapshot derived from three different dataset (PFv5.3, G1SST and MURSST, described above) proved to be unconclusive (see Figure S12 as well as complete snapshot series in https://doi.org/10.20383/103.0636). Upwelling events indicated by the moorings in July 8-10 (from F3B05 to F3B06) or July 13-15 (F3B04-06), for instance, do not appear clearly in any of the dataset. PFv5.3 lacks coverage for both periods and the signals are either not clear (July 8-10) or absent (July 13-15) from the other dataset. The model, on the other hand, shows clear upwelling signatures all along the Burin Peninsula and northern coast of Belle Bay. The following aspects may explain this apparent discrepancy: 1/ cloud coverage is severe in this region which particularly affects PFv5.3 AVHHR data (Donnet et al., 2022) but also likely affects blended analyses such as G1SST and MURSST, 2/ the blending and interpolation used in G1SST and MURSST, albeit necessary to provide gap-free coverage, may significantly smooth our signals that are largely contained within a thin band near the coast (~5 km), 3/ the (also necessary) daily averaging of all the SST products used may smooth signals that are very transient in nature (possibly < 1 d as a detectable surface signal) and 4/ the model is initialized with horizontally homogeneous conditions which are unlikely to exist in reality, particularly at the surface.

Overall, although the flat bottom models are prone to downwelling overshooting, they perform well at reproducing the main events observed. The extended model tends to out-perform the local model during large events occurring in Fortune Bay notably during July 14-16 and September 20-23; suggesting a possible remote effect captured by the former. In the latter cases, strong wind shifted swiftly from negative to positive along-shore forcing (NE to SW). The absence of the downwelling event of July 9$^{th}$ from the local model also suggests possible remote effect.

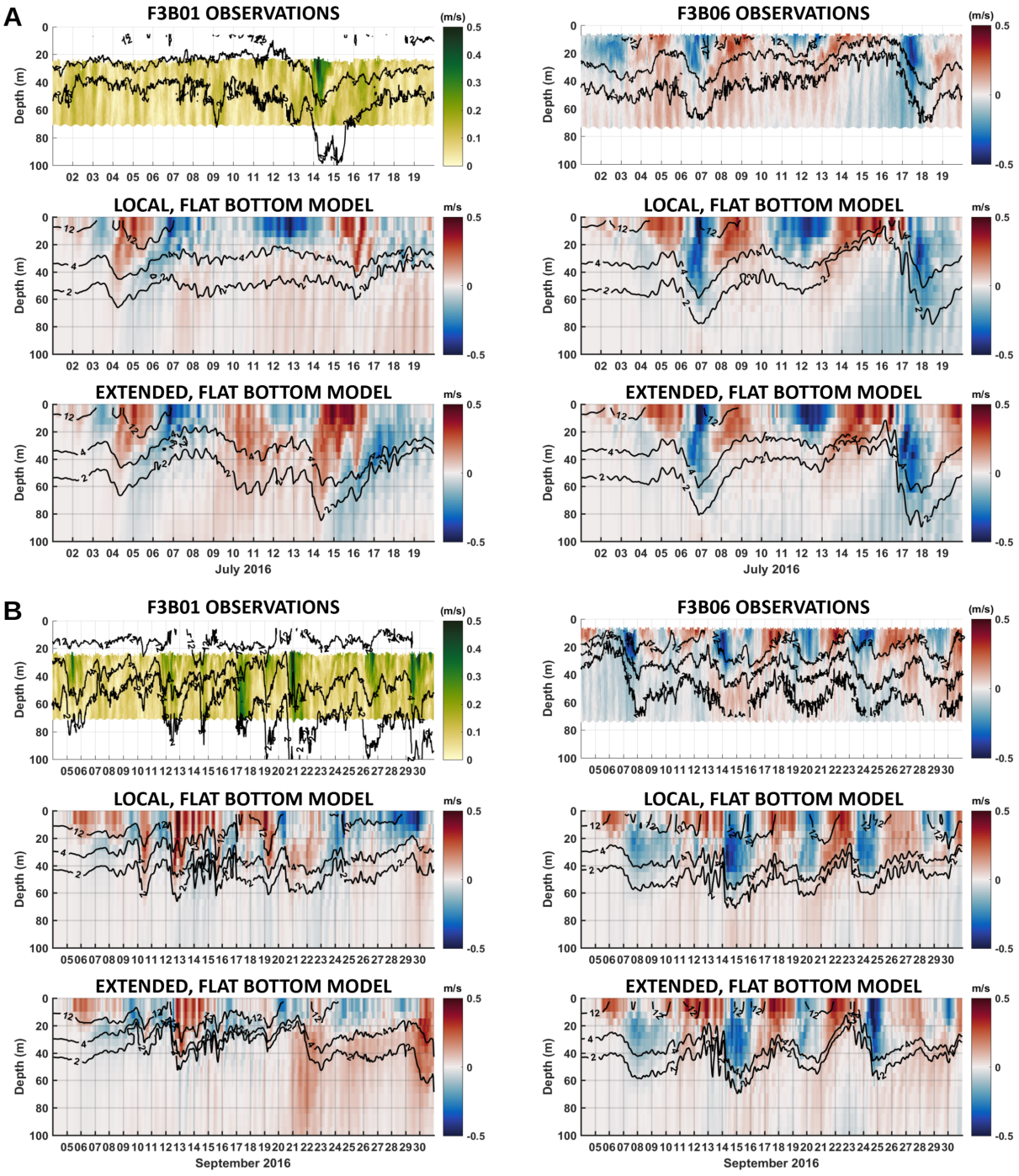


*Figure 6: model validation using July events (A) and September events (B). Observed current speed scalar only are represented at F3B01 due to data limitations (Donnet et al., 2020). Observed along-shore currents are represented otherwise at F3B06 and at both sites with the models. Along-shore is positive for a flow going into the bay (red color) and negative (blue color) for an outgoing flow.*

Linear correlations between observed and modeled 4 °C isotherm's depth as well as along-shore currents were computed to quantify the agreement. The analysis used unfiltered, raw signals; therefore making it a direct comparison between observations (which include the full variability of the ocean) and model (which is idealised). In July, correlation coefficient squared $R^2$ values of 0.1 (F3B01-05) to 0.6 (F3B08-06) are found with the isotherms using the local domain; increasing to 0.6-0.7 using the extended domain. Adjusting for small phase lags (2 and 4 hours; local and extended model, respectively) $R^2$ values increases to 0.2-0.7 (local) and to 0.6-0.8 (extended). Correlations are lower with the currents, but still significant and equal to

0.5 for both the local and extended model results (F3B08-06). No improvement were found using lagged correlations on along-shore currents from either the local or extended models. In September, correlations were performed on day 9-29 window, as for the zero-crossing analysis performed earlier; taking into account the probable influence of past events on the first few days of the simulation and of complex signal interactions or internal mixing toward the end of the series. Overall, $R^2$ values are lower for the September events, however, only reaching about 0.3 (local) to 0.4 (extended) for the 4 °C isotherm depth and 0.2 (extended) to 0.3 (local) for the along-shore currents across all sites. Lagged correlations slightly improved the isotherm depth correlations of the extended model to 0.4 (with a lag of about 10 hours) and improved the currents from 0.2 to 0.4 (extended; 9 hr lag) and from 0.3 to 0.4 (local; 5 hr lag). Thus, for this period, the extended model did not improve the results. RMSE values on the order of 6-7 m for the isotherms and 0.1 m/s for the currents are found for both July and September events (and for both local and extended model results). In all cases but for the first event of July with the local model and with the extended model of July at F3B08-06 (both events), the observations were found to be leading the model; by a few hours, generally. Observation gaps affected the results; particularly at F3B08 where the 4 °C isotherm outcropped the observations for a large part of the series in July (8-16), i.e. times when the isotherm was located above the shallowest observation point (located around 20 m at F3B08). The lack of along-shore current data at F3B01, 05 and 07 was also a limiting factor.

# IDEALISTIC MODEL CASES

To investigate the effect of wind forcing direction on the response observed in Fortune Bay and untangle local vs. remote effects, idealized wind conditions were applied using summer hydrographic conditions. Only results from the extended mesh are considered; local vs. remote effects were investigated by applying wind forcing on a specific area of the mesh (Fortune Bay vs. Placentia Bay, respectively; see Figure 2).

Four main directions were chosen, representative of the main along and across-shore directions of Fortune Bay: northeast (NE), northwest (NW), southwest (SW) and southeast (SE). Note that while NW and SE are across-shore directions for Fortune Bay's main basin they are also along-shore directions for Belle Bay. For each direction, a 10 m/s wind speed (0.14 $N/m^2$ stress) was applied for 2 days with a linear ramp-up and ramp-down period of 6 hr to each end (i.e. 6 hr ramp-up, 36 hr full speed and 6 hr ramp-down). This can be considered as a strong, yet comparable, forcing scenario to the observations (Figure 4) and consistent with the findings of previous studies on typical cyclone activity in the region (Donnet et al., 2022; Plante et al. 2015).

Sensitivity tests were performed using a wind speed of 5 m/s (0.04 $N/m^2$) and using wind of same intensity (10 m/s) but lesser duration (1 day; same ramps than with the 2 d scenario) and resulted in much weaker responses for both scenarios and in both isotherms displacement and along-shore currents, as one would expect (see Figure S13 for illustrations). The propagation speed is comparable for all scenarios but the pulse generated (either upwelling under NE wind or downwelling under SW wind) is of smaller duration for both weaker and shorter wind forcing scenarios (by about a day at F3B08). These results indicate the need for relatively strong winds (>=10 m/s) and of sufficient duration (>1 d) to generate the type of response most visible in Figure 4 and presented herein.

## HOMOGENEOUS WIND

Figure 7 (top panels) illustrates the water column responses to NE and SW along-shore winds applied homogeneously on the whole extended domain. Wind was applied from run time t = 0 up until run time t = 2 days (d).

A SW wind forcing (left panel) initially generates a downwelling at F3B01&05 and upwelling at FB03&06 (first two days), consistent with expected Ekman transport. The amplitude of the response is about 5 m (F3B01) to 10 m (F3B05). This forced downwelling pulse, i.e. generated during the wind forcing, rapidly propagate cyclonically, reaching F3B08&04 during day 2, and F3B03&06 during day 3; therefore taking about 2 days to travel from F3B01 to F3B06. The downwelling pulse, which is about 2 d long, is followed by a much broader and somewhat weaker upwelling one which last about 5 d and which is followed by another downwelling pulse (from t = 7 d at F3B01), noticeably weaker also and more diffuse than the first downwelling one.

Under a NE wind forcing (right panel) an opposite response is initially felt: upwelling at F3B01&05 and downwelling at F3B03&06 (t = 1 d), while isotherms stay about flat at both F3B08&04. The amplitude of this initial response is about 15 m at F3B01 to 20 m at F3B05. About ½ day before the wind cease (t = 1.5 d), the upwelling signal arrives at F3B08 and then F3B04 and steadily develops for about 2-3 days. Shortly before the wind ceases a sharp downwelling is being generated at F3B01 (first) and F3B05 (about ½ day later). This downwelling pulse propagates cyclonically, clearly losing strength while doing so; the temperature front broadens (in time) and associated surface currents occupy less vertical space (from more than 50 m at F3B05 to less than 20 m at F3B06). In contrast, the upwelling pulse preceding the downwelling pulse seems to retain its strength, in both isotherm displacement and currents, from F3B08 to F3B06 (F3B04 currents being weaker is all simulations due to its position with respect to the jet; an effect of the coastline complexity of Belle Bay). The event, from its upwelling to downwelling phase (ingoing and outgoing flow) last about 5-6 days at all sites and it takes about 3 days for the downwelling pulse to travel around the bay from F3B01 to 06. Following the passage of this downwelling pulse, the isotherms gradually rise to return at the initial state.

Two main and distinct downwelling dynamics can thus be seen: a ‘forced’ pulse, generated during a SW wind event and a ‘relaxation’ pulse, generated right after a NE wind event ceased and occurring during the downwelling phase. In both cases, the upwelling phase occurring before (under NE) or after (under SW) the downwelling is associated with broader (time-wise) and weaker currents (and/or more constraint vertically). The relaxation pulse is characterized by a rather sharp front at its genesis (F3B01 & 05) which appears to flaten fairly quickly as it propagates around the bay. In contrast, the forced pulse appears to increase in strength (isotherms vertical displacement) during its propagation. The forced pulse is also sizeably quicker, taking about 2 days to propagate from F3B01 to F3B06 (180 km) vs 3 days for the relaxation pulse to travel the same distance; thus a factor 1.5 in phase speed (0.7 m/s vs. 1 m/s).

Responses from across-shore winds (NW and SE) are presented in the supplementary material (Figure S14) and are much weaker. Results from SE stress resemble that of SW (with about 1-2 d delay at all sites) but is much less dynamic (factor 2 or more) and results from NW show small and short downwelling occurring during the wind event at F3B01&05 (while F3B08&04 are upwelling) followed by the formation of a broad (2-4 d) and weak upwelling pulse at F3B01&05 and of a downwelling pulse from F3B08 to F3B06 (travelling cyclonically). As expected, however, Fortune Bay main’s basin along-shore stress response is much larger.

Similar cross-correlations than for the validation exercise were performed on the SW and NE forcing scenarios and are summarized in Table 2 (see also Figure S15 for illustrations). The results of those cross-correlations show that while the propagation of the signal has a constant phase speed under a NE wind forcing event (0.6-0.7 m/s, roughly equal to the free, mode 1, long internal wave speed found earlier; Figure 3) it varies significantly within the bay under a SW wind forcing event (by more than a factor 3 from F3B01-08 to F3B08-06). The amplitude of the response also differs between the two scenarios: while it stays about the same from F3B01 to F3B06 under a NE forcing it is much enhanced under a SW forcing. These results from idealized scenarios compare well with those of the real wind from July 2016 which indicated the same order in phase speed and its variability between the two main events identified and an enhancement of the signal during the first event versus an attenuation during the second event (Table 1). This suggests that the propagation of the first event of July would be dominated by the initial SW wind forcing response (downwelling favourable, locally) while the propagation of the second event of July would be dominated by the initial NE wind forcing response (upwelling favourable). It also indicates that while the propagation speed of an upwelling response (both forcing and relaxation phase) are about the same than the free, mode 1, long internal wave, the propagation speed of a downwelling response is much faster (by a factor 2) and that during locally downwelling favorable wind, a slow-down occur within the head of the bay (F3B08-06).

## LOCAL VS REMOTE WIND

During the validation exercise, important differences between the local and extended model results were noted, at moorings F3B01 & 05 during the July events, in particular (Figure 6 and Figures S8&9). The main difference between the local and extended mesh is the inclusion of the large neighbouring bay located to the east of Fortune (Placentia Bay; see Figure 1 and Figure 2). The differences in response are thus likely to originate from this latter bay since the signals are propagating cyclonically in Fortune Bay and that Placentia Bay is located upstream. To isolate the possible remote effects of Placentia Bay on Fortune Bay, same along-shore wind stress scenarios were run using the extended mesh but applying the stress on Fortune Bay area only (thereafter called ‘FB only’) and on Placentia Bay only (thereafter called ‘PB only’).

The results of a SW wind stress applied locally (FB only, Figure 7 left middle panel) are very similar to the results of the homogeneous wind. The first, and strongest, downwelling generated is essentially of the same strength (isotherms amplitude and associated currents) and appears to travel at the same speed than under a SW wind stress applied regionally (upper panel). The following broad upwelling is, however, slightly weaker (both in terms of isotherms migration and currents) than the one that occurs under homogeneous wind and no second downwelling appears either (after t = 7 d at F3B01). In contrast, the results of a local NE wind stress (right middle panel) are quite different. While the first upwelling is similar (in both strength and duration) the downwelling pulse that follows is markedly less strong and visibly broader than under the homogeneous wind scenario. This pulse also occurs later than during the homogeneous scenario, reaching F3B01 (and all the other sites) about 0.5-1 d later.

With a wind stress applied on PB only, the bottom panels of Figure 7 essentially show pictures of what a subtraction of local wind results from the homogeneous wind results would provide. Under a SW wind stress, a broad upwelling event occurs from t = 2 d at F3B01 and ends by a downwelling pulse which occurs after t = 7 d. Under NE wind, a strong and fairly broad downwelling event (about 20 m range, 4 days long) appears near the end of the wind event at F3B01 (t = 1.5 d) and propagates around the bay as under an homogenous forcing although a little quicker (about 1 day less for the pulse to reach F3B06 from F3B01).

Cross-correlation analyses results (Table 2 and Figures S16&17) show that a locally generated downwelling event (FB only, SW wind scenario) is the signal that propagates the most rapidly (2 d to reach F3B06 from F3B01) and is also the signal changing the most during its propagation with a phase speed propagation decreasing by a factor of 3 from F3B01-08 to F3B08-06 and a downwelling amplitude increasing by more than 200% (between F3B01&06); similarly to the homogeneous wind scenario and the first event observed in July 2016. In contrast, a downwelling event generated remotely (PB only, NE wind scenario) propagates at a near constant speed, slightly less than 1 m/s (thus higher than a freely propagating mode 1) and undergoes little amplitude change (7% between F3B01&06). Upwelling scenarios, whether locally or remotely generated (NE, FB only and SW, PB only, respectively) do not show much changes in amplitude but do show a change in propagation speed, decreasing by a factor of 2 from F3B01-08 to F3B08-06 (from about 1 m/s to 0.5 m/s, respectively).

These scenarios confirm that additional downwelling and upwelling events generated in Placentia Bay likely propagate into Fortune Bay and interact with existing local conditions; thereby either enhancing existing conditions (e.g. upwelling phase following the first downwelling pulse under SW forcing) or adding a separate event a few days later (e.g. second downwelling pulse under SW forcing). The largest difference in response is seen under the NE wind forcing scenario which results in a strong enhancement of the downwelling pulse, propagating vigorously around the bay. The difference between local and homogeneous scenarios is on the order of a factor 2 with this forcing, in both vertical migration of the thermocline and associated current pulse (20 vs 40 m and 0.25 vs 0.5 m/s at F3B01&05, respectively). The timing of the main downwelling pulse is also affected (occurring earlier under homogeneous wind), suggesting interactions between the two responses (i.e. local and remote). The results of cross-correlation analyses further points towards likely interactions between the local and remote response during a NE wind event. Hence, during such forcing, the local upwelling event slows down within the head of the bay (from 0.9 m/s between F3B01&08 to 0.4 m/s between F3B08&06) while the remote, downwelling, event travels at a constant speed all along (0.8 to 0.9 m/s); indicating a likely interaction (i.e. a downwelling pulse ‘catching-up’ on an upwelling pulse). Given that the time for the downwelling pulse generated in Placentia Bay to reach Fortune Bay also roughly correspond to the time by which the wind stress applied decreases to zero (1.5 d), downwelling enhancement can be expected. One can note that those 2 interactions act in opposite ways: while the ‘catching up effect’ should reduce the amplitude of the downwelling (via its interaction with an upwelling phase or existing conditions), the ‘timing of arrival’ should enhance the response. Effect on when the pulse will be observed around the bay also results from this interaction, by advancing the arrival of the downwelling pulse in that case (by about 0.5-1 d).

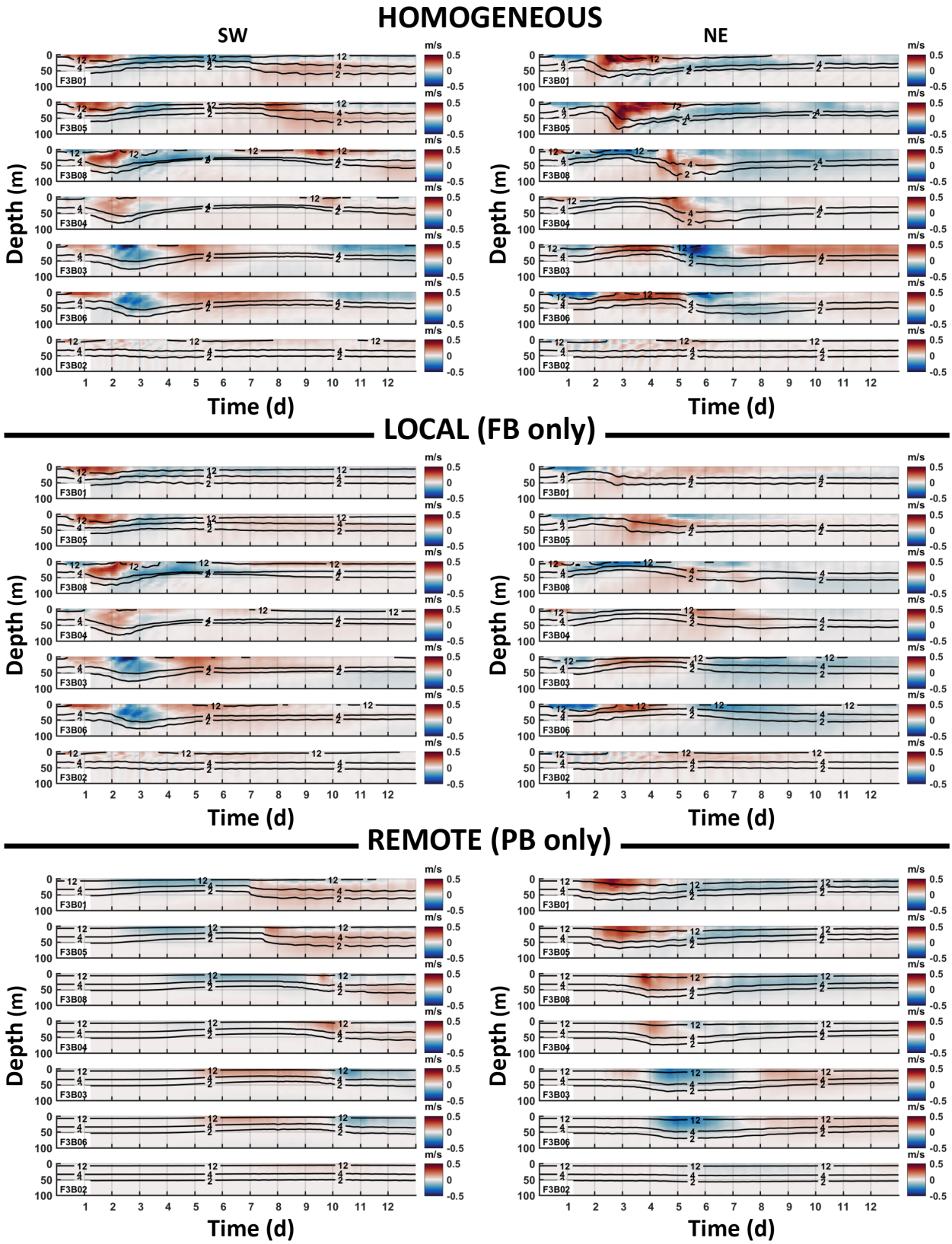


*Figure 7: Fortune Bay idealized along-shore wind model forcing results (Southwest, left panels, and Northeast, right panels, wind forcing). Isotherms 2, 4 and 12 °C are represented (black lines) over along-shore currents (blue to red colors, positive into the bay) at mooring locations F3B01, 05, 08, 04, 03, 06 and 02 (cyclonic distribution around the bay). X-axis represent run time elapsed, in days.*

*Table 2: lagged cross-correlation model results (extended mesh; idealized wind). Lag (L) is negative when first mooring of the pair is leading the second (e.g. F3B01 leading F3B06). C = phase speed calculated as distance between mooring pair (indicated in bracket) divided by L. DWdiff = Downwelling amplitude difference between the mooring pair; a positive sign indicate second mooring observed a larger downwelling than the first (e.g. F3B06 downwelling resulting from NE forcing was smaller than F3B01 one by 3 m).*

| Mooring pair | Wind forcing | R (lag=0) | Rmax (%var) | L (Rmax) | C | DWdiff (% change) |
|---|---|---|---|---|---|---|
| **F3B01-06 (180 km)** | SW Homogeneous | -0.35 (12%) | 0.60 (36%) | -1.8 d | 1.2 m/s | 14 m (272%) |
| **F3B01-08 (120 km)** | | 0.45 (20%) | 0.74 (55%) | -0.7 d | 2.0 m/s | 14 m (100%) |
| **F3B08-06 (60 km)** | | 0.45 (20%) | 0.96 (93%) | -1.2 d | 0.6 m/s | 0 m (0%) |
| | | | | | | |
| **F3B01-06 (180 km)** | NE Homogeneous | -0.64 (41%) | 0.81 (65%) | -3.2 d | 0.7 m/s | -1 m (8%) |
| **F3B01-08 (120 km)** | | -0.23 (5%) | 0.76 (58%) | -2.1 d | 0.7 m/s | 4 m (24%) |
| **F3B08-06 (60 km)** | | 0.57 (31%) | 0.95 (91%) | -1.1 d | 0.6 m/s | -5 m (26%) |
| | | | | | | |
| **F3B01-06 (180 km)** | SW FB only (local DW) | -0.50 (25%) | 0.63 (40%) | -2.1 d | 1.0 m/s | 14 m (259%) |
| **F3B01-08 (120 km)** | | 0.57 (33%) | 0.89 (80%) | -0.9 d | 1.5 m/s | 14 m (256%) |
| **F3B08-06 (60 km)** | | 0.25 (6%) | 0.91 (83%) | -1.3 d | 0.5 m/s | 0 m (1%) |
| | | | | | | |
| **F3B01-06 (180 km)** | NE FB only (local UW) | -0.40 (15%) | 0.74 (55%) | -3.2 d | 0.7 m/s | 2 m (8%) |
| **F3B01-08 (120 km)** | | 0.32 (10%) | 0.84 (70%) | -1.6 d | 0.9 m/s | 1 m (8%) |
| **F3B08-06 (60 km)** | | 0.55 (31%) | 0.96 (92%) | -1.6 d | 0.4 m/s | 0 m (0%) |
| | | | | | | |
| **F3B01-06 (180 km)** | SW PB only (remote UW) | 0.16 (3%) | 0.99 (97%) | -3.0 d | 0.7 m/s | -2 m (18%) |
| **F3B01-08 (120 km)** | | 0.67 (44%) | 0.96 (93%) | -1.6 d | 0.9 m/s | -2 m (15%) |
| **F3B08-06 (60 km)** | | 0.67 (45%) | 0.99 (98%) | -1.4 d | 0.5 m/s | 0 m (3%) |
| | | | | | | |
| **F3B01-06 (180 km)** | NE PB only (remote DW) | 0.31 (10%) | 0.95 (90%) | -2.5 d | 0.8 m/s | 1 m (7%) |
| **F3B01-08 (120 km)** | | 0.62 (39%) | 0.95 (91%) | -1.6 d | 0.9 m/s | 4 m (33%) |
| **F3B08-06 (60 km)** | | 0.86 (74%) | 0.99 (97%) | -0.8 d | 0.9 m/s | -3 m (20%) |

## SPATIAL ASPECTS

To determine the origin and scale (along and across-shore) of the downwelling and upwelling events, and better understand their propagation, surface maps illustrating the thermocline depth and currents of the surface layer were made (Figure 8 and Figure 9). Thermocline depth variation is represented using the depth anomaly of a selected isotherm. Same isotherm and depth-average procedure as for the validation exercise were used, i.e. 4 °C isotherm depth. Depth anomaly was calculated using a value of 35 m at rest (i.e. 4 °C depth value from the climatology profile used to initialize the model) and is positive downwards (i.e. downwelling are red and upwelling are blue).

Figure 8 shows the response under the idealized SW wind forcing scenario. 6 days are represented from when wind stress was fully applied (i.e. model run elapsed time = 1 day = 18 hr after ramp-up). Clear downwelling and upwelling areas are visible along the Burin peninsula shores (Fortune Bay side and Placentia Bay side, respectively); consistent with Ekman transport expectations. The onset of a downwelling is nearly immediate along the Fortune Bay side of the Burin peninsula (as seen at F3B01 and F3B05 in Figure 7) and is already propagating northward after 1 day. Behind this downwelling, the upwelling area occuring on the southern shore of the Burin Peninsula and along the Placentia Bay side increases in strength by day 2. After 2 days, the downwelling is concentrated in the northeastern end of Fortune Bay and in Belle Bay and is exiting the latter at t = 3 d. Meanwhile, the following upwelling propagates into Fortune Bay and is, itself, followed by another downwelling coming from the northern part of Placentia Bay. Strong currents are clearly associated with the downwelling and upwelling areas and enhancement of both thermocline migration and upper-layer current appear to occur in Belle Bay. The cross-shore length scale of the features is about 5 km; consistent with the estimate of internal Rossby radius presented earlier. The long-shore scale of the wave (i.e. downwelling + upwelling length) is on the order of twice the length of the Burin Peninsula, that is about 300 km; also consistent with previous estimates based on observations.

Under a NE wind forcing scenario (Figure 9), clear upwelling and downwelling areas are also visible along the Burin peninsula shores at t = 1 d; the situation being reversed from that of the SW scenario, i.e. upwelling on Fortune Bay side and downwelling on Placentia Bay side. As under the SW scenario, the downwelling and upwelling areas are clearly associated with the strongest currents. At t = 1 d, the downwelling has, in fact, already started to propagate and its ‘head’ is located at the southern tip of Fortune Bay. A day later (t = 2 d) the upwelling area moved up into BB while the downwelling is moving around the tip of the peninsula and is starting its propagation into Fortune Bay; F3B01 site being located close to the node between the upwelling and the downwelling. At t = 3 d, the downwelling has established itself along half the Fortune shore of the Burin peninsula. The northward progression of this downwelling continues at t = 4 d and it reaches Belle Bay (F3B08 & 04) at t = 5 d; turning cyclonically around its shores until exiting at run t = 6 d. The propagation of the upwelling illustrated here (Figure 9) and thus of the downwelling following it, is clearly slower than the downwelling locally generated under SW wind (Figure 8). Cross-shore and along-shore scales are however comparable with that of the SW scenario (about 5 km cross-shore and 300 km along-shore).

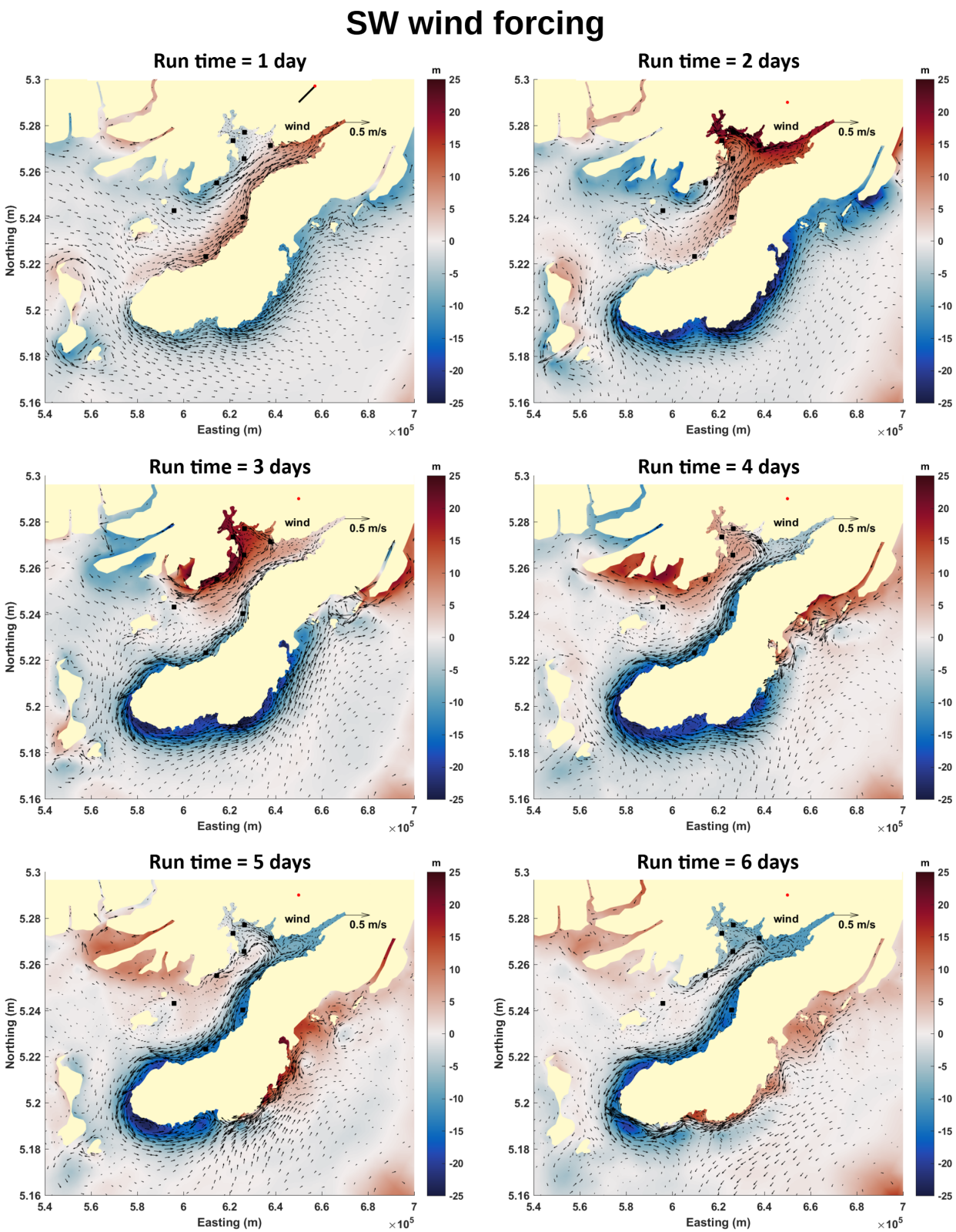


*Figure 8: isotherm 4 °C depth anomaly and upper layer current response under SW idealized along-shore wind forcing (2 days forcing). Positive anomaly (red) represents downwelling while negative anomaly (blue) corresponds to upwelling conditions. Upper layer current is depth-averaged from the surface down to the 4 °C isotherm depth. For clarity, the resolution was reduced by a factor of 5 to draw the arrows (currents). Black boxes represent the mooring sites listed in Figure 1.*

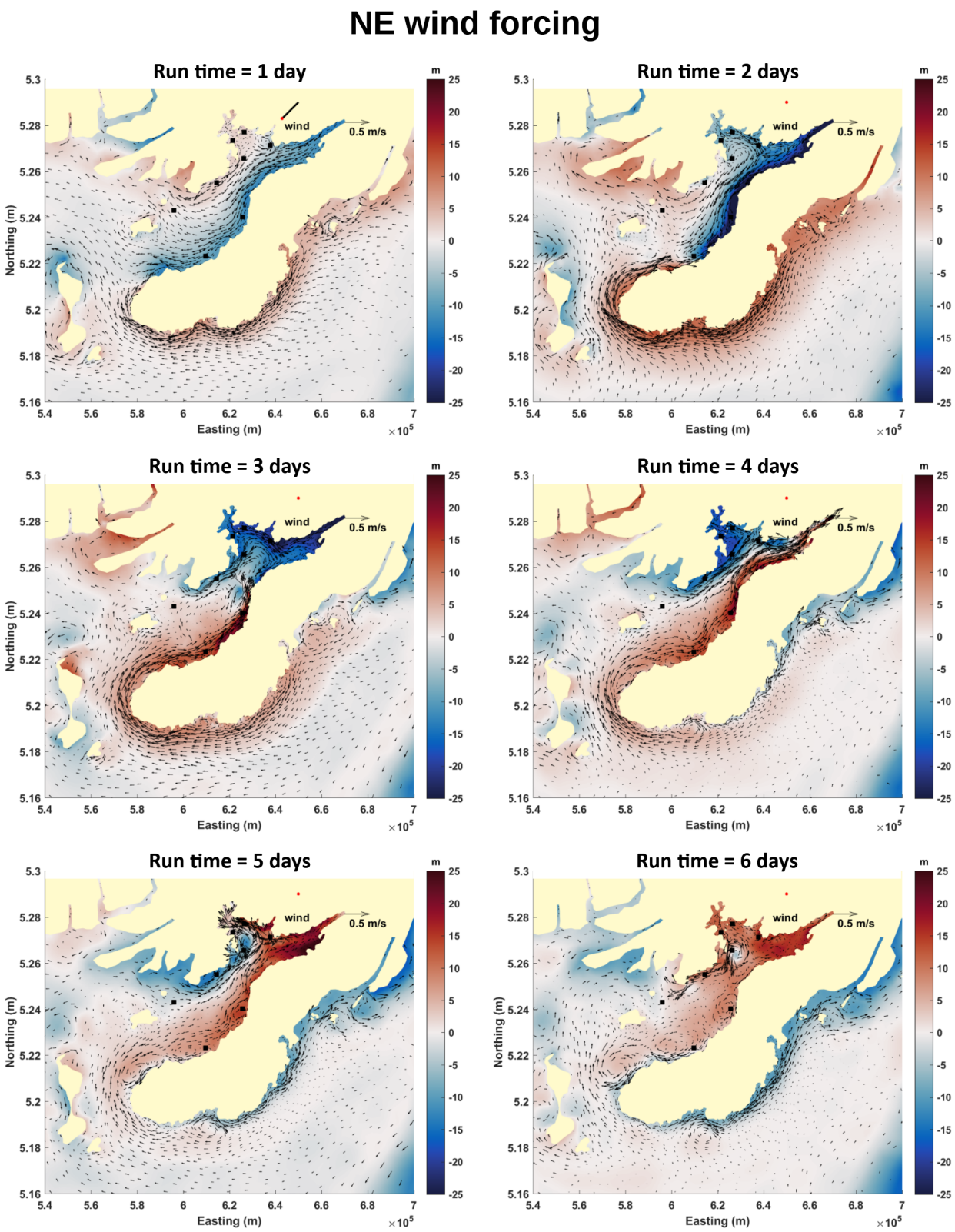


*Figure 9: isotherm 4 °C depth anomaly and upper layer current response under NE idealized along-shore wind forcing (2 days forcing). Positive anomaly (red) represents downwelling while negative anomaly (blue) corresponds to upwelling conditions. Upper layer current is depth-averaged from the surface down to the 4 °C isotherm depth. For clarity, the resolution was reduced by a factor of 5 to draw the arrows (currents). Black boxes represent the mooring sites listed in Figure 1.*

# DISCUSSION

The objectives of this paper are to: 1/ determine the nature of the dominant process acting in Fortune Bay during the stratified seasons and expressed as sub-inertial, baroclinic, signals (Donnet et al., 2022); 2/ determine the origin of this process (forcing and geographic) and 3/ describe its propagation within the fjord. We will now discuss the main results considering these objectives and what is known from the literature (theoretical or experimental studies).

## NATURE OF THE PROCESS

Fortune Bay' stratification and topographic characteristics, as embedded in the Stratification parameter S (i.e. ratio of internal Rossby radius to shelf-slope width) indicate that sub-inertial, coastally trapped motions, would take the form of baroclinic Kelvin waves in most of the fjord (S>>1). This hypothesis was tested using a fully non-linear, 3-dimensional, flat bottom numerical model initialised by climatological stratification and forced by wind only (both horizontally homogenous fields). This setup should only allow the CTWs generation of Kelvin nature in the sub-inertial band. Our model results show a rapidly responding system to wind forcing; generating Ekman transport and associated, geostrophically-balanced, coastal jet near the surface (Charney, 1955) and propagating signals around the bay (Figure 7). These signals take the form of downwelling and upwelling events associated with strong baroclinic currents which clearly dominate the response and have the characteristics of iKWs (e.g. unidirectional propagation and across-shore scale on the order of a Rossby radius). Owing to the shape of the bay, which is semi-opened on its western side, most of the energy exit before reaching its mouth, i.e. before reaching F3B02 (Figure 8 and Figure 9); thereby precluding excitation of potential natural oscillations (seiche) within the surface layers. Higher frequency signals (near-inertial) are produced and attributed to Poincare-type waves. While visible from the model results but not observed by in-situ measurements (most likely due to their proximity to the coast), those latter signals do not dominate the response (Figure 6). The model was shown to be capable of reproducing up to 80% of isotherms oscillations (i.e. downwelling and upwelling signals) and up to 50% of the upper layer along-shore current variability (Figures S8-11); strongly suggesting that iKWs dominate the response to wind forcing in Fortune Bay during summer. This result is consistent with a number of other studies which have shown the importance of this process in deep, stratified and broad embayment or large lakes (e.g. Csanady and Scott, 1974, Proehl and Rattray, 1984, Yao, 1986, de Young et al., 1993, Stoylen and Fer 2014, Inall et al., 2015, Fraser and Inall, 2018; the latter two being defined as CTWs but having characteristics close to that of Kelvin waves).

The existence of CTWs dynamics, which have recently been observed around the nearby archipelago of Saint-Pierre and Miquelon (Lazure et al., 2018) should not be excluded, however, particularly in the outer part of Fortune Bay where the shelf-slope widen. At F3B01 and 05 locations, for instance, the shelf-slope width is on the order of 10-15 km, leading a stratification parameter of 0.4-0.6 (thus, <1). The shelf is also noticeably larger and more complex (with the presence of islands) on the Placentia Bay side (Figure 1). The presence of a non-negligeable shelf-slope region would have 3 main consequences (see Brink, 1991 for a review of CTW characteristics): the modal structure of the signals would be more complex (on the vertical) with the nodes extending offshore (see Figure 6 of Masoud et al., 2019 for a recent and illustrative investigation of this in the Caspian Sea for a studied shore of ~500 km long and 30-300 km varying shelf-slope width and S values ranging from slightly less than 1 to more than 10), the phase speed would

decrease (for the baroclinic signals) and a larger barotropic signal would be observed (e.g. on sea level). The presence of CTW-like dynamics may, at least partially, explain the larger differences found between the observations and our model results at F3B01 and F3B05 (Figure 6 and Figures S8-11). A number of model runs were attempted using a realistic bathymetry but proved to be unsuccessful due to over-mixing issues. Keeping stratification over steep slopes and in the presence of large vertical isopycnal variations such as presented here is a well known challenge for terrain-following coordinates models such as FVCOM (see Haney, 1991 and Mellor et al., 1994 for a discussion on this). Despite increasing the horizontal resolution down to 100 m and smoothing the bathymetry to reduce the gradients, experimenting with a range of dH/H of 0.3 to 0.5 (where dH is the maximum depth change and H is the mean depth of any given mesh cell; see Foreman et al. 2009) we were not able to resolve this issue satisfactorily.

# ORIGIN OF THE PROCESS

Given the close representation of the (raw) observations by the model, which is solely forced by wind, we can deduce that the latter is the main forcing mechanism responsible for the dominant sub-inertial and baroclinic dynamics observed in Fortune Bay in summer (with periods of the order of a few days). This is consistent with and complement previous observations-based findings which showed a modest contribution of the tides (9-34%; weakest at the head, in Belle Bay, and strongest at F3B02) and a weak mean seasonal circulation (order of 1-5 cm/s; Donnet et al., 2022).

By implementing the model (and forcing) on two geographical areas, one centered on the fjord (local area) and one including the neighboring bay to the east (extended or remote area), we show that the response observed is both from local and remote, i.e. neighboring bay, origin. Most of the variability appears to be locally generated from southwesterly winds which result in rapidly propagating downwelling pulses around the fjord (about 2 days propagation time) as observed in early July 2016 and in September 2016 (Figure 5). The largest events observed such as the one of July 13-20, 2016, however, are generated by winds shifting from the northeast to the southwest which result in an upwelling event generated in the fjord and a downwelling event generated in the neighboring bay. If timing is right and that the remotely generated downwelling event arrives in the fjord at the same time that the locally generated upwelling is relaxing, e.g. due to wind dropping or changing direction, both signals adds-up and a larger downwelling occurs (Figure 6A). Results from idealized scenarios, used to better understand the process, show that it takes about 1.5 day for a remotely generated downwelling event to arrive in Fortune Bay at our sampling site F3B01 (Figure 7). The resulting amplification, in both isotherms migration and along-shore currents, can be large and found to be of the order of a factor 2 under the scenarios used in this study (which were similar to the main events observed). Considering a typical cyclone duration of about 4 days in the region (Plante et al., 2015), a 2-day duration for a 180° shift in wind direction could be quite common as seen during the periods selected for our study (July and September 2016; Figure 5). This regional periodicity in wind direction is further indicated by the earlier work of Yao (1986) who found significant coherence between the along-shore wind stress and upper-layer along-shore currents within a 0.2 cpd frequency band, i.e. 5 days period, in the similarly oriented and geographically close Trinity Bay (about 100 km northeastward from Fortune Bay; Figure 1). Thus, downwelling enhancement during NE-SW wind events might be quite common in Fortune Bay.

Although much weaker, remote effects from SW winds also occur and are mainly expressed as a broad upwelling event, about 6 d in duration, followed by a downwelling pulse propagating in the fjord about 5

days after a wind event (i.e. from t = 7 d at F3B01, Figure 7). While the upwelling phase comes from the western side of Placentia Bay, along the burin peninsula (and generated from Ekman transport as for the remote downwelling discussed earlier under NE forcing), the downwelling pulse comes from the eastern side of the bay (Figure 8 and Figure S18 for a broader view). Similarly, a weak upwelling signature, propagating from that shore is also apparent after a NE wind event (seen in Figure 9, t = 3-6 d snapshots, in particular) and would, should no counter-forcing mechanism or complete dissipation to occur, make its way into the fjord.

In fact, given the complexity of the coastline, wind from any direction can generate a response in Fortune Bay. The scale of the response is determined by the length of the coast, anywhere in Fortune and/or Placentia Bay, that is oriented along the wind and where the offshore scale allows Ekman transport to take place, i.e. where it is larger than the internal Rossby radius (e.g. Crepon and Richez, 1982). The focus of this study was on investigating the dominant coastal responses, therefore those induced by wind acting along the main axis of the fjord (which also happen to be the main axis of a peninsula), i.e. under either NE or SW forcing. Yet, simulations using across-shore winds, i.e. winds from the NW or SE show that responses are also generated, which are on the order of a factor 2 less in strength (being isopycnal vertical variation or baroclinic, along-shore, currents) from that of the along-shore winds (Figure S14).

With respect to the wavelength of the response, additional model runs show how winds from the NW and SE can induce upwelling and downwelling, respectively, around the southern end of the Burin Penninsula which are about half as large (in length) than those induced by NE and SW winds (Figure S18). The response is also complicated by the existence of constricted places smaller than the internal Rossby radius, such as the head of Belle Bay, where upwelling and downwelling can occur upstream or downstream wind forcing, respectively. Our model, using a much simplified northern and eastern coastline of Placentia Bay, also shows that upwelling and downwelling signal generated along those coasts could propagate into Fortune Bay (as discussed above). It is probable, however, that this latter effect be attenuated with the complexity of the real coastline. Nevertheless, and under a continuously variable wind field, the dynamics of Fortune Bay are likely to be the result of a combination of responses occurring at different places and time in both Fortune Bay and Placentia Bay and around the Burin Peninsula, in particular. The strength and duration of the response being a function of forcing strength, duration and direction (Figures S13-14).

# SIGNAL PROPAGATION

Having determined the nature of the process as well as its forcing and geographic origin, a last important piece of the puzzle is to understand its propagation. We will attempt to do so by further describing the observations and combining the model results.

The most striking propagation characteristic found from both observations and model simulations is the coherence of the signal, propagating cyclonically around the bay (Figure 5 and Figure 7) and supporting the hypothesis of a coastally trapped wave of Kelvin properties. The second most striking aspect concerns the variation in phase speed and amplitude of the signal (summarised in Table 1 and Table 2). That is, a factor 3-4 (200-300%) change in signal amplitude associated with a factor 3 change in propagating speed for a locally generated downwelling event and a factor 2 difference in phase speed between a locally generated downwelling event and a remotely generated one that follows a local upwelling event between F3B01 and F3B06. The last notable observation was the apparent change of signal frequency from the outer to the

inner part of the bay during the more frequent event of September (factor of 2 change).

Results from the model using idealized wind forcing applied homogeneously over the whole model domain suggest two main things: that the first event observed in July was dominated by the propagation of a locally forced and rapidly propagating wave while the second event observed was dominated by a much slower and freely propagating wave and that there must exist factor(s) influencing the amplitude of the response during its propagation which do not act similarly during a forced vs freely propagating response and/or on a downwelling vs. upwelling phase. Results from further idealized model scenarios in which the wind was set to blow on a limited area of the extended model (either Fortune Bay or Placentia Bay) give us more insight. The results of these scenarios are summarized and compared, along with the homogeneous wind scenarios mentioned above in Figure 10 (see also Figures S16&17 and Table S1 for more details).

Figure 10 shows that a SW wind, solely applied on Fortune Bay (FB only line) generates a rather narrow downwelling, about 2 d duration, at F3B01 (panel A) followed by a long plateau of slightly upwelled waters (-5 m isotherm depth anomaly). The shape of this wave is 'solitary-like', i.e. crest only with no through, and is 5 m in amplitude. This downwelling peak then increases drastically to attain a maximum of 20 m amplitude at F3B06 before rebounding somewhat less vigorously towards a neutral position and then rising slowly after t = 6 d (panel B). Overall, the downwelling duration increases from 2 d at F3B01 to about 4 d at F3B06. The phase speed of this event changes drastically, from 1.5 m/s between F3B01 and 08 to 0.5 m/s between F3B08 to 06; similarly to the SW homogeneous wind scenario (Table 2) and comparable with the observations of the first event of July 2016 (Table 1). Thus, with a phase speed decreasing by a factor 3 between F3B08 and F3B06 but a period (duration) only doubling, the wavelength of this event must have reduced to about 2/3 from its original size. Simultaneously, a SW wind applied on Placentia Bay only (PB only line) generates a much broader upwelling event at F3B01, of about 6 d in duration, followed by a slow downwelling phase. Arrived at F3B06, this upwelling event lost a little of its strength, decreasing in amplitude by about 25% from F3B01 (from about 13 m to 10 m) but stays about the same in duration; thus retaining much of its shape (and wavelength) unlike the signal generated in Fortune. This upwelling event also slowed down along the way, by a factor 2 from F3B01-08 to F3B08-06 (0.9 m/s to 0.5 m/s). Linearly adding those two signals together (FB+PB dash lines) results in a pattern similar to that of the homogeneous SW wind forcing scenario applied to the whole model domain (SW whole) at both sites, indicating a near-linear interaction between the two events.

A local NE forcing (FBonly line; Figure 10C&D) also generates a narrow (in time) but large (in amplitude and in comparison to the corresponding SW result; 15-20 m rise vs. 5 m down, respectively) upwelling. This event broadens dramatically from a duration of about 3 d at F3B01 to more than 8 d once arrived at F3B06 all the while retaining its large amplitude. Given that its phase speed decreased by a factor 2 between F3B08 and 06 (from 0.9 m/s between F3B01&08 to 0.4 m/s from F3B08&06; Table 2) the wavelength of this event thus increased to about 3/2 its original size (using a event duration of 9 d at F3B06). On the other hand, the downwelling event generated remotely (PB only lines) keeps its shape all along from F3B01 to F3B06 (about 12.5 m amplitude and 6 d duration) and propagates at a constant speed (about 0.8 m/s; Table S1). This propagation speed is, however, slightly higher than the locally generated upwelling one (2.5 days to propagate from F3B01 to 06 vs. 3.2 days for the upwelling). The main difference in speed occurs between F3B08&06 (0.4 m/s for an FB event vs. 0.9 m/s for a PB event; Table S1) and indicates that interaction between those two events may occur (probably upstream, though). Adding the signals together (dashed line) leads to a result markedly different from the whole domain forcing scenario (NE whole) this time,

particularly at F3B06; indicating that non-linear effects are important in the interaction of the responses (local with remote) from a NE forcing. As with the SW forcing, the local response can largely be described as a solitary-like wave while the remote wave presents a rising part which would suggest a more sinusoidal-like shape once/would the system return to a state of rest. This latter phase, can be attributed to the upwelling pulse generated on the east side of Placentia bay and making its way into Fortune, however, i.e. a second remote effect (Figure 9).

In summary, the ocean response to wind forcing in Fortune Bay is the result of complex interactions between locally generated forced waves and remotely generated, and freely propagating, waves. Forced waves change shape drastically during their travel in Fortune Bay, either in amplitude (SW case) or in duration (NE case). In both cases, their propagation speed also change importantly along the way but more so in the case of a forced downwelling event (factor 3 change) than of a forced upwelling event (factor 2 change). Overall, a forced downwelling event (SW forcing) will propagate about 1.5 time faster than a forced upwelling event (NE forcing) taking 2 days for the peak of the current pulse to reach F3B06 for the former vs. 3 days for the latter. On the other hand, remotely generated waves do not change shape significantly during their travel in Fortune Bay. They do propagate at different speed, however; a downwelling event travelling more rapidly than an upwelling one (by about 20%). This difference mainly occur in the head of bay where the upwelling undergoes a slow down (factor 2; 0.9 m/s to 0.5 m/s) while the downwelling propagation speed stays constant all along (0.8-0.9 m/s). The combination of those signals (local + remote) results in the generation of a strong but rather narrow (in time) and rapidly propagating downwelling, increasing in amplitude along the way (the local response) followed by a much broader and more slowly propagating upwelling (the remote response) in the SW case (Figure 10A&B). This combination is largely linear. In the NE case (locally upwelling favorable), the combination result in a broadening (along the way) and slowly propagating upwelling (the local response) followed by a sharp downwelling front propagating more rapidly (the remote response) and which is substantially attenuated in amplitude along its way (by about 30%; Figure 10C&D) presumably due to the interaction between the two signals. This combination is rather non-linear. Overall, the combined response from a SW forcing propagates at about the speed of a local, forced downwelling wave (about 2 days to go around the bay) while the combined response from a NE forcing propagates at a comparable speed than a forced, locally generated upwelling one (about 3 days to go around the bay). Thus, the propagation of the combined wave appear to be dominated by the propagation of the leading (local) wave.

In September, good performance of the local model indicates the dominance of local responses to forcing (Figure 6). The situation is rather complex, however, since that while the 3 main downwelling events propagating from F3B08 to F3B06 can be understood as (mainly) local responses resulting from the 3 main SW wind events, it is unclear why higher frequency signals would occur downstream at F3B01&05 (Figure 5). Remote effects, as described above, should somewhat temper locally generated downwelling by bringing upwelling pulses about 2 days after each wind event and last for about 5 d after (Figure 7 and Figure 8). These upwelling are indicated by the rising of the 2 °C in (e.g. from September 13, 18 and 22) but the first two are rather quickly followed (~1-2 d) by another downwelling pulse from unknown origin (September 14-15, 19). Remote effect from the east side of Placentia Bay, expressed as a downwelling arriving 5 d after the end of a wind event (Figure 7) is therefore unlikely given these short intervals. Possibly, and given the frequency of wind events during this period of the year (Figure 4), the system was far from being at rest at the beginning of the series studied and those pulses may be the reminiscence of previous wind events. As

such the system has an “effective memory” from previous forcing (see Beletsky et al., 1997 for a use of this terminology). Under SW wind, for instance, the effects of 1 event of 2 d duration could last for more than 2 weeks according to the results presented herein (2 d forcing + 2 d propagation + 5-6 d first remote response + 5-6 d for the second remote response). Yet, the “low-pass” filtering of those frequent events occurring in the outer part of the bay (F3B01&05) by the inner part of the bay (F3B08-06) is also unclear. Since the length of Belle Bay is about a quarter of that of Fortune Bay (30 km vs. 120 km, respectively), resonance effects could be suspected. However, this would translate into an amplification of the signal and a periodicity of about 2.5 d (with a natural mode phase speed of 0.6 m/s). Neither effects are seen in the observations: the amplitude of the events are comparable across sites and the periodicity is of 6 d (3 events in 20 d). Possibly, the large slow-down of locally generated downwelling event in the inner part of the bay described above (factor 3) could have an influence and effectively “merge” several fast travelling pulses arriving from the outer bay. A more throughout analysis of this latter possible interaction would be, however, necessary to better elucidate these observations.

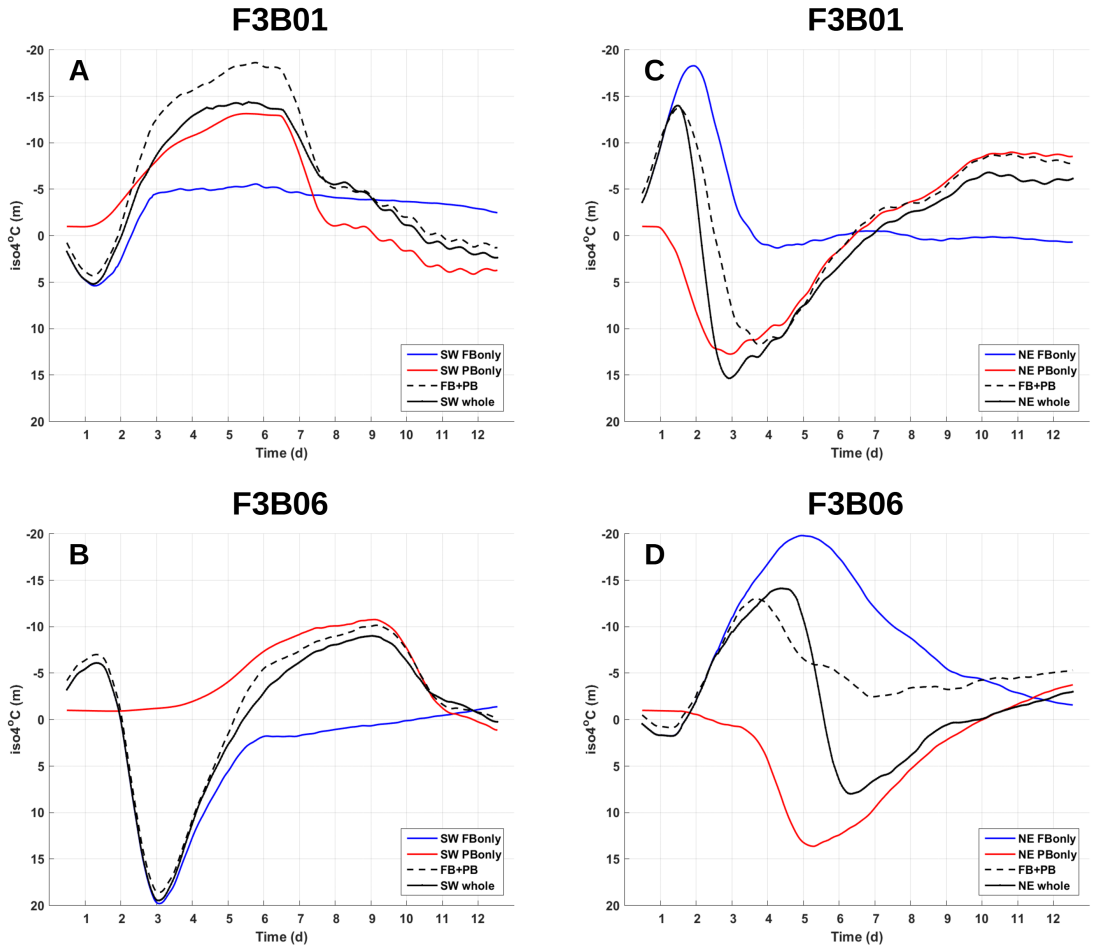


*Figure 10: isotherm 4 °C depth anomaly (iso4 °C) at F3B01 (top) and F3B06 (bottom) and under various idealized model scenarios. SW FB only = southwest wind forcing applied on Fortune Bay area only, SW PB only = southwest wind forcing applied on Placentia Bay only, FB + PB = sum of FB only and PB only scenarios, SW whole = southwest wind forcing applied over the whole model domain (i.e. over FB and PB areas); NE = northeast wind forcing. Note: series were low-pass filtered using a 24 hr window running-average.*

# CONCLUSION

Since the early observations of Mortimer (1968) and others made in the great lakes in the 60s and 70s a large number of studies have described the occurrence and importance of internal Kelvin waves in the coastal environment (as listed in the introduction). Interestingly, it appears to us that most of those works have focused on the upwelling phase of the process; most likely due to the importance on the fisheries. In this study, a lot more emphasis was given to the downwelling phase due to the visibly stronger dynamics it involves, i.e. stronger and larger vertical extent of the along-shore currents. This, in turn, certainly has importance with respect to the dispersal of marine larvae and of any type of organic or inorganic particles resulting from natural or human activities that can occur in this region.

With respect to numerical modelling efforts, it is certainly worth citing the early work of Suginohara (1974) and the (later) work of Beletsky et al. (1997). The former was probably one of the first to illustrate the solitary-like shape of a propagating upwelling, along a strait coast, in details. He was also able to generate both an iKW propagating the generated upwelling and a CSW under the presence of a simplified shelf-slope bottom although with limited coupling (stated as “negligibly small”). Here, we show that the upwelling and downwelling events generated around a peninsula appear as long and large solitary-like waves (of Kelvin properties) which can interact (NE wind scenario). Beletsky et al. (1997) reproduced the propagation of iKWs in broad lakes (idealized and realistic shape) and nicely illustrated the marked difference between the ‘cold front’ (upwelling) and ‘warm front’ (downwelling); the latter being much sharper. Our results corroborate this finding (e.g. see our Figure 10 vs their Figures 4 and 6) and seem to further support the early theoretical work of Bennett (1973) who showed that non-linearity steepens the downwelling phase of Kelvin waves (see his Figures 2 & 3, in particular). Beletsky et al. (1997) also showed that with the presence of an idealized (parabolic) sloping bottom, the dissipation increases noticeably. While our model simulations do overestimate the amplitude of some of the downwelling events they marginally overestimate the along-shore currents (Figure 6 and Figure S8-11). This suggests that bottom dissipation might not be that important in Fortune Bay, although more analyses and model runs with realistic bathymetry would be necessary to properly assess this aspect. With respect to upwelling dynamics in broad fjords, another study worth citing is that of Cushman-Roisin et al. (1994). Their study mainly used a rather simple (and linear) analytical model of ‘wind impulse’ originally proposed by Csanady (1977) and which assumes steady state (of the response). They showed that cross-shore interaction (in terms of offshore extent of upwelling and downwelling fronts) were possible even when the width of the fjord is larger than the internal Rossby radius (in their case, about 3 times larger). They also showed that the depth of the fjord could be a limiting factor in the amplitude of the response (to a lesser degree than the presence of an other coast that would be felt, however). We did not investigated the potential ‘wall-to-wall’ effects, i.e. width of the fjord effects, in details but showed that the cross-shore scale of the process is indeed that of the internal Rossby radius and that the wave does have the necessary room to circulate cyclonicly around the fjord. The complicated coastline, however, and, in particular, the presence of a rather narrow inlet at one end and of a large side bay (Belle Bay) may explain, at least partly, the changes in wave shape that we found (e.g. increase of amplitude and reduction in wavelength during a locally forced downwelling). More recently, a number of numerical model based studies have investigated the propagation of CTWs and their associated remote effect either on different sections of a coastline (e.g. Batifoulier et al., 2012, Illig et al., 2018) or on a large fjord (e.g. Fraser et al. 2018). They all show the great distance those signals can travel (100s to 1000s of km) and, therefore, the importance of remote effects on any coastal location subject to such processes.

Regionally, in Newfoundland, the studies of Yao (1986), de Young et al. (1993) and Davidson et al. (2001) were a strong motivation and had an important influence in our early reflections on Fortune Bay. In a sense, the Fortune Bay – Placentia Bay system could be considered somewhat as a 'mirror-image' of the Trinity Bay – Conception Bay system investigated by these earlier researchers given their common geographic characteristics (seasonally stratified wide and deep bays, mainly oriented SW-NE on two opposite coasts; Figure 1). Interestingly, Yao used the linear theory of Gill and Clarke (1974) and was rather successful in understanding the propagation dynamics by assuming a continuity of the wave along Trinity Bay, i.e. an upwelling on one side (west, under SW wind) and downwelling on the other side forming a 'complete' wave with well defined crest (upwelling phase) and through (downwelling phase). De Young et al. (1993) were also largely successful in reproducing remote effects using a linear reduced-gravity model, thus not considering topographic nor non-linear aspects. Davidson et al. (2001) used a fully non-linear model and run sensitivity tests with a realistic bathymetry. They showed that non-linearity increased the alongshore asymmetry of the response between the opposite coasts of the bay while adding a realistic bathymetry did not significantly affect near-surface currents. Those previous studies, however, did not investigate the potential interactions between the local and remote responses in great details (e.g. between upwelling and downwelling events). In this study, we got more insight in separating the process into local and remote responses. The resulting dynamics then appear as a combination of solitary-like waves generated both locally and remotely (neighbouring bay). The combination of those does form a 'sinusoid-like' wave around the penninsula responsible for the generation of those positive (say, downwelling) and negative (say, upwelling) phases but they also appear to interact with one-another, i.e. a leading wave largely determining the propagation speed while a following wave potentially enhancing the response (as seen during the large downwelling event of late July 2016). We showed that this combination can be rather non-linear and that important changes in the locally generated response occur during its propagation (amplitude and wavelength).

While we hope to shed more light regionally and to provide a useful contribution to the broader field of coastally trapped iKW, this study is not without significant limitations. Perhaps the most important of all is on its use of a simplified model with absence of a realistic bathymetry. As such, we may respond to the original hypothesis of iKW dynamics but fall short in reproducing the more comprehensive motions of CTWs. The effect of the bay's shape, and the reflection in its large (but complex in shape) head in particular, would also benefit from further investigations to better understand the propagation of the waves and their changes in wavelength and amplitude. Simplifications in the model setup with its absence of air-sea and shelf exchanges, notably, preclude the use of the model for long period of time (e.g. seasonal scale). In this study, we found that the model could reasonably be run over a period of 20 days but that finding a state of rest to initialize the model over such period of time could be difficult, especially during the fall, when wind forcing is nearly continuous. Estuarine and mean circulation (e.g. influenced by the shelf), which are of importance when considering water renewalls, could also not be assessed via this study and the results of this model.

Nevertheless, the good performance of the model in reproducing the observations, unfiltered from the effects of the processes mentioned above and ignored by the model, indicates the dominance of the process examined here (i.e. iKW) and the potential for the model results to be used for further studies such as for fisheries and aquaculture-environment interactions. In particular, studies of crustacean larvae (e.g. lobster), sea-lice and viruses dispersion affecting aquaculture activities, which are all of economic

importance regionally as well as of dissolved oxygen availability, which depends on water temperature and which recently resulted in significant farmed fish losses (Fisheries and Marine Institute of Memorial University of Newfoundland, 2020) would greatly benefit from the use of such results. Issues related to organic loading from aquaculture farms, however, would certainly need a further development of the model including bathymetry features to be reasonably realistic. Nevertheless, and until the availability of a more realistic model, those results could still help provide with some first estimates.

# ACKNOWLEDGMENTS

This research was supported by the Aquaculture Collaborative Research and Development Program (project #15-1-N-02). It was enabled in part by support provided by ACENET (https://www.ace-net.ca/), BC DRI Group and the Digital Research Alliance of Canada (alliancecan.ca). SD would also like to thanks Adam Drozdowski for his helpful discussions, his help in sourcing ECCC's HRDPS model data and help in trying to implement a more realistic bathymetry.

# REFERENCES

Albrecht, N., Vennell, R., Williams, M., Stevens, C., Langhorne, P., Leonard, G., Haskell, T., 2006. Observation of sub-inertial internal tides in McMurdo Sound, Antarctica. Geophys. Res. Lett. 33, L24606. https://doi.org/10.1029/2006GL027377

Batifoulier, F., Lazure, P., Bonneton, P., 2012. Poleward coastal jets induced by westerlies in the Bay of Biscay. J. Geophys. Res. 117, https://doi.org/10.1029/2011JC007658

Beletsky, D., O'Connor, W.P., Schwab, D.J., Dietrich, D.E., 1997. Numerical Simulation of Internal Kelvin Waves and Coastal Upwelling Fronts. Journal of Physical Oceanography 27, 1197–1215. https://doi.org/10.1175/1520-0485(1997)027<1197:NSOIKW>2.0.CO;2

Bennett, J.R., 1973. A Theory of Large-Amplitude Kelvin Waves. Journal of Physical Oceanography 3, 57–60. https://doi.org/10.1175/1520-0485(1973)003<0057:ATOLAK>2.0.CO;2

Brink, K., 1991. Coastal-trapped waves and wind-driven currents over the continental shelf. Annual Review of Fluid Mechanics 23, 389–412.

Burger, A.P., 1958. Scale Consideration of Planetary Motions of the Atmosphere. Tellus 10, 195–205. https://doi.org/10.1111/j.2153-3490.1958.tb02005.x

Carmack, E.C., Kulikov, E.A., 1998. Wind-forced upwelling and internal Kelvin wave generation in Mackenzie Canyon, Beaufort Sea. J. Geophys. Res. 103, 18447–18458. https://doi.org/10.1029/98JC00113

Chao, Y., Li, Z., Farrara, J.D., Hung, P., 2009. Blending Sea Surface Temperatures from Multiple Satellites and In Situ Observations for Coastal Oceans. Journal of Atmospheric and Oceanic Technology 26, 1415–1426. https://doi.org/10.1175/2009JTECHO592.1

Charney, J., 1955. Generation of oceanic currents by wind. J. Marine Res. 14, 477–498.

Chen, C., Beardsley, R.C., Cowles, G., Qi, J., Lai, Z., Gao, G., Stuebe, D., Liu, H., Xu, Q., Xue, P., Ge, J., Hu, S., Ji, R., Tian, R., Huang, H., Wu, L., Lin, H., Sun, Y., Zhao, L., 2013. An unstructured grid, finite-volume community

ocean model FVCOM User Manual, v3.1.6 (User Manual No. SMAST/UMASSD-13-0701, 4th ed.). University of Massachusetts-Dartmouth and Woods Hole Oceanographic Institution.

Chen, C., Liu, H., Beardsley, R.C., 2003. An Unstructured Grid, Finite-Volume, Three-Dimensional, Primitive Equations Ocean Model: Application to Coastal Ocean and Estuaries. Journal of Atmospheric and Oceanic Technology 20, 159–186. https://doi.org/10.1175/1520-0426(2003)020<0159:AUGFVT>2.0.CO;2

Chin, T.M., Vazquez-Cuervo, J., Armstrong, E.M., 2017. A multi-scale high-resolution analysis of global sea surface temperature. Remote Sensing of Environment 200, 154–169. https://doi.org/10.1016/j.rse.2017.07.029

Crépon, M., Richez, C., 1982. Transient Upwelling Generated by Two-Dimensional Atmospheric Forcing and Variability in the Coastline. Journal of Physical Oceanography 12, 1437–1457. https://doi.org/10.1175/1520-0485(1982)012<1437:TUGBTD>2.0.CO;2

Csanady, G., 1977. The coastal jet conceptual model in the dynamics of shallow seas. The sea 6, 117–144.

Csanady, G.T., Scott, J.T., 1974. Baroclinic Coastal Jets in Lake Ontario during IFYGL. Journal of Physical Oceanography 4, 524–541. https://doi.org/10.1175/1520-0485(1974)004<0524:BCJILO>2.0.CO;2

Cushman-Roisin, B., Asplin, L., Svendsen, H., 1994. Upwelling in broad fjords. Continental Shelf Research 14, 1701–1721. https://doi.org/10.1016/0278-4343(94)90044-2

Cyr, F., Snook, S., Bishop, C., Galbraith, P.S., Chen, N., and Han, G. 2022. Physical Oceanographic Conditions on the Newfoundland and Labrador Shelf during 2021 (DFO Can. Sci. Advis. Sec. Res. Doc. 2022/040). https://waves-vagues.dfo-mpo.gc.ca/library-bibliotheque/40960754.pdf (accessed 26-Sep-2022)

Davidson, F.J.M., Greatbatch, R.J., de Young, B., 2001. Asymmetry in the response of a stratified coastal embayment to wind forcing. J. Geophys. Res. 106, 7001–7015. https://doi.org/10.1029/2000JC900052

de Ruggiero, P., Napolitano, E., Iacono, R., Pierini, S., Spezie, G., 2018. A baroclinic coastal trapped wave event in the Gulf of Naples (Tyrrhenian Sea). Ocean Dynamics 68, 1683–1694. https://doi.org/10.1007/s10236-018-1221-1

de Young, B., Hay, A.E., 1987. Density Current Flow into Fortune Bay, Newfoundland. J. Phys. Oceanogr. 17, 1066–1070. https://doi.org/10.1175/1520-0485(1987)017<1066:DCFIFB>2.0.CO;2

de Young, B., Otterson, T., Greatbatch, R.J., 1993. The Local and Nonlocal Response of Conception Bay to Wind Forcing. Journal of Physical Oceanography 23, 2636–2649. https://doi.org/10.1175/1520-0485(1993)023<2636:TLANRO>2.0.CO;2

Donnet, S., Ratsimandresy, A.W., Goulet, P., Doody, C., Burke, S., Cross, S., 2018a. Coast of Bays Metrics: Geography, Hydrology and Physical Oceanography of an Aquaculture Area of the South Coast of Newfoundland (DFO Can. Sci. Advis. Sec. Res. Doc. No. 2017/076). https://waves-vagues.dfo-mpo.gc.ca/library-bibliotheque/40655945.pdf (accessed 26-Sep-2022)

Donnet, S., Cross, S., Goulet, P., Ratsimandresy, A.W., 2018b. Coast of Bays seawater vertical and horizontal structure (2009-13): Hydrographic structure, spatial variability and seasonality based on the Program for Aquaculture Regulatory Research (PARR) 2009-13 oceanographic surveys (DFO Can. Sci. Advis. Sec. Res. Doc. No. 2017/077). https://waves-vagues.dfo-mpo.gc.ca/library-bibliotheque/40654473.pdf (accessed 26-Sep-

2022)

Donnet, S., Lazure, P., Ratsimandresy, A., Han, G., 2020. A comprehensive oceanographic dataset of a subpolar, mid-latitude broad fjord: Fortune Bay, Newfoundland, Canada. Earth Syst. Sci. Data 12, 1877–1896. https://doi.org/10.5194/essd-12-1877-2020

Donnet, S., Lazure, P., Ratsimandresy, A., Han, G., 2022. The physical oceanography of Fortune Bay, an overview. Regional Studies in Marine Science 56, 102698. https://doi.org/10.1016/j.rsma.2022.102698

ECCC, 2022. Data and Products of the High Resolution Deterministic Prediction System [WWW Document]. MSC Open Data / Données ouvertes du SMC. URL https://eccc-msc.github.io/open-data/msc-data/nwp_hrdps/readme_hrdps_en/ (accessed 28-Sep-2021).

FAO, 2020. The State of World Fisheries and Aquaculture 2020. Sustainability in action. Rome. https://doi.org/10.4060/ca9229en

Fennel, W., Radtke, H., Schmidt, M., Neumann, T., 2010. Transient upwelling in the central Baltic Sea. Continental Shelf Research 30, 2015–2026. https://doi.org/10.1016/j.csr.2010.10.002

Fisheries and Marine Institute of Memorial University of Newfoundland, 2020. A Review of the 2019 Newfoundland and Labrador South Coast Cultured Atlantic Salmon Mortality Event. Fisheries and Marine Institute of Memorial University of Newfoundland. https://www.gov.nl.ca/ffa/files/publications-pdf-2019-salmon-review-final-report.pdf (accessed 27-Sep-2022)

Foreman, M.G.G., Czajko, P., Stucchi, D.J., Guo, M., 2009. A finite volume model simulation for the Broughton Archipelago, Canada. Ocean Modelling 30, 29–47. https://doi.org/10.1016/j.ocemod.2009.05.009

Fraser, N.J., Inall, M.E., 2018. Influence of Barrier Wind Forcing on Heat Delivery Toward the Greenland Ice Sheet. J. Geophys. Res. Oceans 123, 2513–2538. https://doi.org/10.1002/2017JC013464

Fraser, N.J., Inall, M.E., Magaldi, M.G., Haine, T.W.N., Jones, S.C., 2018. Wintertime Fjord-Shelf Interaction and Ice Sheet Melting in Southeast Greenland. J. Geophys. Res. Oceans 123, 9156–9177. https://doi.org/10.1029/2018JC014435

Gill, A.E., Clarke, A.J., 1974. Wind-induced upwelling, coastal currents and sea-level changes. Deep Sea Research and Oceanographic Abstracts 21, 325–345. https://doi.org/10.1016/0011-7471(74)90038-2

Grinsted, A., Moore, J.C., Jevrejeva, S., 2004. Application of the cross wavelet transform and wavelet coherence to geophysical time series. Nonlin. Processes Geophys. 11, 561–566. https://doi.org/10.5194/npg-11-561-2004

Hallock, Z.R., Teague, W.J., Jarosz, E., 2009. Subinertial Slope-Trapped Waves in the Northeastern Gulf of Mexico. Journal of Physical Oceanography 39, 1475–1485. https://doi.org/10.1175/2009JPO3925.1

Haney, R.L., 1991. On the pressure gradient force over steep topography in sigma coordinate ocean models.

Hersbach, H., Bell, B., Berrisford, P., Biavati, G., Horányi, A., Muñoz Sabater, J., Nicolas, J., Peubey, C., Radu, R., Rozum, I., Schepers, D., Simmons, A., Soci, C., Dee, D., Thépaut, J.-N., 2018. ERA5 hourly data on single levels from 1959 to present [WWW Document]. Copernicus Climate Change Service (C3S) Climate Data Store (CDS). https://cds.climate.copernicus.eu/cdsapp#!/dataset/reanalysis-era5-single-levels?tab=form

(accessed 6-Oct-2021)

Huthnance, J.M., 1978. On Coastal Trapped Waves: Analysis and Numerical Calculation by Inverse Iteration. Journal of Physical Oceanography 8, 74–92. https://doi.org/10.1175/1520-0485(1978)008<0074:OCTWAA>2.0.CO;2

Illig, S., Cadier, E., Bachèlery, M., Kersalé, M., 2018. Subseasonal Coastal-Trapped Wave Propagations in the Southeastern Pacific and Atlantic Oceans: 1. A New Approach to Estimate Wave Amplitude. J. Geophys. Res. Oceans 123, 3915–3941. https://doi.org/10.1029/2017JC013539

Inall, M.E., Nilsen, F., Cottier, F.R., Daae, R., 2015. Shelf/fjord exchange driven by coastal-trapped waves in the A rctic. J. Geophys. Res. Oceans 120, 8283–8303. https://doi.org/10.1002/2015JC011277

Jackson, R.H., Lentz, S.J., Straneo, F., 2018. The Dynamics of Shelf Forcing in Greenlandic Fjords. Journal of Physical Oceanography 48, 2799–2827. https://doi.org/10.1175/JPO-D-18-0057.1

JPL MUR MEaSUREs Project, 2015. GHRSST Level 4 MUR Global Foundation Sea Surface Temperature Analysis (v4.1). https://doi.org/10.5067/GHGMR-4FJ04

JPL OurOcean, 2010. GHRSST Level 4 G1SST Global Foundation Sea Surface Temperature Analysis. https://doi.org/10.5067/GHG1S-4FP01

Kitade, Y., Matsuyama, M., Iwata, S., Watabe, I., 1998. SDP and LP fluctuations observed along the coast of Sagami Bay. Journal of Oceanography 54, 297–312.

Klinck J., 1999. DYNMODES. An ocean dynamic vertical modes software. https://github.com/sea-mat/dynmodes/blob/master/dynmodes.m (accessed 21-Sep-2022)

Large, W.G., Pond, S., 1981. Open Ocean Momentum Flux Measurements in Moderate to Strong Winds. Journal of Physical Oceanography 11, 324–336. https://doi.org/10.1175/1520-0485(1981)011<0324:OOMFMI>2.0.CO;2

Lazure, P., Le Cann, B., Bezaud, M., 2018. Large diurnal bottom temperature oscillations around the Saint Pierre and Miquelon archipelago. Sci Rep 8, 13882. https://doi.org/10.1038/s41598-018-31857-w

Lemmin, U., Mortimer, C.H., Bäuerle, E., 2005. Internal seiche dynamics in Lake Geneva. Limnol. Oceanogr. 50, 207–216. https://doi.org/10.4319/lo.2005.50.1.0207

Loder, J.W., 1998. The coastal ocean off northeastern North America: A large-scale view. The sea 11, 105–138.

Ma, Z., Han, G., Chassé, J., 2016. Simulation of Circulation and Ice over the Newfoundland and Labrador Shelves: The Mean and Seasonal Cycle. Atmosphere-Ocean 54, 248–263. https://doi.org/10.1080/07055900.2015.1077325

Masoud, M., Pawlowicz, R., Montazeri Namin, M., 2019. Low frequency variations in currents on the southern continental shelf of the Caspian Sea. Dynamics of Atmospheres and Oceans 87, 101095. https://doi.org/10.1016/j.dynatmoce.2019.05.004

Masunaga, E., Fringer, O.B., Kitade, Y., Yamazaki, H., Gallager, S.M., 2017. Dynamics and Energetics of Trapped Diurnal Internal Kelvin Waves around a Midlatitude Island. Journal of Physical Oceanography 47, 2479–2498. https://doi.org/10.1175/JPO-D-16-0167.1

Mellor, G.L., Ezer, T., Oey, L.-Y., 1994. The Pressure Gradient Conundrum of Sigma Coordinate Ocean Models. Journal of Atmospheric and Oceanic Technology 11, 1126–1134. https://doi.org/10.1175/1520-0426(1994)011<1126:TPGCOS>2.0.CO;2

Mortimer, C.H., 1968. Internal waves and associated currents observed in Lake Michigan during the summer of 1963 (Special Report No. 1). Center for Great Lakes Studies, Milwaukee, Wisconsin (US). https://minds.wisconsin.edu/bitstream/handle/1793/54939/Mortimer?sequence=1 (accessed 27-Sep-2022)

Plante, M., Son, S.-W., Atallah, E., Gyakum, J., Grise, K., 2015. Extratropical cyclone climatology across eastern Canada: EXTRATROPICAL CYCLONE CLIMATOLOGY ACROSS EASTERN CANADA. Int. J. Climatol. 35, 2759–2776. https://doi.org/10.1002/joc.4170

Proehl, J.A., Ratrray, M., 1984. Low-Frequency Response of Wide Deep Estuaries to Non-Loca1 Atmospheric Forcing. Journal of Physical Oceanography 14, 904–921. https://doi.org/10.1175/1520-0485(1984)014<0904:LFROWD>2.0.CO;2

Ratsimandresy, A.W., Donnet, S., Goulet, P., 2020. Identification of geographic zones of influence associated with surface circulation for Aquaculture Bay Management Area application. Journal of Marine Systems 204, 103291. https://doi.org/10.1016/j.jmarsys.2019.103291

Ratsimandresy, A.W., Donnet, S., Snook, S., Goulet, P., 2019. Analysis of the variability of the ocean currents in the Coast of Bays area (DFO Can. Sci. Advis. Sec. Res. Doc. No. 2019/008). https://waves-vagues.dfo-mpo.gc.ca/library-bibliotheque/40805116.pdf (accessed 26-Sep-2022)

Romea, R.D., Smith, R.L., 1983. Further Evidence for Coastal Trapped Waves along the Peru Coast. Journal of Physical Oceanography 13, 1341–1356. https://doi.org/10.1175/1520-0485(1983)013<1341:FEFCTW>2.0.CO;2

Saggio, A., Imberger, J., 1998. Internal wave weather in a stratified lake. Limnol. Oceanogr. 43, 1780–1795. https://doi.org/10.4319/lo.1998.43.8.1780

Saha, K., Zhao, X., Zhang, H.-M., Casey, K.S., Zhang, D., Baker-Yeboah, S., Kilpatrick, K.A., Evans, R.H., Ryan, T., Relph, J.M., 2018. AVHRR Pathfinder version 5.3 level 3 collated (L3C) global 4km sea surface temperature for 1981-Present. https://doi.org/10.7289/V52J68XX

Salcedo-Castro, J., Ratsimandresy, A.W., 2013. Oceanographic response to the passage of hurricanes in Belle Bay, Newfoundland. Estuarine, Coastal and Shelf Science 133, 224–234. https://doi.org/10.1016/j.ecss.2013.08.031

Shah, P., Sajeev, R., Thara, K.J., George, G., Shafeeque, M., Akash, S., Platt, T., 2019. A Holistic Approach to Upwelling and Downwelling along the South-West Coast of India. Marine Geodesy 42, 64–84. https://doi.org/10.1080/01490419.2018.1553805

SHOM, 2022. Tide gauge SAINT-PIERRE-ET-MIQUELON [WWW Document]. DATA.SHOM.FR. URL http://dx.doi.org/10.17183/REFMAR#115 (accessed 21-Sep-2022)

Smagorinsky, J., 1963. GENERAL CIRCULATION EXPERIMENTS WITH THE PRIMITIVE EQUATIONS: I. THE BASIC EXPERIMENT. Monthly Weather Review 91, 99–164. https://doi.org/10.1175/1520-0493(1963)091<0099:GCEWTP>2.3.CO;2

Smith, E., Soule, F., Mosby, O., 1937. The MARION expedition to Davis Strait and Baffin Bay: Part II. Physical Oceanography. United State Coast Guard Bulletin.

Støylen, E., Fer, I., 2014. Tidally induced internal motion in an Arctic fjord. Nonlin. Processes Geophys. 21, 87–100. https://doi.org/10.5194/npg-21-87-2014

Suginohara, N., 1974. Onset of coastal upwelling in a two-layer ocean by wind stress with longshore variation. Journal of the Oceanographical Society of Japan 30, 23–33. https://doi.org/10.1007/BF02112888

Svendsen, H., Beszczynska-Møller, A., Hagen, J.O., Lefauconnier, B., Tverberg, V., Gerland, S., Børre Ørbæk, J., Bischof, K., Papucci, C., Zajaczkowski, M., Azzolini, R., Bruland, O., Wiencke, C., 2002. The physical environment of Kongsfjorden–Krossfjorden, an Arctic fjord system in Svalbard. Polar Research 21, 133–166. https://doi.org/10.3402/polar.v21i1.6479

Thomson, W., 1880. 1. On Gravitational Oscillations of Rotating Water. Proc. R. Soc. Edinb. 10, 92–100. https://doi.org/10.1017/S0370164600043467

Vilibić, I., Orlić, M., 1999. Surface Seiches and Internal Kelvin Waves Observed Off Zadar (East Adriatic). Estuarine, Coastal and Shelf Science 48, 125–136. https://doi.org/10.1006/ecss.1998.0403

Walin, G., 1972. Some observations of temperature fluctuations in the coastal region of the Baltic. Tellus 24, 187–198. https://doi.org/10.1111/j.2153-3490.1972.tb01546.x

Wang, B., 2002. Kelvin waves. Encyclopedia of atmospheric sciences, 1062-1068.

Wang, C., Picaut, J., 2004. Understanding Enso Physics—A Review, in: Earth's Climate. American Geophysical Union (AGU), pp. 21–48. https://doi.org/10.1029/147GM02

Weber, J.E.H., Ghaffari, P., 2014. Mass transport in internal coastal Kelvin waves. European Journal of Mechanics - B/Fluids 47, 151–157. https://doi.org/10.1016/j.euromechflu.2014.02.006

Wessel, P., Smith, W.H.F., 1996. A global, self-consistent, hierarchical, high-resolution shoreline database. J. Geophys. Res. 101, 8741–8743. https://doi.org/10.1029/96JB00104

Wessel, Paul, Smith, Walter H. F., 2018. A Global Self-consistent, Hierarchical, High-resolution Geography Database [WWW Document]. GSHHG. https://www.soest.hawaii.edu/pwessel/gshhg/ (accessed 28-Aug-2022)

White, M., Hay, A.E., 1994. Dense overflow into a large silled embayment: Tidal modulation, fronts and basin modes. issn: 0022-2402 52, 459–487. https://doi.org/10.1357/0022240943077055

Yao, T., 1986. The response of currents in Trinity Bay, Newfoundland, to local wind forcing. Atmosphere-Ocean 24, 235–252. https://doi.org/10.1080/07055900.1986.9649249

# Internal Kelvin waves in a broad, mid-latitude fjord

**Supplementary Material**

Sebastien Donnet[1,4], Pascal Lazure[2], Andry Ratsimandresy[3] and Guoqi Han[1]

To be submitted to Journal of Geophysical Research: Oceans

[1] Fisheries and Oceans Canada, Institute of Ocean Sciences, P.O. Box 6000, Sidney BC, V8L 4B2, Canada

[2] Ifremer (French Research Institute for Exploitation of the Sea) Laboratoire d'Océanographie Physique et Spatiale, Centre Bretagne, ZI de la Pointe du Diable, CS 10070, 29280 Plouzané, France

[3] Fisheries and Oceans Canada, Northwest Atlantic Fisheries Centre, 80 East White Hills Rd, St. John's NL, A1C 5X1, Canada

[4] Université de Bretagne Occidentale, Ecole Doctorale N°598 Science de la Mer et du littoral, Brest, France.

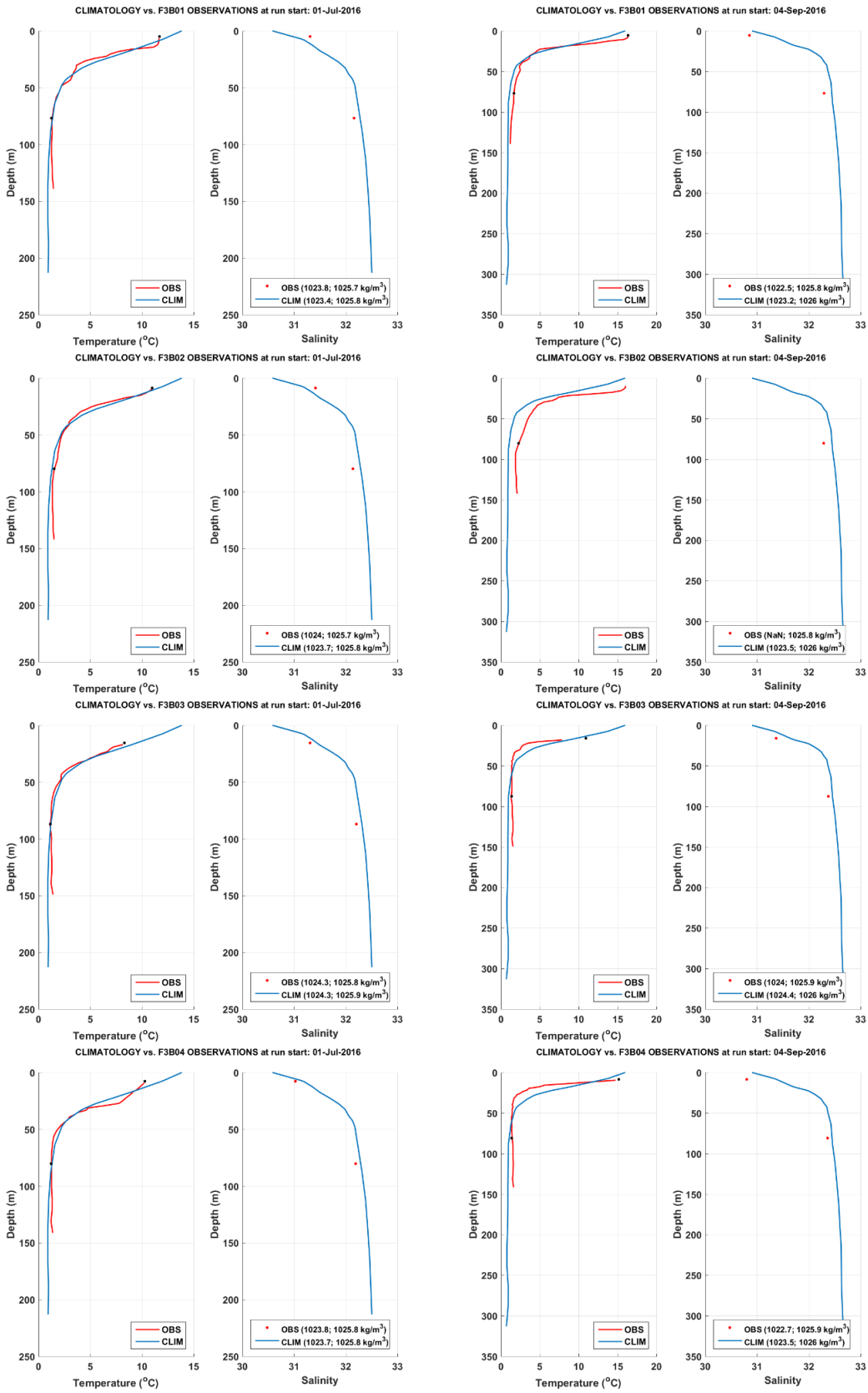


*Figure S1: hydrographic climatology (CLIM) vs. observations (OBS) at numerical simulations start (July events, left and September events, right). Observed temperature profiles come from thermistor lines and black dots represent the temperature measured by moored CTDs (see Donnet et al., 2020 for details).*

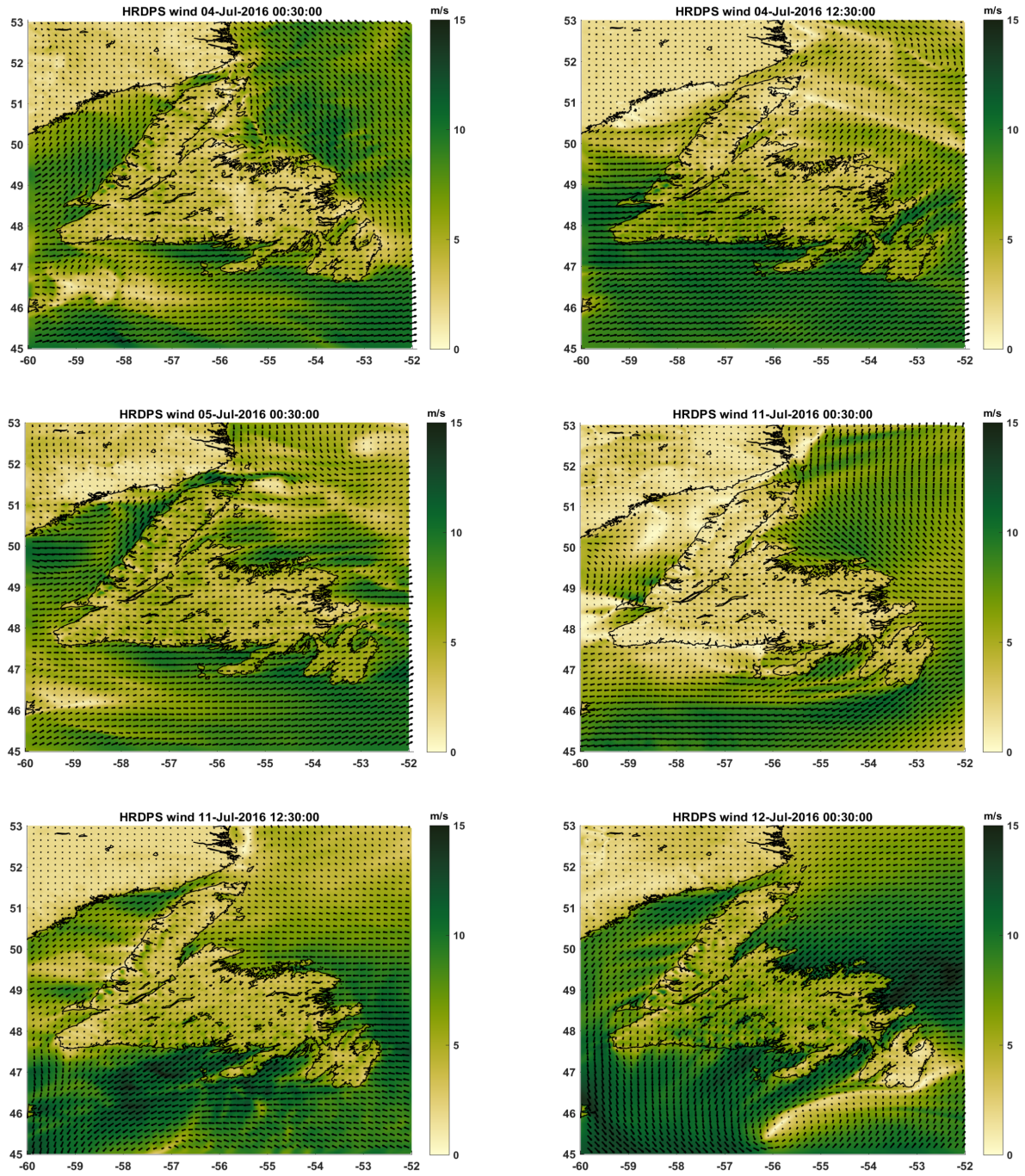


*Figure S2: Environment and Climate Change Canada (ECCC) High Resolution Deterministic Prediction System (HRDPS) wind fields in July 2016; selected snapshots during strong wind events.*

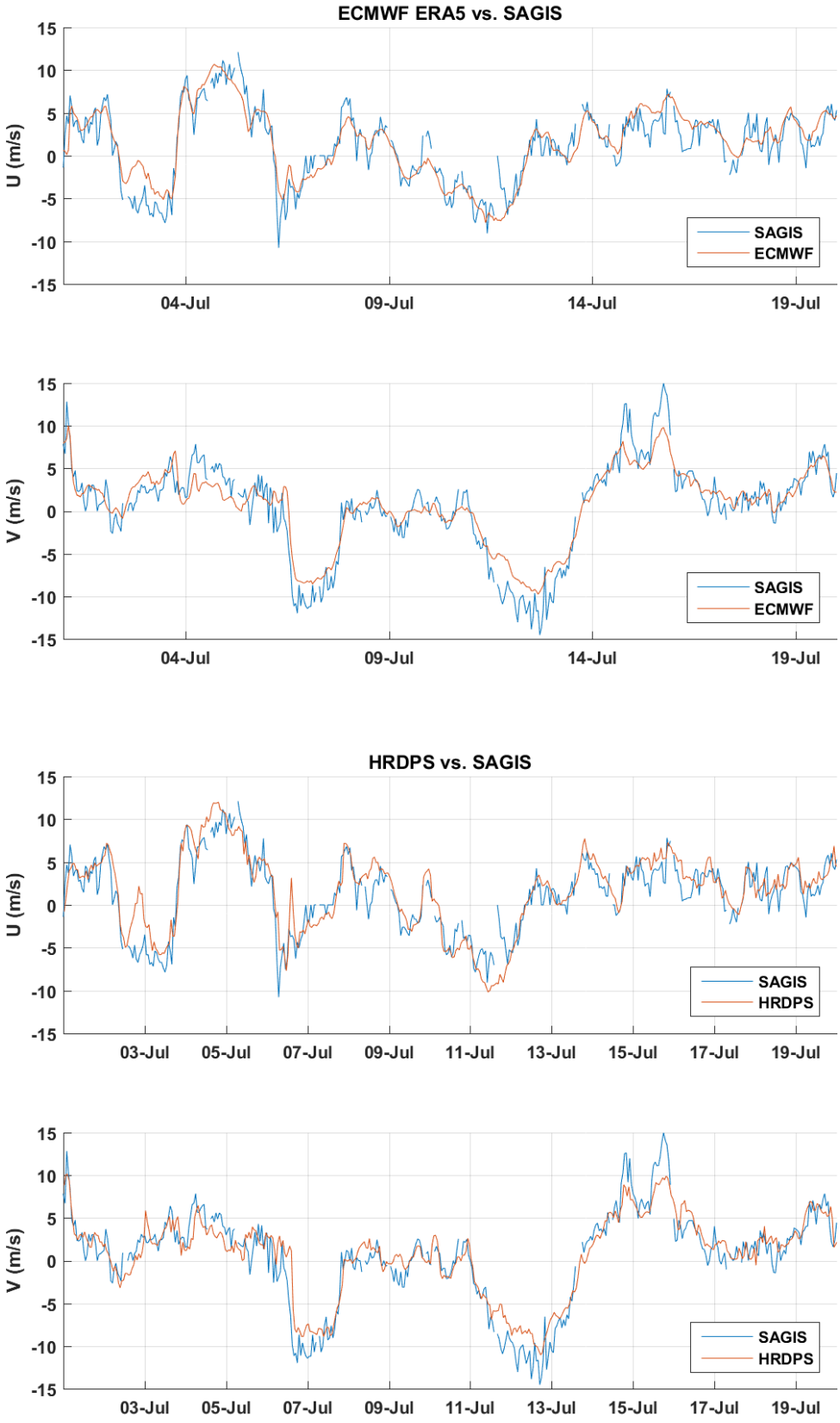


*Figure S3: ECMWF ERA5 (top) and HRDPS (bottom) modeled wind speed comparison with observations at SAGIS.*

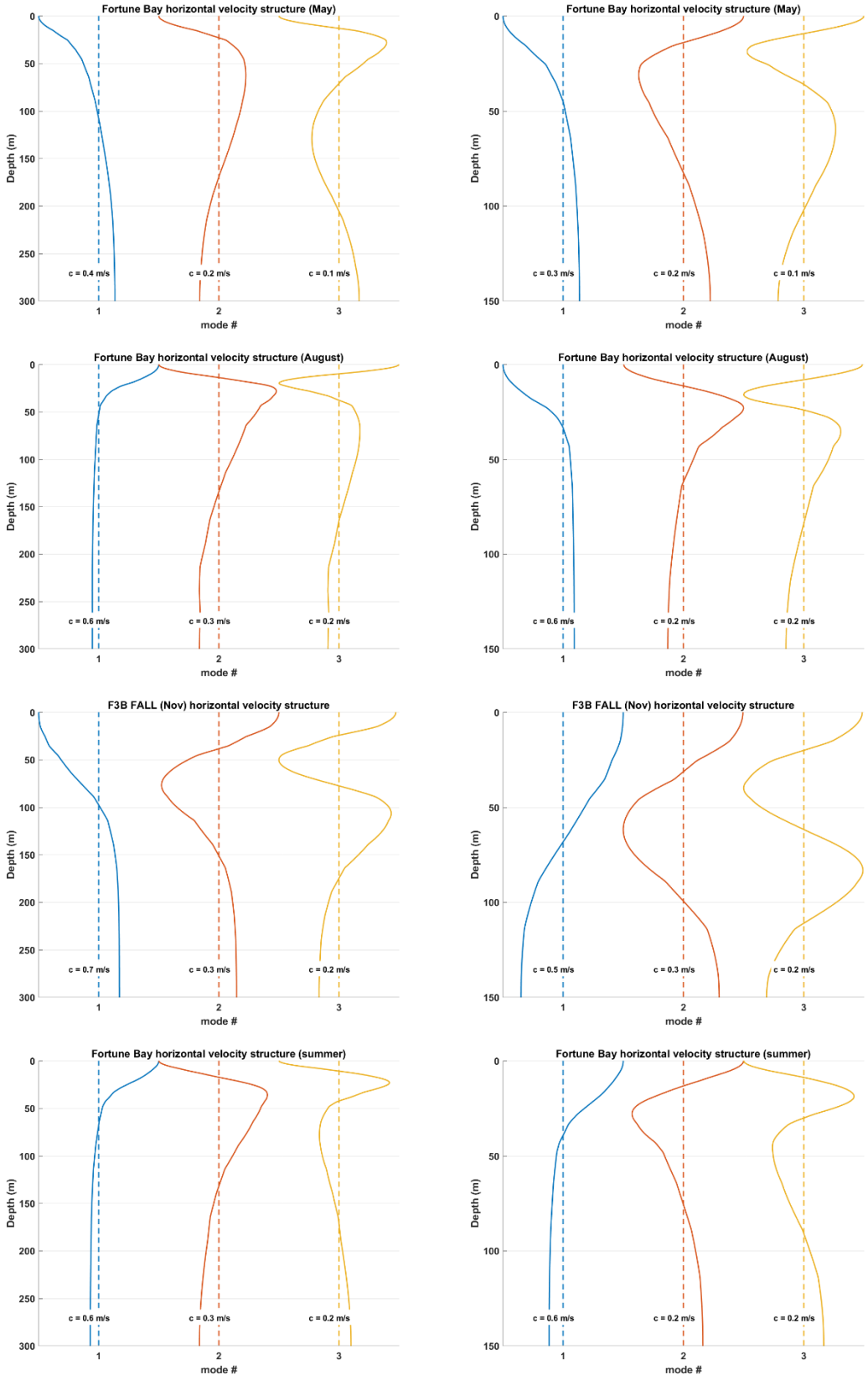


*Figure S4: internal wave horizontal velocity structure from normal mode analysis (using Klinck, 1999). First three modes are represented with phase speed (c) indicated at the bottom of each profile. Two depths were considered, using climatological T&S profiles: 300 m (left) and 150 m (right).*

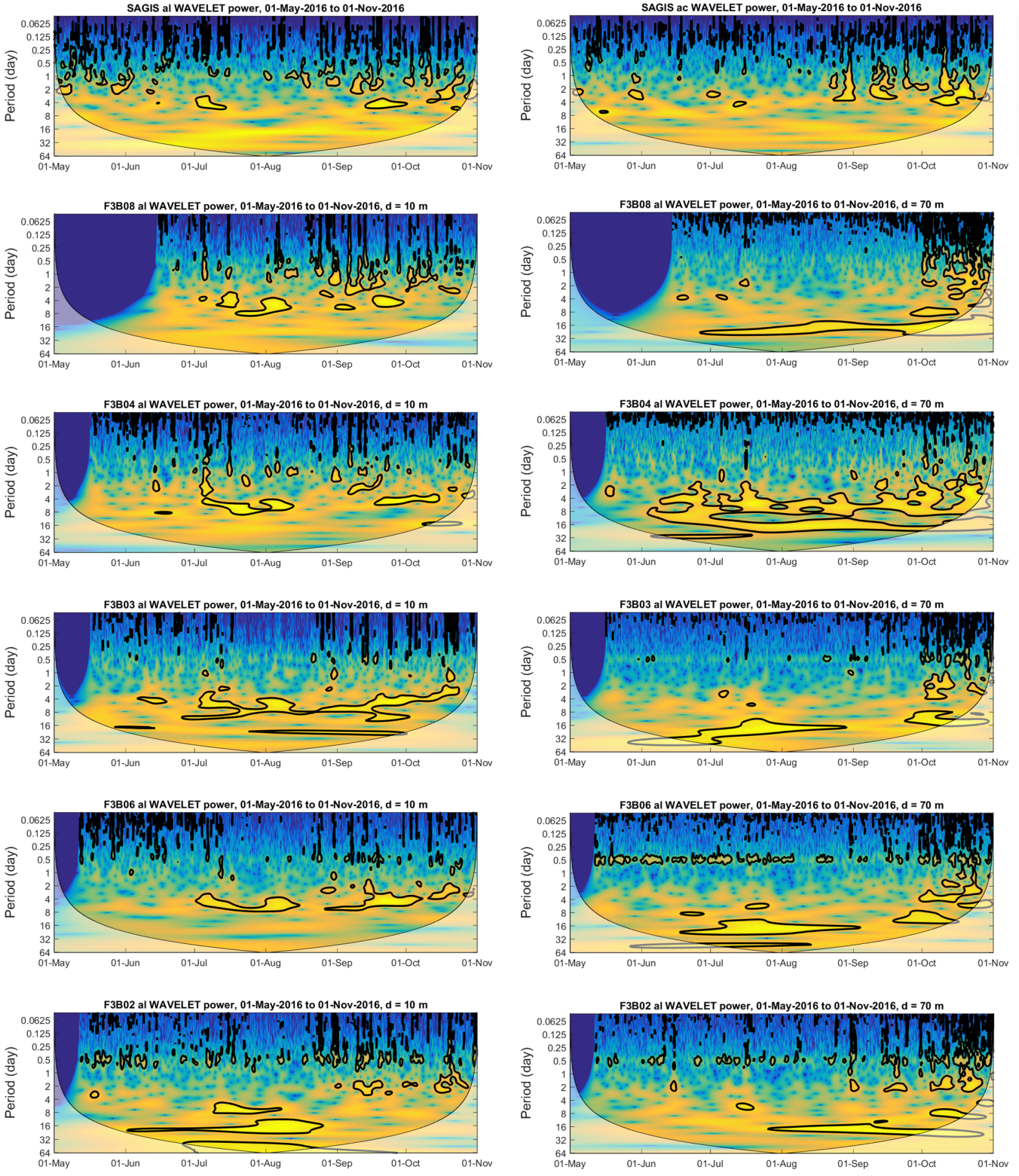


*Figure S5: Wavelet analysis (using Grinsted et al., 2004). First row is based on along-shore ('al', left) and accross-shore ('ac', right) wind speed while all the panels below are based on the along-shore current component observed around Fortune Bay from F3B08 to F3B02 (location of the moorings are illustrated in Figure 1 of the main text). The along-shore currents analyses were done on 2 depths (d): 10 m (left) and 70 m (right). Thick black contour designates the 95% significance level against red noise and the cone of influence (COI) where edge effects might distort the picture is shown as a lighter shade.*

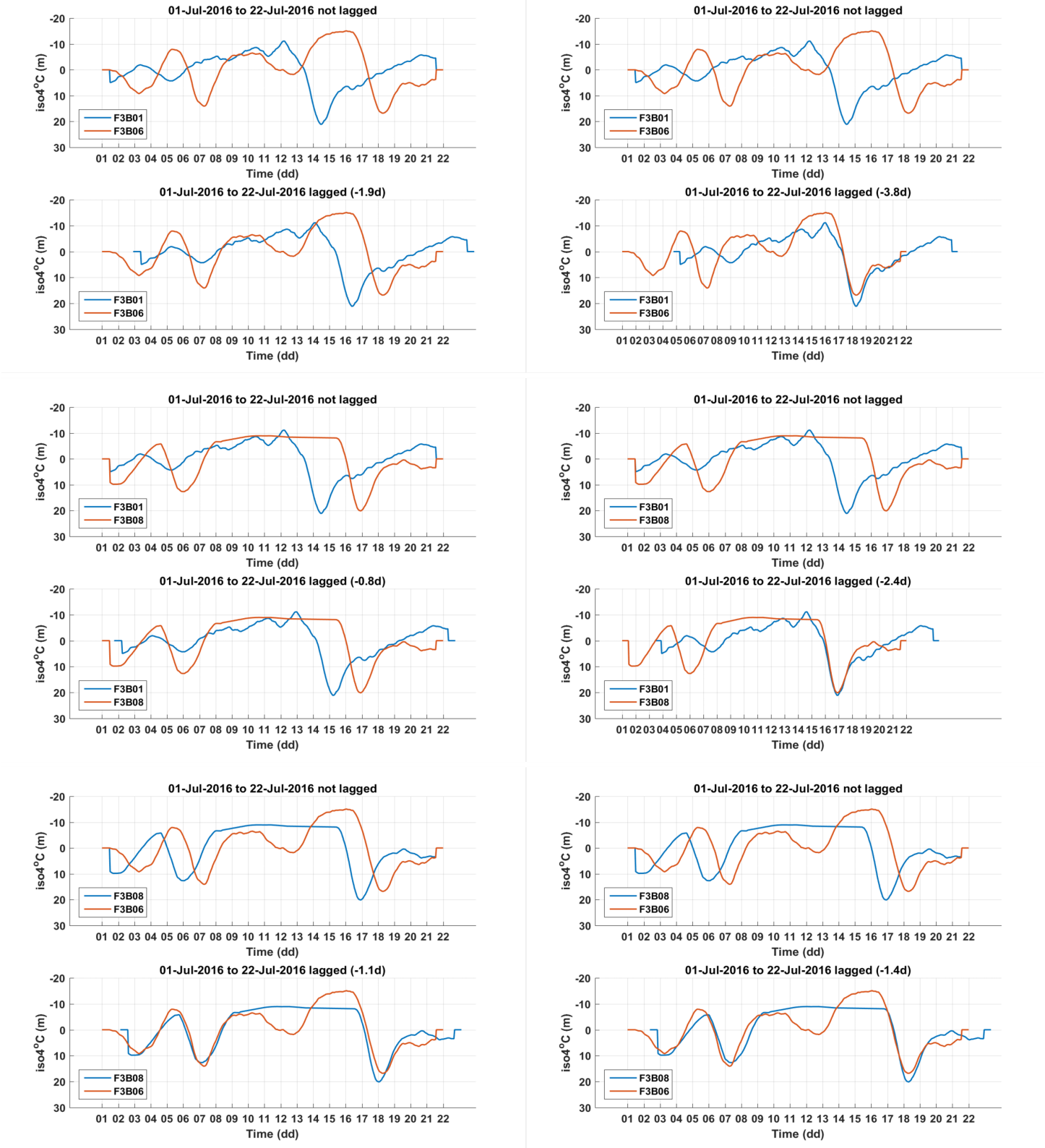


*Figure S6: Lagged cross-correlation of July events (01-10 July window, left; 10-20 July window, right) between selected mooring pairs (indicated in the legends). 4 °C isotherm depth was detrended and move-averaged (24 h window) before applying the cross-correlation. Period of constant, flat-looking isotherm depth indicate outcropping (most notably occurring at F3B08; see details in main text).*

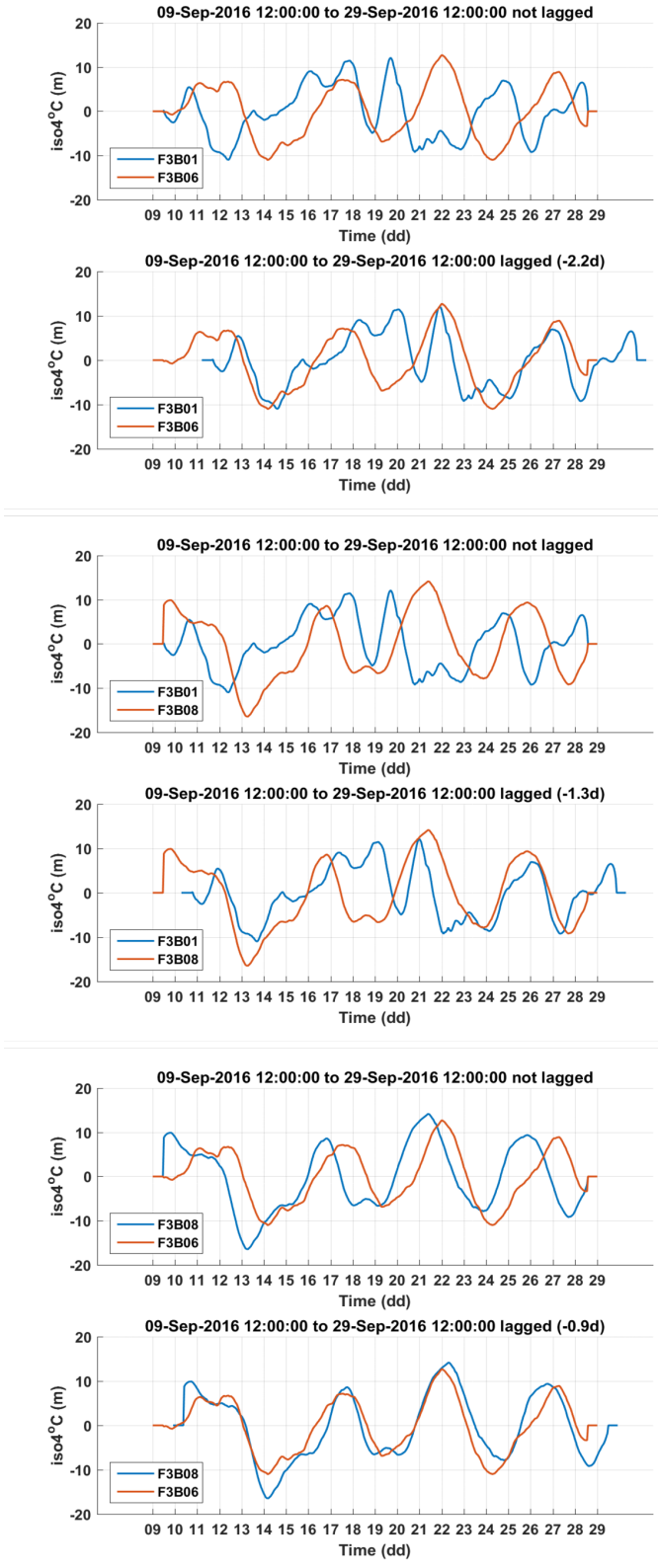


*Figure S7: Lagged cross-correlation of September events (09-29) made similarly to Figure 7.*

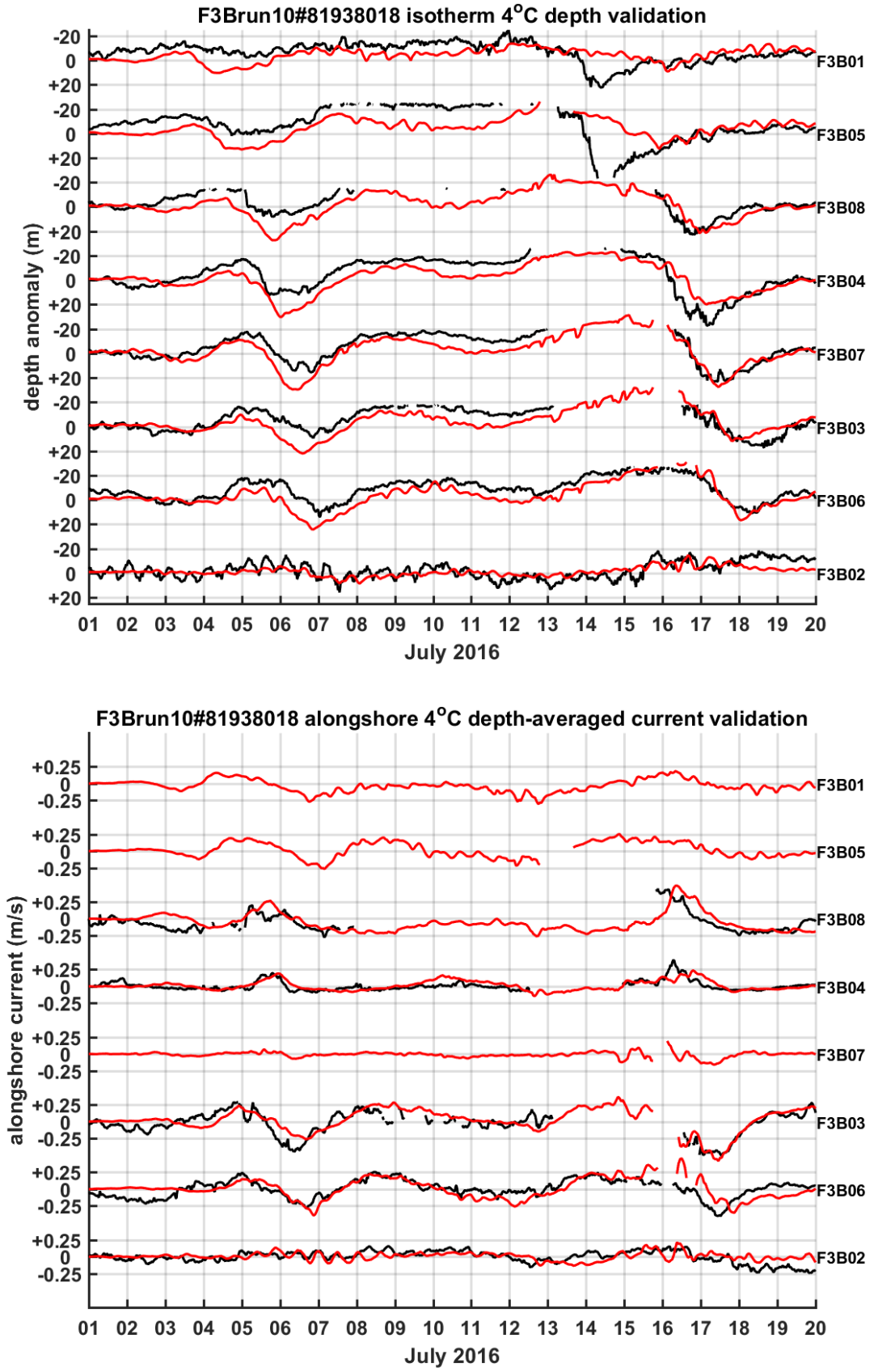


*Figure S8: July 2016 local model validation. Observations (black lines) vs. model (red lines) 4 °C isotherm depth anomaly (top) and depth-averaged alongshore current (bottom). Depth-averaged current is calculated from sea-surface to isotherm 4 °C depth.*

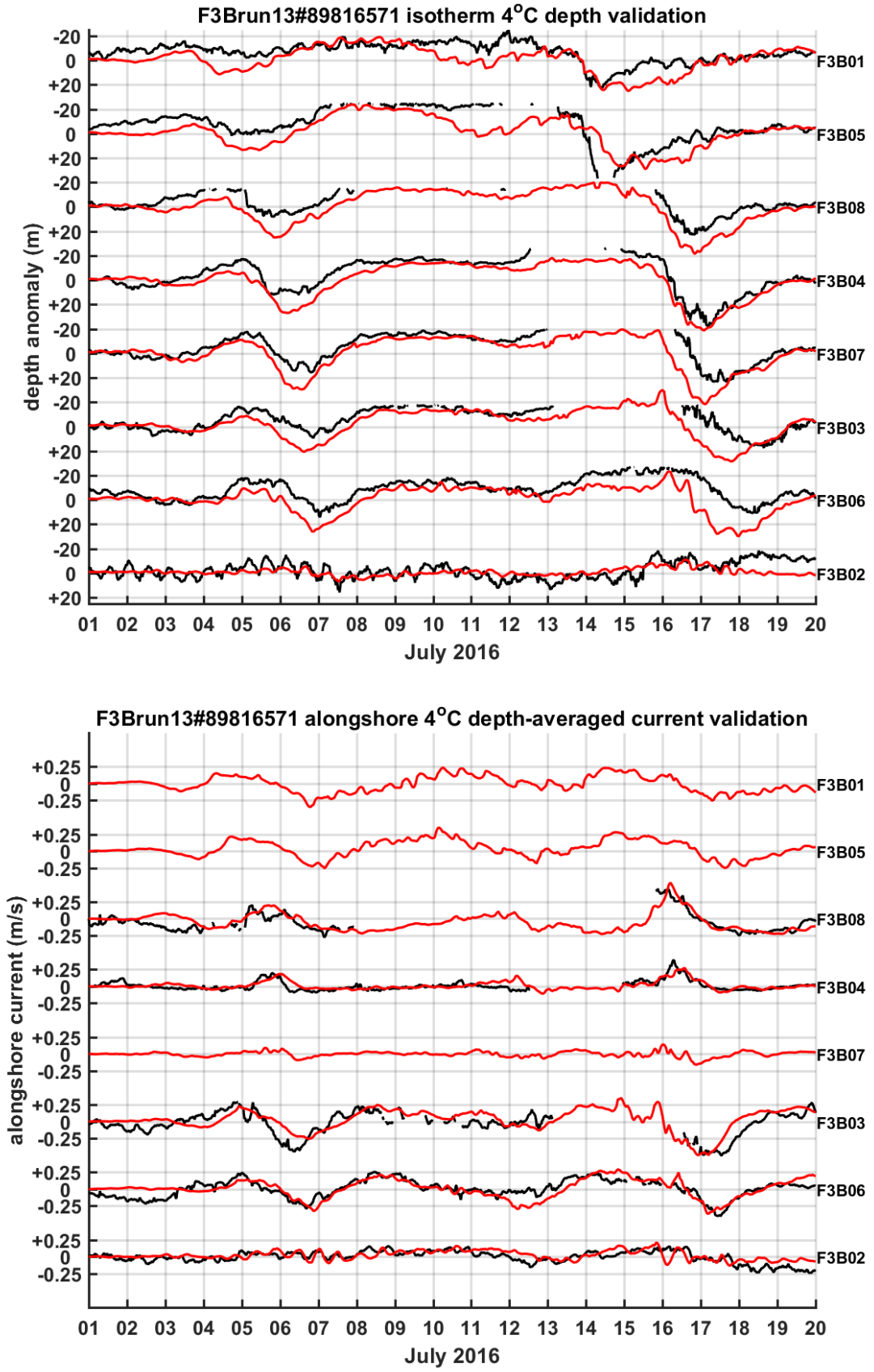


*Figure S9: July 2016 extended model validation. Observations (black lines) vs. model (red lines) 4 °C isotherm depth anomaly (top) and depth-averaged alongshore current (bottom). Depth-averaged current is calculated from sea-surface to isotherm 4 °C depth.*

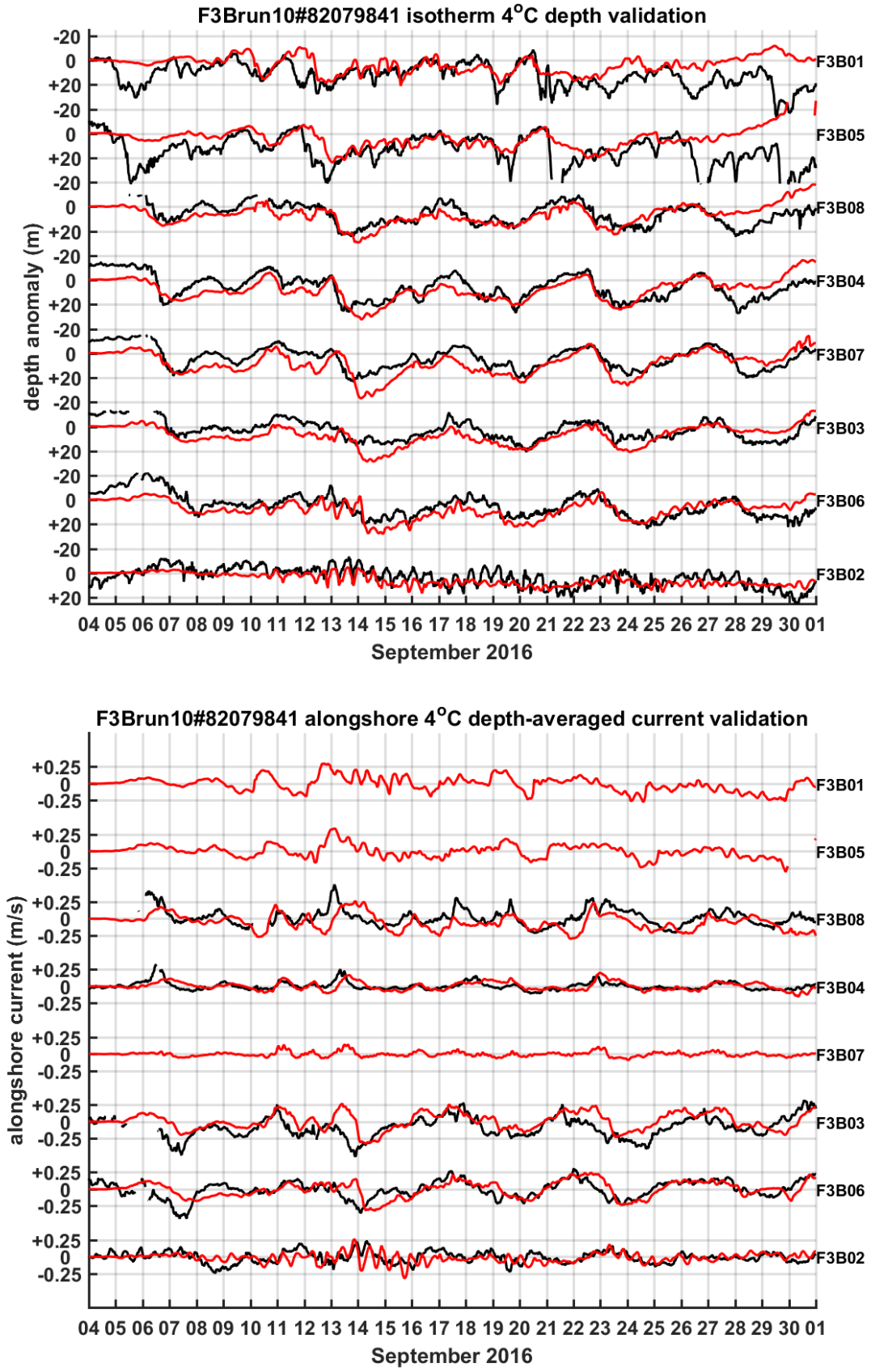


*Figure S10: September 2016 local model validation. Observations (black lines) vs. model (red lines) 4 °C isotherm depth (top) and depth-averaged alongshore current (bottom). Depth-averaged current is calculated from sea-surface to isotherm 4 °C depth.*

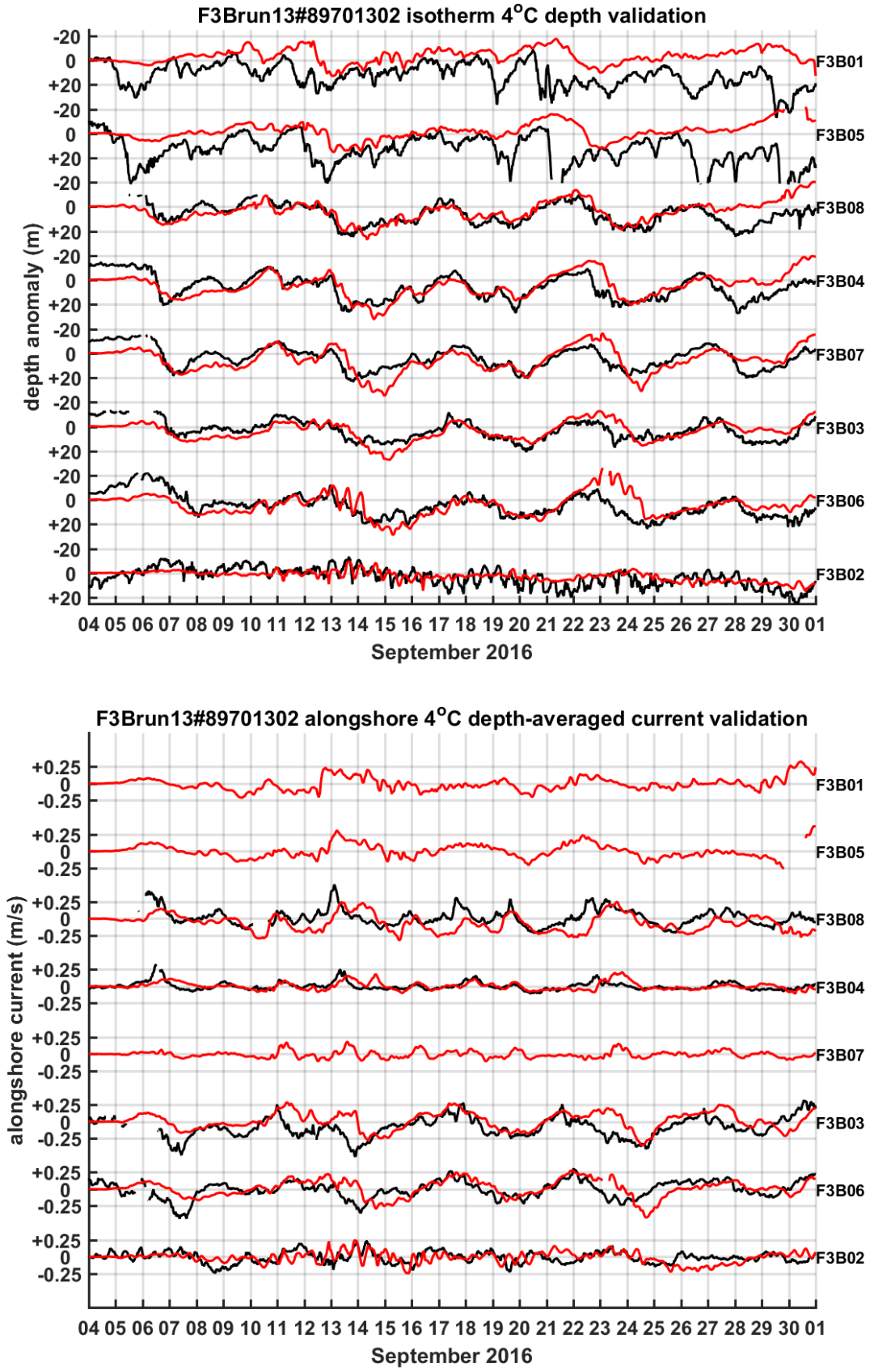


*Figure S11: September 2016 extended model validation. Observations (black lines) vs. model (red lines) 4 °C isotherm depth (top) and depth-averaged alongshore current (bottom). Depth-averaged current is calculated from sea-surface to isotherm 4 °C depth.*

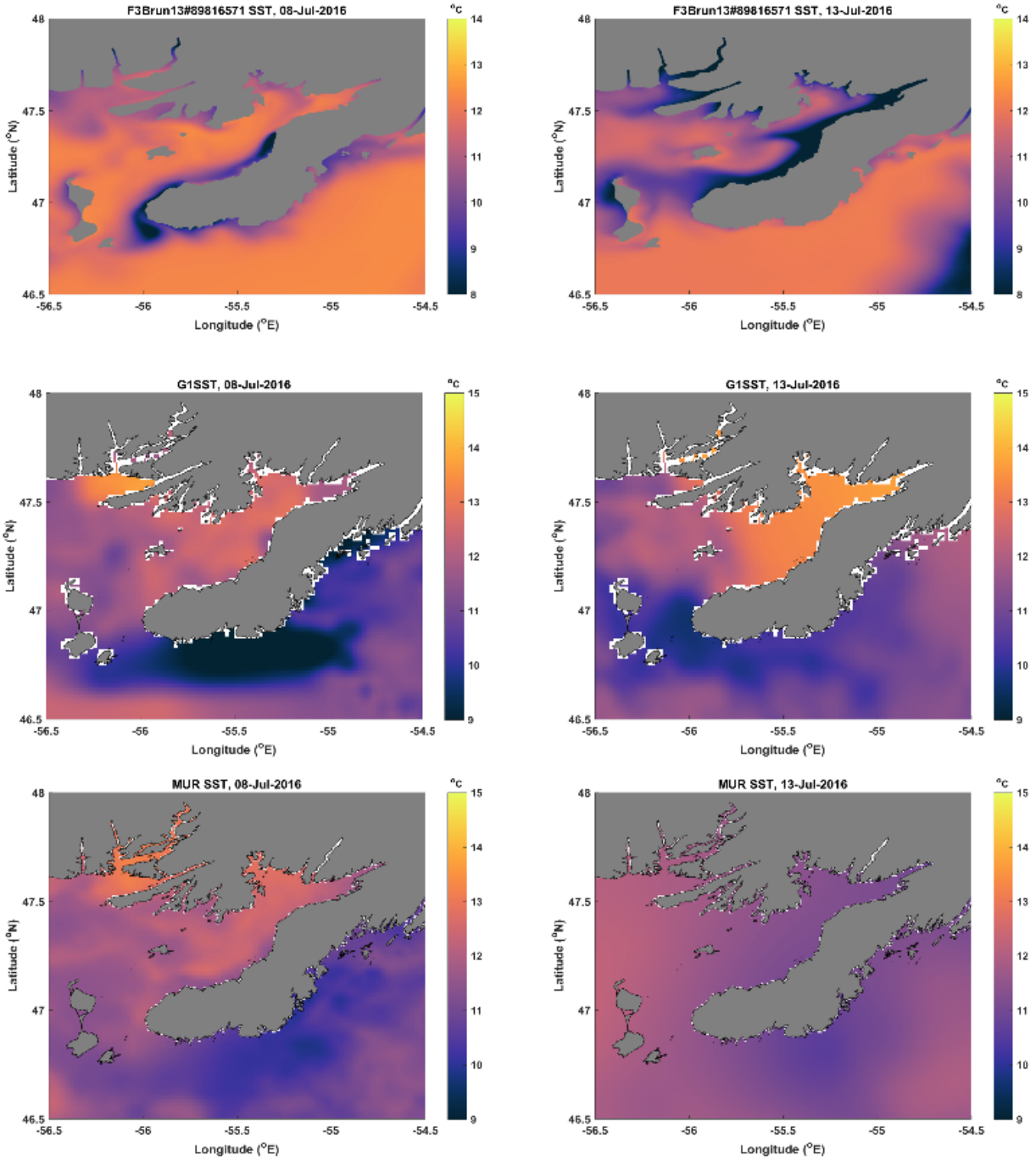


*Figure S12: daily averaged Sea Surface Temperature (SST) from the model (top row) vs. from blended and interpolated observation products (G1SST and MURSST) during the strongest upwelling events occurring in July 2016 in Fortune Bay. Coverage from Pathfinder's AVHRR data is blank for this time period (likely due to cloud cover) and is, therefore, not shown. NOTE: color range was adjusted to 1 °C higher for the observations to account for the difference between model and observed surface layer thickness (5 m vs millimeters, respectively).*

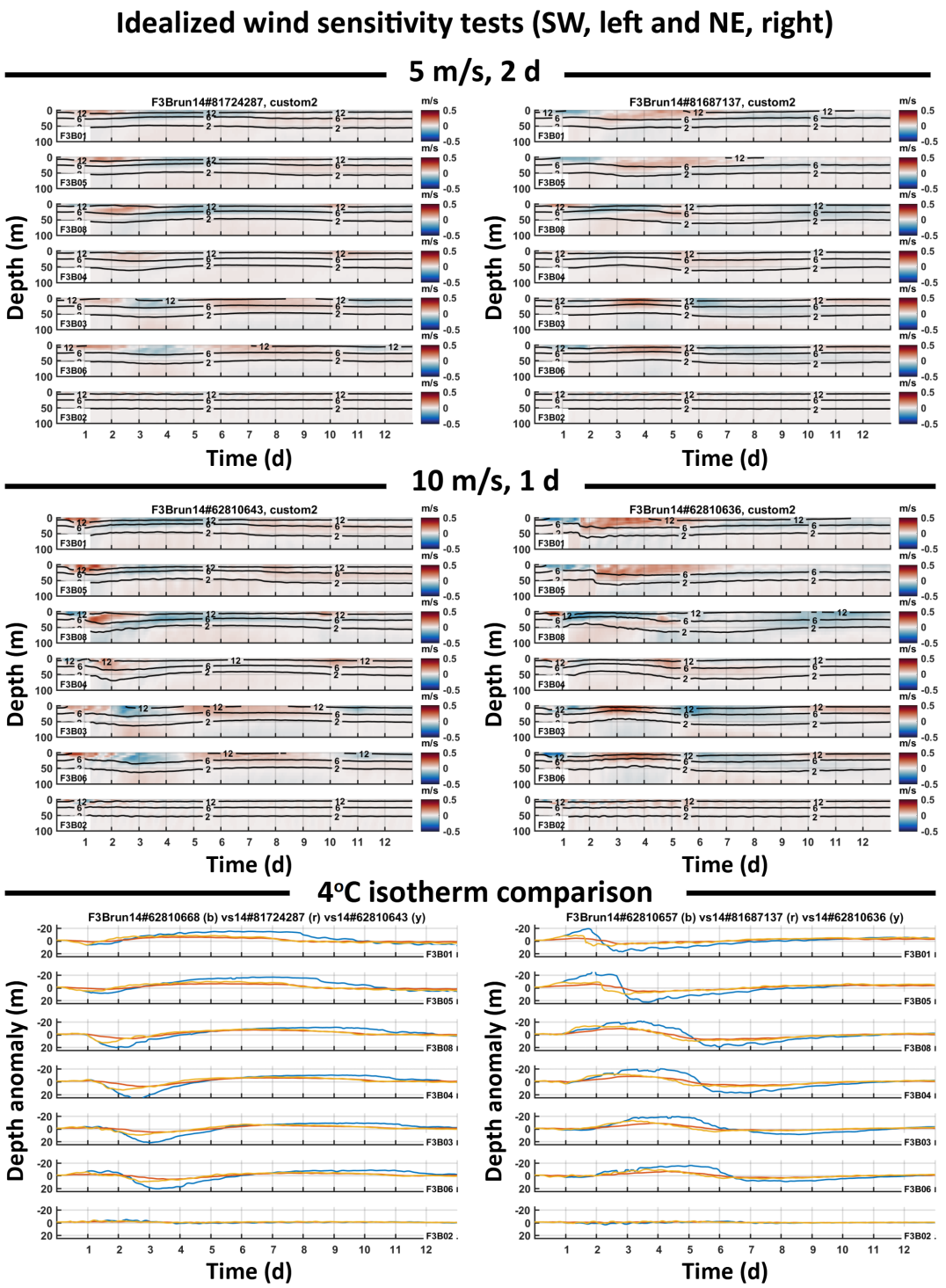


*Figure S13: Model sensitivity tests to various wind forcing (extended MESH; 150 m flat bottom). Top panels: a 5 m/s wind applied during 2 days (d). Middle panels: a 10 m/s wind applied during 1 day (d). Bottom panel: 4 °C isotherm depth anomaly comparison between 2 d, 10 m/s wind forcing (blue line), 2 d, 5 m/s wind forcing (red line) and 1 d, 10 m/s wind forcing (orange line). 2 forcing directions are considered: from the Southwest (SW; left) and from the Northeast (NE; right). Isotherms 2, 6 and 12 °C are represented (black lines) over along-shore currents (blue to red colors, positive into the bay) at mooring locations F3B01, 05, 08, 04, 03, 06 and 02 (cyclonic distribution around the bay; see main text for a map with exact locations). X-axis are model elapsed time (t) in days (d) from a state at rest at t = 0 d. Wind forcing is applied from t = 0 (d); linearly increasing over a duration of 6 hr to reach its peak. Ramp-down is done over the same duration to complete the cycle desired (i.e. 1 or 2 d total duration).*

# Idealized wind, 2 d forcing (10 m/s), extended MESH

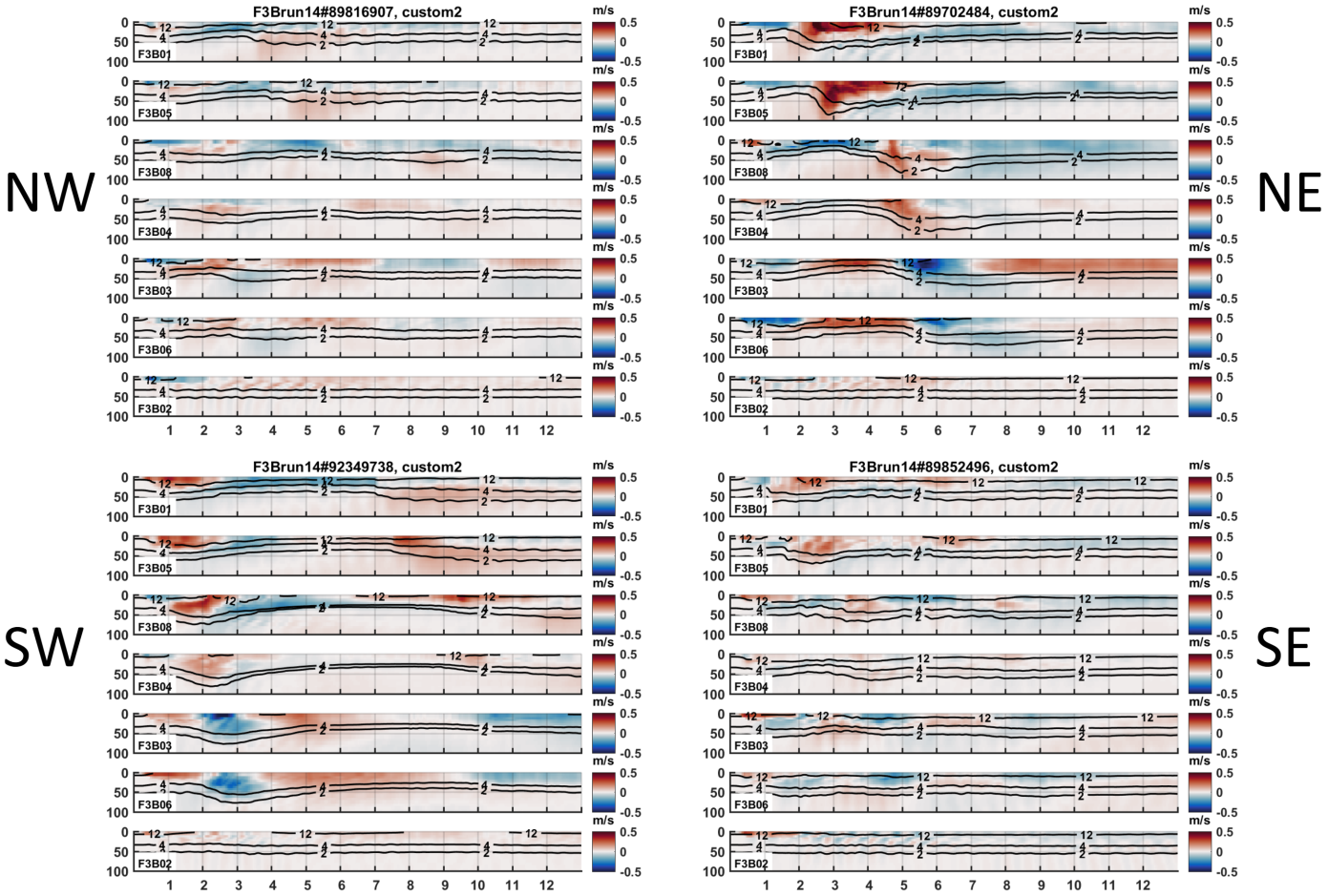


*Figure S14: 2 days (2d), idealized 10 m/s wind speed (0.14 N/m$^2$ stress) forcing model results on extended mesh from 4 main directions: Northeast (NE), Northwest (NW), Southwest (SW) and Southeast (SE). Isotherms 2, 4 and 12 °C are represented (black lines) over along-shore current (blue to red colors, positive into the bay) at mooring locations F3B01, 05, 08, 04, 03, 06 and 02 (cyclonic distribution around the bay; see main text for a map with exact locations). X-axis represent model elapsed time (t) in days (d). Y-axis is depth in meters (m).*

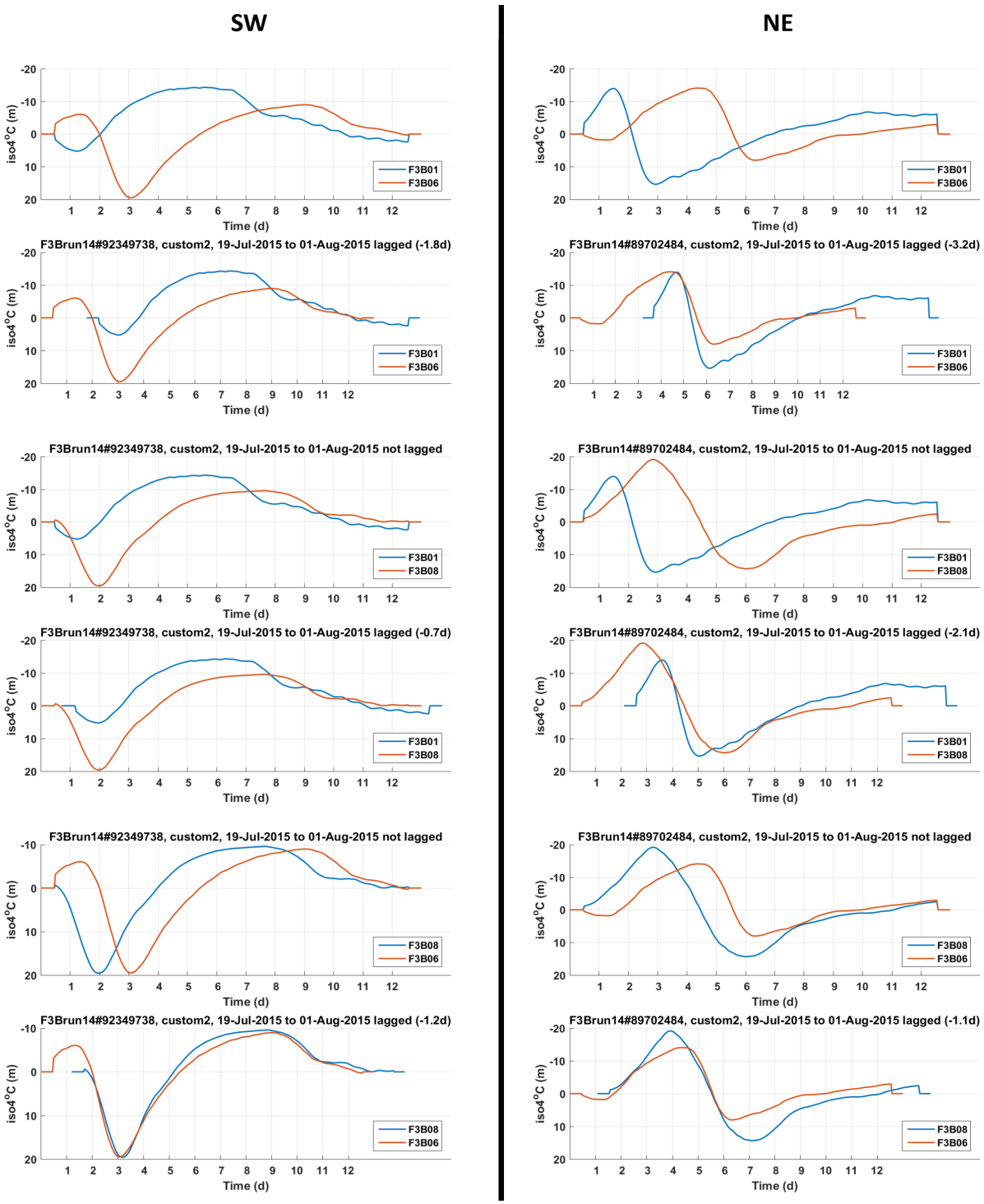


*Figure S15: lagged cross-correlations of 4 °C isotherm anomaly (from a 35 m state of rest) resulting from idealized wind events (SW, left and NE, right) made with the extended model mesh (300 m depth, flat bottom). Series were move-averaged over a 24 hr window. Mooring sites are indicated in the legend.*

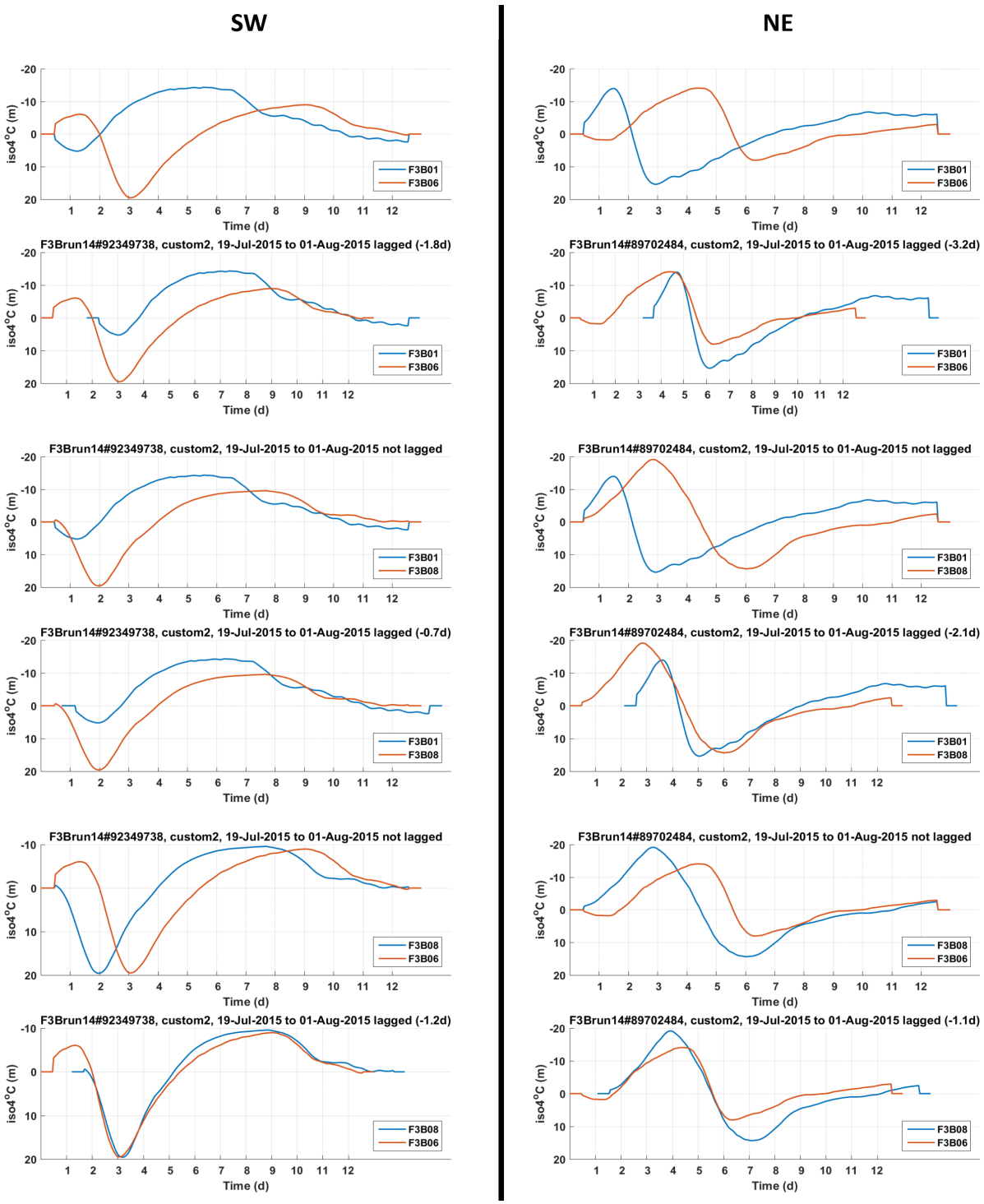


*Figure S16: lagged cross-correlations of 4 °C isotherm anomaly (from a 35 m state of rest) resulting from idealized wind events under Fortune Bay area forcing only (SW, left and NE, right) made with the extended model mesh (300 m depth, flat bottom). Series were move-averaged over a 24 hr window. Mooring sites are indicated in the legend.*

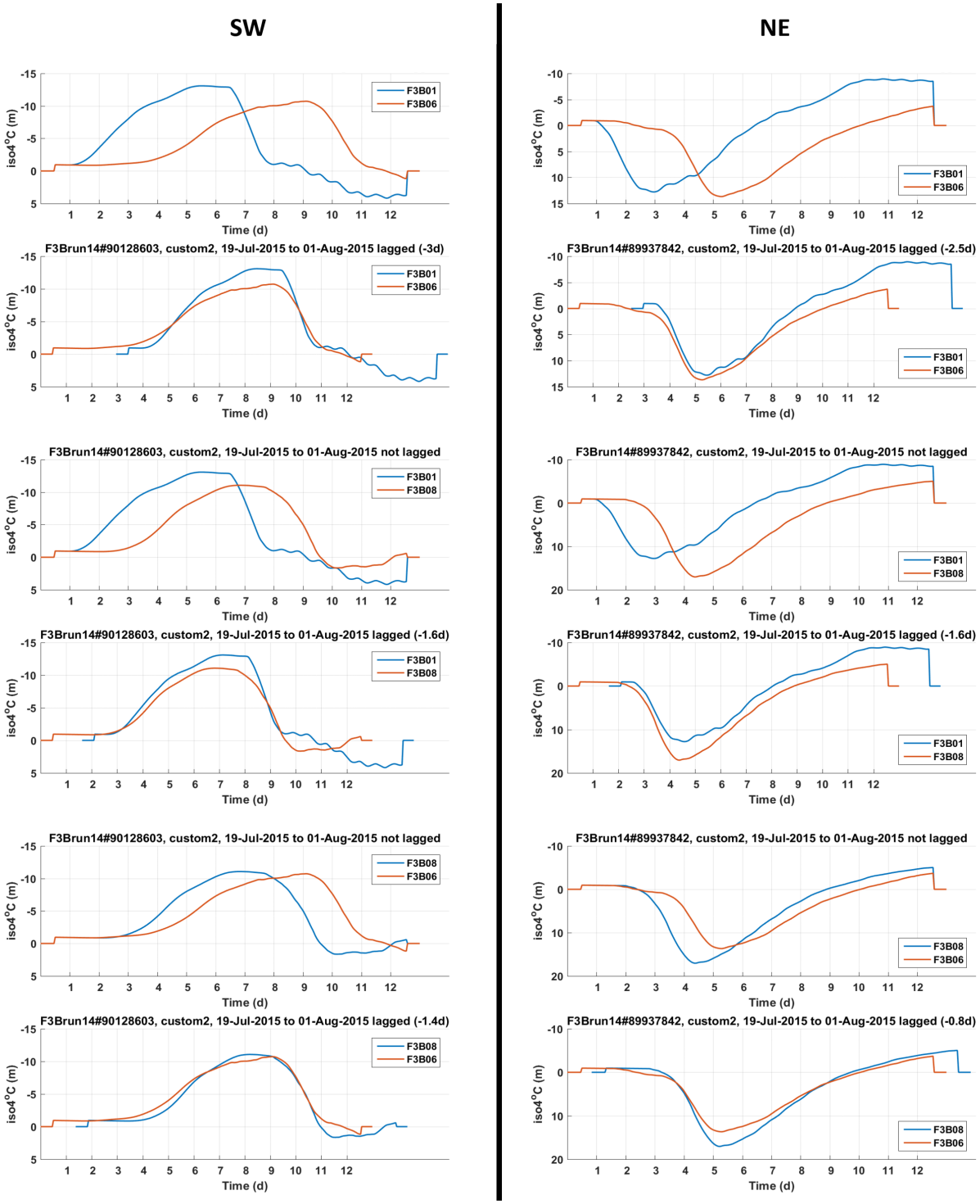


*Figure S17: lagged cross-correlations of 4 °C isotherm anomaly (from a 35 m state of rest) resulting from idealized wind events under Placentia Bay area forcing only (SW, left and NE, right) made with the extended model mesh (300 m depth, flat bottom). Series were move-averaged over a 24 hr window. Mooring sites are indicated in the legend.*

# Idealized wind, 10 m/s forcing, t=1d, extended MESH

NW

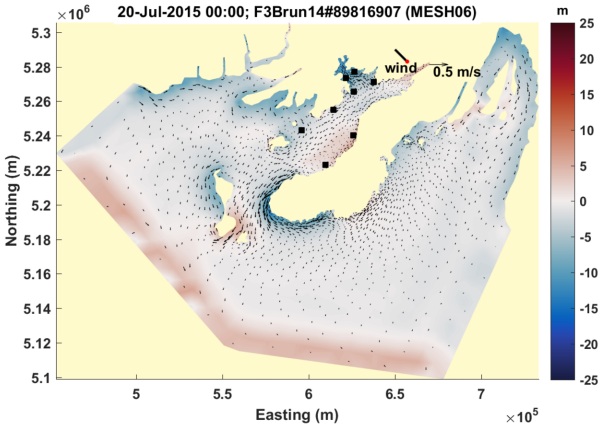


NE

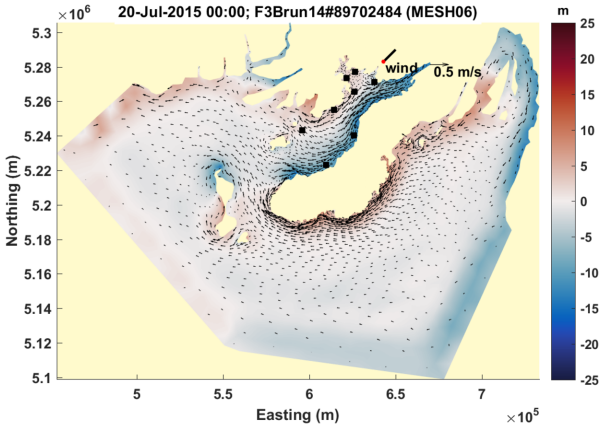


SW

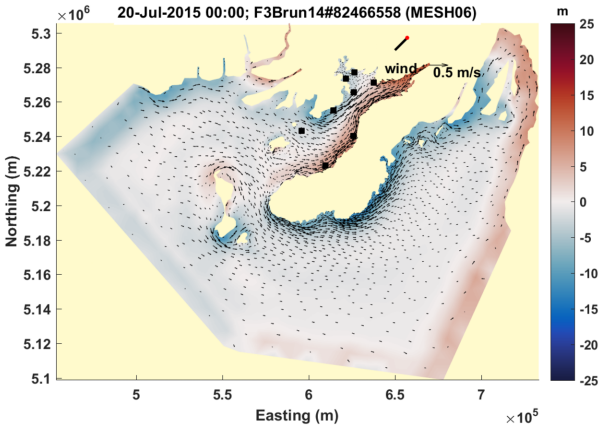


SE

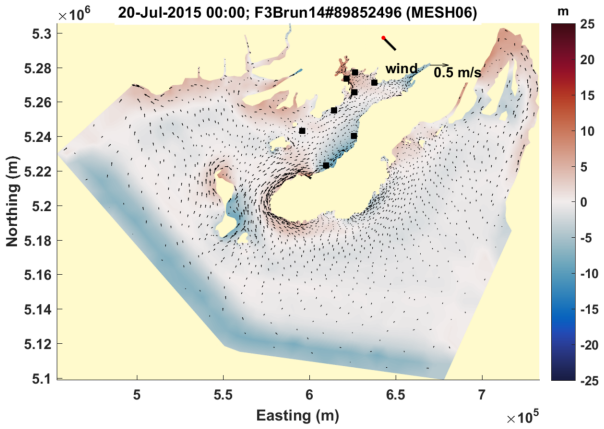


*Figure S18: surface snapshots after 1 model run day of idealized wind forcing from the 4 main quadrant (NW, NE, SW and SE) illustrating the areas of upwelling and downwelling generation. In colors is the 4 °C isotherm anomaly calculated from a state of rest of 35 m. Positive anomaly (red) represents downwelling while negative anomaly (blue) corresponds to upwelling conditions. Arrows are the upper layer current, depth-averaged from the surface down to the 4 °C isotherm depth. Black boxes represent the mooring sites used all along this study.*

# CONCLUSION

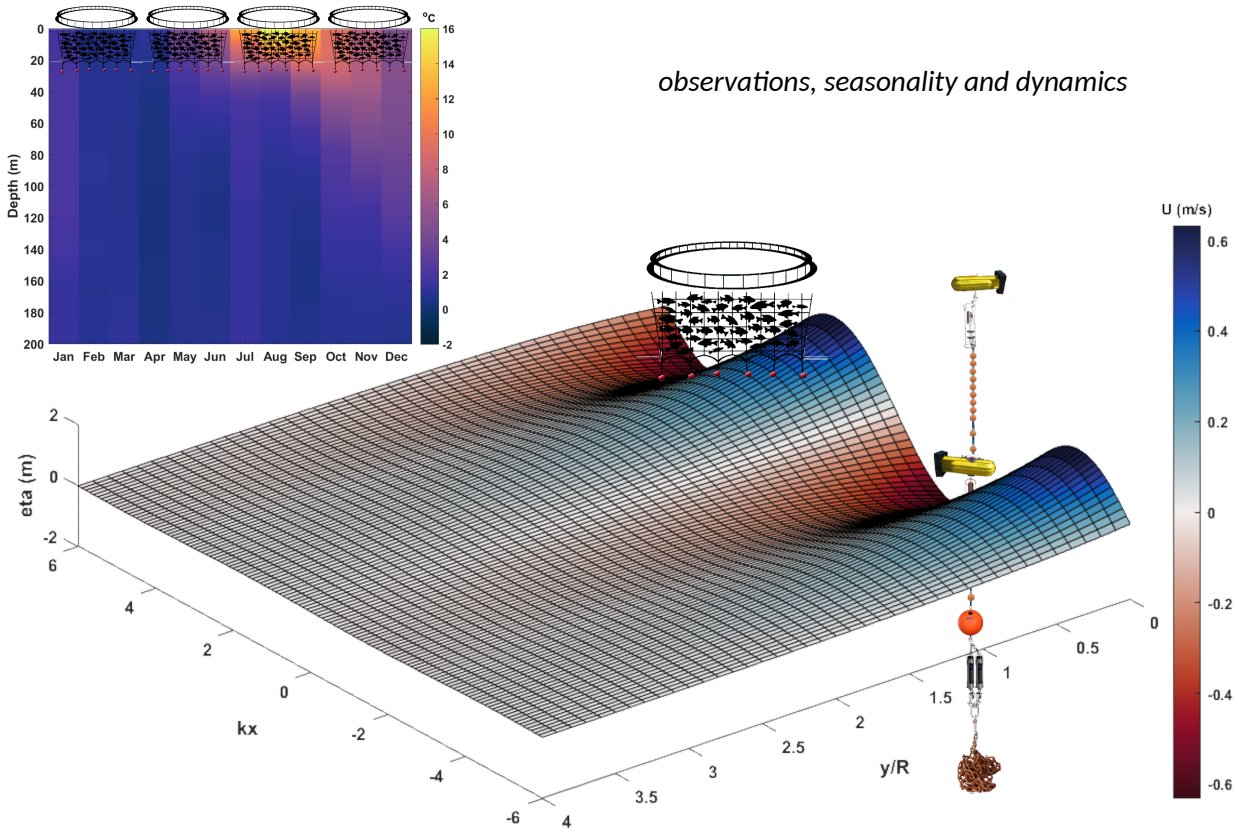


*Illustrations summarizing key elements of this thesis. On the top left, the seasonal cycle of the temperature of Fortune Bay, as a whole and from the surface to 200 m, is represented. This plot is overlaid by a drawing of fish that are farmed in the region in open nets within the first 20 to 40 m, typically. On the bottom left, the propagation of a Kelvin wave is shown along with an open net and an oceanographic mooring such as used in this study. The x and y axis represent the distance (x) as a function of the wave number (k) and the distance (y) as a function of the Rossby radius (R); they are unitless. On the z axis, the elevation (eta) from a state of rest (zero) is used. The colors represent the horizontal current (U), flowing parallel to the coast. The colors are set so that currents associated with a cold phase (upwelling) are blue and currents associated with a warm phase (downwelling) are red. This plot is not strictly correct in the sense that it represents the solution of a 2 d period, barotropic wave of amplitude 2 m over an ocean of 100 m depth. In this study, baroclinic waves about 10 times larger in amplitude were observed for similar horizontal currents.*

*Source: the Kelvin wave solutions used to make the plot are from Simpson and Sharples, 2012. Introduction to the Physical and Biological Oceanography of Shelf Seas, Cambridge University press, 424 p. (eq. 3.68, p78).*

# Concluding remarks and critique

This thesis aimed at observing, describing, and identifying the main mechanisms responsible for the current variability of the upper layers (first 150 m) of Fortune Bay, a broad fjord of Eastern Canada. While arguably regionally focused, several aspects brought here and learned from this study could be usefull to the broader community. This is discussed below along with a critique of the limitations of the study as well as proposed ways forward and potential applications.

Chapter 1 describes the challenges and successes in making observations in a broad embayment, subject to the effect of rotation as well as large seasonal and higher frequency variability in both stratification and ocean currents. The program took place in two main phases: a first phase aiming at observing the upper two layers of the fjord in their entirety, i.e. first 150 m, at four sites (2015-16) and a second phase trading the vertical extent of the ocean currents observations (from 150 m to 80 m) for the collection of data at more sites (from 4 to 10), thereby increasing the horizontal sampling resolution (2016-17). Though not without setbacks, the program achieved a usable data return of 90% (from initial expectations).

While not novel, a relatively simple method for continuously observing water thermal and current structure simultaneously, i.e. stratification and dynamics, is presented. By using Dyneema ropes and simple, low-cost, temperature loggers the mooring line was both of low drag (small rope diameter) and high vertical resolution (up to 2 m resolution in our case but could easily be increased). More expensive salinity sensors were placed at the most useful depths; that is within the upper, seasonally stratified, layer and within the deeper and more stable, layer. These mooring lines have proven to be effective in this environment, that is: a strongly stratified environment subject to currents up to about 1 knot (0.5 m/s). They allow simultaneous measurement of key physical parameters, high vertical resolution and were subject to minimal tilt (<5 degrees, on average) and knock down (5-15 m max for a mooring depth of order 150 m). The use of SUBS, a streamlined flotation devise reducing drag and improving mooring stability, also limited the tilt effect for the ADCPs. They are also fairly easy to manipulate (e.g. ropes can be stored in totes during deployment) which allow them to be deployed from small boats (e.g. we redeployed F3B08 in June 2016, in 200 m depth, using a 25 ft fibreglass boat). In environments with stronger currents, similar design could be used but would need added buoyancy. In fact, we used the same design in one of the most narrow entrance of Fortune Bay (strait between mainland and the island of Saint-Pierre) later on and the line performed well up to about 0.75 m/s where tilt started to be too large for in-line mounted ADCPs (SUBS would have performed better, though). In further deployments done in neighbouring bays, we added buoyancy between the top of the line and ADCP location which led to an appreciable improvement in both deployment (less probability for line entanglement) and in-situ behaviour. Based on this experience and that of others (Yao, 1986; de Young and Sanderson, 1995; Hart et al., 1999; Schillinger et al., 2000; Tittensor et al., 2002a&b) nominal depths of 120-180 m would seem to be a good compromise to study the seasonality of the water stratification and of the main coastal dynamics of higher frequency occurring on the shelf-slope regions around Newfoundland (sub-inertial upwelling and downwelling events, namely). At such depths, a more complete picture of the water column dynamics could be obtained using a couple of 300 kHz ADCPs mounted side by side and looking upward and downward (simultaneously). This is, in fact, a design that we are currently testing in another fjord of the Newfoundland south coast with expected recovery in September 2022. Such lines should capture the seasonal surface stratification processes (build-up and break-down) as evidenced by our

data (chapter 2) as well as most of the coastal upwelling and downwelling variability. The latter assumes, of-course, that the 120-180 m isobaths would be within one internal Rossby radius away from the coast (i.e. around 5 km), which is often the case in the large bays surrounding the island (see chapter 2 for a map and list of those major bays). Most deep-water renewal processes, however, which occur in many of the deep embayment of the island would be missed by such observations. This later aspect would probably be more important on the south coast which is influenced by the presence of the deep, warm, salty and of low dissolved oxygen content water mass of Atlantic origin (see chapter 2) than on the northern shore which is isolated from this water mass. Concurrent wind observations are also critical, as for being the main forcing agent and are unfortunately not always available locally and thus require careful consideration when designing an oceanographic experiment in this region. Another interest and motivation into making this chapter was to provide the entire dataset collected publicly and to make it easily accessible to the community. This is also not novel and is a practice that is becoming more common nowadays thanks to the initiatives of publishers such as Copernicus Publications (via their Earth System Science Data journal) and repository providers such as SEANOE (among others) and to the more recent and more overarching FAIR Data initiative (COPDESS, 2022). Yet, we did not find many other examples of comparable dataset collected in similar environment, i.e. broad fjord, at the time, hopefully making it of interest to not only the local but also the broader community.

Despite its successes, several aspects of the observation program limited the analysis of the system in important ways. Of all the limitations, perhaps the two most important of all were the near-surface gap in observations from the moorings (first 5-15 m) and the absence of cross-shore measurements. Because of the former, an important part of the estuarine circulation may have been missed (as seen in chapter 2) and because of the latter, cross-shore variability could not be captured; hindering a direct assessment of the potential effect of the bathymetry on the oceanic response studied in chapter 3 (namely, coastal trapped waves). Obviously, and as stated in the introduction, equipment availability is not limitless and trade-offs are necessary but, if further observation-based investigations were to be taken in this area, these aspects should be considered carefully.

Finally, in the rapidly evolving context of operational oceanography and associated permanent observatories (see Brink and Kirincich 2017, Davidson et al. 2019, de Young et al. 2019 and Revelard et al. 2022 for recent reviews, among others) it is hoped that the results of this study can help in designing and selecting sites of interest. The location of a recently deployed surface buoy in the outer part of Fortune Bay as part of the Smart Bay program (SmartAtlantic, 2022) could, for instance, be revisited. Hence, should it be located within one internal Rossby radius from the coast (5 km), its observations (e.g. temperature) could be very helpful in predicting the conditions to be expected in the inner part of the bay up to few days in advance (i.e. upwelling or downwelling; that is, cold or warm water conditions; as shown in chapter 3 where the aquaculture activities occur.

In chapter 2 we make use of this newly collected dataset as well as data collected historically to provide a general overview of the physical oceanography of the area at, mainly, seasonal scale. The preparation of this state of knowledge appeared timely given the important gaps identified at the beginning of the project (listed in the introduction) and given the time span since studies dedicated to this fjord occurred (more than 30 years). This effort led to: 1/ the establishment of the water column seasonal stratification allowing the

deduction of some of the likely processes acting on it such as local freshwater runoff, surface wind forcing (inducing mixing) and deep water renewal (along with shelf influence); 2/ a presentation of the mean circulation based on the newly acquired, longer-term, data; 3/ a confirmation of the weather band (i.e. wind) as being the dominant source of currents variability; 4/ the identification of current pulses and associated pycnocline fluctuations (downwelling and upwelling events) propagating coherently around the fjord; 5/ the confirmation of the tide as being a second order player in the currents variability and to the appreciable presence of both higher and lower frequency barotropic signals attributed to potential seiche and shelf oscillations (respectively) and 6/ some estimates of water flushing rate (or renewal) for all the layers of the system. This study also lays the ground for the more focused, process-oriented, study presented in chapter 3 by providing with a broader view, and physical context, of the study site.

This overview is somewhat unusual in the sense that it does not build upon a large literature of the area but, rather, provides analyses based on recent surveys and on historical data that had not been fully exploited yet. The reason for this is mainly due to the limited amount of previous studies available in the region and to the newly acquired set of observations still unexploited. That said, this comprehensive description should not only be useful to the local community but could also serve as an illustrated example of the physical settings and dynamics of broad fjords more generally. Examples alike include the works of Svendsen (1995), Svendsen et al. (2002) and Lundesgaard et al. (2020) but do not seem to abound. Those examples follow a similar approach, that is: a description of the physical setting (bathymetry and water column structure, mainly) and forces acting upon (tides, winds and buoyancy inputs) with an overarching goal of understanding the balance of forces, their variability (typically at seasonal scale) and, eventually for some, to provide estimate of water exchanges.

Beside the local and larger context of broad fjord studies, it appeared important to contribute to the regional one. Hence, while there is a large body of literature dedicated to the shelf (e.g. see Petrie and Anderson, 1983, Loder et al., 1998 and Ma et al., 2016 and references therein) as well as sustained monitoring programs (DFO, 2022) there is, to this day, just over a dozen of published papers dedicated to the physical oceanography of the inner (coastal) waters of Newfoundland (Yao 1986, de Young and Hay 1987, Hay and de Young 1989, de Young et al. 1993a & b, White and Hay 1994, de Young and Sanderson 1995, Davidson et al. 2001, Ma et al. 2012, Salcedo and Ratsimandresy 2013, Ratsimandresy et al. 2014, Ma et al. 2017, Xu et al. 2019 and Ratsimandresy et al. 2020). That is, perhaps, on the order of 10 times less than for the shelf. This is despite their importance to fisheries as being nursing areas for cod and caplins (Buren et al., 2014) and to their importance to the growing development of the aquaculture sector (both finfish and shellfish, see DFA 2014 for a review) and other coastal activities. It is thus hoped that the results of this work will help shed more light to this interesting environment which is still, in many regards, largely unknown.

A number of future analyses could be done to refine and/or build upon this study. A quantification of the baroclinic vs barotropic contributions as well as cross-spectrum correlations and rotary spectrum could help understanding what processes are taking into effect and when (during the year). Similarly, EOF (Empirical Orthogonal Functions) analyses would also be useful in qualifying and quantifying the process(es). These would complement the numerical modeling results presented in Chapter 3. Exchanges with the shelf could be further studied using the long-term data collected at Station 27; a site located on the eastern side of the island, about 450 km upstream from Fortune Bay (in the sense of the main current flowing on the shelf). Quantifying these exchanges for the upper and intermediate layers would be particularly useful.

Chapter 3 is a process-oriented study that focuses on what appeared to be the dominant dynamics occurring during the stratified season from the results of chapter 2 (May to November). That is, large downwelling and upwelling events associated with strong along-shore currents. This study follows suite and was strongly inspired by the previous works that took place on the Northern shore of the island in the 80s and 90s and which demonstrated the importance of internal Kelvin wave dynamics in large embayment similar to ours (in a sense of bay width vs. internal Rossby radius, stratification seasonality, great depths and of steep slopes). Hence, Yao (1986), using current meters and temperature data collected at 4 sites around Trinity Bay (see Figure 1 of chapter 2 and 3) showed that during the spring-fall periods (June to October) the currents were strongly correlated with local winds (>50%) and could be reproduced (to an extent) using the forced internal Kelvin waves analytical model of Gill and Clarke (1974). De Young et al. (1993b) went a little further, using a reduced gravity model which considered a realistic coastline and a larger scale system encompassing two adjacent bays (including Trinity Bay). Davidson (2001) studied the local response of Trinity Bay in more details and pointed out the importance of non-linearity in the response as well as the second order importance of the bathymetry on surface currents. With the benefit of technology advances since, we could observe the oceanic response in much more details and implement a more sophisticated model considering not only a realistic coastline and large enough domain to include neighbouring bays but also realistic stratification, vertical mixing and non-linear effects. We show that not only the remote response is important to the local (receiving) system, as was shown by de Young et al. (1993b), but also that the interaction between responses is not straight forward (i.e. non-linear) and can play a significant role in the amplitude of the events occurring downstream.

The importance of coastal upwelling & downwelling dynamics to the regional fisheries has been long recognized (e.g. Templeman 1966). Their effects on nursing grounds, in particular, has been studied by several authors (e.g. Frank and Leggett, 1982, Taggart and Leggett, 1987, Ings et al., 2008). Unfortunately, there seems to be long-standing confusions regarding the basic mechanisms of upwelling & downwelling in the fisheries community in terms of the role played by the wind forcing and on how a stratified ocean bounded by a coast responds to it. In particular, on the scale (thus coherence of the response) and on the forcing direction that matter (cross-shore vs. along-shore winds) as well as on the importance of the propagation of the disturbances (as demonstrated by Gill and Clarke 1974). It is an issue that was described by Mertz et al (1994) which shed a good light in distinguishing the effects and importance of cross-shore wind vs. along-shore wind but which, on the other hand, did not account for disturbances propagation accurately. Given the potential importance of this process on the recruitment of a keystone specie such as Capelin, whose role is fundamental to the rest of the food chain (Buren et al., 2014), it seems clear that a more systematic consideration of the process described here and earlier on by Yao (1986) and de Young et al. (1993b), in particular, is necessary.

Beside the need of more holistic ecoystem approach, much work remains in the comprehension of the physical environment. Among the most important questions to resolve about the internal Kelvin wave dynamics presented here, finding out the underlying mechanism at the origin of the change in wave shape while it propagates within the fjord is certainly one. That is, why does a locally generated downwelling increases in amplitude and diminishes in wavelength while a locally generated upwelling increases in wavelength but does not change in amplitude? Another-one concerns the change of phase speed while propagating around the inner bay. Our results seems to contradict Clarke (1976) theory of increasing wave

speed around a bay. Possibly, the complicated shape of the main head, with its prominent headlands, have a role in this and precludes a smooth travel, resulting in some reflection. Finally, another unanswered problem concerns the change of frequency in the response of the system to frequent forcing, as identified in the observations in September 2016. Propagation speed between subsequent waves and/or reflection effects might be at play but need to be investigated more thoroughly. Beside internal Kelvin wave dynamics, more general coastal trapped wave dynamics could be investigated by implementing a realistic bathymetry. One interesting question or outcome of this could be to find out how are the waves changing from the outer part of the bay where shelf is wide (and thus S is small) to the inner part of the bay where the shelf is narrow (and S increases). This could be complemented with a targeted, and of smaller scale than for this study, mooring deployment to support (validate) the numerical results. Refinement with the wind forcing could also be undertaken by applying spatially varying wind fields, instead of our single-point assumption. Determining the residual circulation induced by the main process studied here or in the future (i.e. internal Kelvin waves or coastal trapped waves) and its effect(s) on water renewals would be useful in untangling the net effect of this process versus all the others mentioned in chapter 2.

Direct applications of this work could include: sealice and virus dispersion as well as water renewal and oxygen content availability which are all critical issues currently facing the aquaculture activities in Fortune Bay (e.g. Hamoutene et al., 2022, Romero et al., 2022, Fisheries and Marine Institute of Memorial University of Newfoundland, 2020). Examples of such applications in the Canadian context can be found in Stucchi et al. (2011) for sealice, Foreman et al. (2015) for the ISA virus and Page et al. (2005) for dissolved oxygen. Dispersion of lobster larvae could also be of interest given the importance of this fishery at local and regional levels (DFO, 2021). Dispersion studies related to invasive species such as green crab and tunicate would also be of benefit to its management and possible mitigation(s) (Matheson et al., 2016).

In summary, this thesis was motivated by a need to better understand the physical environment in which farmed fish are being raised at a rapidly increasing level. This rapid development is putting pressure on an environment that is otherwise not well known and in which other human activities (fisheries) are taking place; thereby raising potential conflicts of environmental usage. To manage these activities in a sustainable way, a solid science background is necessary and this work shall only be a small, but certainly not negligible, part in it. Much work remains regarding, for example, aquaculture-environment interactions such as sea-lice and virus spread, carrying capacity including oxygen availability vs use and better assessments of sea-bottom organic loading from the farms. Questions regarding fish and crustacean larvae as well as those pertaining to the growing pressure of invasive species spread in the region could also finds direct answers using the results of this work.

Further work is also needed to refine and extend the analyses provided here. Better flushing rates estimates (e.g. using the results of the numerical model and/or further simulations) as well as a proper consideration of the bathymetry by the numerical model and simulations over longer periods and/or for different seasons (i.e. stratification conditions) are only few of the critical aspects to tackle in order to respond to the issues listed above.

This study also sits in a larger regional context of coastal dynamics in a cold environment, strongly stratified seasonally and dominated by wind forcing and shelf exchanges. It was inspired by earlier efforts that took place in the region and, hopefully, will prove to be a meaningful contribution regionally. It is also hoped that

it will find interest and be useful to the larger community working in coastal environments, in particular the one working in similar fjords.

# REFERENCES


Brink, K.H., Kirincich, A.R., 2017. Some considerations about coastal ocean observing systems. j mar res 75, 161–188. https://doi.org/10.1357/002224017821836743

Buren, A.D., Koen-Alonso, M., Pepin, P., Mowbray, F., Nakashima, B., Stenson, G., Ollerhead, N., Montevecchi, W.A., 2014. Bottom-Up Regulation of Capelin, a Keystone Forage Species. PLoS ONE 9, e87589. https://doi.org/10.1371/journal.pone.0087589

Clarke, A.J., 1976. Coastal Upwelling and Coastally Trapped Long Waves. (PhD Thesis). University of Cambridge.

COPDESS, 2022. Coalition for Publishing Data in the Earth and Space Sciences [WWW Document]. URL https://copdess.org/ (accessed 13-Sep-2022)

Cyr, F., Snook, S., Bishop, C., Galbraith, P.S., Chen, N., Han, G., 2022. Physical oceanographic conditions on the Newfoundland and Labrador shelf during 2021 (DFO Can. Sci. Advis. Sec. Res. Doc. No. 2022/040). https://waves-vagues.dfo-mpo.gc.ca/library-bibliotheque/40960754.pdf (accessed 26-Sep-2022)

Davidson, F., Alvera-Azcárate, A., Barth, A., Brassington, G.B., Chassignet, E.P., Clementi, E., De Mey-Frémaux, P., Divakaran, P., Harris, C., Hernandez, F., Hogan, P., Hole, L.R., Holt, J., Liu, G., Lu, Y., Lorente, P., Maksymczuk, J., Martin, M., Mehra, A., Melsom, A., Mo, H., Moore, A., Oddo, P., Pascual, A., Pequignet, A.-C., Kourafalou, V., Ryan, A., Siddorn, J., Smith, G., Spindler, D., Spindler, T., Stanev, E.V., Staneva, J., Storto, A., Tanajura, C., Vinayachandran, P.N., Wan, L., Wang, H., Zhang, Y., Zhu, X., Zu, Z., 2019. Synergies in Operational Oceanography: The Intrinsic Need for Sustained Ocean Observations. Front. Mar. Sci. 6, 450. https://doi.org/10.3389/fmars.2019.00450

Davidson, F.J.M., Greatbatch, R.J., de Young, B., 2001. Asymmetry in the response of a stratified coastal embayment to wind forcing. J. Geophys. Res. 106, 7001–7015. https://doi.org/10.1029/2000JC900052

de Young, B., Greatbatch, R.J., Forward, K.B., 1993a. A Diagnostic Coastal Circulation Model with Application to Conception Bay, Newfoundland. Journal of Physical Oceanography 23, 2617–2635. https://doi.org/10.1175/1520-0485(1993)023<2617:ADCCMW>2.0.CO;2

de Young, B., Hay, A.E., 1987. Density Current Flow into Fortune Bay, Newfoundland. J. Phys. Oceanogr. 17, 1066–1070. https://doi.org/10.1175/1520-0485(1987)017<1066:DCFIFB>2.0.CO;2

de Young, B., Otterson, T., Greatbatch, R.J., 1993b. The Local and Nonlocal Response of Conception Bay to Wind Forcing. Journal of Physical Oceanography 23, 2636–2649. https://doi.org/10.1175/1520-0485(1993)023<2636:TLANRO>2.0.CO;2

de Young, B., Sanderson, B., 1995. The circulation and hydrography of conception bay, Newfoundland. Atmosphere-Ocean 33, 135–162. https://doi.org/10.1080/07055900.1995.9649528

de Young, B., Visbeck, M., de Araujo Filho, M.C., Baringer, M.O., Black, C., Buch, E., Canonico, G., Coelho, P., Duha, J.T., Edwards, M., Fischer, A., Fritz, J.-S., Ketelhake, S., Muelbert, J.-H., Monteiro, P., Nolan, G.,

O'Rourke, E., Ott, M., Le Traon, P.Y., Pouliquen, S., Sousa-Pinto, I., Tanhua, T., Velho, F.V., Willis, Z., 2019. An Integrated All-Atlantic Ocean Observing System in 2030. Front. Mar. Sci. 6, 428. https://doi.org/10.3389/fmars.2019.00428

Department of Fisheries and Aquaculture, 2014. Economic impacts of the newfoundland and Labrador aquaculture industry. Newfoundland and Labrador, St John's. NL. https://www.gov.nl.ca/ffa/files/publications-pdf-aquaculture-macro-final.pdf (accessed 27-Sep-2022)

DFO, 2021. Assessment of American Lobster in Newfoundland (DFO Can. Sci. Advis. Sec. Sci. Advis. Rep. No. 2021/008). Fisheries and Oceans Canada. https://waves-vagues.dfo-mpo.gc.ca/library-bibliotheque/40965788.pdf (accessed 27-Sep-2022)

Fisheries and Oceans Canada, 2022. Atlantic Zone Monitoring Program (AZMP) [WWW Document]. URL https://www.dfo-mpo.gc.ca/science/data-donnees/azmp-pmza/index-eng.html (accessed 27-Sep-2022)

Foreman, M.G.G., Guo, M., Garver, K.A., Stucchi, D., Chandler, P., Wan, D., Morrison, J., Tuele, D., 2015. Modelling Infectious Hematopoietic Necrosis Virus Dispersion from Marine Salmon Farms in the Discovery Islands, British Columbia, Canada. PLoS ONE 10, e0130951. https://doi.org/10.1371/journal.pone.0130951

Frank, K.T., Leggett, W.C., 1982. Coastal Water Mass Replacement: Its Effect on Zooplankton Dynamics and the Predator–Prey Complex Associated with Larval Capelin ( Mallotus villosus ). Can. J. Fish. Aquat. Sci. 39, 991–1003. https://doi.org/10.1139/f82-134

Gill, A.E., Clarke, A.J., 1974. Wind-induced upwelling, coastal currents and sea-level changes. Deep Sea Research and Oceanographic Abstracts 21, 325–345. https://doi.org/10.1016/0011-7471(74)90038-2

Hamoutene, D., Oldford, V., Donnet, S., 2022. Drug and pesticide usage for sea lice treatment in salmon aquaculture sites in a Canadian province from 2016 to 2019. Sci Rep 12, 4475. https://doi.org/10.1038/s41598-022-08538-w

Hart, D.J., De Young, B., Foley, J.S., 1999. Observations of Currents, Temperature and Salinity in Placentia Bay, Newfoundland 1998-9 (Data Report No. 99–3). Department of Physics and Physical Oceanography, Memorial University of Newfoundland, St. John's, NL. https://www.physics.mun.ca/~bdeyoung/hart-deyoun_placentia_bay_1999.pdf (accessed 26-Sep-2022)

Hay, A.E., de Young, B., 1989. An oceanographic flip-flop: deep water exchange in Fortune Bay, Newfoundland. J. Geophys. Res. 94, 843. https://doi.org/10.1029/JC094iC01p00843

Ings, D.W., Gregory, R.S., Schneider, D.C., 2008. Episodic downwelling predicts recruitment of Atlantic cod, Greenland cod and white hake to Newfoundland coastal waters. J Mar Res 66, 529–561. https://doi.org/10.1357/002224008787157476

Leggett, W.C., Frank, K.T., Carscadden, J.E., 1984. Meteorological and Hydrographic Regulation of Year-Class Strength in Capelin ( Mallotus villosus ). Can. J. Fish. Aquat. Sci. 41, 1193–1201. https://doi.org/10.1139/f84-141

Loder, J.W., Petrie, B., Gawarkiewicz, G., 1998. The coastal ocean off northeastern North America: A large-scale view. The sea 11, 105–138.

Lundesgaard, Ø., Winsor, P., Truffer, M., Merrifield, M., Powell, B., Statscewich, H., Eidam, E., Smith, C.R.,

2020. Hydrography and energetics of a cold subpolar fjord: Andvord Bay, western Antarctic Peninsula. Progress in Oceanography 181, 102224. https://doi.org/10.1016/j.pocean.2019.102224

Ma, Z., Han, G., Chassé, J., 2016. Simulation of Circulation and Ice over the Newfoundland and Labrador Shelves: The Mean and Seasonal Cycle. Atmosphere-Ocean 54, 248–263. https://doi.org/10.1080/07055900.2015.1077325

Ma, Z., Han, G., de Young, B., 2017. Modelling the response of Placentia Bay to hurricanes Igor and Leslie. Ocean Modelling 112, 112–124. https://doi.org/10.1016/j.ocemod.2017.03.002

Ma, Z., Han, G., deYoung, B., 2012. Modelling Temperature, Currents and Stratification in Placentia Bay. Atmosphere-Ocean 50, 244–260. https://doi.org/10.1080/07055900.2012.677413

Matheson, K., McKenzie, C., Gregory, R., Robichaud, D., Bradbury, I., Snelgrove, P., Rose, G., 2016. Linking eelgrass decline and impacts on associated fish communities to European green crab Carcinus maenas invasion. Mar. Ecol. Prog. Ser. 548, 31–45. https://doi.org/10.3354/meps11674

Mertz, G., Helbig, J.A., Colbourne, E., 1994. Revisiting Newfoundland capelin (Mallotus villosus) recruitment: is there a wind effect? Journal of Northwest Atlantic Fishery Science 17.

Petrie, B., Anderson, C., 1983. Circulation on the newfoundland continental shelf. Atmosphere-Ocean 21, 207–226. https://doi.org/10.1080/07055900.1983.9649165

Ratsimandresy, A.W., Donnet, S., Goulet, P., 2020. Identification of geographic zones of influence associated with surface circulation for Aquaculture Bay Management Area application. Journal of Marine Systems 204, 103291. https://doi.org/10.1016/j.jmarsys.2019.103291

Ratsimandresy, A.W., Donnet, S., Goulet, P., Bachmayer, R., Claus, B., 2014. Variation in the structure of the water column as captured by Slocum glider CTD and by CTD from a research vessel and assessment of internal waves, in: 2014 Oceans - St. John's. Presented at the OCEANS 2014, IEEE, St. John's, NL, pp. 1–10. https://doi.org/10.1109/OCEANS.2014.7003283

Révelard, A., Tintoré, J., Verron, J., Bahurel, P., Barth, J.A., Belbéoch, M., Benveniste, J., Bonnefond, P., Chassignet, E.P., Cravatte, S., Davidson, F., deYoung, B., Heupel, M., Heslop, E., Hörstmann, C., Karstensen, J., Le Traon, P.Y., Marques, M., McLean, C., Medina, R., Paluszkiewicz, T., Pascual, A., Pearlman, J., Petihakis, G., Pinardi, N., Pouliquen, S., Rayner, R., Shepherd, I., Sprintall, J., Tanhua, T., Testor, P., Seppälä, J., Siddorn, J., Thomsen, S., Valdés, L., Visbeck, M., Waite, A.M., Werner, F., Wilkin, J., Williams, B., 2022. Ocean Integration: The Needs and Challenges of Effective Coordination Within the Ocean Observing System. Front. Mar. Sci. 8, 737671. https://doi.org/10.3389/fmars.2021.737671

Romero, J.F., Gardner, I.A., Hammell, L., Groman, D., Whelan, D., O'Brien, N., Hawkins, L.J., Burnley, H., Thakur, K., 2022. Descriptive epidemiology of variants of infectious salmon anaemia virus in four Atlantic salmon farms in Newfoundland and Labrador, Canada. Journal of Fish Diseases 45, 919–930. https://doi.org/10.1111/jfd.13617

Salcedo-Castro, J., Ratsimandresy, A.W., 2013. Oceanographic response to the passage of hurricanes in Belle Bay, Newfoundland. Estuarine, Coastal and Shelf Science 133, 224–234. https://doi.org/10.1016/j.ecss.2013.08.031

Schillinger, D.J., Simmons, P., De Young, B., 2000. Analysis of the mean circulation in Placentia Bay: spring

and summer 1999 (Data Report No. 2000–1). Department of Physics and Physical Oceanography, Memorial University of Newfoundland. https://www.physics.mun.ca/~bdeyoung/schillinger_placentiabay_2000-1.pdf (accessed 26-Sep-2022)

SmartAtlantic, 2022. Fortune Bay Buoy [WWW Document]. URL https://www.smartatlantic.ca/station_alt.html?id=fortune_bay (accessed 13-Sep-2022)

Stucchi, D.J., Guo, M., Foreman, M.G.G., Czajko, P., Galbraith, M., Mackas, D.L., Gillibrand, P.A., 2011. Modeling Sea Lice Production and Concentrations in the Broughton Archipelago, British Columbia, in: Jones, S., Beamish, R. (Eds.), Salmon Lice. Wiley, pp. 117–150. https://doi.org/10.1002/9780470961568.ch4

Svendsen, H., 1995. Physical oceanography of coupled fjord-coast systems in northern Norway with special focus on frontal dynamics and tides. Ecology of fjords and coastal waters 149–164.

Svendsen, H., Beszczynska-Møller, A., Hagen, J.O., Lefauconnier, B., Tverberg, V., Gerland, S., Børre Ørbæk, J., Bischof, K., Papucci, C., Zajaczkowski, M., Azzolini, R., Bruland, O., Wiencke, C., 2002. The physical environment of Kongsfjorden–Krossfjorden, an Arctic fjord system in Svalbard. Polar Research 21, 133–166. https://doi.org/10.3402/polar.v21i1.6479

Taggart, C.T., Leggett, W.C., 1987. Wind-Forced Hydrodynamics and Their Interaction with Larval Fish and Plankton Abundance: A Time-Series Analysis of Physical–Biological Data. Can. J. Fish. Aquat. Sci. 44, 438–451. https://doi.org/10.1139/f87-052

Templeman, W., 1966. Marine resources of Newfoundland. Bull. Fish. Res. Bd Can. 154, 170.

Tittensor, D.P., De Young, B., Foley, J., 2002a. Analysis of physical oceanographic data from Trinity Bay, May-August 2002 (Data Report No. 2002–2). Department of Physics and Physical Oceanography, Memorial University of Newfoundland. https://www.physics.mun.ca/~bdeyoung/tittensor_trinity_bay_2002-2.pdf (accessed 26-Sep-2022)

Tittensor, D.P., Richard, N., De Young, B., Foley, J., 2002b. Analysis of physical oceanographic data from Trinity Bay, May-August 2001 (Data Report No. 2002–1). Department of Physics and Physical Oceanography, Memorial University of Newfoundland. https://www.physics.mun.ca/~bdeyoung/tittensor_trinitybay_2002-1.pdf (accessed 26-Sep-2022)

White, M., Hay, A.E., 1994. Dense overflow into a large silled embayment: Tidal modulation, fronts and basin modes. issn: 0022-2402 52, 459–487. https://doi.org/10.1357/0022240943077055

Xu, G., Han, G., Dong, C., Yang, J., DeYoung, B., 2019. Observing and Modeling the Response of Placentia Bay to an Extratropical Cyclone. Atmosphere 10, 724. https://doi.org/10.3390/atmos10110724

Yao, T., 1986. The response of currents in Trinity Bay, Newfoundland, to local wind forcing. Atmosphere-Ocean 24, 235–252. https://doi.org/10.1080/07055900.1986.9649249

# Afterword

Music is a very important companion of my life. Most of this work was accomplished while listening to vibes that, one way or another, inspired my thoughts and/or gave me strength to persevere.

It has been said (I think) that music is a universal language, which I would agree. It has also been said that language is a source of misunderstandings; which I also agree. In the end, I believe that we should all pay more attention into communicating with each-other not just with words; they are simply too limiting.

Only a small sample of those vibes is listed below as I only started to roughly keep track of it during the last stage of writing. Perhaps some of those will inspire you and/or 'transport' you in a similar way that it did to me. Whatever it does to you, though, and if you ever try some of those, I hope it to be good.

_ ACDC: Thunderstruck, Hells Bells and probably others

_ Alain Bashung: Bleu Petrole (whole album)

_ Alborosie: Diversity, Herbalist, The Rising Stars Riddim, Streets, Tribal War and many others

_ Ali Farka Toure: Talking Timbuktu (whole album)

_ Alpha: ComeFromHeaven (whole album)

_ Amadou et Mariam: un Dimanche a Bamako (whole album)

_ Amy Winehouse:  Back to Black (whole album is worth)

_ Anis: Gadjo Decale and La Chance (whole albums)

_ Ayo: Joyful (whole album)

_ Batlik; 99 pas (#03) | Si (#12) | En arriere (#14) [album Utilité, whole album is worth]

_ Benabar: Bénabar, Couche-tard et lève-tot and Les Risques du métier (too many songs to chose from)

_ Block Party: Silent Party (just about the whole album)

_ Bon Iver: Bon Iver (whole album)

_ Bonobo: just about anything from Animal Magic, One offs remixes, Sweetness and Dial m for monkey.

_ Cafe del Mar: Desire (Ambient Mix) in particular

_ Coldplay: Parachutes, A Rush Of Blood To The Head & X&Y (too many songs to chose from)

_ Daft Punk: Random Access Memory (whole album; 10th anniversary edition also well worth it)

_ Deadmau5: Right this second & Raise Your Weapon

_ Dire Straits: Brothers In Arms

_ Eminem: Rabbit Run and 8 mile

_ Ennio Morricone: The very best of (whole collection, 2000)

_ Errors (How Clean is Your Acid House): Mr Milk

_ Fridge (The Sun): Comets (#07) and Years and Years (#10)

_ Francis Cabrel: Des Roses Et Des Orties & Sarbacane (whole albums)

_ Gainsbourg: "Electronica" (whole album) and "Bad news from the stars" (whole album) (#10, in particular)

_ Gramatik: Day of The So Called Glory, Who Got Juice, The Uprising, The Unfallen Kingdom, Fiesta and many others

_ Greg Anderson (Forecast 1): Birth 2.0

_ Gregoire Lourme: Letters Home (from 1914-1918 Never Forget) & Memories (from Life)

_ Johnny Cash: American Recordings (I-VI), in particular (too many songs to list), Folsom Prison also a must.

_ Kraked Unit: La Ballade de Neus (Les Poupées Russes soundtrack)

_ Lemon Jelly: a good number from Lost Horizon and Ky

_ M83: You and the Night (whole album)

_ Manu Chao: Por la Caratera, Mentira [and whole Clandestino album] + so many others

_ Mattafix: Signs of a Struggle (whole album)

_ Moby: Whispering Wind and quite a few others from albums 18, Hotel and Play

_ Neil Young and the Crazy Horse: Live at the Fillmore 1970 (#3 and #6, in particular; favourite of Random Island road).

_ Nordgroove (Suburban Simphony): Stars go down

_ Oursvince (Dragon Flight): Falling Stars

_ Pink Flyod: The Dark Side of the Moon (whole album) and Division Bell (whole album)

_ StrangeZero (Rapidly Unexpected): Burnin Star

_ Sweet Play (Colours Of The Day): Light of Freedom

_ The Polish Ambassador (Pushing Through The Pavement): Gathering of the Tribes

_ Thievery Corporation: too many to list from Abductions and Reconstructions, The Mirror Conspiracy, Cosmic Game and Radio Retaliation, in particular

_ Tiken Jah Fakoly: L'Africain (whole album), Africain Revolution (#1 and #7; in particular)

_ Xavier Rudd: To Let, 9 Times a Day and any with didgeridoo (Live in Canada rocks)

_ Zen Circus: Catene and Viva from Vivi si muore album

_ Movie soundtracks: Amelie Poulain, Drive, Blade Runner, De rouille et d'os, Deja mort, Dune, Kill Bill, L'auberge Espagnole, Le Grand Bleu, Les Choristes, Les Poupées Russes, Matrix, Snatch.

“Les grandes personnes ne comprennent jamais rien toutes seules, et c'est fatigant, pour les enfants, de toujours et toujours leur donner des explications.”

Le Petit Prince (1943).

DOCTORAT SCIENCES BRETAGNE DE LA MER LOIRE ET DU LITTORAL

Université de Bretagne Occidentale

Titre : Océanographie physique d'un large fjord des latitudes moyennes: observations, saisonnalité et réponse au vent de la baie de Fortune (Terre-Neuve, Canada).

**Mots clés :** fjord, climat sub-arctique, vent, downwelling & upwelling, onde interne de Kelvin, mouillage.

**Résumé :** Cette thèse porte sur l'environnement physique de la baie de Fortune, un grand fjord de latitude moyenne situé à Terre-Neuve, au Canada. Elle présente les résultats de deux années d'observations continues ainsi que l'analyse de données historiques et de simulations de modèles numériques. Les observations nouvellement recueillies révèlent la présence de signaux cohérents de downwelling et de upwelling, associés à de vigoureux courants littoraux, se propageant de manière cyclonique autour du fjord. Avec les données historiques, elles permettent également de déterminer le climat saisonnier de la structure de l'eau et certains de ses principaux forçages (vent, marées et ruissellement d'eau douce) ainsi que certaines mesures de la variabilité interannuelle. La mise en œuvre d'un modèle numérique tridimensionnel entièrement non-linéaire permet d'identifier le processus principal responsable de ces signaux dominants ainsi que leur origine et certaines de leurs caractéristiques de propagation.

Il est démontré que la baie de Fortune est fortement stratifiée de façon saisonnière étant influencée par le ruissellement local d'eau douce, le forçage éolien et l'apport du plateau. Elle est plus chaude que le plateau à la fois à la surface et à une profondeur intermédiaire en raison de la stratification saline pour la première et du renouvellement des eaux profondes chaudes pour la seconde. Le renouvellement des eaux profondes se produit deux fois par an à partir de deux masses d'eau distinctes, l'une froide et relativement douce pendant l'été, l'autre chaude et salée pendant l'hiver. La circulation moyenne est plutôt faible ainsi que l'influence des marées. Les courants sont dominés par la bande météorologique et sont très variables. La saison stratifiée est dominée dynamiquement par des impulsions de courant barocline transitoires associées à des événements de downwelling et de upwelling. Ces événements se traduisent principalement par de longues ondes de Kelvin internes qui sont générées à la fois localement et à distance. La génération de signaux locaux et distants entraîne des interactions assez complexes qui peuvent augmenter ou diminuer l'amplitude de la réponse dans le fjord. L'effet de la forme et de la dimension des baies sur ces signaux est aussi suspecté mais n'a pas été clairement déterminé.

Title : The Physical Oceanography of a broad, mid-latitude fjord: observations, seasonality and wind response of Fortune Bay (Newfoundland, Canada).

**Keywords :** broad fjord, sub-arctic climate, wind, downwelling & upwelling, internal Kelvin wave, mooring.

**Abstract :** This thesis is concerned with the physical environment of Fortune Bay, a mid-latitude broad fjord located in Newfoundland, Canada. It presents the results of 2-years of continuous observations as well as of the analysis of historical records and numerical model simulations. Newly collected observations reveal the presence of coherent downwelling and upwelling signals, associated with vigorous alongshore currents, propagating cyclonically around the fjord. Along with the historical data, they also allow the determination of the seasonal climate of the water structure and some of its main forcing (wind, tides and freshwater runoff) as well as some measures of inter-annual variability. The implementation of a fully non-linear, 3-dimensional, numerical model allows the identification of the main process responsible for those dominant signals as well as their origin and some of their propagation characteristics.

It is shown that Fortune Bay is seasonally and strongly stratified; influenced by local freshwater runoff, wind forcing and shelf input and that it is warmer than the shelf both at the surface and at intermediary depth due to saline stratification for the former and warm deep water renewal for the latter. Deep water renewal occurs bi-annually from two distinct water masses, one cold and fresh during the summer, the other warm and salty during the winter. Mean circulation is rather weak and so is the tidal influence. Currents are dominated by the weather band and are highly variable. The stratified season is dynamically dominated by transient baroclinic current pulses associated with downwelling and upwelling events. Those events are predominantly expressed as long internal Kelvin waves which are generated both locally and remotely. The generation of local and remote signals result in rather complex interactions which can enhance or diminish the amplitude of the response within the fjord. The effect of bay' shape and dimension on the signals is suspected but was not clearly determined.